THE UTILISATION OF INFORMATION AVIALABLE IN A SENSORLESS CONTROL SYSTEM OF AN AC INDUCTION MOTOR FOR CONDITION MONITORING

by

SAMIEH A. ABU SAAD

A thesis submitted to the University of Huddersfield in partial fulfilment of the requirements for the degree of Doctor of Philosophy

December 2015

Abstract

Induction motor driven mechanical transmission systems are widely utilised in many applications across numerous sectors including industry, power generation and transportation. They are however subject to common failure modes primarily associated with faults in the driven mechanical components. Notably, gearboxes, couplings and bearings can cause significant defects in both the electrical and mechanical systems. Condition monitoring (CM) undertakes a key role in the detection of potential defects in the early development stages and in turn avoiding catastrophic operational and financial consequences caused by unplanned breakdowns. Meanwhile, variable speed drives (VSDs) have been increasingly deployed in recent years to achieve accurate speed control and higher operational efficiency. Among the different speed control designs, sensorless VSDs deliver improved dynamic performance and obviate speed measurement devices. This solution however results in heightened noise levels and continual changes in the power supply parameters that potentially impede the detection of minute fault features.

This study addresses the gap identified through a systematic review of the literature on the monitoring of mechanical systems utilise induction motors (IM) with sensorless VSDs. Specifically, existing techniques prove ineffective for common mechanical faults that develop in gearboxes and friction induced scenarios. The primary aim of this research centres on the development of a more effective and accurate diagnostic solution for VSD systems using the data available in a VSD. An experimental research approach is based to model and simulate VSD systems under different fault conditions and gather in-depth data on changes in electrical supply parameters: current, voltage and power. Corresponding techniques including model based methods and dynamic signature analysis methods were developed for extracting the changes from noise measurements.

An observer based detection technique is developed based on speed and flux observers that are deployed to generate power residuals. Both static and dynamic techniques are incorporated for the first time in order to detect the mechanical misalignment and lubrication degradation, each with different degrees of severities. The results of this study

demonstrate that observer based approaches utilising power residual signalling can be effective in the identification of different faults in the monitoring of sensorless VSD driven mechanical systems. Specifically, the combination between dynamic and static components of the power supply parameters and control data has proved effective in separating the four types of common faults: shaft misalignment, lubricant shortage, viscosity changes and water contamination. The static data based approach outperforms the dynamic data based approach in detecting shaft misalignments under sensorless operating modes. The dynamic components of power signals, however, records superior results in the detection of different oil degradation problems. Nevertheless, static components of torque related variables, power and voltage can be used jointly in separating the three tested lubricant faults.

Acknowledgements

I would like first to express my sincere gratitude to Prof. Andrew Ball for his continued support, assistance and immense knowledge provided during the course of my research. I appreciate his patience motivation and skills that have greatly enriched my graduate experience. I would like also to thank him for the guidance and opportunity to write, publish and participate in international conferences.

My thanks are also extended to my second supervisor, Dr Fengshou Gu, whose expertise, encouragement and direction were vital in completing my research project and writing this thesis. His persistence, understanding and kindness enabled me to develop a robust theoretical framework in a logical and consistent manner and guided me to perform experimental work to the highest standards. These words fail to fully convey my appreciation and deepest gratitude, and I am in his debt.

I would like also to convey my thanks to all colleagues at the Centre for Efficiency and Performance Engineering and research fellows and staff members who have over the years made my time such a great experience on a professional and personal level.

Last but not least, I would especially like to thank and dedicate this thesis to my wonderful family, my wife, daughters: Hadeel, Heiam and Hedayah; and sons: Abdulmohaimen, Abdulmomin, for their continued support, encouragement and love. A special and grateful thanks to my mother, soul of my father and all my brothers and sisters for their high expectations and belief in me.

Statement of Originality

I hereby certify that all of the work described within this thesis is the original work of the author. Any published (or unpublished) ideas and/or techniques from the work of others are fully acknowledged in accordance with the standard referencing practices.

(Samieh Abu Saad)

Publications

1. Abusaad, S., Benghozzi, A., Shao, Y., Gu, F. and Ball, A. (2013) 'Utilizing Data from a Sensorless AC Variable Speed Drive for Detecting Mechanical Misalignments' Key Engineering Materials , 569, pp. 465-472. ISSN 1013-9826

2. Abusaad, S., Benghozzi, A., Brethee, K., Gu, F. and Ball, A. (2014) 'Investigating the Effect of Water Contamination on Gearbox Lubrication based upon Motor Control Data from a Sensorless Drive '. In: 3rd International Workshop and Congress on eMaintenance, 17th - 18th June 2014, Lulea, Sweden

3. Abusaad, S., Benghozzi, A., Smith, A., Gu, F. and Ball, A. (2015) 'The Detection of Shaft Misalignments Using Motor Current Signals from a Sensorless Variable Speed Drive'. In: Vibration Engineering and Technology of Machinery. : Springer. pp. 173-182. ISBN 978-3-319-09918-7

4. Abusaad, S., Brethee, K., Assaeh, M., Zhang, R., Gu, F., & Ball, A. D. (2015, July). 'The detection of lubricating oil viscosity changes in gearbox transmission systems driven by sensorless variable speed drives using electrical supply parameters'. In Journal of Physics: Conference Series (Vol. 628, No. 1, p. 012078). IOP Publishing, 2015.

5. Abusaad, S., Gu, F. and Ball, A. (2015) 'Observer-based Fault Detection and Diagnosis for Mechanical Transmission Systems with Sensorless Variable Speed Drives'. In: 28th International Congress of Condition Monitoring and Diagnostic Engineering Management (COMADEM 2015), 1st - 4th December 2015, Buenos Aires, Argentina

6. Shaeboub, A., Abusaad, S., Hu, N., Gu, F. and Ball, A. (2015) 'Detection and Diagnosis of Motor Stator Faults using Electric Signals from Variable Speed Drives'. In: Proceedings of the 21st International Conference on Automation and Computing (ICAC). : IEEE. . ISBN 978-0-9926801-0-7

Table of Contents

List of Figures

List of Tables

List of Abbreviations

u_{sd}	The d axis stator phase voltage
u_{sq}	The q axis stator phase voltage
i_{sd}	The d axis stator phase current
i_{sq}	The q axis stator phase current
R_s	Stator resistance
R_r	R resistance
ψ_s	Stator flux
ψ_r	Rotor flux
L_{ls}	Stator leakage inductance
L_{lr}	Rotor leakage inductance
L_s	Stator inductance
L_r	Rotor inductance
σ	Motor leakage coefficient
T_e	Electromagnetic torque
T_l	Load torque
J	Load and motor total inertia
B_m	System viscose friction coefficient
L_m	Motor mutual inductance
T_r	Rotor time constant
Subscripts d and q	Represent the d-q reference frame coordinates
Subscripts α and β	Represent the stationery reference frame coordinates
f_s	Electrical source frequency
ω_e, ω_s	Motor synchronous (electrical) angular frequency
ω_r, ω_m	Rotor angular mechanical frequency
ω_{sl}	Slip angular frequency
N_p	Motor pole number
α_I	The phase angle between voltage and current
α_ψ	The phase angle between stator flux and voltage
C_{out}	PI controller output
K_p	PI controller proportional gain
K_i	PI controller integral gain
K_d	PI controller integral gain

Chapter 1

Introduction

1.1 Introduction

Condition monitoring represents a vital area of technology for operational excellence in industry. It is critically dependent on a number of key elements: precise understanding of the construction and performance of the monitored machines; failure behaviour; analysis of signals; signal processing and presentation in a comprehensible and informative way [1, 2].

AC induction motors (ACIM) are the major prime movers and actuators in industrial motion control systems. A number of advantages are associated with these kinds of motors: reliability, simplified construction and jagged-based design; low operating cost; direct connection to an AC power supply; and long life span and premium energy [1, 3]. They are, however, subject to several failure modes, mainly due to faults in the driven mechanical system components. For instance components in gearbox transmission systems such as gearboxes, couplings and bearings can cause significant defects in both the electrical and mechanical systems [5].

The importance of induction motors and their cost in addition to the costs of failure have emphasised the necessity of performing condition monitoring (CM) in order to enhance the ability to detect defects developing in the early stages and thus avoid unplanned breakdowns. Furthermore, they perform an important role in maximising machine efficiency, performance and life span while improving the reliability of induction motors and driven machines [3, 5].

Many applications of induction motor (IM) driven systems require accurate speed regulation and good dynamic response to different load and speed operational conditions. This generates a requirement for VSDs and more complex closed loop speed/torque control systems [6]. Different speed control schemes are offered in the market and options vary depending on the requirements of each application. For

instance, the basic V/Hz (open-loop) scheme is applied when precise speed control and/or full torque at high speeds is not required. On the other hand closed-loop schemes with speed feedback measuring devices provide an accurate speed regulation, whereas vector control schemes allow for optimum dynamic performance when necessary for some applications, with or without speed measuring devices (Sensorless VSDs) [7].

Sensorless VSDs are widely utilised in many industrial applications. They enable precise control of the IM speed without speed feedback sensors. Sensorless VSDs have a higher level of dynamic performance, lower cost and greater reliability. Such drives provide accurate steady-state and stable transient operations [8]. However in order to maintain speed and torque, the drive's control system acts on the power supply parameters thereby altering its behaviour and increases the noise levels. Such actions can considerably influence the condition monitoring scheme in the case of a developing fault within the mechanical system [6].

In addition mechanical transmission systems are exposed to mechanical faults that can influence the operation of the system and may cause catastrophic. Problems in the driven mechanical systems, such as mechanical shaft misalignment, water contaminated oil, oil viscosity change and lubrication shortages are very common in industry [110, 111, 125, 128-129]. The detection of such faults in the mechanical driven systems under sensorless VSD is not yet well discovered.

This research focuses on assessing the data available from an AC three phase asynchronous squirrel-cage induction motor control system and investigates the use of control parameters as a source for condition monitoring. Experimental tests are undertaken based on a 13kW transmission system to replicate real common faults across different degrees of severity. Namely, mechanical misalignment, water contaminated lubrication, oil viscosity change and lubrication shortages are tested. All faults investigated in degrees typical of such faults in industrial situations. Analysis of the data available from the control system is used to explain relationship between the developed faults and control system behaviour and response. The primary aim is to develop a new cost effective and reliable condition monitoring technique based on the information available from sensorless ACIM VSDs.

1.2 Background

Numerous techniques have been reported and examined for monitoring conditions of equipment. The monitored conditions and the type of the machine restrict the approach utilised. Vibration analysis (machinery vibration), temperature monitoring (thermal measurements), motor current signature analysis (MCSA), and acoustics are some of the commonly used CM techniques. Studies in this area have focused on improving the reliability and certainty of CM systems as well as decreasing implementation costs [10].

Ideally, efficient and effective condition monitoring needs to be implemented with minimal data collection and instrumentation, within a fast, accurate and clear analytical and processing scheme. Several attempts have been performed to achieve such requirements [11, 12].

Nonetheless, faults in the driven mechanical transmission system, such as mechanical misalignment and lubrication degradation, may cause additional speed and load oscillations and change in the power consumed by the drive. Mechanical problems, such as mechanical shaft misalignment, lubrication degradation, can change the behaviour of the control system [110, 111, 125, 128-129].

That is the sensorless VSD continuously acts on the motor's supply parameters and changes its values in order to maintain the system speed stable at the reference [13]. In the event of a fault in the mechanical system, the oscillations the fault causes are treated by the control system as disturbances. The drive changes the power fed to the motor to compensate for these oscillations to stabilise system performance. As the fault deteriorates, the power fed to the motor by the drive may also increase leading to catastrophic failure.

Moreover, the drive manipulates the power supply variables such as frequency, current and voltage to adjust the speed and the torque of the induction motor which may change the features that are normally used for fault detection and diagnosis. Therefore fault detection approaches developed for line-fed or open loop controlled IM need to be revised when applied to those fed by closed loop VSDs. The influences of uncertainties related to non-stationary signals, nonlinearity of the machine model, accuracy of

parameters estimation and tuning parameters of the observers and regulators as well as the control process actions need to be considered [5, 6, 14].

Rapid development in technology and control system theory has greatly impacted the field of condition monitoring and fault detection driving it toward the development of increasingly advanced techniques that can be used in such complex systems. Many approaches have been advanced for systems driven with VSD proposing the detection of several faults that may occur within the induction machine. Among these approaches, observer based fault detection has been widely researched over the last few years and proven effective [15].

On a basic level, an observer based fault detection scheme is developed to generate an alarm in the event of a fault. A comparison between estimated and measured states is made to generate residual signals. Fault alert is raised when the residual signal exceeds a pre-set threshold. Further action is then required, either online (automatically) or off line, to locate the fault and to estimate its severity by performing additional analysis.

Therefore, in this research the observer based fault detection scheme is developed based on observers which are utilised for control purposes. The research focuses on the detection of mechanical faults within the mechanical transmission systems. Particularly, mechanical shaft misalignment, water in oil contamination, oil viscosity changes and less lubrication, which are common problems in industry, are discovered.

1.3 Research Motivation

Conventional condition monitoring techniques generally require supplementary equipment, such as sensors, data processing and acquisition system, in addition to data analysis rendering such techniques costly. Further drawbacks include limited accessibility in terms of mounting sensors and transducers, sensor location, sensitivity and the interference of other environmental and ambient parameters [16]. Additionally, when sensorless VSDs exist, conventional techniques may not be valid as the VSD changes the supply parameters and increases the level of noise due to actions by the regulators which mask faults.

This issue underlines an increasing need to explore power supply parameters and control data in mechanical systems driven with closed loop VSDs in order to develop more reliable and cost effective fault detection and diagnosis schemes [16]. That is these drives make available a wide range of parameters, data and signals that can be further analysed and checked for their behaviour in cases of abnormalities. Data include line current and voltage signal measurements; state observers such as speed, flux and torque; and calculated variables such as direct and quadrature current components [9].

One of the main advantages of diagnosing mechanical systems faults using power supply parameters and control data is that control information is already available at the drive. Additionally, terminal signals are passed through all the drive regulators for speed regulation. Hence, signals inside the drive such as estimated state parameters, error signals and regulators outputs may contain information about the health of the system [14, 16].

To conclude, the main advantages of using data from a sensorless ACIM VSDs for fault diagnosis and condition monitoring include, but are not limited to:

- The fact that as most AC drives are microprocessor based, allows for an imbedded CM scheme. Drives can be simply connected with computers either via the network or locally and data can be extracted directly for off line and/or online remote CM.
- Signals utilised by the control system are already available at the drive and can be investigated for the CM purposes simultaneously, without additional measurements.
- A wide range of information can be obtained including current, voltage and frequency as well as induction motor parameters and state variables.
- Operators and maintenance engineers can be encouraged in the monitoring process as they possess in-depth understanding of the relevant control system and processes under their operation.
- Processed signals are mostly related to the system being monitored, thereby reducing interference with other equipment signals.
- Prevention of the use of additional equipment and sensors, avoids many related issues such as space, location, reliability, accuracy and noise.

- Removes need for system modifications as all signals already available. Parameters only need to be extracted from the drive to the processing computer when remote or off line analysis is conducted.
- In most cases drives are connected to the control room via a network which simplifies the remote online condition monitoring process while avoiding further expense.

It would be economical and reliable to develop a condition monitoring and diagnosis technique based on the data and tools already available at the control system. Control and operational engineers have enhanced understanding of the operations and processes being monitored, and are therefore well placed and capable to indicate faults within the machine during their routine duties. Utilising control parameters to identify and locate different mechanical faults on the downstream system can dramatically improve the machine's availability and increase the reliability of the condition monitoring system. Furthermore, in addition to enhancing equipment performance, monitoring costs are significantly decreased.

1.4 Research Aim and Objective

1.4.1 Research Aim

This study aims to discover the diagnostic information from data available at the sensorless AC induction motor VSDs. It further seeks to identify the potential of developing a new cost effective and reliable approach for condition monitoring of mechanical systems by using information and signals available in sensorless ACIM VSDs for fault detection and diagnosis. The work includes the development of a mechanical fault detection technique based on the control system incorporated by the sensorless VSD.

1.4.2 Research Objectives

The principal goal of this research is to investigate the potential of leveraging existing data and tools present in typical sensorless VSDs to perform condition monitoring and

fault diagnosis in a driven mechanical gear transmission system. In order to fulfil the research goal a number of objectives are identified and prioritised as follows:

Objective 1. To develop an observer based fault detection scheme based on the available observers in sensorless VSDs.

Objective 2. To investigate residuals generation scheme from the developed observers to detect common mechanical fault under different operation conditions.

Objective 3. To investigate/evaluate the diagnostic capability of the available information in the sensorless VSDs. This includes an effective data analysis scheme to explore the potential for detecting the mechanical faults without the need for additional resources.

Objective 4. To replicate common mechanical faults in gear transmission systems driven with industrial sensorless VSDs. Faults are in degrees typical of such faults in industrial situations.

Objective 5. To perform a literature review and establish the theory, evidence and knowledge gaps in relation to the application of control system for the detection of mechanical faults within driven mechanical systems.

Objective 6. To theoretically study the response of the IM VSD in the case of mechanical load oscillations using induction motor and VSD's models.

1.5 Structure of the Thesis

The thesis represents the work performed for achieving the research aim and the stated objectives. It is divided into nine chapters including the current chapter, as follows:

Chapter 2 - presents the literature reviews on the existing CM and fault detection techniques applied for ACIM driven mechanical systems and ACIM driven with VSDs. The objective is to support improved understanding in the field into the problems which can arise when sensorless variable speed drives are utilised for driving mechanical gear transmission systems. This assists in avoiding replication of previous work.

Chapter 3 - describes the basic principles of the ACIM and the theoretical background of the field oriented variable speed drives, focusing on the sensorless VSDs. It

includes details on the sensorless speed estimation based on model reference adaptive system (MRAS).

Chapter 4 - details the test facility used for the study and lists the equipment used together with specifications and operating principles of the rig. Test procedures and faults seeding are also detailed in this chapter.

Chapter 5 - presents the mathematical models of the ACIM and the sensorless variable speed drive; mechanical and electrical equations of the induction motor are explained. The model is based on the ready to use models provided by SimPowerSystems™ component libraries which are available from the MATLab/Simulink environment. The model is used to study the influence of load oscillations on the drive's response and power supply parameters.

Chapter 6 - explains the principles of the observer based fault detection schemes and discusses the theoretical aspects of the field. It also describes the observers developed in this study for the fault detection method suggested. The residual generation and evaluation is also presented in this chapter.

Chapter 7 - provides an in-depth discussion of the results obtained from the tests conducted using one of the most mechanical common gearbox transmission systems faults. The discussion addresses both open loop and sensorless characteristics in the healthy and faulty cases. The baseline data is compared with the corresponding data from faulty tests and both static and dynamic data of power supply and control parameters are presented and analysed.

Chapter 8 - discusses in detail the results obtained from the tests performed using different lubricating common faults with different degrees of severities. The baseline data is compared with the corresponding data from faulty tests. Both static and dynamic data of power supply and control parameters are presented and analysed.

Chapter 9 - presents conclusions based on the findings and outlines recommendations for future work.

Figure 1.1 outlines the general structure of the research work and the scheme developed.

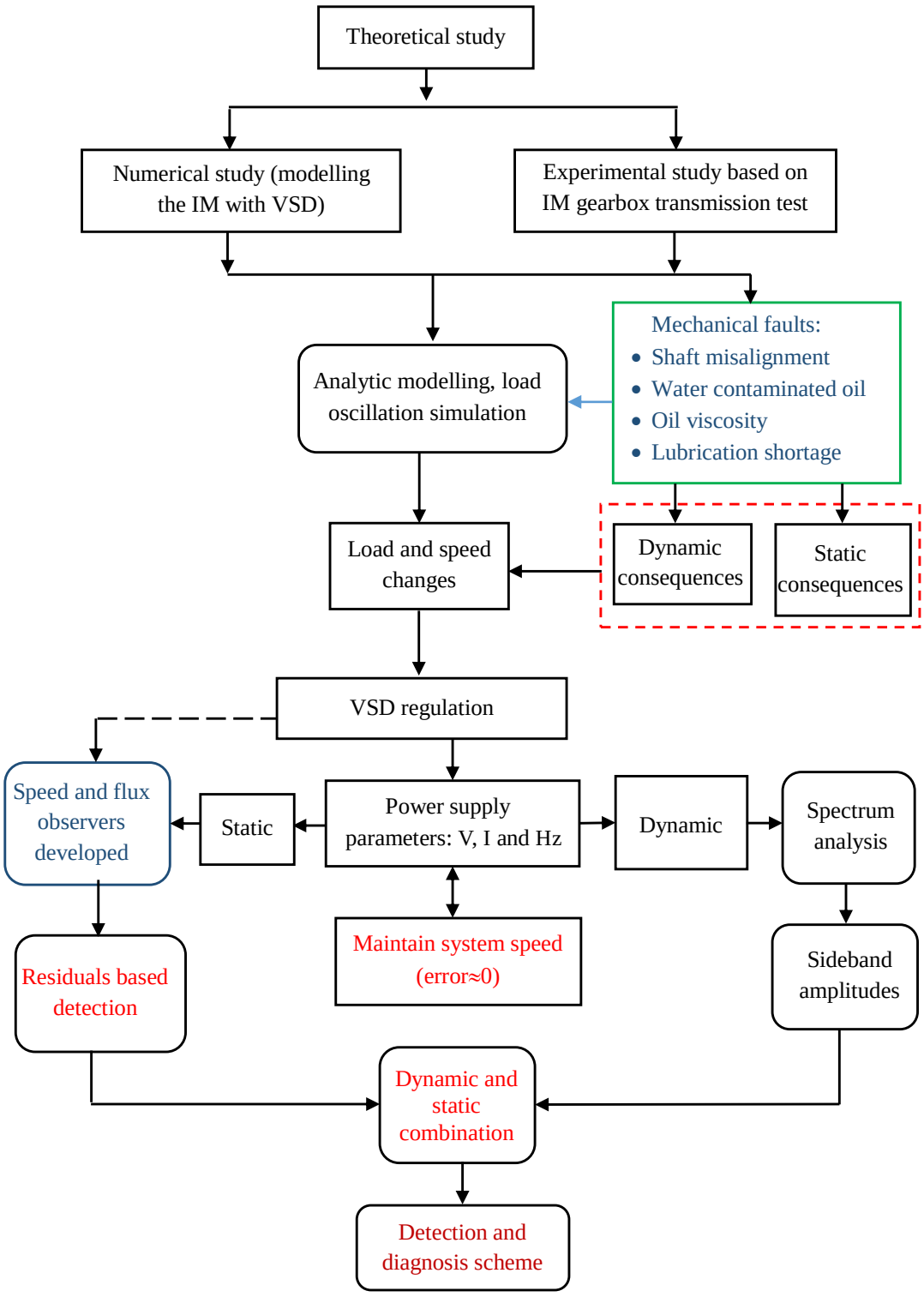

Figure 1.1 The research work and the developed scheme flowchart

Chapter 2
Literature Review

This chapter reviews the literature on the existing CM and fault detection techniques applied for ACIM driven mechanical systems and ACIM driven with VSDs. It includes a summary of the main benefits of using the condition monitoring systems and lists some of the most prevalent traditionally applied schemes. It also contains a review of condition monitoring techniques and their application in industry when the control system is included in the monitored machines.

2.1 Introduction

According to Tavner et al, (2008) condition monitoring (CM) can be defined as "the continuous evaluation of the health of plant and equipment throughout its serviceable life". The CM is principally developed to assess the physical characteristics that identify the current machine conditions and utilise these measures to anticipate and/or identify potential faults. However, CM may be attempted to include protection, but its main essential function is to identify any changes in machine behaviour and anticipate faults at an early stage. Such process would provide a desirable advanced warning that can be used to recognise the need for maintenance at an earlier stage and gives more time to maintenance engineers to schedule interruptions in a suitable manner, resulting in minor capitalised losses and reduced down time [5].

2.2 The Importance of Condition Monitoring

Advantages obtained by applying the CM strategies include but are not limited to [17]:

- Ensuring longer operating periods,
- Decreasing number of unplanned breakdowns,
- Reducing total maintenance costs,
- Enhancing operators and equipment safety,
- Improving manufacturing efficiency,
- Reducing the spare parts inventory

- Improving machine reliability and availability
- Bettering machines performance and productivity

A CM system should have the capability to provide an accurate information in relation to the state of the machines, anticipating the needs for maintenance prior to severe deterioration, failure or breakdown. This must incorporate clear detection, fault location and diagnosis combined, when possible, with an approximation of the machine's lifespan [5, 17]. Analysis and interpretation of CM systems can be conducted offline by experts, and can also be performed online by utilising advanced technologies.

2.3 Conventional CM Systems for Induction Machines

Conventional CM systems normally comprise four key elements. They are shown in Figure 2-1 [5].

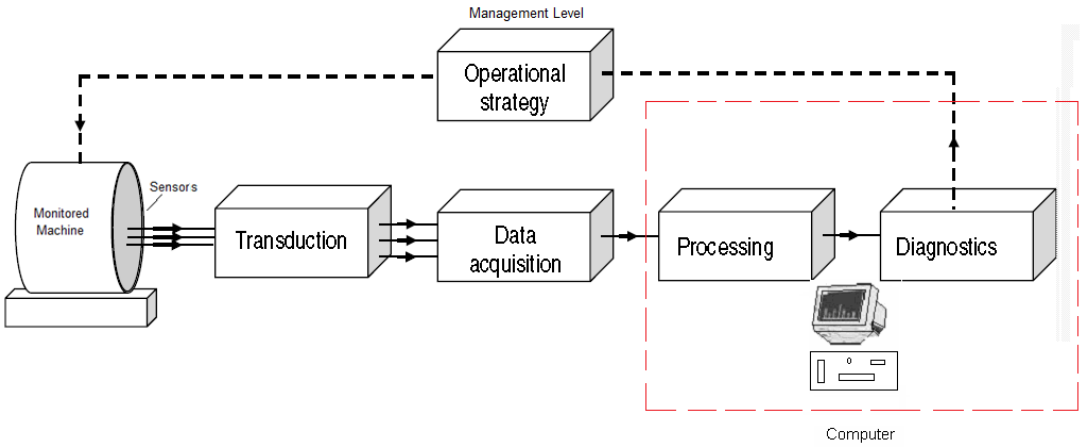

Figure 2.1 Key elements of a conventional condition monitoring, amended from [5]

As shown in Figure 2.1, conventional CM systems normally comprise [5]:

- ✓ Sensors which provide real information about the monitored equipment to the CM system. Signals from sensors may be treated in order to be suitable for the data acquisition system.
- ✓ Data acquisition system which acquires, amplifies and pre-processes signals from sensors making them available for analysis and diagnoses.
- ✓ Signal processing and diagnosis with the primary purpose to investigate the acquired signals and discover changes from the "normal" conditions.

Conventionally, a wide variety of techniques have been developed and utilised to monitor conditions of a machine and all are noted to have their respective advantages and disadvantages [18]. Methods vary from visual inspection, vibration analysis and acoustic emission technique to ultrasound function, temperature monitoring and motor current signature analysis (MCSA) [19].

Selecting the appropriate CM technique is highly dependent on the process, machine or component being monitored and the objectives of maintenance services. For example, visual inspection can be adequate to investigate the health of a machine when near to fail; on the other hand advanced CM approaches need to be performed for sophisticated and complex course of actions [20]. However both monitoring costs and targets are taken into account when selecting the CM technique. In the following a brief summary of some of most common conventional CM techniques:

2.3.1 Visual Inspection

Visual inspection is a basic practice and the most generally used CM technique in industry [21]. It is conducted by experienced personal who visually investigate a machine to physically assess its condition and to detect any potential degradation, damage, or changes in the appearance. Tools and hand held equipment may be used for visual inspection to obtain more accurate and reliable results as well as to help inspectors in investigate parts or components which are neither clear nor directly visible [22].

Visual inspection provides instant information about the health of a machine condition. The main disadvantages of the visual inspection include [22] [21]:

- Individual base test, different inspectors may provide different reports for the same machine as people are comprised of varying skills, background and knowledge.
- Limited to visible and clearly apparent components and parts.
- Mostly required to be conducted while the machine is stationery, although some inspections need to be carried out while the machine is running.

- Need to be conducted by experienced and skilled operators and maintenance people. Therefore more workforce and maintenance time is required.

However, [21] emphasises that visual inspection of machinery and systems is vital and must be regularly performed in a plant as it can detect potential problems such as cracks, corrosion, and leaking that may missed by other CM techniques. Regular visual inspection of all significant machinery would enhance entire condition monitoring system and detect potential faults before serious damage may occur.

2.3.2 Vibration Monitoring

Vibration is one of the most pervasive and widely known condition monitoring and fault detection techniques. It provides useful information about the condition of components in the machine-driven chain [5].

A historical baseline of the machine's vibration level is created, and then compared with the current vibration level to assess the machine's condition. Numerous techniques have been developed for processing and analysing vibration signals which shown effective at detecting problems in a variety of equipment and components [5].

On the other hand, vibration based techniques are found to be inadequate and/or show poor diagnostic capability to detect faults in the early development stage [5].

Problems can arise for a number of different reasons including: the presence of different vibration and noise sources; presence of non-stationary phenomena; the influence of the transfer functions between vibration sources and transducers; transducers locations; and sophisticated and extreme signal processing needed to obtain better information [24].

2.3.3 Acoustic Emission Monitoring

The use of acoustic emissions (AE) for condition monitoring has advanced significantly in recent years. Machines usually generate noise and create vibration due to the contact of two media in motion. The AE methodology is used to analyse the produced acoustic and/or noise waveforms captured by microphones. Microphones are sensitive and easy to mount, and appropriate and comprehensive information can be obtained due to wide

frequency response ranges. Acoustic emissions can be identified in frequency ranges of 20 kHz to 1 MHz, and have been detailed at frequencies of up to 100 MHz. This technique has been found to be an effective option for gearboxes, bearings, tools and engines. Moreover, as acoustics are generated at micro level the technique is highly sensitive and provides the opportunity for identifying developed faults at an earlier stage when compared to certain other CM techniques [23].

However as a result of the fact that machines generate airborne noise, the acoustic waveforms can be contaminated by noisy background signals from similar neighbouring machinery. Effects also include interference from other related sound sources such as the driving motor, loading generator and cooling fan, and reflecting surfaces [25].

2.3.4 Temperature Monitoring (Thermal Measurements)

This technique conventionally involves the measurement of the temperature of specific areas such as stator core, bearings and drive windings. These measurements can provide indications of the changes occurring within the machine. Temperature measurement is critically effective if fitted in carefully selected locations. For instance bearings temperature is traditionally measured and, together with vibration measurements, can provide the standard approach to the assessment of these elements' condition [5].

However, temperature measurement also subjected to fundamental difficulty in resolving confusion between point temperature sensing that is easy to measure but provides local information only, and entire temperature measurements that are more difficult and run the risk of supervising local hot-points. One more issue with this method is monitoring the temperature of active and live parts, such as rotor windings and core [2].

2.3.5 Electrical Signature Analysis (ESA)

To address the problems of conventional fault detection methods, motor current signature analysis (MCSA) is suggested to detect a wide range of induction motor faults. Electrical signals are customarily measured for control purposes removing the

requirement for additional measurements [26]. Studies [26-28] have demonstrated that faults occurring in downstream driven equipment can be detected using the changes in the induction motor current signal. A wide body of research provides surveys on the condition monitoring techniques developed for induction motors and driven mechanical systems, for instance, [10-12, 17-19, 26, 29, 30], which provide an extensive overview on the fault detection and analysis schemes as well as signal processing techniques suggested for different faults that commonly occur in systems driven by induction motors. They are mainly based on analysis of the IM supply measurements and analysis.

Review of these studies reveals strong opportunities for the stator electrical signals analysis techniques to be exploited [28]. Further, studies have shown that IMS electrical supply signals can contain important information and components related to the health of the driven mechanical equipment such as pumps, mixers, gearboxes and conveyors. In particular, the IM rotation frequency component can be detected in the electrical signals spectra which constitutes the use of electrical supply signals to detect fault features such as those from gearboxes, bearing and shaft misalignments [9, 28].

Different strategies and analysis techniques have been suggested to extract such frequency components and fault features. For instance, Alwodai et al (2013) [31] have investigated the Bispectrum analysis of the induction motor current to detect and diagnose motor bearing faults. It was found that motor bearing faults causes small modulations to supply current components with high noise levels, therefore using a modulation signal bispectrum can overcome these issues and such defects on motor bearings could be detected. Benbouzid et al (1999) [32] examined different advanced analysis techniques on the motor current signal for detecting different induction motor faults. Faults tested included supply voltage imbalance, broken rotor bars, bearings failure and eccentricity. However a high resolution data analysis is required in order to extract clear information from the motor stator current signal.

MCSA has been also used to detect downstream equipment such as gear transmission systems; e.g. Chen et al (2012) [33] investigated the supply current measured from an induction motor for detecting faults in a gear transmission system using novel

modulation signal (MS) bispectrum method. Both gear faults and shaft misalignment have been detected using this technique. Kar and Mohanty (2004) [34] suggest replacing the conventional vibration monitoring method for mechanical transmission systems by analysing the motor current. The developed method tested on a multi-stage gearbox transmission system. A discrete wavelet transform (DWT) was used to decompose the current signal coupled with FFT analysis to extract the sidebands at high frequencies. The results show that DWT with MCSA can be utilised to replace conventional vibration monitoring. Current measurements have been used in [35] to detect planetary gearbox faults. The proposed approach investigates the spectrum region around the resonance frequency in the motor current signals to extract the feature components related to the planetary gearbox faults.

To conclude, MCSA has gained extensive interest in recent research however significant work remains to evaluate the proposed techniques and test their applicability for real life applications. Moreover further investigation may be required to extract better information, removing noise from the obtained current signal using less complicated calculations and reduced resources. Additionally, reviewed studies were mostly applied on directly fed or open loop controlled induction motors.

2.4 Control System Based Condition Monitoring

The previous section highlighted that most conventional condition monitoring techniques require additional equipment such as sensors, transducers, and data acquisition systems in order to gather information about machines being monitored. Moreover, a relatively skilled and trained human resource is critical to perform a range of tasks. These include the monitoring process, physical processes such as mounting sensors on machines and wiring them back to a device to gather data, and analysis and interpretation. These techniques are sophisticated and costly.

To perform an effective control, ACIM drives measure, calculate and estimate many parameters that affect the induction motor speed. That is AC current and voltage are measured at the drives' terminals. These signals then are used to control the speed and torque utilising certain calculations. Regardless of the control techniques being used by

the drive, most closed loop drives need these signals to perform an efficient control and provide the required performance.

The control system behaviour in relation to any changes can reflect the health of the system being controlled. Any signal treated inside the controller can carry a sign to a certain fault. In other words, any change in the driven mechanical system leads into a change in the system time constant and consequently the stability conditions, which appears in the response of the control system and can be observed on transient and/or steady state responses.

In this section a review on the previous work that has applied this idea is presented. The review is divided into two main parts. The first explores the application of such a scheme in industry while the other discusses the techniques developed for exploiting the control system in fault detection and diagnosis.

2.4.1 Application in Industry

The integration of control systems with monitoring conditions and fault detection has been successfully applied in different types of technical processes to improve performance, reliability and safety and reduce costs. Studies [36] show that there is an increasing interaction during fault development between the control system and process being controlled. A case study in [36] used evidence to demonstrate the advantages of including information from electrical and mechanical data proceeded by the control system for abnormality detection and CM system.

This system has been applied in various contexts including power generation stations, wind turbines, air plane engines, industrial robots and machine tools. For instance, the study in [37], reported the steps taken by TransGrid to apply an online condition monitoring system for the electrical grid managed by the company. The control system is incorporated with the monitoring system which led to improvements in the reliability and accuracy of the general performance of the grid and in particular the control system.

In aircrafts where a very high standard of safety is usually applied, the control system is used for early fault detection and diagnostic as suggested in [38]. An artificial immune system (AIS) algorithm is developed and applied for aircraft fault detection. The developed approach is based on the intelligent flight control (IFC) conventionally utilised in aircrafts. The approach detects any abnormalities from analysis data available at the control system that is used for the normal operational behaviour of the aircraft.

These approaches have also been developed in industries that include process control schemes. For example, [39] aimed to developing a robust condition monitoring and control strategy for condenser cooling water systems. A model based approach is used with a hybrid quick search (HQS) method for optimising system performance and at the same time for online fault detection and health monitoring.

Control data saved by the supervisory control and data acquisition (SCADA) has also attracted many researchers to use it for diagnostic and fault detection and analysis. For instance, in wind turbine generators [40-42] and industrial process [43-45].

To conclude, employing control system parameters and performance in fault detection and diagnostics has received attention in different industrial applications. Electrical grids, industrial processes, wind turbine generators and power generation are examples of applications in which fault detection techniques can be performed (or at least with assistance) through the control systems. It is well known that any changes in the controlled mechanical or electrical system will directly affect the response of the control system. Analysing the control system response and behaviour may lead to the detection of any abnormality within the system.

2.4.2 Techniques Applied for IM Driven Systems

Enormous amounts of articles have been published investigating different techniques and methods for the detection of mechanical and electrical faults occurring in ACIM drives. However, research on the detection of faults utilising signals and information from control systems and variable speed drives of the ACIMs is limited [5].

Bellini et al, (2000) [46] extensively studied the impact of IM closed loop control systems on the diagnostic and fault features. They claimed that the conventional fault detection methods may not be suitable for these systems. The amplitudes of specific frequency components introduced in different variables spectra by the faults are investigated and compared with the corresponding signals of open loop. Additionally, torque current component is found to have strong dependency with the drive control loop actions and load conditions. The study proposed instead to use the reference of the field current component which is, they report, independent of the drive control actions and the topology of a closed loop field-oriented controlled drive with constant flux control loop bandwidth. The proposed approach was tested on motors with broken rotor bar and stator shorted circuit. However, the study did not report on the correlation between the suggested indices and the faults tested.

Similarly, Cunha et al, (2007) [47] studied the d-q components of the stator current error signals, which are already existing at any closed loop controlled drives. The signals are passed through a band-pass digital filter bank and current signature analysis has been used to extract the required information. They concluded that appropriate features can be effectively utilised for diagnosis and detecting motor rotor asymmetry faults from the analysis of current components when the system is under field oriented controlled IMs.

A Vienna monitoring method (VMM) is proposed in [48] to detect rotor cage asymmetries for an inverter-fed drive. The machine's torque is estimated using two models, i.e. current model and voltage model. Any deviances in a rotor fixed reference frame are detected on the estimated torque signals. The proposed technique was examined only on a single rotor bar fault. Later in [49] the same authors improve this method to deploy it without speed feedback sensors.

A parameter estimation based technique is developed in [50] to detect inter-turn stator short circuits in the IM. The strategy developed employs the hyperbolic cross points (HCP) scheme to estimate certain parameters from the voltage and current data and applies the global optimisation algorithm to detect the faults tested.

As indicated in [51], speed regulators in the closed loop IMs drives can change the fault signature from the current signal into the voltage signal depending on the regulators bandwidth and fault feature frequency. Fault features that are higher than the speed regulator bandwidth, e.g. stator winding turn fault, are mostly found in the voltage signals. The study suggested the use of neural networks for detecting the stator winding turn faults in the voltage signals when a closed loop drive is used. These findings have been also confirmed in [52].

The impact of rotor faults on the field oriented control drives have also been discovered for faults detection. The estimated rotor flux [53], for instance, can provide indicative information about the health of the IM rotor. Rotor flux signals show good performance when time varying loads exist. Similar results have been reported in [54], where broken rotor bar (BRB) symptoms are clearly defined in the sensorless VSD. Nonetheless, they reported, tuning parameters of the controllers, observer design and observer tuning conditions are the most significant factors that affect the clarity of detecting corresponding features. Torque current components have been also analysed in [14] for detecting rotor faults. The strategy uses the ratio between amplitude at the frequency component of the rotor fault and the average of the torque current component to estimate the fault severity. The spectra of the power signals from sensorless control VSDs have been also used to detect and diagnose the broken rotor bars in IMs as illustrated in [55]. The study shows that the spectra of the power composes components at twice slip frequency and can effectively separate different broken rotor bars fault severities under sensorless control modes.

Mechanical faults inside the induction motor have also been considered when driven by FOC VSDs. Faults such as rotor eccentricity and bearings faults are critically studied in order to develop a fault detection scheme that considers the effect of closed loop actions. For instance, in [56] there is a comparison between the MCSA and estimated speed signals when load oscillations exist due to the bearing faults. The detection based on the current measurements relies on the frequency response of the drive control loops and has to be adjusted onto a certain fundamental frequency range. On the other hand, the detection based on the estimated speed provides wider frequency ranges and the

detection performance can be further improved by manipulating the dynamic of the speed observer.

The angular domain order tracking analysis (AD-OT) method is applied in [57] to detect static eccentricity faults in a FOC driven IM. The scheme is tested under different degrees of severities at different speed and load operation conditions. They claim that the use of AD-OT is advantageous as it is time and frequency invariant which makes it suitable for analysing stationary or non-stationary currents. However, it needs an encoder measuring device fitted.

When sensorless VSDs are used, terminal power supply parameters are incorporated together with IM mathematical models to estimate both flux and speed. Such estimation schemes basically relying on the state parameters observers. The observer estimates system variables to produce errors or residual signals in conjunction with corresponding measurements. The residual signals are then relied on to tune control parameters to maintain operational performance even if there are considerable disturbances such as noises and component faults [58, 59].

Notably, this control strategy outcomes provide robust control performances. However, it can result in adverse consequences to the system when faults progress to high severity. To prevent the occurrences of such consequences, different schemes have been suggested to include residuals from the observers in the fault detection and diagnosis tasks. For instance, the reference in [60] used a state observer to generate a vector of specific residuals for the detection of induction motor stator faults. The residuals are decompensated to obtain the negative sequence component which is then used as fault indicator. The study in [61] developed an observer based algorithm that is independent of load and speed oscillations and able to detect inter-turn short circuit faults in the stator. However, it was sensitive to motor parameters and needed to be adjusted for each motor condition and type.

To overcome the problem of parameter estimation and improve the accuracy of the observer based schemes, different approaches have been suggested. For instance [62] presented an induction motor parameter observer, where changes in the estimated

parameters can also be used for fault detection and localisation strategy. This method is used for stator and rotor faults detection. Observer based fault detection has also been widely used for current and speed sensors fault detection as proposed in [63-65].

On the other hand, the literature shows that the detection of faults in the mechanical systems driven by closed loop control drives has received less attention than those faults occur in the IMs [66]. The difficulties in monitoring the condition of the mechanical systems driven with closed loop controlled VSDs include: the fact that the fundamental supply frequency is widely changing [67], compensation effects of the drive which masks the features that these faults cause [66], and the high level of noise from the power electronic devices on the drive [46]. Even so, model based fault and monitoring strategy detection approaches which rely on observer schemes can provide better indication and allow for deep understanding of the process condition [68].

For example, in study [66] an approach is suggested to investigate the potential of detecting the gearbox features from the estimated load torque. A torsional load observer is developed in order to monitor the oscillations in the mechanical system. The estimated load oscillation is filtered using a first-order low-pass filter (PLPF) in order to keep the features of concern on the signal. However, the approach was not experimentally tested on real applications. Load torque oscillation has been also observed in [69] for detecting faults in mechanical transmission systems. The suggested observer is used for both control and fault detection purposes. Features such as those from gearbox related frequency components have been detected, with very small amplitudes, in the estimated load oscillations. However again the proposed observer is not tested on a faulty gearbox and real applications. Likewise, torsional vibration in systems driven by sensorless VSDs have been observed in [66] using the IM electrical supply voltages and currents. The observed signals are analysed and investigated in order to extract and locate frequency components which are induced by the gearbox in the torsional vibration. These frequency components are then used for diagnosis and fault detection purposes.

2.5 Mechanical Faults Tested

As indicated earlier, the detection of mechanical faults within mechanical transmission systems are no yet well discovered when systems driven with sensorless VSDs. Particularly, shaft misalignments, water in oil contamination, oil viscosity changes and less gear lubrication faults are very common in industry, and the gap in detection of such faults using power supply and control data is clear. In the following sections a review on these particular faults and their influence on the power supply parameters.

2.5.1 Shaft Misalignment

It is widely acknowledged that zero misalignment cannot be practically obtained [120], and rather an acceptable degree of misalignment is used. However such degree of misalignment may not always be maintained constant as the operating conditions and dynamics of movement in parts could effect it and change the alignment settings, leading to deterioration over time.

Shaft misalignment occurs between two coupled rotating shafts, where the centrelines of the coupled shafts do not concur. Shaft misalignment generates different extra forces that may affect the rotating machinery. Some examples include centrifugal forces which cause rotating load imbalance, friction forces in the bearings, parametric forces related to the variable components of rigidity of rotating objects and their supports and finally shock forces which are excited by the interaction of separate friction elements together with their resilience. Shaft misalignment is very common in industry and may lead to catastrophic machinery malfunctions. It causes additional vibration to the system, shaft failure, decreases the lifetime of couplings and motor bearings, reduces system efficiency and increases power consumption.

Shaft misalignments give rise to significant problems in rotating machines, frequently causing additional dynamic loads and vibrations in the system. It hence leads to early damages and causes additional electrical energy losses [112]. Studies show that misaligned machines can cost a factory 20% to 30% of machines' downtime [109]. Additionally, as stated in [110] precisely aligned machines can save from 3 to 10% of energy consumption. Other studies show that misalignment is the source of 70% of

vibration problems [111]. Many studies have been conducted using different diagnosis and detection techniques for early and effectively detecting shaft misalignments. These include vibration [113, 114], wireless sensors [108, 115], model based fault diagnosis [116, 117], and motor current signature analysis [118, 119]. However, most of these studies were performed on motors fed through either direct mains or V/Hz drives

Shaft misalignment is categorised into three types: parallel misalignment that occurs when two shafts centrelines are not in the in the same line; angular misalignment that occurs when there is different angles between the two shafts, and the third type combines the previous two types.

A review of the literature shows that the detection of shaft misalignments in mechanical systems driven by sensorless VSDs has been limited [120, 121]. One of the main difficulties in misalignment detection with systems driven with sensorless control is that the drives compensate for any dynamic effects caused by the fault and introduce more noise to the measured data. In addition, the harmonic contents at motor terminals from the drive's output, particularly stator currents and voltages, is high which does not facilitate the identification of small changes in terminal supply parameters [46, 52].

2.5.1.1 Effects of Mechanical Faults on Static and Dynamic Power Supply

Different attempts have been made to estimate the forces and torque as well as vibration generated from misaligned couplings, such as [120, 122-124]. Different parameters can effect on the behaviour of the misaligned shafts. For instance, as explained in [124]forces and moment generated are a function of the flexible coupling compliance. That is the restoring reactions of the coupling tends to bend the shafts. The bending forces increase with speed and load, thus leading to increases in vibration. The work in [108] details the modelling equations and summarises the forces generated in misaligned flexible couplings and shafts. Such forces are shown to push the rotating shafts sideways, generating additional load torque that oscillates at the rotating frequency of each shaft. Hence, change in the frequency component of the misaligned shaft as well as its sidebands across the supply frequency is expected.

In the case of two rotors misaligned, more vibrations are generated due to reaction forces and moments that are produced through the coupling [122]. In a study by [108] the forces generated by two misaligned shafts are examined. The work includes deriving the equations of motion of two shafts coupled with flexible spider coupling and the equations are solved using Lagrange Euler equation. Figure 7.1 shows a simplified schematic of two coupled shafts with a parallel misalignment:

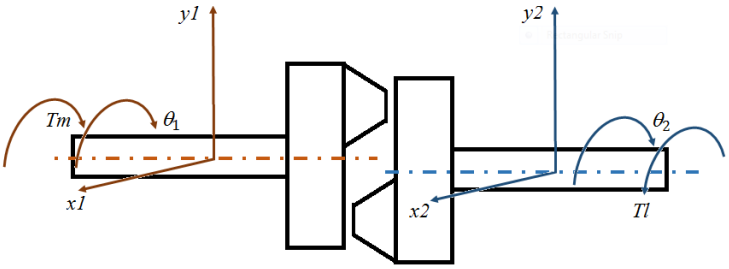

Figure 2.2 Parallel misaligned shafts

As calculated by [108], the oscillating torque T_{oscmg} generated by parallel misaligned couplings can be described as:

$$T_{oscmg} = NK_b \frac{e}{2}(x_1 \sin(\theta_1 - \theta_0) + y_1 \cos(\theta_1 - \theta_0) - x_2 \sin(\theta_1 - \theta_0) + y_2 \cos(\theta_1 - \theta_0) \quad (2.1)$$

Additionally, oscillating torques T_{ecc1} and T_{ecc2} will also be generated due to the unbalanced mass in both shafts due to the misalignment:

$$T_{ecc1} = 9.81 e_c \, m_{e1} \cos(\theta_1' - \theta_0') \quad (2.2)$$

$$T_{ecc2} = 9.81 e_c \, m_{e2} \cos(2' - \theta_0') \quad (2.3)$$

where e represents the misalignment between shafts, θ_1' and θ_2' are the angular speed of the first and second shafts respectively, θ_0 is reference angular speed, x_1, y_1, x_2 and y_2 are the displacements of the first and second shafts respectively, K_b represents the coupling stiffness of each pair of jaw/ring, m_{e1} and m_{e2} represent the mass of shafts at the physical eccentric centre, e_c is the geometric mass centre from rotational centre, e is the misalignment between shaft and eccentricity of the mass from geometric centre, and $N\ is$ the number of equivalent pins/rings in each flange.

This shows that when two shafts are misaligned, a total oscillating torque will be generated:

$$T_{osc} = T_{oscmg} + T_{ecc1} + T_{ecc2} \tag{2.4}$$

This oscillating torque will be at a frequency relating to the rotating angles of the shafts, $(\theta_1 - \theta_0)$and $(\theta_1 - \theta_0)$, with an amplitude dependent on the size of misalignment and shaft properties. When shaft properties are constant, this indicates that the change of oscillation will be highly dependent on the size of the misalignment. Additionally, as reported in [162], static forces are generated due to the misalignment causing a constant torque T_{mgc} in addition to the periodical oscillations described earlier. The fixed torque is dependent on the type of misalignment and coupling. Therefore, the torque resulting from shaft misalignment can be represented as follows:

$$T_{mg} = T_{mgc} + T_{osc} \tag{2.5}$$

As a result, shaft misalignment generates a torsional vibration that induces additional oscillations to the air gap magnetic field and modulates the flux based on the rotating frequency of each rotor. Additionally when the air gap flux is oscillated, the system speed also fluctuates which motivates the drive regulators to damp such fluctuations in the speed and maintain it at the reference. Moreover, the static torque component generated by the misalignment will cause additional static load to the motor.

2.5.2 Lubrication Oil Degradation

Gearbox lubricants are critical in maintaining efficient and effective operations [125]. Lubricating oils must reduce wear and friction at the contact surfaces and separate them to ensure appropriate operation and avoid failures. Lube oil properties also affect gear dynamics, such as vibration, power characteristics and heating [126]. Therefore, continuously monitoring changes in lubricant properties is crucial for avoiding defects within machines [127] and to prevent unexpected breakdowns.

Studies show that oil properties considerably affect gearbox behaviours and performance due to churning and splashing [135]. Oil churning causes significant power losses in the gearbox. Churning losses rise with increasing viscosity at low

speeds, yet these losses decrease at high speeds [163, 164]. Further, as found in [165] viscosity increases temperature due to internal lube friction. However a high temperature motivates chemical activities and good tribological layer formation. Conversely this will decrease the viscosity and hence a thinner oil film is formed.

The formation of the lubricant film is highly dependent on the viscosity. It is acknowledged that higher oil viscosity results in a thicker film, and consequently in lower wear and improved damping properties and also improved deterioration load capacity. Viscosity is mostly used for condition monitoring and degradation detection for gearbox lubricants [126, 166].

Lubricants in gearboxes are degraded mainly due to oxidation, particle, insufficient oil volumes and water contaminations [125]. Both oxidation [110] and water [128, 129] generally increase the lube viscosity. Water causes significant chemical and physical changes [169]. A study conducted by [134] shows that corrosion due to water in the lube oil is responsible for 20% of all failures to equipment. Hence, water contamination detection has received significant attention to avoid catastrophic failures and increase the life cycle of equipment [127]. More details on the negative consequences of water contamination in gearbox oils can be found in [170] and [171]. Moreover, studies [129] and [128] show that the most significant and immediate consequence is distinct changes in lubricant viscosity. This means that the dynamic and static behaviour of gearbox transmission systems will also change accordingly.

Similarly, insufficient oil quantity in a gearbox can cause less lubrication at gearing and bearings resulting in damage. Oil shortage may also indicate a leak from seals or gaskets. On the other hand, if the recommended oil level is exceeded, operational efficiency will decrease due to the increase in power losses from churning and higher operating temperature. Oil and seal lifetimes can be dramatically decreased when operating temperature is higher than manufacturer recommendations. Additionally, high oil volumes contribute to oil seal leakages.

Continuing and widespread efforts are being applied to oil condition monitoring and diagnostic system development and research. However most suggested techniques

require additional equipment and are not always able to be utilised for online measurement. This implies a significant need for a cost effective and reliable oil degradation technique [125].

In general, electrical power supply signature analysis and vibration are the most widely used techniques for fault detection and condition monitoring [171, 172]. Nevertheless there is no evidence in the literature shows that these techniques have been used for lube oil degradation detection and diagnosis. There is clearly a limited knowledge of the potential of using signatures from electrical measurements in systems driven with sensorless VSDs to detect lube oil problems [127].

2.5.2.1 Effects of Lubrication Properties on Power Supply

Based on gear lubrication mechanisms, an increase in viscosity will maintain more oil on the surfaces of meshing teeth and hence is likely to form thicker hydrodynamic films leading to a reduction of frictional force. On the other hand, a decrease in viscosity will lead to higher friction. Furthermore, as the occurrence of tooth meshing is a time-varying process according with the meshing period, it is expected that change in frictional forces will alter the vibration responses of the gearbox at meshing frequencies at their high order harmonics. As shown in [171], the vibration spectrum is strongly related to the lubricant viscosity in a high frequency range from 2300 Hz to 7000Hz based on a 0.34kW gearbox.

In addition, it is also likely that this change in tribological behaviour will affect the dynamic responses of components associated with gear shaft rotation frequencies. These components exist as a result of avoidable gear manufacturing errors such as misalignments and accumulative pitch deviations, which cause a non-uniform meshing process and eventually lead to change in dynamic responses at shaft frequencies.

Inevitably change in tribological behaviour will also lead to alterations in average friction losses. It means that the overall load of the system will be varied for different oil contents.

According to the study [173], oil density, viscosity and oil squeezing will also lead to considerable losses of power, reflecting on static measurements such as average supply

current, voltage and thus the power. Oil degradation therefore changes the lubrication properties and hence the dynamic behaviour of the gear will also correspondingly change.

Power loss sources in a gear transmission relate to various gear parameters [125, 174] such as teeth geometry, specific sliding, and lube properties. However, viscosity is a key element in improving gearbox efficiency and performance. Research in [125, 174] show that the use of a lubricant with a suitable viscosity could reduce up to 20% of power losses. Power losses P_T in gears can be approximated as follows [174]:

$$P_T = P_{fr} + P_{spl} + P_{M1} + P_{M0} + P_{sl} \tag{2.6}$$

where P_{fr} denotes gear friction power loss, P_{spl} is gear churning power loss, which are more significant compared with these other three losses: P_{M1} denoting load dependent power loss in rolling bearings, P_{M0} denoting power loss in rolling bearings, and P_{sl} denoting seal power loss. The gear frictional power losses are load dependent and also related to gear geometry, number of teeth of both gear and pinion (z_1, $z_2$respectively), and friction coefficient (μ_m), and can be estimated based on [175-177]:

$$P_{fr} = \pi \left(\frac{1}{z_1} + \frac{1}{z_2}\right)\left(1 - \left(\frac{g_f + g_a}{p_b}\right) + \left(\frac{g_f}{p_b}\right)^2 + \left(\frac{g_a}{p_b}\right)^2\right) P_{in}\mu_m \tag{2.7}$$

It shows that the average friction coefficient has a significant impact on P_{fr}. According to [175, 176, 178] the friction coefficient can be calculated from the following equation:

$$\mu_m = 0.048 \left(\frac{F_{bt}/b}{v \,.\, \rho_c}\right)^{0.2} \eta_{oil}^{-0.05} {R_a}^{-0.25} X_L \tag{2.8}$$

Equation (8.3) shows that μ_m is inversely proportional to the lube viscosity η_{oil} and velocity v. On the other hand, the churning loss P_{spl} in a gear are load independent losses, and mainly depend on the velocity, geometry of the moving parts immersed in the oil and oil density ρ and viscosity, which can be estimated from [175, 176, 178]

$$P_{spl} = \frac{\pi}{30} . n . \left[\frac{1}{2} . \rho \left(\frac{\pi . n}{30}\right)^2 A_i \left(\frac{d}{2}\right)^3\right] \left[\left(\frac{2.h}{d}\right)^{0.45} \left(\frac{V_{oil}}{d}\right)^{0.1} F_R^{-0.6} Re^{-0.21}\right] \tag{2.9}$$

Equation (2.9) shows the complex influence of gear geometry and velocity on the power losses due to oil churning and splashing. The Reynolds number R_e depends on the oil density and viscosity and is given as:

$$R_e = \frac{\rho U D}{\eta_{oil}} \tag{2.10}$$

While losses from churning in bearings depend on bearing type and size, bearing arrangement, and lubricant viscosity [163], and can be calculated from [178]:

$$P_{M0} = \frac{\pi}{30}.n.G_{Br}.{\eta_{oil}}^{2/3}.10^{-3} \tag{2.11}$$

where: P_{in} denotes input power, g_f is the length of approach, g_a represents the length of recess, F_R is the Froude number, R_a means roughness, p_b is base pitch, F_{bt} is tooth normal force in the transverse section, X_L is an adjustable parameter relating to each lubricant, b is face width, $v_{\Sigma c}$ represents sum velocity at pitch point, ρ_c is equivalent curvature radius at pitch point, ρ denotes specific weight, V_{oil} is oil volume, G_{Br} is a parameter depending on the bearings geometry, n is input speed (rpm), D represents a characteristic linear dimension, U is the mean velocity of the flow and η_{oil} is the dynamic viscosity.

Equations (2.7) to (2.11) show that oil viscosity has a significant effect on gearbox power losses. The frictional power loss is inversely proportional to viscosity values and operating speeds, as shown by Equations (2.7) and (2.8). Conversely, the power losses from churning increase as the speed, viscosity and oil volume increase, as shown by Equations (2.9) to (2.11). Nevertheless, the churning induced loss may be more dominant as its fractional power value is higher although both these two types of losses will also alter the dynamics of gear transmission. In particular, the churning effect can reduce the effect of damping and increase the moment of inertia of the rotational system. Consequently, it leads to more oscillatory motion of the system.

Changes in lube properties can, therefore, be represented by the sideband components at frequencies related to supply and shaft frequencies. The amplitude changes at the supply frequency can be used as a basis to examine the dynamic effects. In systems driven by sensorless VSDs the supply parameters are adjusted by the control system. This may provide more opportunities to observe such effects; in contrast to sole usage of the feature frequency components based on the high slippage changes under direct voltage/Hz control methods.

2.6 Observations from a Review of the Literature

The observations from reviewed articles point to the application of numerous methods to derive information about the health of processes including visual inspections, vibration, thermal monitoring and acoustics emission monitoring. In the case of induction motor driven systems, motor electrical signals signature analysis has received increasing attention as it is already available, in most instances, at the motors' terminals; hence there is no need for additional measuring devices. Additionally, detailed information about the health of the monitored system, either electrical or mechanical, can be obtained from these signals.

The review of the literature has also showed that fewer schemes have been developed for detecting faults in induction motors driven with closed loop VSDs. Yet, most developed strategies are for detecting, either, faults occur inside the induction motor, such as rotor, stator and bearings faults, or faults related to speed and current sensors. Less work appears to have been performed on the detection of mechanical misalignments and oil degradation such as water contamination, less lubrication and viscosity change faults that develop in the mechanical systems components driven by the induction motor and VSDs. The need for the detection of such faults without the addition of complex calculations and consumption of extra resources from the sensorless VSD while using the same information that the drive's control system uses is clear.

Moreover, common mechanical faults in industry, i.e. mechanical shaft misalignments, water contaminated oil, oil viscosity changes and oil level change, were not yet discovered. Particularly, no previous work has looked at the potential of detecting and diagnosing these type of mechanical faults using data available at the sensorless VSDs.

Therefore this research work aims to fill this gap and develop a condition monitoring scheme for detecting mechanical misalignments and oil degradation problems such as water contamination, less lubrication and viscosity change faults in mechanical transmission systems driven with sensorless VSD based on observers that are usually employed for control purposes.

Chapter 3
Sensorless Flux Vector AC Induction Motor Drives

This chapter is provided to study the theoretical aspects of induction motor, speed control systems and sensorless variable speed drives. Based on the theory, it then examines the effect of the mechanical fault on the power supply parameters and the role played by the drive in this case. Thus, in this chapter, the induction motor working principles and construction is firstly presented followed by a description of the base concepts of the control system and theory. This is followed by details on the induction motor drives and main induction motor speed control schemes. The principles of the sensorless drives are also explained while finally the effect of mechanical faults on the supply parameters and the response of the sensorless VSD is presented.

3.1 Introduction

AC induction motors (ACIM) are widely utilised in industrial motion systems, for their reliability, simple construction and jagged design, low operating cost, direct connection to the power supply, long life span and premium energy efficiency [1, 3].

To operate efficiently [13], an ACIM must run with a small slip. The two variables that determine the speed are the pole number and the supply frequency. Therefore when continuously adjustable speed over a wide range is desired, the best method is to provide a variable-frequency supply [13]. This is carried out by means of an inverter or as commonly called Variable Speed Drives (VSDs). This is also named Variable Frequency Drives (VFDs) and Adjustable Speed/Frequency Drives (ASDs, AFDs) [70]

Various types of ACIMs and VSDs are available for different applications, and diverse methodologies are used for monitoring their conditions. However, this research mainly focuses on the Sensorless Flux Vector Control for AC three phase asynchronous squirrel-cage induction motors.

3.2 Basic Concepts of Control Systems

The term control system here is used to refer to a system that is utilised to maintain a variable(s) at a desired (set-point or reference) value(s) within accepted limits [71]. Normally control systems are represented by block diagrams and transfer functions, in the S-Domain, describing each component in the system. [72].

3.2.1 Open-Loop and Closed-Loop Control Systems

The open-loop control system is represented in Figure 3.1, where the controller obtains the setpoint and uses it to generate the control output [72].

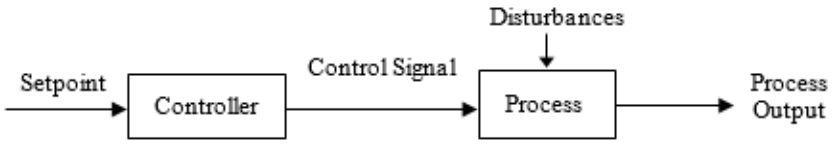

Figure 3.1 Input-output configuration of an open loop control system, redrawn [72].

The closed loop control system is shown in Figure 3.2. It shows that a "feedback" line was added to the open loop path which allows to compare system measurement with the reference [71, 72].

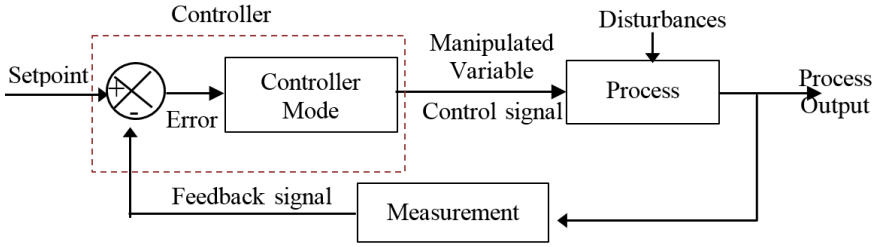

Figure 3.2 Block diagram of a closed loop control system, adapted from [71].

3.2.2 Time Response and System Performance

The system time response represents the overall system performance and shows how the system behaves and changes with respect to time to evaluate the entire system behaviours. It describes the Dynamic or "Transient" and Static or "Steady-State" performances, as in Figure 3.3. Figure 3.4 represents the most important time response parameters [8, 13].

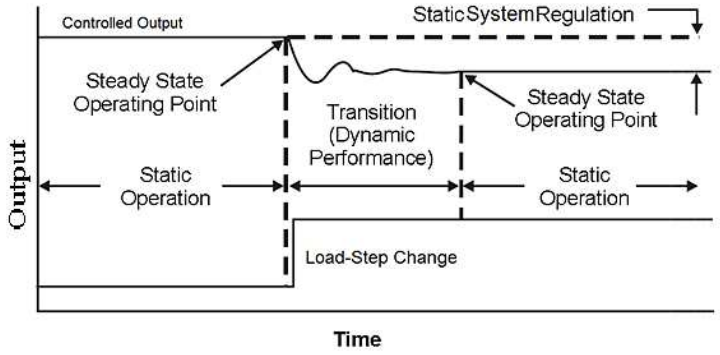

Figure 3.3 System performance as shown by its time response, redrawn from [13].

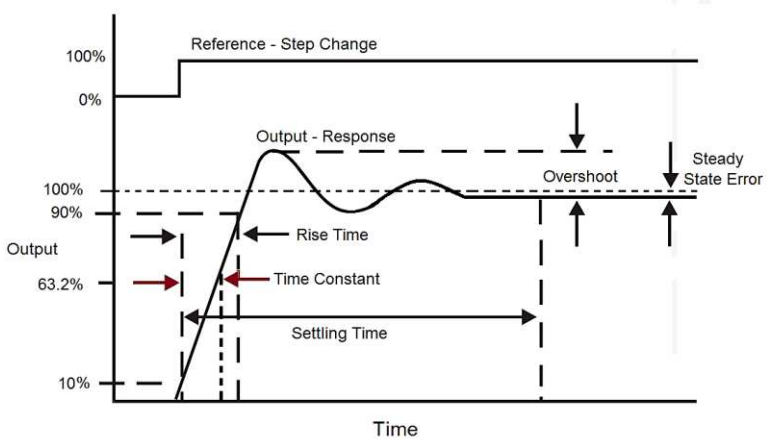

Figure 3.4 Time response characteristics after reference step change, amended from [8].

The Bandwidth (frequency response) in radians/sec (ω) or in hertz (Hz), is another parameter commonly used particularly in speed control systems. It is defined as [8] "the maximum frequency range of input signal that the output can follow" [13].

3.2.3 System Stability

Stability refers to the system behaviour as responding to reference or demand changes. If the system oscillates in constant or growing amplitude in time then the system is referred to as an unstable system. Figure 3.5 depicts different types of system responses to a step change [8, 13].

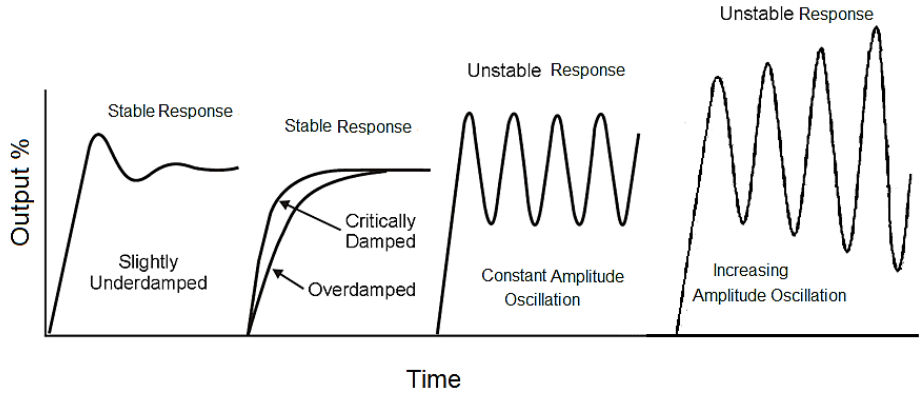

Figure 3.5 Stable and unstable system responses[8].

3.2.4 PID Controllers

The term PID refers to Proportion, Integral and Derivative controller algorithms. The controller can be proportional only, proportional plus integral or a combination of the three PID controller modes [73].

- Proportional controller provides an output proportional to the error signal [73]:

$$C_{out} = K_p\, e(t) \tag{3.1}$$

- Integral control mode provides an output proportional to the integral of the error. The output of the PI controller is given as follows [73]:

$$C_{out} = K_p\, e(t) + K_i \int e(t)dt \tag{3.2}$$

- Derivative action produces a signal proportional to the derivative of the error [73]:

$$C_{out} = K_p\, e(t) + K_d(de(t)/dt) \tag{3.3}$$

- The PID controller uses the three modes to produce the output [73]:

$$C_{out} = K_p\, e(t) + K_i \int e(t)dt + K_d(de(t)/dt) \tag{3.4}$$

Figure 3.6 represents an example of a speed process control where many variables are processed to maintain the speed at the desired value. Additionally, the process includes multiple control loops that are connected in series (cascade control system) [8].

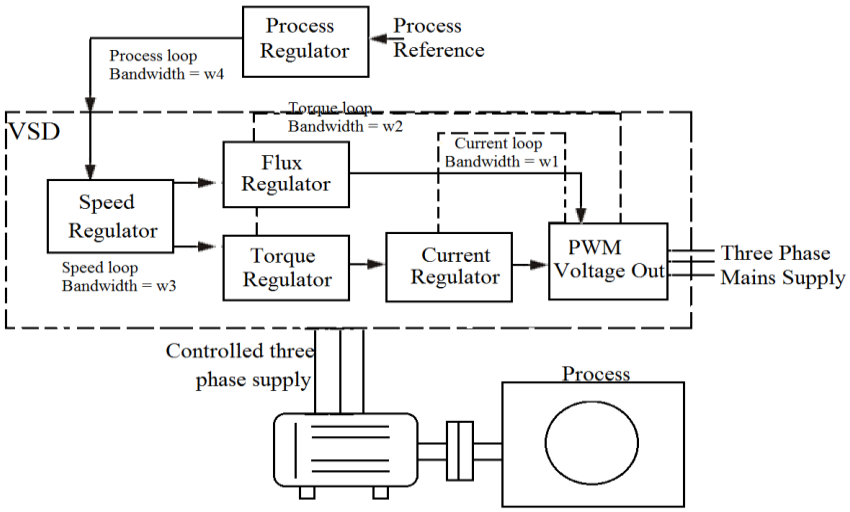

Figure 3.6 Speed control system with multiple control loops, adapted from [8].

3.3 AC Motors: Construction and Work Principle

The ACIMs are constructed from the stator which is connected to the power source and the rotor that spins inside the stator within a precisely engineered air gap. Currents are induced into the rotor via the air gap from the stator side. The stator and the rotor are made of highly magnetisable core sheet providing low eddy current and hysteresis losses [13]. Figure 3.7 shows an exploded view of a typical ACIM.

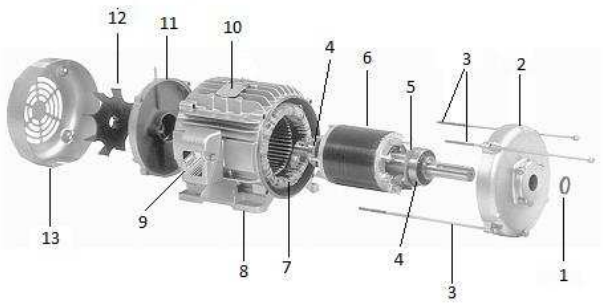

Item	Description	Item	Description	Item	Description
1	Shaft sealing ring	6	Rotor, complete	10	Rating plate
2	End shield	7	Stator, complete	11	End shield
3	Assembly screws	8	Housing foot	12	Cooling fan
4	Rolling-contact bearing	9	Terminal box, complete	13	Cooling fan cover
5	Spring washer				

Figure 3.7 An enlarged view of a typical AC induction motor [74].

3.3.1 The Stator

The stator core is usually made of a doughnut-shaped stack of thin steel laminations with insulated slots. Slots are opening to the inside diameter holding the stator coils (windings) and held together by suitable means. Each core lamination is separated from the other. The teeth are separating the slots and carry the magnetic flux from stator windings to the rotor through the air gap [74] Figure 3.8 (a) shows the stator core slots.

Stator windings are made from insulated copper wires embedded in the slots. A number of identical array of uniform coils are twisted around each stator tooth. Coils are connected together to form the three phase windings, circulated around the stator, and symmetrically located with respect to one another [74].

Currents in the stator windings are supposed of equal amplitude but differ in phase by one-third of a cycle $(2\pi/3)$ forming a balanced three phase set. As current flows through the coil on the first tooth, it creates a magnetic field of polarity that opposes the polarity of the opposite tooth, as shown in Figure 3.8(b) [75].

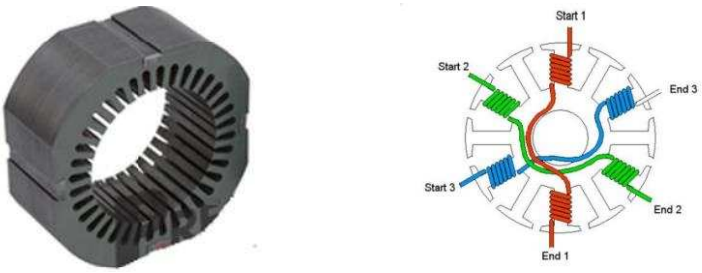

a) Stator core slots b) Windings distribution in stator slots

Figure 3.8 Stator slots and windings [77].

3.3.2 The Rotor

The rotor is constructed of the shaft and cage conductors, as shown in Figure 3.9. The rotor shaft is made up of cylindrical cast iron core. The squirrel cage rotor windings consist of a number of heavy, straight and embedded copper or cast aluminium bars, regularly circulated about the periphery, and connected at both ends by end rings. The slots accommodate the rotor conductors; and are skewed to minimise torque pulsations. Blades are attached to the end rings to function as a cooling fan [75].

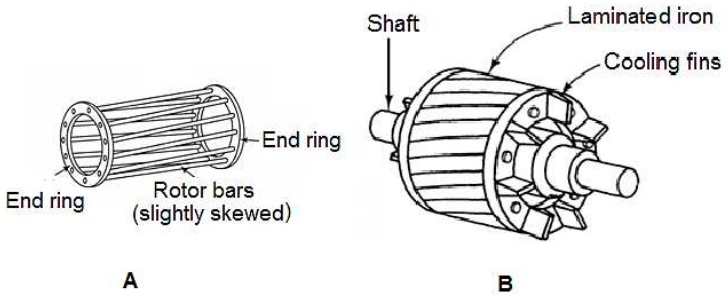

Figure 3.9 Squirrel-cage rotor: (A) cage construction; (B) assembled [71]

3.3.3 Other ACIM Parts

As shown in Figure 3.7, the induction motor assembly contains other parts including the motor shield, assembly screws, spring washers, cooling fan and the cover. As indicated earlier, the air gap between rotor and stator is minimised as much as possible. Thus, the shaft should be made short and rigid to avoid any deflection; even a very small deflection may cause large irregularities in the air gap which can cause an unbalanced magnetic field. Accurate cantering bearings are used to help in avoiding any asymmetries [76].

3.3.4 ACIM Motor Current, Speed, Load and Torque

The torque is produced by the interaction between the radial flux from the stator and the axial currents in the rotor. The torque acts in the same direction as the rotation and causes it to drag the rotor along by the field. The rotor will never reach the synchronous speed as, if it did, there would be no rotor current, no emf, and hence no torque. Typical torque-speed-current curves for a squirrel cage IM are shown in Figure 3.10 [13].

When starting the induction motor from the rated supply voltage, a high starting current is induced into the rotor known as the “Locked Rotor Current (LRC).” This current develops a significant amount of induced emf in the rotor, which generates the “Starting” or “Locked Rotor” Torque (LRT). However, as the rotor accelerates both current and torque alter slightly with the rotor speed, and if the supply voltage remains constant the torque reaches its minimum value referred to as the “Pull-up” torque. As the rotor speed increases and approaches full speed (about 80-90% of synchronous

speed), the torque grows to the maximum point which is known as the "pull-out or breakdown" torque accompanied by a slight drop in the current. As the rotor accelerates further towards the rated motor speed, with no load, both current and torque would rapidly fall to minimal values. [8, 13].

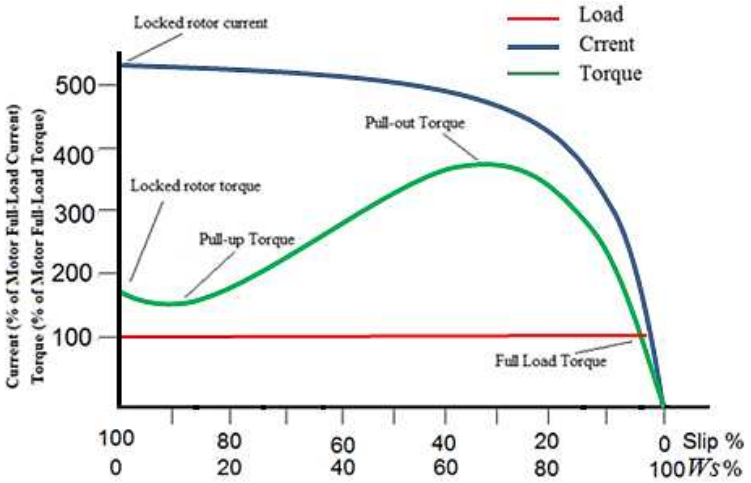

Figure 3.10 Typical torque-speed-current curves for the ACIM, amended from [79].

3.3.5 Induction Motor Equivalent Circuit

Due to the similarity, in the steady state case, the three phase induction motor is generally represented in the same way as a three phase transformer. The stator windings represent the primary windings and the rotor windings represent the secondary windings. The stator and rotor iron transfer the flux between them acting as a core in the transformer [77]. The one phase equivalent circuit of a three phase induction motor is depicted in Figure 3.11.

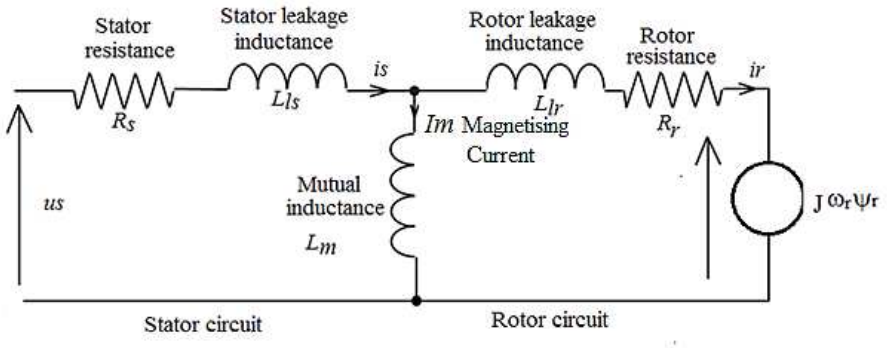

Figure 3.11 Per-phase induction motor equivalent circuit, adapted from [78].

The stator windings can be connected in delta or star, the definition of the i_s and u_s needs to be considered accordingly. In the delta connected winding the u_s is the line to line voltage while the i_s is the phase current. In the star case, the u_s represents the phase voltage and i_s represents the line current. The line current in delta connected motors is lagging by $2\pi/6$ from their corresponding phase and is times $\sqrt{3}$ in magnitude [77].

3.3.6 Principles of Operation

Physically, the stator and the rotor are not connected. AC currents are induced into the rotor via the air gap from the rotating magnetic fields in the stator side. The motor power supply creates an electromagnetic field in the stator windings that cuts through the air gap into the rotor windings. This electromagnetic field induces a voltage in the rotor bars, as described by Lenz's law, and stimulates a current that circulates within them. Hence, another electromagnetic field is created that interacts with the electromagnetic field of the stator. The interaction between both electromagnet fields generates a twisting force, or a rotating torque, that rotates the rotor in the direction of the resultant torque [8, 13, 79].

The field in the stator takes a half-cycle to move from one pole to the next while the field crosses one pole pair in each electrical cycle. The number of pole pairs specifies the number of the electrical cycles the field needs to complete one revolution. When the rotor spends at the field revolution, it is then synchronised with the field [74]. The following general formula [13, 74] describes the speed of the field produced (synchronous speed):

$$\omega_s = 120 f_s / N_p \tag{3.5}$$

The rotor cannot run at synchronous speed for the reason that rotation of the rotor at synchronous speed entails that its relative velocity with respect to the field would be zero and no emf are induced to the rotor bars. This results in an absence of force, and a lack of any torque on the rotor [13, 80]. The relative velocity between the rotor speed and the synchronous speed is called slip (s), and expressed as a ratio as follows [13]:

$$s = \frac{\omega_s - \omega_r}{\omega_s} \tag{3.6}$$

3.4 Principles of AC Drives and Traditional Drives

Three phase VSDs principally consist of: a Rectifier that converts the AC power supply into a DC; a DC link which is used for filtration and smoothing the DC signal from the rectifier; an Inverter that converts the DC signal received from the rectifier via the DC link into a controlled variable frequency and variable AC voltage signals; and finally the Control Circuits that are used to control either both inverter and rectifier bridges or inverter bridge to produce the required supply level and frequency [8].

3.4.1 Principles of AC VSDs

The speed of an ACIM generally can be controlled by adjusting both voltage and frequency [8, 13]. The synchronous speed and slip are described by the expressions 3.5 and 3.6 respectively. When the IM is supplied by a three phase sinusoidal voltage and neglecting the voltage drop across the stator windings, the magnitude of the voltage (u) can be approximated during the steady state as follows [81]:

$$u \approx \omega_s \psi_s \tag{3.7}$$

$$\psi_s \approx \frac{u}{\omega_s} = \frac{u}{2\pi f_s} \tag{3.8}$$

The Equation 3.5 illustrates that motor speed is determined by the supply frequency, while the formula 3.8 shows that the stator flux remains constant when the voltage per frequency ratio is maintained at a constant level [13, 81]. However, at low frequency and hence low V/Hz ratio, the voltage drop across the stator windings is considerable and needs to be compensated. On the other hand, at elevated speed the frequency needed is high and hence high voltage is also required to keep the V/Hz ratio constant. High voltage may exceed the rated voltage values and may burn the winding insulators. In this case there is a need to break the V/Hz ratio rule and adjustment in the voltage is required to prevent the damage. The rated voltage value must not be exceeded [81].

Principally, the AC drive changes a fixed supply voltage (V) and frequency (Hz) into a variable voltage and frequency. The output frequency determines the speed of the motor, while the V/Hz ratio regulates the electromagnetic torque generated [8].

Figure 3.12 illustrates the electromagnetic torque and speed of an induction motor fed with different voltage and frequency values. For a fixed current value, the electromagnetic torque of the motor is constant as long as the motor speed is less than the rated speed. This is called the constant torque region, where the voltage, hence the power, is variable up to the rated motor voltage and the breakdown torque is constant for the entire region. When the motor speed reaches the rated value, the power supply enters the constant power region [79, 82].

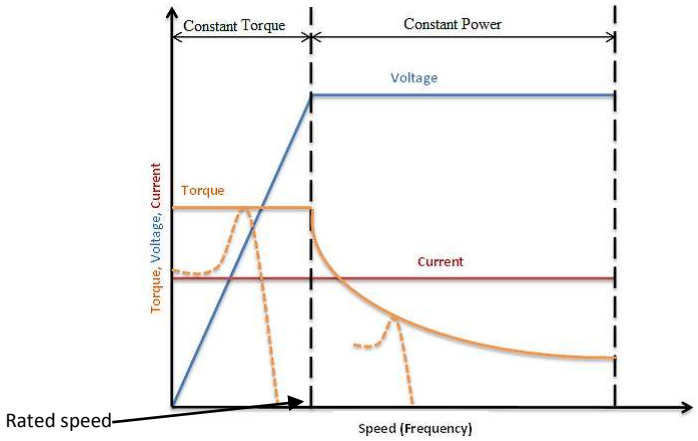

Figure 3.12 Motor torque-power characteristics, adapted from [84].

Nevertheless, for every frequency value there will be a torque-speed curve in which all torque speed curves have the same breakdown torque value in the constant torque region. Therefore different operating points can be found on the torque-speed curves when they cross the 100% torque level, indicating the rated torque. Figure 3.13 illustrates the motor torque curves at different supply frequencies [8, 13, 83].

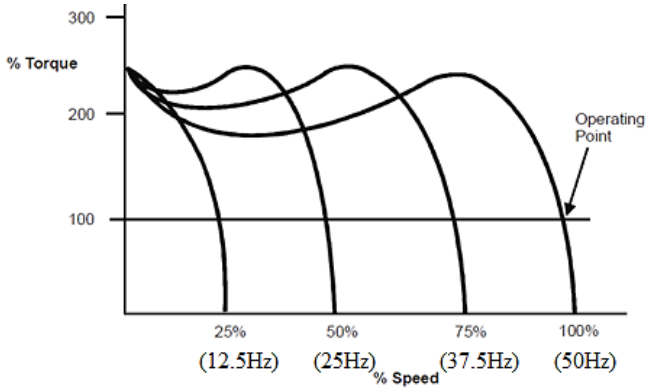

Figure 3.13 Motor torque vs. supply frequency [8].

The pulse-width modulator (PWM) drive can be given as an example of the construction of VSDs. The PWM basic structure is shown in Figure 3.14. PWM drives mostly possess the same structure, with appropriate variances in hardware and software components [8].

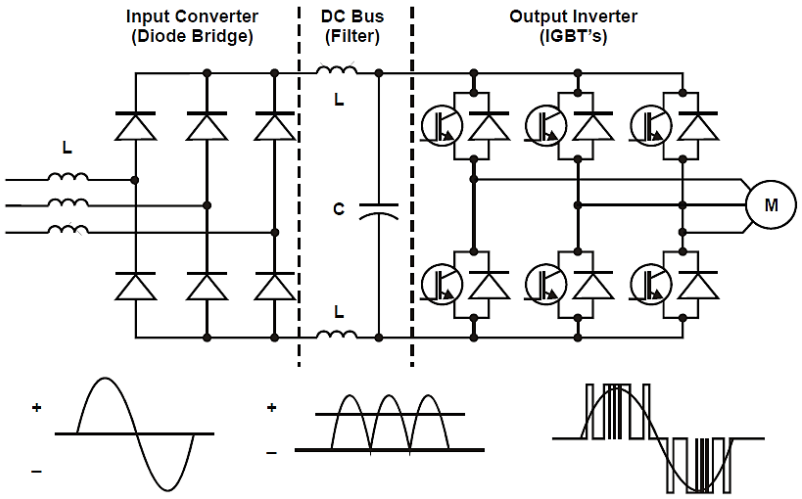

Figure 3.14 A block diagram of a PWM drive as an example of VSDs [86].

As shown in Figure 3.14 the diodes bridge converts the negative parts of the waveform into positive. The average of the DC voltage is: Line voltage × 1.414 = DC bus voltage. The rectifier output is filtered by combining both the inductor and the capacitor circuit.

The inverter utilises insulated gate bipolar transistors (IGBTs) that act as power switches to regulate the DC bus voltage at specific intervals in order to create a variable AC voltage and frequency output. The control part of the IGBT is turned "on" and "off" as needed by control circuits, at specified intervals providing an output in a form of voltage pulses that have a constant magnitude in height, as illustrated in Figure 3.15 [84].

The control board in the drive activates the drive's circuits turning the supply waveform positive or negative, creating a three-phase output. The amplitude of the output voltage is defined by the length of time the IGBT remains on, while the signal frequency is set by the length of time the IGBT is off, as shown in Figure 3.16 [8]

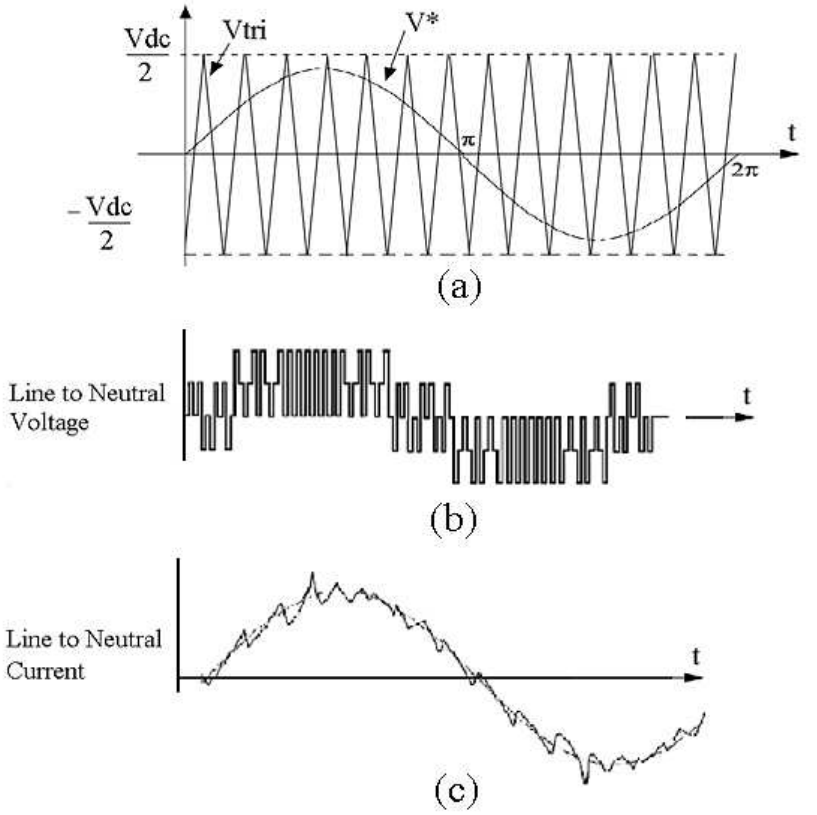

a) Reference Signal and Carrier Signal, (b) Load voltage, (c) Current

Figure 3.15 Voltage and current waveform of a PWM [8].

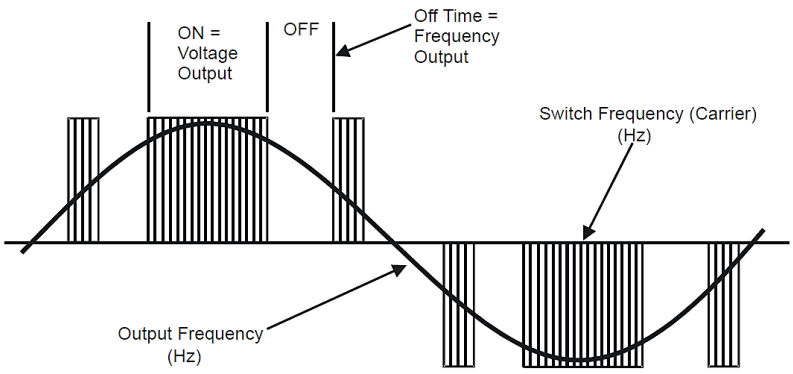

Figure 3.16 Frequency and voltage creation from PWM [86].

3.4.2 Traditional VSDs

There are three common traditional AC drives, namely: Variable Voltage Inverter (VVI), Current Source Inverter (CSI), and Pulse Width Modulation Inverter (PWM) [70].

- Variable Voltage Inverter (VVI)

The main advantages of the VVI drives include: wide speed range; multiple motors control (within current limit), and simplicity. However there are a number of disadvantages, principally: input power factor drops as the motor speed decreases; generates line spikes due to the SCR control technology utilised at front end; additional output harmonics are applied to the AC motor; creates motor cogging (shaft pulsations/jerky motion) at low speed, and which may cause many equipment problems. The block diagram of VVIs is shown in Figure 3.17 [85].

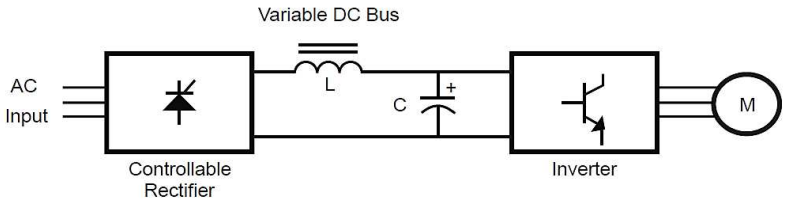

Figure 3.17 Block diagram of a typical VVI drive [8].

- Current Source Inverter (CSI),

The construction of CSIs is similar to VVIs. The input rectifier provides a variable voltage to the DC bus utilising SCR devices. Figure 3.18 shows the block diagram of a typical CSI [85].

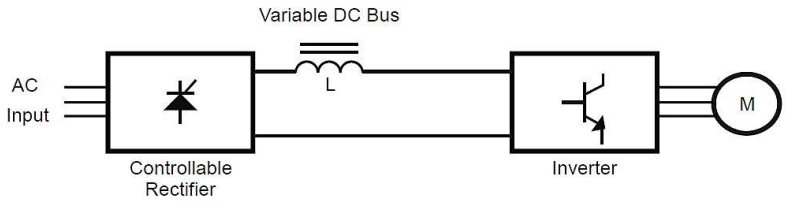

Figure 3.18 Block diagram of a typical CSI [8].

The advantages of CSI drives include: higher efficiency and high power factor; the production of a reliable short-circuit protection due to the current regulation within the drive, and the ability to continuously operate with a faulty device [70].

However, there are also specific drawbacks: lower input power factor at low speeds; motor cogging at low speed; limited speed range, and generation of line spikes by the drive due to the use of SCR technology in the front end. Finally, the characteristics of the motor must be matched to the drive and in most cases the motor is an integral part of the drive system [85].

- PWM Drives

The general construction PWM is explained earlier in Figure 3.15. Some advantages of a PWM drive can be concluded: higher efficiency, wider speed control range, with no low speed cogging at less than 20 Hz operation. Other advantages include: the capability of power loss ride-through, open circuit protection, and a fixed input power factor due to the constant diode front end and DC bus inductor. Moreover it allows multi-motor operations (within the drive current limits). However there are also a number of disadvantages related to the need for additional components for line regenerative capability. Line side harmonics are also a considerable disadvantage with PWM drives. Furthermore in some applications it has been shown to heat the motor and damage the insulation [86].

3.5 Field Oriented Control

3.5.1 Basic Principles of Field Oriented Drives

The term field oriented control (FOC) refers to the manner in which these drives operate. It is also sometimes called the Flux Vector Control Drives (FVC). Primarily FOC drives are based on IM field orientation control (FOC) to simulate the operation of the DC motors. The field producing current is maintained constant ensuring that field windings always have a constant flux [8, 86, 87]. The IM stator is supplied from the drive, and at any one time will have currents of magnitudes i_a, i_b, and i_c, in a phase shifted by $2\pi/3$ between each current. The stator current is mathematically decoupled, using a suitable field orientation, into a torque and a flux producing components. The drive then independently varies their phase and amplitudes [87, 88]. Figure 3.19 displays the three phase currents and the manner in which the FOC drives mainly transfers it into two dimensional quantities for the flux control system.

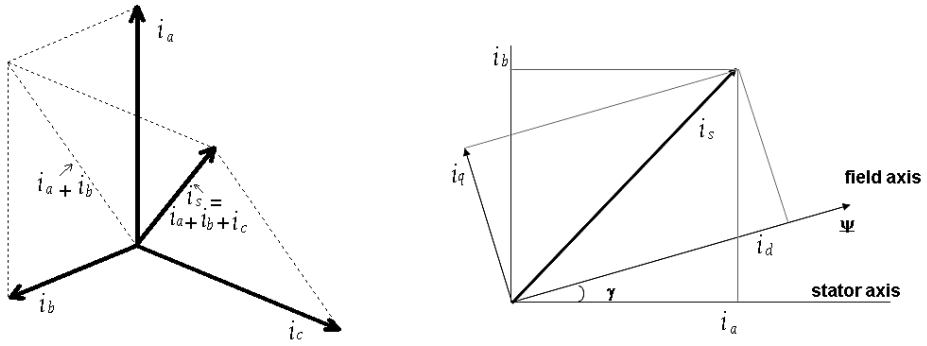

Figure 3.19 The principle of FOC control [87]

3.5.2 Implementing the FOC Scheme

The theory of field orientation is based on the fact that the three phase supply current inside the motor results in a magnetic field and a torque as depicted in Figure 3.20. Any change in the motor supply (i_a, i_b and i_c) results in change the magnetic field and torque. The functional block C represents the transformation from stator co-ordinates to field-orientated co-ordinates that occurs inside the motor [87]. Hence, FOC is implemented by compensating for this transformation as shown in Figure 3.21.

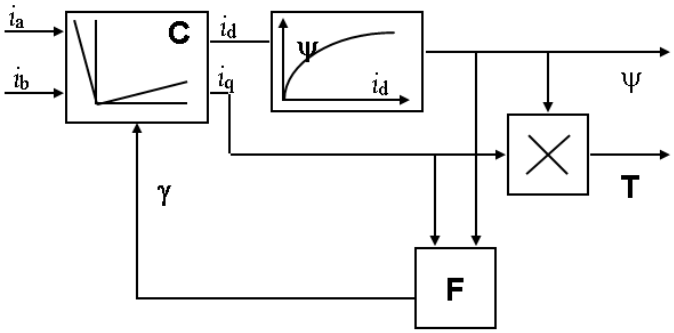

Figure 3.20 The orientation inside the ACIM [59, 89].

In a FOC drive, the three phase supply quantities are transformed into two dimensional d-q quantities. The d-q variables are then adjusted based on their reference values and fed through the modulator to the ACIM. The electromagnet torque is regulated by adjusting the q-axis current component, while the motor field is controlled by regulating the d-axis current component [83, 87].

FOC drives are classified, in terms of flux measurement, into direct and indirect drives. In the direct scheme, the rotor flux and position are directly measured using a sensor located within the motor windings. While in the indirect scheme drives, the rotor flux and position are mathematically calculated from the power supply measurements [89].

Indirect FOC drives can be closed loop vector control where the information about the rotor angle is determined using a pulse encoder. A contrasting approach, known as a Sensorless (encoderless) FOC, does not employ any position or speed sensors. This research focuses on the sensorless type detailed in the next section.

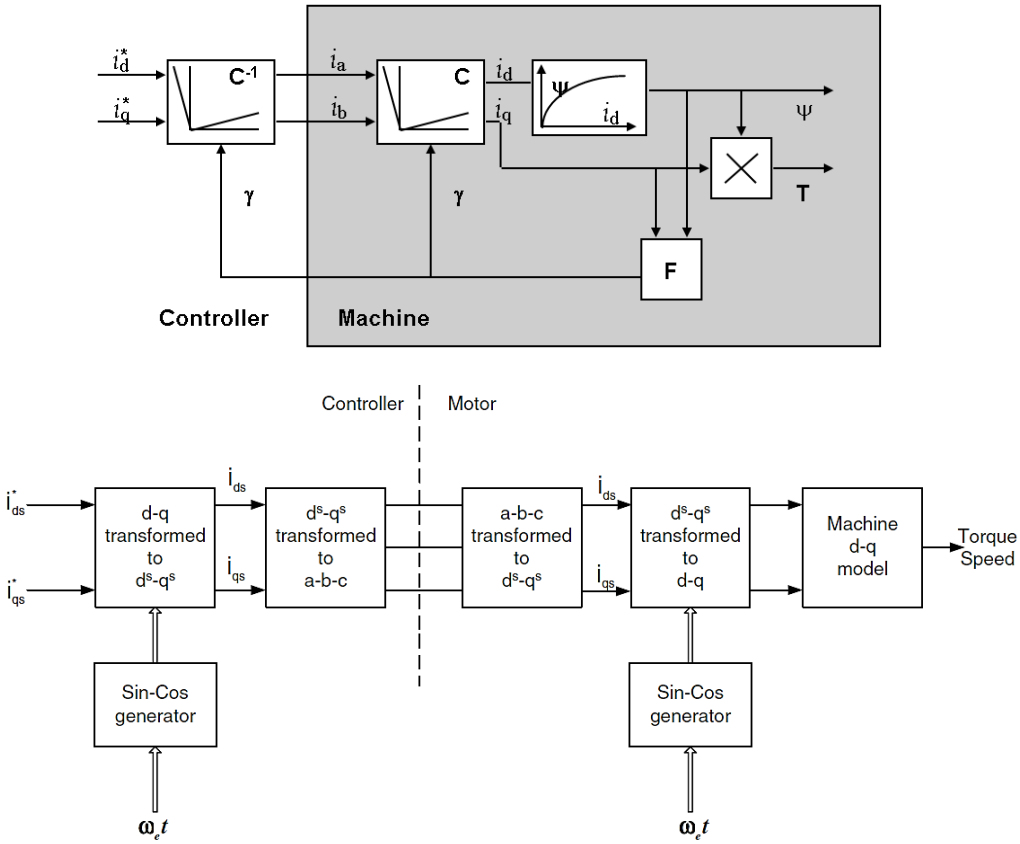

Figure 3.21 Compensating for the coordinate transformation to achieve vector control [59, 89]

3.6 Sensorless FOC Drives

Sensorless FOC drives control the IMs speed without any speed feedback devices. Motor model and parameters together with supply measurements are utilised to control the d-q axis electrical supply quantities. Sensorless FOC drives provide [8, 90]:

- High motor torque at low output frequencies
- Automatic slip compensation
- Improved dynamic response to demand and load variations
- Compactness with less maintenance
- Simpler application with no need for wires
- Avoidance of the cost of encoders
- Suitability for different environments, including temperature.

The d-q axis voltage components that are required to achieve the magnetising current demanded for particular load are calculated from motor parameters, e.g. resistances, inductances and name plate data. The motor model is also used to form the right equations for the calculations. The motor equivalent circuit is shown in Figure 3.22 [87, 91].

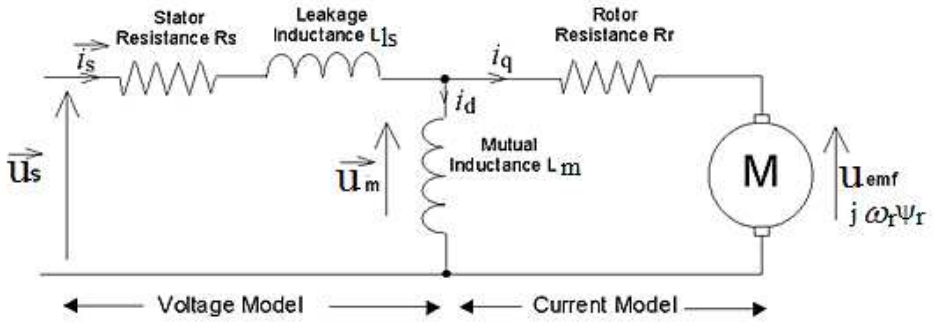

Figure 3.22 ACIM equivalent circuit, redrawn from [93]

The analysis of the motor stator circuit based on the equivalent circuit in Figure 3.22 can be simplified as shown in figure 3.23.

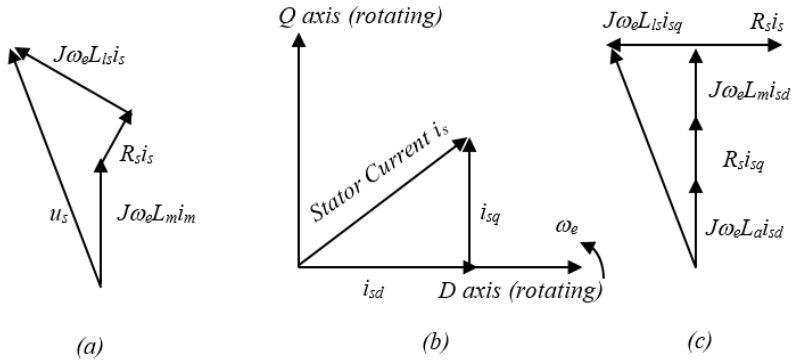

Figure 3.23 Stator circuit: (a) Stator voltage, (b) Stator current, (c) Stator voltage in d-q [87]

The stator voltage given [87, 91] from:

$$u_{ds} = R_s i_{ds} - \omega_e L_{ls} i_{sq} \tag{3.9}$$

$$u_{qs} = R_s i_{qs} + \omega_e (L_a + L_b) i_{ds} \tag{3.10}$$

Based on Equations 3.9 and 3.10, if the d current component is aligned with the rotor flux, the q-axis of the rotor flux component will be zero, and hence the relations between flux, torque and current can be represented as follows [92]:

$$\psi_r = \frac{L_m}{1+T_r s}(i_{ds}) \tag{3.11}$$

$$T_e = \frac{3}{2}\frac{1}{p}\frac{L_m}{L_r}\psi_r i_{qs} \tag{3.12}$$

Equation 3.11 shows that the i_{ds} controls the flux quantity, while equation 3.12 shows that the q-axis current i_{qs} can be used as a measure of load torque for slip compensation and electromagnetic torque control [93]. Therefore, to achieve improved dynamic torque performance, the field current component i_{ds} is kept constant at a value that maintains a maximum flux. The torque control is then performed by adjusting the i_{qs} [87, 91].

To keep a constant flux, the u_{ds} must be relative to the supply frequency for speeds up to the rated value. While the drive voltage limit restricts the maximum voltage that can be fed to the motor. Above the rated speed, u_{ds} is kept constant so that the flux falls with increasing frequency to give flux-weakening operation. This is to ensure that both drive and motor voltage limits are not exceeded and to provide the maximum available torque even at or higher than the rated motor frequency [91, 94, 95]. The VSD scheme is represented in Figure 3.24 [87]. This also shows that the drive can act on the supply voltages based on the changes in the reference values of current components.

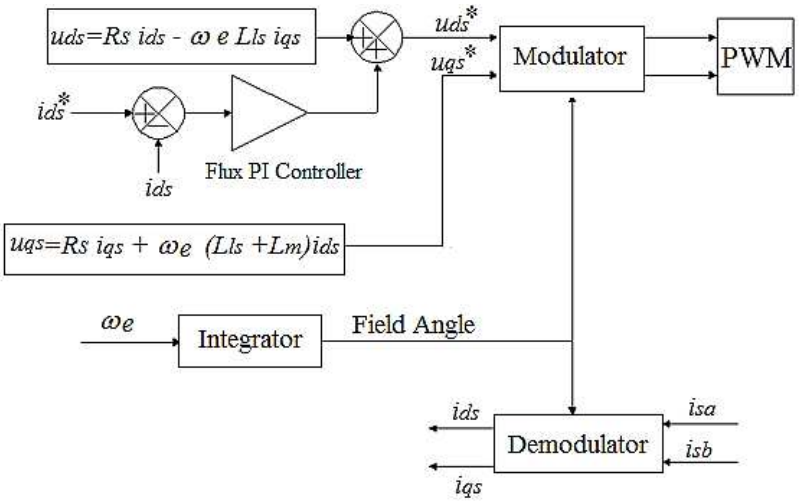

Figure 3.24 A schematic diagram of VSD scheme, redrawn from [87].

Sensorless FOC drive simultaneously estimates rotor speed and flux rather than measuring them. Significant developments in this field have resulted in the availability of several techniques for speed and flux estimation. These approaches imply the terminal measurements only for speed estimation [91]. Among them, Model Reference Adaptive System (MRAS) is one of the most frequently used schemes in industrial applications [85, 87, 94, 96]. The MRAS approach is simple to apply and implies less computational effort compared to other approaches [96]. It is also represented here as it is used in the test rig drive upon which this study is based.

MRAS utilises two independent machine models for estimating the same state variable. These are referred to as the reference model, which lacks incorporation of the estimated variable, and the adjustable model containing the estimated variable. Comparison between the two models outputs generates an error signal that is treated by an adaptation mechanism, normally a PI controller, and used to modify the adjustable model [94, 96]. Figure 3.25 represents an MRAS speed estimator based on voltage (reference model) and current (adjustable or adaptive) model.

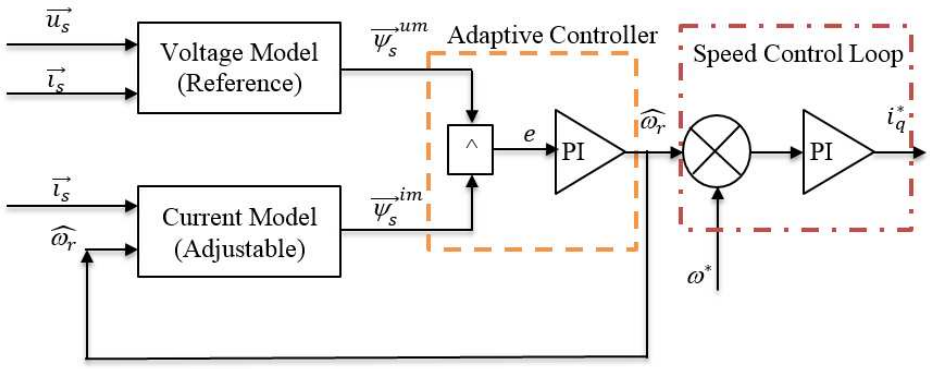

Figure 3.25 Schematic of MRAS and speed loop in a Sensorless drive, redrawn from [87, 96]

Both reference and adaptive models are derived from IM motor equations and its equivalent circuit represented in Figure 3.22 [94; 58] in the stationary reference frame. The reference model is composed of the stator voltage equations as follows [97, 98]:

$$\frac{d\psi_{\alpha r}^{u}}{dt} = \frac{L_r}{L_m}\left(u_{\alpha s} - R_s i_{\alpha s} - \sigma L_s \frac{di_{\alpha s}}{dt}\right) \tag{3.13}$$

$$\frac{d\psi_{\beta r}^{u}}{dt} = \frac{L_r}{L_m}\left(u_{\beta s} - R_s i_{\beta s} - \sigma L_s \frac{di_{\beta s}}{dt}\right) \tag{3.14}$$

The adjustable (adaptive) model is represented as follows [97, 98]:

$$\frac{d\psi_{\alpha r}^{i}}{dt} = \frac{1}{T_r}\left(L_m i_{\alpha s} - \psi_{\alpha r}^{i} - T_r \widehat{\omega}_r \psi_{\beta r}^{i}\right) \tag{3.15}$$

$$\frac{d\psi_{\beta r}^{i}}{dt} = \frac{1}{T_r}\left(L_m i_{\beta s} - \psi_{\beta r}^{i} + T_r \widehat{\omega}_r \psi_{\alpha r}^{i}\right) \tag{3.16}$$

$$\sigma = 1 - \frac{L_m^2}{L_r L_s} \tag{3.17}$$

The error e between the two models is calculated in the following way [96]:

$$e = \psi_{\beta r}^{u}\psi_{\alpha r}^{i} - \psi_{\alpha r}^{u}\psi_{\beta r}^{i} \tag{3.18}$$

The error is treated by the adaptation mechanism producing an output that is used for adjusting the adaptive model. The most common method used for the adaptation mechanism is the PI controller, although certain other techniques are used such as fuzzy and neural network control systems. The output from the PI controller replaces the estimated value in the adjustable model. The MRAS continually modifies the estimated variable quantity maintaining the error between the two models [96, 99].

The estimated speed is then used to calculate the rotor flux angle θ_e as follows:

$$\theta_e = \int \omega_e \, dt \tag{3.19}$$

The estimated speed from MRAS is fed into the speed loop for speed control as illustrated in Figure 3.25. The speed loop then compares the estimated signal with the reference and utilises a PI controller to process the error signal. This generates an output represented as a reference torque current component i_q^* which is sent to the current control loop. The current loop sets the reference for the quadrature voltage which is adjusted by controlling the switching of the PWM [96, 99]. A block diagram of a general sensorless flux vector control drive is shown in Figure 3.26.

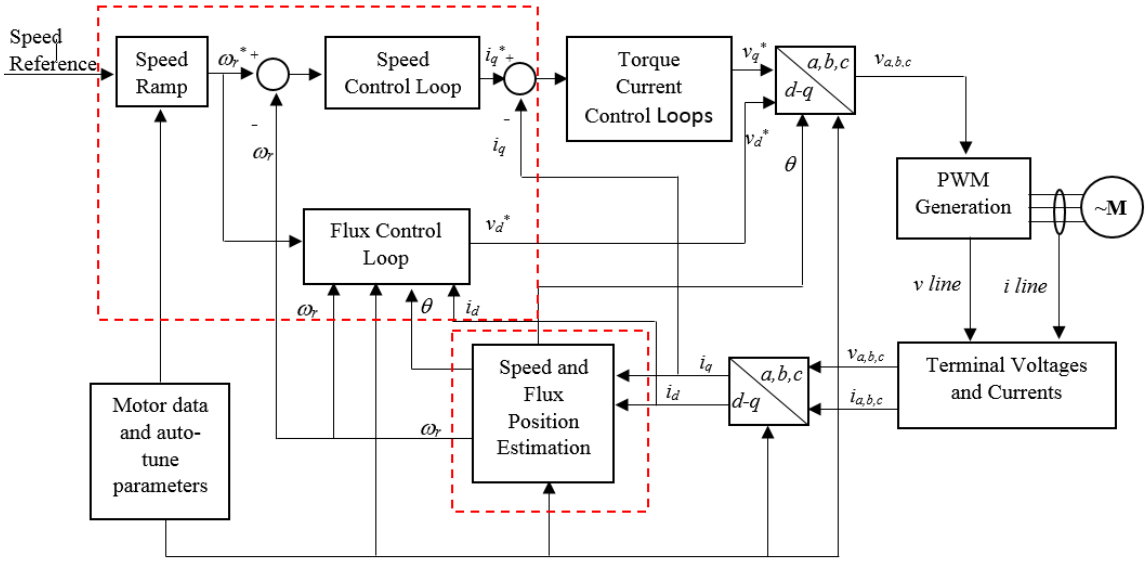

Figure 3.26 A block diagram of a general FOC drive, adapted from [77]

3.7 Characteristics of Electrical Parameters from the Drive

3.7.1 Electrical Parameters in a Healthy Condition

As described in Figure 3.6 and Figure 3.26, the sensorless VSD regulates the IM speed by decoupling the torque and field components. Each component then is regulated separately using cascade control loops. The outer control loop is the main speed regulator which sets the reference for both components loop. The first inner loop is the torque component loop that is constructed from three inner cascade control loops; the

torque regulator which obtains the reference torque signal from the speed regulator and then sets the torque current component reference to the current loop. The current control loop establishes the reference torque voltage based on the difference between the feedback torque current component and reference from the torque loop. Lastly the voltage controller that provides the reference torque voltage component. The second inner control line is for field control which maintains the field at the rated value when the speed is less than the base speed. When the speed is at or over the rated speed, the flux is reduced by $1/\omega_r$. This control loops generates the reference field voltage component.

To maintain stability in a cascade control system, the outer control loop must be at least three times slower and with narrower bandwidth than the inner control loops [100]. The controller activates its output only when the input changes within the controller bandwidth. The electromagnetic torque is controlled by changing the i_{qs} as follows [101, 102]:

$$i_{qs}^{*} = \frac{2}{3}\,\frac{1}{p}\,\frac{L_r}{L_m}\frac{T_e^{*}}{\psi_r} \tag{3.20}$$

While the motor flux is controlled by the i_{ds} as follows [101, 102]:

$$i_{ds}^{*} = \frac{\psi_r^{*}}{L_m} \tag{3.21}$$

The slip frequency is determined using the torque current reference in the following way [101, 102]:

$$\omega_{sl} = \frac{L_m}{T_r \psi_r} i_{qs}^{*} \tag{3.22}$$

Then the electrical flux angle is determined as follows [101, 102]:

$$\theta = \int (\omega_{sl} + \omega_m)\, dt \tag{3.23}$$

Meanwhile the per phase current and voltage of the induction motor running at a constant speed in the healthy case are, respectively, given as follows [103]:

$$i(t) = \sqrt{2} I \cos(2\pi f_s t - \alpha_I) \tag{3.24}$$

$$u(t) = \sqrt{2} U \cos(2\pi f_s t) \tag{3.25}$$

While per phase power is the product of both phase voltage and current as shown in the following [104]:

$$p(t) = IU[\cos(2\pi(2f_s)t - \alpha_I) + \cos(\alpha_I)] \quad (3.26)$$

The corresponding magnetic flux in the motor stator and the resulted electromagnetic torque is calculated respectively as [103]:

$$\psi_s(t) = \sqrt{2}\psi \cos\left(2\pi f_s t - \alpha_\psi\right) \quad (3.27)$$

$$T_e(t) = 3N_p\psi I \sin\left(\alpha_I - \alpha_\psi\right) \quad (3.28)$$

Where: I, U, and ψ are the rms values of phase current, voltage, and stator flux respectively.

As can be seen from Equation 3.26 the spectrum of the power contains constant components at double supply frequency. The total power of a three phase IM can be derived from 3.26 by multiplying one phase by 3, or from the resulting sum of the power in each phase.

In the normal operations, the terminal supply quantities are converted into the reference frame for control purposes. Changes in references and load are reflected also in the reference frame values. The role of the drive regulators is to smoothly maintain the system speed at the reference compensating for any changes.

3.7.2 Effect of a Fault on the Electrical Parameters

Proved in [105] that mechanical abnormalities cause additional load oscillations that are mostly modulated at frequencies (f_F) that is related to the rotating speed (f_r) and supply frequency, and normally calculated at [106]:

$$f_F = f(f_s, f_r) \quad (3.27)$$

Therefore mechanical oscillations due to the fault are found to be sinusoidal and cause an angular displacement of α_F, with current amplitude of I_F. This angular displacement results in oscillatory torque ΔT_e that is described as the following [103, 107]:

$$\Delta T_e = 3N_p\psi I_F \sin\left(2\pi f_F t - \left(\alpha_I - \alpha_\psi\right) - \alpha_F\right) \quad (3.28)$$

The mechanical equation of the induction motor speed is represented as follows [14]:

$$\frac{d\omega_{\mathrm{r}}(\mathrm{t})}{dt} = \frac{1}{J}\left(T_e(t) - T_l(t)\right) \tag{3.29}$$

From Equation 3.28 and Equation 3.29, the motor speed (ω_{r}) will also fluctuate due to the fault. The produced amplitude of electromagnetic torque from the motor is equal to the amplitude of the load torque. Hence the speed fluctuation $\Delta\omega_{\mathrm{r}}$ caused by the fault is then calculated as follows:

$$\Delta\omega_{\mathrm{r}} = \frac{N_p}{J}\int \Delta T_e dt = -\frac{3{N_p}^2\psi \mathrm{I}_F}{2\pi f_F J}\sin\left(2\pi f_F t - (\alpha_I - \alpha_\psi) - \alpha_{\mathrm{F}}\right)\, dt \tag{3.30}$$

This results in fluctuation in the rotor angular position as follows [103]:

$$\Delta\theta = \Delta\alpha_{\mathrm{F}} = \frac{N_p}{J}\int \Delta\omega dt = \frac{3{N_p}^2\psi \mathrm{I}_F}{4\pi^2 f_F^2 J}\sin\left(2\pi f_F t - (\alpha_I - \alpha_\psi) - \alpha_{\mathrm{F}}\right)\, dt \tag{3.31}$$

Equations 3.30 and 3.31 show that the load oscillations due to mechanical fault generate an alternating torque component that modulates the system speed and causes speed oscillation at fluctuation thus changing the rotor position.

The fluctuation in the rotor position effects the slip frequency as in Equation 3.23 and therefore the torque current component will also be infected by the fault based on the Equation 3.22. Hence the rotor flux may be also oscillated and significantly impacted. This can be clear from its dependency on the slip frequency and torque signal as shown in Equations 3.20 and 2.22. Therefore both torque and field current components will carry signatures related to the load oscillations due to the modulations occurring in speed, rotor position and rotor flux signals. As explained in [103, 108], such signatures are found at the fundamental component frequency of the fault profile, e.g. multi-stage gear shafts rotating frequencies.

This will also produce two sidebands around the fundamental supply frequency. The corresponding stator flux variation is given as [108]:

$$\psi_s^F(t) = \sqrt{2}\psi\cos\{2\pi f_F t - \alpha_\psi - \Delta\psi\sin[2\pi f_F t - (\alpha_I - \alpha_\psi) - \alpha_{\mathrm{F}}]\} \tag{3.32}$$

The interaction between the modulus of stator flux and the equivalent circuit impedance generates sideband components around the supply frequency of both current and voltage signals as follows [24, 103]:

$$i^F(t) = \sqrt{2}I\cos\left(2\pi f_s t - \alpha_I\right) + I_l\cos(2\pi(f_s - f_F)t - \alpha_I - \alpha_F - \varphi) - I_r\cos\left(2\pi(f_s - f_F)t - 2\alpha_\psi + \alpha_I - \varphi_F - \varphi\right) \quad (3.33)$$

$$u^F(t) = \sqrt{2}U\cos\left(2\pi f_s t\right) + U_l\cos(2\pi(f_s - f_F)t - \alpha_F - \varphi) - U_r\cos\left(2\pi(f_s - f_F)t - 2\alpha_\psi + \varphi_F - \varphi\right) \quad (3.34)$$

The resulting power in the case of the fault is described in the following simplified formula [104]:

$$p^F(t) = IU[\cos\left(2\pi(2f_s)t - \alpha_I\right) + \cos(\alpha_I)] + (IU)_l\cos(2\pi(2f_s - 2f_F)t - 2\alpha_F - 2\varphi) - (IU)_r\cos\left(2\pi(2f_s - 2f_F)t - 2\alpha_\psi + 2\varphi_F - \varphi\right) + (IU)_l\cos(2\pi(2f_s - f_F)t - \alpha_F - \varphi) - (IU)_r\cos\left(2\pi(2f_s - f_F)t - \alpha_\psi + \varphi_F - \varphi\right) \quad (3.35)$$

Equation 3.35 shows that the spectrum of the electrical power has more characteristic frequency components than that of voltage and current. Specifically, there will be two sidebands at $2f_s \pm 2f_F$ in addition to two sidebands at $2f_s \pm f_F$.

These characteristic components in each electrical parameter will motivate the drive's regulators in order to maintain the system speed. However, due to the structure of the drive, such frequency components may or may not be detected by all the drive regulators dependent on the design and tuning parameters of the drive.

For instance, the outer control loop, i.e. speed control loop, detects these load oscillations if the frequency of oscillations is within its bandwidth. When the speed regulator is a PI controller, it acts like a low-pass filter. The reference i_{qs}^*signal to inner torque control loop is generated based on the following general PI controller formula:

$$i_{qs}^{*} = (\omega_r^{*} - \omega_{\mathrm{r}} + \Delta\omega_{\mathrm{r}})(k_p + \frac{k_i}{s}) \tag{3.36}$$

While the field current reference is also produced by a PI field controller as follows:

$$i_{ds}^{*} = (\psi_r^{*} - \psi_r + \Delta\psi_r)(k_p + \frac{k_i}{s}) \tag{3.37}$$

Equations 3.36 and 3.37 show that the bandwidth of the speed, torque and field current components' regulators have significant influence on performance of the drive. Additionally, both speed and field controller are the outer control loops, and hence torque, current and voltage loop will have wider bandwidth than that of the speed and field regulators. As a result the current control loop can respond more rapidly than the speed control loop, and faults at frequencies outside of the speed control loop bandwidth may be detected by the current loop. However, the current control loop bandwidth is limited by the voltage control loop bandwidth and not all frequency ranges will pass through the current regulators.

Additionally, Equations 3.27 to 3.30 show that oscillations due to faults add a very small static value to the fundamental signals. This means that the magnitude of the load torque will also increase due to the fault. Nevertheless, the drive manages the resulting load increase and forces the supply parameters to increase the electromagnetic torque from the motor to maintain the speed.

Based on the above discussion, from the condition monitoring perspective almost all power supply signals are more likely to be infected by the fault. The actions of the drive may increase the level of noise and create further difficulties in detecting small changes in the investigated signals due to the fault. The operation of the flux vector control drives is based on transferring the three phase electrical supply parameters into a particular frame of reference. This means that signals are mainly static values, most of which are utilised by the drive for control purposes. Hence it would be valuable to incorporate these static parameters for fault detection and diagnostics. Further advantages ensue from their ready availability at the drive and the absence of need for additional measurements. Also, the control strategy incorporates all supply parameters for control purposes. Observing these parameters can help in developing fault detection approach based on the control system response.

Chapter 4
Test Facilities

This chapter describes the general specifications of the test facility used in this study. It outlines the mechanical systems and control systems and specifies the mechanical faults that were seeded and studied on the rig. Furthermore, data acquisition systems, measuring equipment and sensors are also outlined to show the basic requirement of the data acquisition system in a typical CM system. Additionally, test rig repeatability is assessed and different signal performances are investigated.

4.1 Introduction

In order to investigate the proposed technique different experimental tests were performed using a laboratory transmission test system. These aimed at examining the developed condition monitoring scheme based on a real type industrial application. This also allows for replicating a variety of real faults that generally occur in industry within different operation conditions and different severities.

The test rig employed is designed to perform a repeatable, deterministic series of tests and to obtain data from tests in different speed, load and fault conditions. Tests can be repeated identically for both health and fault circumstances. Different fault severities can also be applied for approximately the same conditions. The test rig is designed based on real industrial equipment made for real applications of the mechanical transmission system. This chapter provides the construction of the test facility utilised, data acquisition used, and finally the operation principles of the rig.

4.2 Test Rig Construction

The test rig has two main parts, the mechanical system and the electrical control system, in addition to the measuring devices and data acquisition systems.

4.2.1 The Mechanical Part

The mechanical/electromechanical part of the system outlined in Figure 4.1 consists of a 15kW 3 phase AC induction motor as the prime driver, and two back to back two stage helical gearboxes for coupling the AC motor with a load generator using flexible spider rubber couplings. Couplings are a hard rubber three jaw type with a size of 150mm and a transmission power up to 100kW at 1600rpm speed. The transmission power of each gearbox is 13kW. The first gearbox (GB1) operates as a speed reducer while the other (GB2) is a speed increaser so that the system maintains adequate speed for the load generator to produce sufficient load to the AC motor through the two gearboxes. The main specifications of the AC motor, gearboxes, DC motor and couplings are given in Table 1, Table 2, Table 3 and Table 4 respectively.

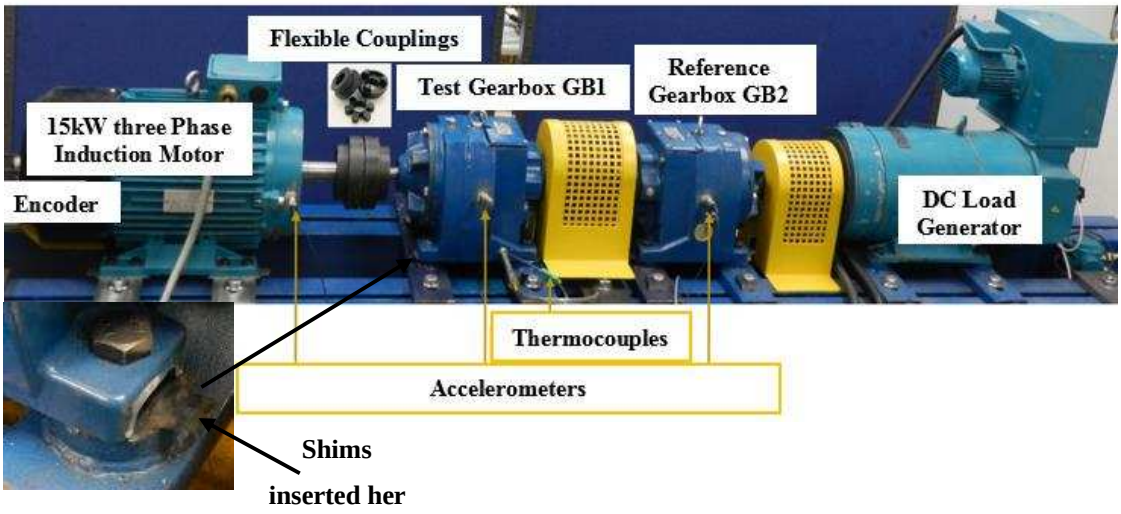

Figure 4.1 Mechanical part of the test rig

Table 1. AC Motor specifications	
Manufacturer	Invensys, Brook Crompton
Motor model	T-DA160LA
Number of poles	4
Frequency	50 Hz
Power	15 kW, 3 Phase
Voltage (frequency 50 Hz)	415 V
Rated Current	27.13 A
Connection	Delta Δ
Rated Speed	1460 rpm
Power factor (Cos Φ)	0.87
Full load torque	98.3 N.m
Stator resistance	0.8607 ohm
Stator Leakage Inductance	0.01678 H
Rotor time constant	0.270 sec
Rotor resistance	0.5247 ohm
Rotor Leakage Inductance	0.08678 H
Mutual Inductance	0.1706 H
Inertia	0.09 $kg.m^2$

Table 2. Gearbox specifications	
Manufacturer	Radicon
IT TYPE	M07223.6BRC-1-----
Ratio	3.678
DB oil grade	6E
Oil type	EP 320 (mineral oil)
Oil volume	2.6 L
Output torque	306N.m @1450rpm
Overhung load	3.50kN
Z1:Z2:Z3:Z4	58:47:13:59

Table 3. DC Motor Specifications	
Manufacturer	Invensys, Brook Crompton
Size	MD 132LC
No	B:99021436
Power	15 kW
Ins Class	F
Armature voltage	380 V
Field current	2.37 A
Speed	2100 rpm
Duty type	S1
Wd	Shunt
Brg	N.D.E.6202Z
Enclosure	IP23
Mass	13.7 Kg

Table 4. Flexible Coupling Specifications	
Manufacturer	Fenner
Type	HRC150H
Size	150mm
Rated speed	1600 rpm
Nominal torque	600 N.m
Mass	7.11kg
Inertia	0.01810kg.m2
Dynamic Stiffness	175 Nm/o
Maximum parallel misalignment	0.4mm
Maximum axial misalignment	+0.9mm
Maximum angular misalignment	1º
Element type	Nitrile spider

4.2.2 The Control System

The control system consists of a programmable logic controller (PLC) for establishing test profiles as specified by the operator, an AC VSD, for adjusting the speed of the system, and finally a DC VSD, for ensuring a controlled load to the AC motor by

regulating the torque of the load generator. The control panel is equiped with a LCD touch screen to enter the required test profile and to monitor the key variables when the rig is running. Figure 4.2 details the control system of the rig.

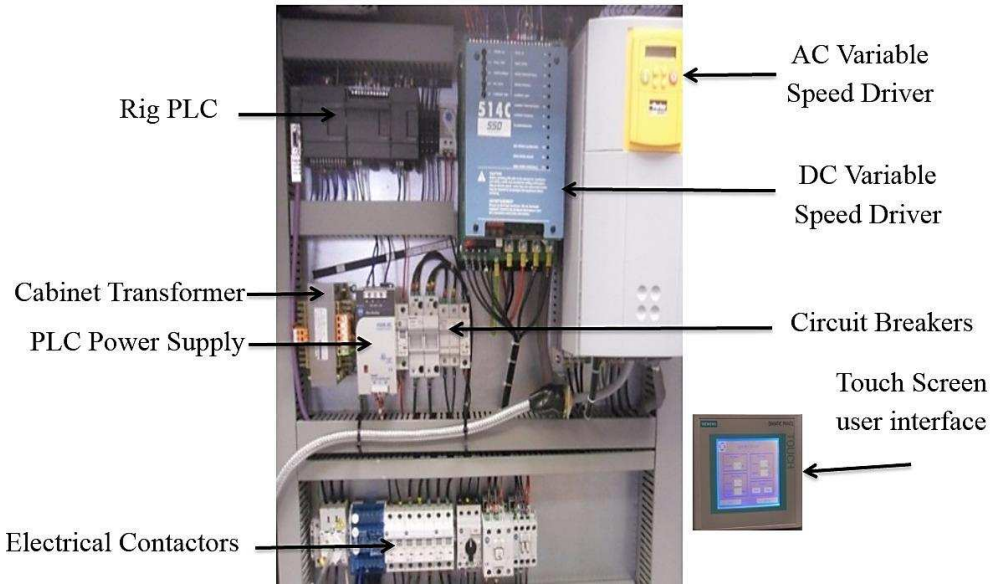

Figure 4.2 Test rig control system

4.2.2.1 Test Rig PLC

The function of the PLC is to perform tests exactly as requested by the operator. The test programme includes time duration, load references, speed references and number of steps. The PLC is SIEMENS, SIMATIC S67-200 which is constructed from:

PLC processor, SIEMENS CPU 222, with RAM and EEPROM slots.

Input Module, EM231 with 4 analogue inputs. Table 5 summarises the technical specifications of this module:

Table 5 The EM231 input module technical specifications	
Model	EM231, 4 inputs × 12 bits
Power loss	2W
Number of analogue Inputs	4
Voltage input range: Bipolar	± 2.5V, ± 5V
Current input range	0~20mA
Resolution	12 bit
Bipolar, full-scale range	-32, 000 to +32, 000
Unipolar, full-scale range	0 to +32, 000
Input impedance	≥ 10M Ω Voltage Input, 250 Ω Current Input
Analogue to digital conversion time	< 250μ s
Maximum input voltage	30V DC
Maximum input current	32mA

Output Module EM232, delivers the signals from the PLC to the external devices. The output module specifications are shown in Table 6.

Table 6. The EM232 output module technical specifications	
Model	EM232 2 outputs × 12bits
Resolution	12 bits
From L+ current consumption	70mA
Power loss	2W
Number of analogue outputs	2
Output voltage range	-10~+10V
Output current range	0~20mA
for voltage outputs	Min: 5KΩ
for current outputs	Max: 0.5KΩ
Basic error	± 0.5% of full range

4.2.2.2 AC Variable Speed Drive

The AC VSD is a Parker 650V which is made for industrial applications. It can be set either to a sensorless flux vector control mode or V/Hz mode for adjusting the speed of

the system. The P3 port permits the drive to be connected to either a network of drives or with a PC. The technical specifications of the drive are presented in Table 7.

Table 7. The 650 V drive technical specifications	
Product Description	AC variable speed drive
Model	650 V
Output Frequency	0-240Hz
Output current	0-33 A
Output voltage	0-460 v ±10%
Rated motor power	15kW
Switching Frequency	3kHz nominal
Voltage Boost	0-25%
Flux Control	1. V/F control with linear or fan law profile 2. Sensorless flux vector
Voltage/Frequency Profile	- Constant torque - Fan Law
Analogue Inputs	2 inputs – one is configurable; voltage or current
Analogue Outputs	1 configurable voltage or current
Digital Inputs	6 configurable 24V dc inputs (2 suitable for encoder)
Basic error	± 0.5% of full range

4.2.2.3 DC Variable Speed Drive

The utilised DC VSD is a Parker 514C series intended for use in an industrial environment. The drive regulates the torque of the DC motor with a linear closed loop and without the need for a feedback from an encoder or a tachometer. The drive utilises the armature voltage to calculate the speed. A summary of the DC drive specifications are shown in Table 8.

Table 8. The 514C DC drive technical specifications	
Product Description	Dc speed drive
Model	514C
Control Action	Closed Loop with Proportional Integral Control
Speed Feedback	Selectable: Armature Voltage or Tachogenerator
100% Load Regulation	2% when Armature Voltage mode used; 0.1% when Tachogenerator mode selected
Maximum Torque/Speed Range	20:1 when Armature Voltage mode used; 100:1 when Tachogenerator mode selected
Analogue inputs	7 non-configurable inputs
Analogue outputs	7 outputs: Setpoint Ramp, Total Setpoint, Speed, Current Demand, Current Meter (Bipolar or Modulus), +10V reference and -10Vreference.
S Ramp and Linear Ramp	Symmetric or asymmetric ramp up and down rates
Current Limit	Adjustable 110% or150%
Supply Voltage	110 – 480 Vac ± 10%
Nominal Armature Voltage	90 Vdc at 110/120 Vac 180 Vdc at 220/240 Vac 320 Vdc at 380/415 Vac
Overload	150% for 60 seconds
Field Current	3 A dc

4.2.3 Data Acquisition

The test rig uses the YE6232B from Global Sensor Technology that has a high speed data acquisition system (DAQS). The DAQS collects the data from sensors measuring vibration, three phase currents and voltages, and gearbox temperatures and sends them into a PC for post processing and analysis. A photograph of the data acquisition system is shown in Figure 4.3 and its main specifications are contained in Table 9.

Figure 4.3 Data acquisition system used for tests

Table 9. YE6232B DAQS specifications	
DAQ system manufacturer	Global Sensor Technology YE6232B
Number of Channels	16 (selectable)
A/D Conversion resolution	24 bit
Sampling rate (maximum)	96kHz per channel, Parallel sampling
Input range	±10 V
Gain	×1, ×10, ×100
Filter	Anti-aliasing
Interface	USB 2.0

During tests data are collected based on the maximum sampling frequency of the DAQS, i.e. 96000 samples/second, and each set of dynamic data has been acquired for 30 seconds. For such settings the length of data collected for each set is 30*96000= 2880000 data points. This data acquisition system is equipped with an antialiasing filter which guarantees that the aliased frequencies are not captured. Additionally, the antialiasing filter is also used to automatically adjust the cut-off frequency of another built in low pass filter based on a pre-selected sampling rate.

Signals from current, voltage and vibration sensors, which represent the instantaneous values, are referred to as dynamic data where it is processed in the frequency domain for analysis. Another PC was used to log data directly from the AC VSD. The logged signals include, line voltage, current, speed and torque. However all this data is in the rms form and referred to as static data. The sampling frequency of static data is as low as 1Hz per data point. So in one minute, around 60 data points are collected, meaning lower resources are required for saving and processing such a relatively low data size.

4.2.4 Tools, Sensors and Measuring Devices

Different measuring tools and devices have been used during tests, which include:

The three phase measurement unit: This measuring device measures the instantaneous three phase currents and voltages based on Hall Effect current and voltage transducers. The voltage transducer is the LEM LV 25-P and the current transducer is the ABB

EL55P2. The photographic and the schematic diagram of the three phase measuring device are shown in Figure 4.4 and the specifications of the voltage and current transducers are presented in Table 10 and 11 respectively.

Accelerometers: the vibration of induction motor, GB1 and GB2 are measured using an ICP-type Accelerometer. The accelerometers are placed horizontally in parallel with shafts centrelines of the machines, as shown in Figure 4.1.

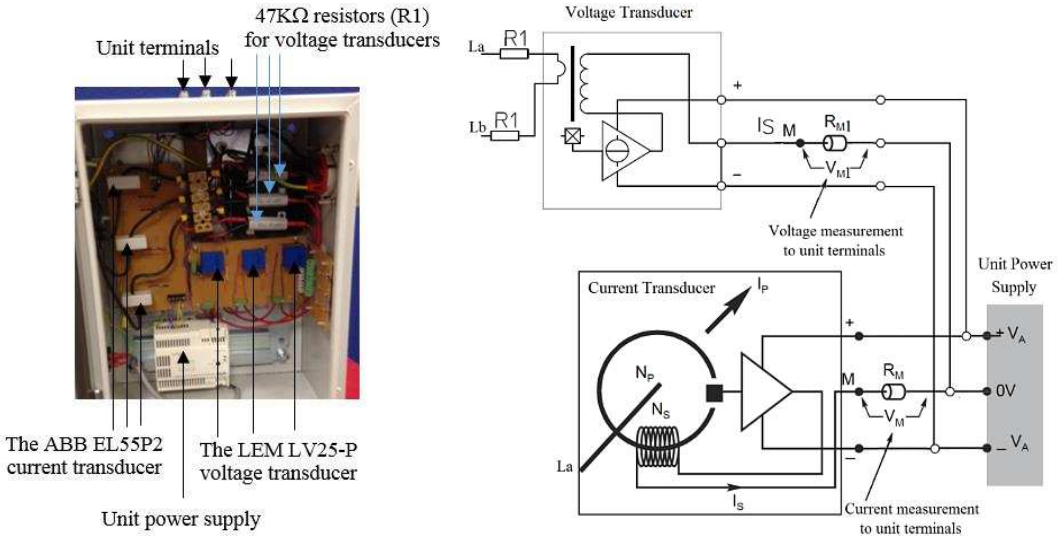

Figure 4.4 Three phase electrical signals measurement device

Table 10. Specifications of the voltage transducer	
Brand and Type	LEM Voltage Transducer LV 25-Pt
Primary nominal voltage (V_{pn})rms	10 : 500 V
Primary nominal current (I_{pn})rms	10 mA
Primary current, measuring range	0 : ±14 mA
Secondary nominal current (I_{sn})rms	25 mA
Supply voltage (±5%)	± (12:15) V
Current consumption	10(@±15V) + I_s mA
Overall accuracy	±0.9% @ (I_{pn} , 25°C and ±15V)
Linearity error	<0.2%
Response time to 90% of I_{pn} step	40μs

Table 11. Specifications of the current transducer	
Brand	ABB
Type	Current Transducer EL55P2
Technology	Hall Effect
Primary nominal current (I_{pn})rms	50 A
Supply voltage (Va)	±(11:15.7) V
Measuring range @ Va	0 : ±80 A
Secondary nominal current (I_{sn}) rms	25 mA
Thermal drift/ I_{sn}	$2*10^{-4}$ /°C
Bandwidth (-1 dB)	0:200 kHz
Accuracy	±0.5% @ (I_{pn} , 0:70°C and ±15V)
Linearity	Better than 10^{-3}
Response time	<0.1 μs
No load current consumption	1 6 (@±15V Va) mA

Thermocouples: the temperature of the oil inside each gearbox is measured using K type thermocouples. The signal from the thermocouple is sent to the temperature processing unit for filtering and magnification.

Speed encoder: An optical speed encoder is attached to the AC motor to measure the system speed. The encoder is the RS32-O/100ER, manufactured by Hengstle. It has two outputs, one producing 100 pulses per revolution and the other 1 pulse per revolution. The encoder is connected to the data acquisition system directly and not utilised in the control system. Figure 4.1 illustrates how the encoder fitted on the rear of the AC motor.

Dial indicator: this tool is used for aligning the rig. It is the EDI-125 and has an accuracy of ±0.005mm, measurement range: 12.7 mm with 0.001mm resolution. The dial indicator is fitted on a magnetic base that allows it to be fitted on the shaft for adjusting the alignment. Figure 4.5 depicts this indicator during an alignment process.

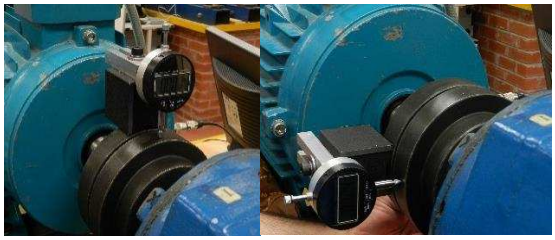

Figure 4.5 Digital dial indicator for shaft alignment (author)

Pre-cut standard shims: sstainless steel standard pre-cut shims are used for adjusting the alignment of the rig and also for seeding the misalignment faults. Different sizes are used to obtain the best possible alignment. To misalign the rig these shims are placed under the item when needed. Figure 4.1 illustrates how these shims are placed under the GB1.

Volumetric measuring tools: a beaker and pipette for measuring the quantities of oil and water respectively.

4.3 Test Rig Operation

The schematic of the rig is shown in Figure 4.6. The operator enters the required test profile via the touch screen interface. The rig PLC obtains this profile which includes number of cycles, speed reference, load reference and time duration for each cycle. Up to 12 cycles can be programmed. When the user starts the rig, the PLC sends the reference values and start commands to both the AC VSD and the DC VSD.

The AC VSD runs the AC motor at the required speed, without feedback speed encoder, benefits from the built in PI controllers and the Model Reference Adaptive System (MRAS). The DC drive feeds the DC load generator with the proper supply based on the load settings from the PLC. The DC drive regulates the armature and field currents of the DC load generator to adjust the load. This provides the ability to study the system's behaviour under different speed and load conditions as well as the transient process between different conditions.

When the AC motor rotates, both gear boxes rotate, the first gearbox reduces the speed, while the second gearbox increases it again to the original speed and rotates the DC motor with the same speed of the AC motor. The PLC obtains feedback signals from

both AC VSD and DC speed driver, including: AC current, load feedback (DC armature current), and speed feedback, and shows them on the rig screen.

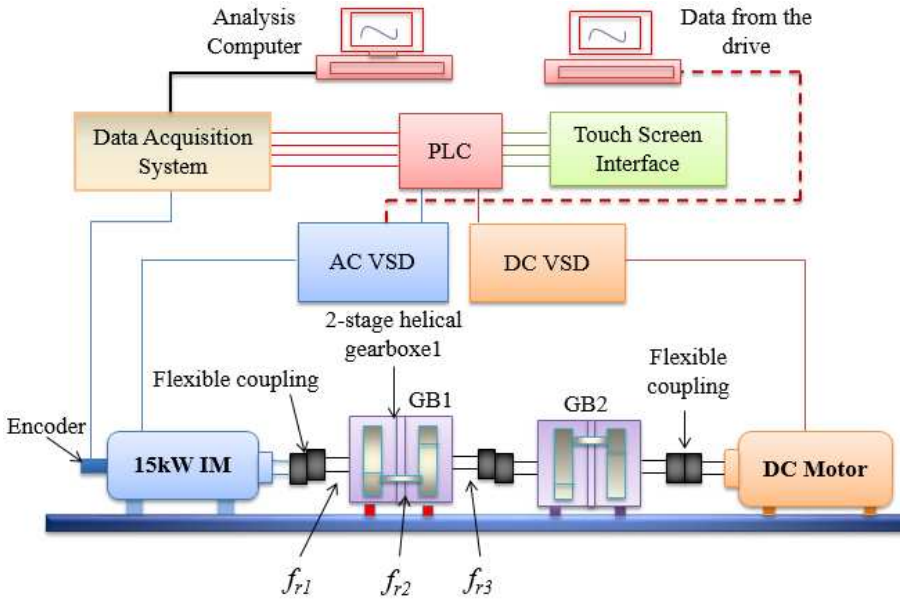

Figure 4.6 Schematic of the test rig

4.4 Faults Simulated

Four different faults were studied, i.e. shaft misalignment, water in oil contamination, gearbox oil viscosity changes and gearbox lubricating shortage referred to as oil level tests. The studied faults represent some of the most common faults that occur in mechanical transmission systems. Additionally, the detection of these faults using power supply parameters within a sensorless controlled transmission system is not yet well discovered. Tests performed are to examine the performance of the fault detection scheme and to investigate the diagnosis capabilities of the power supply parameters together with control data, particularly in the case of a mechanical transmission system driven with a sensorless variable speed drive.

4.4.1 Shaft Misalignment

The misalignment is seeded into the rig by placing standard pre-cut stainless steel shims under the GB1. Four different degrees of parallel shaft misalignments are simulated;

i.e. 0.3 mm, 0.5 mm, 0.7mm, and 1.00 mm successively. The permissible misalignment limit for the couplings is 0.4 mm.

The rig is firstly aligned at the lowest possible misalignment using the dial indicator (this was at 0.04±0.01 mm). A cycle of 5 different load settings was applied, 0%, 25%, 50%, 75% and 100% of the full load. Each load is applied for a period of two minutes. The AC motor speed is set at its full speed during the tests. A set of 10 seconds of dynamic data is collected for each load, while the data from the VSD is logged for the entire cycle.

4.4.2 Oil Degradation Tests

Three different oil degradation tests were seeded, water contaminated oil, oil viscosity changes and less lubrication referred to as oil level changes. In the following the procedure followed and value used for each fault type when such faults were tested.

4.4.2.1 Water Contaminated Oil

As stated in [129] the typical acceptable water content for transmission oils are in the range of 1 to 2% (10 to 20 kppm). Therefore, the contamination levels tested were derived from values both below and above this range, which allows a variety of different underlying measurements to be examined in a wide range for defining their corresponding detection performances. Tests were performed using four incremental water contents: 4.0kppm, 7.0kppm, 20kppm, 30.0kppm, and 60.0kppm, which respectively correspond to 0.4%, 0.7%, 3% and 6% water content of the name plate oil quantity.

4.4.2.2 Oil with Different Viscosities

The British Standard PD ISO/TR 18792:2008 [180] details guidelines on the selection of the lubricant viscosities for different types of gears while the BS 4231:1992 ISO 3448: 1992 [181] provides viscosity classification for industrial liquid lubricants. However, as stated in the American National Standard Institute/American Gear Manufacturers Association standard number (ANSI/AGMA 9005-E02) “the recommendations of the gear manufacturer should be followed, when available, in

selecting a gear lubricant." Also, standards request manufacturers to provide general information about the recommended oil suppliers.

The viscosity is principally specified during the design stage. Generally the speed at the pitch line of gears is used for determining the required viscosity. Hence, the viscosity can be derived using the following empirical equation [182]:

$$v_{40} = \frac{7000}{V^{0.5}} \tag{8.7}$$

Where v_{40} is the lube kinematic viscosity at 40 ^{o}C in (cSt) and V is the operating pitch line velocity in (ft/min) and can be derived from [182]:

$$V = 0.262\, dn \tag{8.8}$$

where d is the operating pitch diameter in inches, and n is the pinion speed in (rev/min).

For the gearbox utilised in this study the manufacturer recommends the EP 320, with Millers Oil Ltd one of the recommended suppliers. Consequently the oil used for regular operation in this study is the EP 320 from this supplier. However, this can be confirmed from the standards and Equations 8.7 and 8.8. The two stage helical gearbox has two pinions; the maximum input shaft speed is 1500 rpm transferred into the second shaft by a rate of (1.234). Hence the highest speed of the second shaft is 1851.1 rpm. Considering the highest speed side pinion and from the gearbox specifications, the pitch line diameter is d=1.275 inches hence:

V=0.262*1.275*1851.1=618.36

The required viscosity at 40 ^{o}C therefore is:

$v_{40} = 7000/618.36^{0.5} = 281.4993$cSt

By following guidelines in the BS 4231:1992 ISO 3448:1992, the recommended viscosity recommended therefore is ISO VG 320, i.e. EP320.

To study the effect of varying oil viscosity in a gearbox, four different oils having different viscosities, EP 100, EP 320, EP650 and EP 1000 respectively, were tested. The gearbox manufacturer recommends the EP 320. The EP 650 was made in the laboratory by mixing 61% of EP 1000 with 39% of EP 100. While the other types have

been provided from a supplier who was recommended by the gearbox manufacturer, with key specifications listed in Table 12.

Table 12. Specifications of the oils used for tests.

Oil type	Specific Gravity (at 15°C)	Kinematic Viscosity at (100°C, c.St)	Kinematic Viscosity at (40°C, c.St)	Viscosity Index	Pour Point (°C)	Flash Point (°C)
EP 100	0.885	10.95	100	93	-9	200
EP 320	0.901	23.5	320	92	-9	200
EP 1000	0.927	71.0	1000	140	-6	200

4.4.2.3 Oil with Different Levels

Three different oil volumes were tested, namely the standard level (BL = 2.6 litres), 600ml less (LL-600 = 77% of the full recommended volume) and 1100ml less (LL-1100 = 57.7% of the full recommended volume).

4.4.2.4 Oil Degradation Test Procedures

Each set of oil tests have been performed separately. However, tests have been carried out with the same test profiles and procedures. This allows variation of different underlying measurements to examine a wide range of faults, with different severities, for defining the corresponding detection methods. Oil degradation tests were carried out on GB1.

The test rig was firstly aligned at the lowest possible misalignment using the dial indicator (this was at 0.04±0.01 mm). Oil is added and removed from GB1 without affecting the alignment condition using the top and drainage holes on the gearbox. The rig is operated at three speed settings: 50%, 75% and 100% of the full motor speed, under four incremental load settings: 0%, 30%, 70%, and 100% of the system full load for each speed cycle. This was aimed at investigation of the detection under variable speed and load operations, which are common scenarios in real applications. Each load setting operated for a period of two minutes and was automatically changed to the next step by the PLC controller. In total, each load cycle lasted 8 minutes. The VSD was set

under sensorless control mode for evaluating the detection capability under this particular mode.

To ensure data quality and reliability, each speed/load cycle was operated five times consecutively for each oil type. During these repeated operations, the lube temperature in GB1 and GB2 was observed and recorded on-line and reached to around 43°C-45°C when the system operating parameters also became stabilised. Thirty seconds length of dynamic data was collected at every load setting. In the meantime, the static data from the VSD was also logged for the entire speed/load cycle. In addition samples of oil were taken after each oil viscosity and water in oil test to measure their viscosity values.

4.5 Data Processing

Dynamic data, i.e. vibration, current, voltage and power signals from sensors, is converted to the frequency domain by implementing the Fast Fourier transform in the Matlab environment. The principle of computing fast Fourier transform (FFT) in a Matlab programme is based on:

$$x(t) = \int_{-\infty}^{\infty} F(f) e^{-2i\pi ft} \tag{4.1}$$

$$F(f) = \int_{-\infty}^{\infty} x(t) e^{2i\pi ft} \tag{4.2}$$

where i= 0, 1, 2, …..n, n number of samples.

The FFT decomposes a series of values into different frequency elements. It is obtained by the following formula:

$$F(f) = FFT[x(t)] = \sum_{-\infty}^{+\infty} x\,(t) e^{-j2\pi f} \tag{4.3}$$

The performance of each signal is then examined by extracting the amplitudes at the corresponding feature frequencies. Amplitudes are then compared for detecting any changes that may occur due to faults.

To investigate vibration changes, vibration signals are applied with a time synchronous average (TSA) procedure and subsequent order spectrum analysis to suppress noise influences which are not time aligned to the second shaft, and hence to obtain vibration

which is more associated with gear meshing dynamics. Brief information on the TSA and order analysis is given in Appendix I. The TSA algorithm is developed by one of research groups at the Centre for Efficiency and Performance Engineering in the University of Huddersfield. Thanks to Dr. Fungshou Gu the algorithm was made available for this study. Meanwhile a direct comparison of the static data is made between the baseline and different cases to examine their detection performance in line with the results from dynamic data.

4.6 Baseline Characteristics

4.6.1 Characteristic Frequencies

The characteristic frequencies of the rig are derived mainly from the gearbox and motor. Gearbox frequencies are the product of the stages frequencies (rotation frequency of each stage in Hz) and their sidebands and harmonics. Additionally, the meshing frequencies which are the product of the stage frequency and number of teeth [136]. These frequencies are mostly modulated by the supply frequency and can mostly be clearly found in the vibration spectrum. To calculate the most important frequencies, Figure 4.7 presents a simplified schematic of the two stage gearboxes.

From Figure 4.7, the frequencies of the different stages can be calculated as follows:

$$f_{r2} = \frac{z_1}{z_2} f_{\mathrm{r1}} = 1.234 * f_{\mathrm{r1}} \tag{4.4}$$

$$f_{r3} = \frac{z_3}{z_4} f_{\mathrm{r2}} = 0.2203 * f_{\mathrm{r2}} \tag{4.5}$$

$$f_{r3} = 0.2719 * f_{\mathrm{r1}} \tag{4.6}$$

In the electrical supply signals, sideband frequency components of the different stage frequencies f_{r1}, f_{r2} and f_{r3} around the supply frequency are defined as:

$$f_{r1sb} = f_s \pm f_{\mathrm{r1}} \tag{4.7}$$

$$f_{r2sb} = f_s \pm f_{\mathrm{r2}} \tag{4.8}$$

$$f_{r3sb} = f_s \pm f_{\mathrm{r3}} \tag{4.9}$$

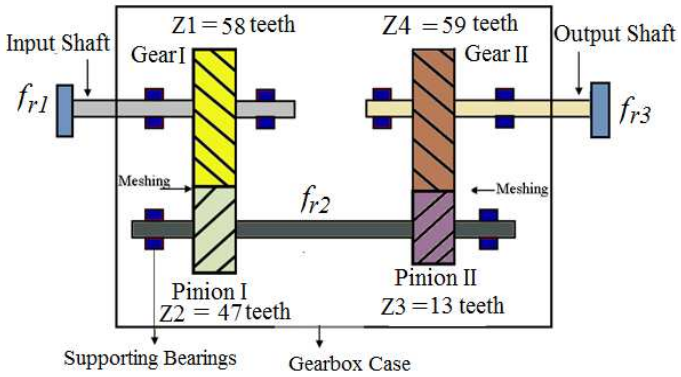

Figure 4.7 General schematic of a two stage gearbox (author)

The f_{r1}, f_{r2} and f_{r3} and their sidebands and harmonics are examined for any changes when diagnosing gearboxes. Particularly, amplitudes at f_{r1} and f_{r3} sidebands and their harmonics can carry information about the gear and the couplings as well. On the other hand the f_{r2} is related to the internal shaft and is expected to carry information related to the internals of the gearbox such as tooth breakage, manufacturing defects and/or lubricating problems.

Other important frequency components from the gearbox vibration are those results derived from tooth mesh. In a two stage gearbox, there are two meshing frequencies, f_{m1} and f_{m2}, that can be calculated as follows [136]:

$$f_{m1} = z_1 * f_{r1} = 58 * f_{r1} \tag{4.10}$$

$$f_{m2} = z_3 * f_{r2} = 13 * f_{r1} \tag{4.11}$$

Further, inherent manufacturing faults and gear imperfection such as eccentricity, misalignment and clearance, make these fundamental frequencies modulate in amplitude and phase at frequency sidebands. These sidebands can be found on both sides of the meshing frequencies as well as their harmonics in the vibration spectrum. Therefore these sidebands are frequently employed for fault detection and diagnosis. The meshing frequency sidebands ($f_{sd,mk}$) are calculated based on the following formula [136]:

$$f_{sd,mk} = m * f_m \pm k * f_r \ , \quad m = 1,2,3,..\ and\ k = 1,2,3,.. \tag{4.12}$$

As clear from Equations 4.4 to 4.12, the exciting components of all frequencies is based on gearbox rotating frequencies. Changes in the gearbox condition due to fault may cause additional oscillations in the speed signal. When the variable speed drive is in the sensorless control mode, the speed is regulated and the drive prevents these oscillations from appearing in the system speed.

4.6.2 Influence of Temperature

To check for repeatability and reliability, two sets of tests have been carried out. Signals checked are mainly static data from the drive, including speed feedback, speed demand, motor current,I_d,I_q, terminal voltages, and power. The test profile explained for the oil tests was applied twice, once after dismantling the rig and reassembling it. This was to ensure that repeatable data is collected even after reassembling the rig. Figure 4.8 shows signals from the lubricant temperature sensors in GB1 and GB2 and averaged speed under different load conditions for the two sets of runs. The repeatability tests were performed under sensorless operation mode.

It can be seen in Figure 4.8 (a and b) that temperature in GB1 and GB2 increases gradually and reaches stable status by the 3rd test when the system stabilised between 40-45^{o}C. In addition, the similarity of temperature trends between GB1 and GB2 shows that tests were conducted with good consistency between different tests. This indicates critically that the rig can provide repeatable and consistent results.

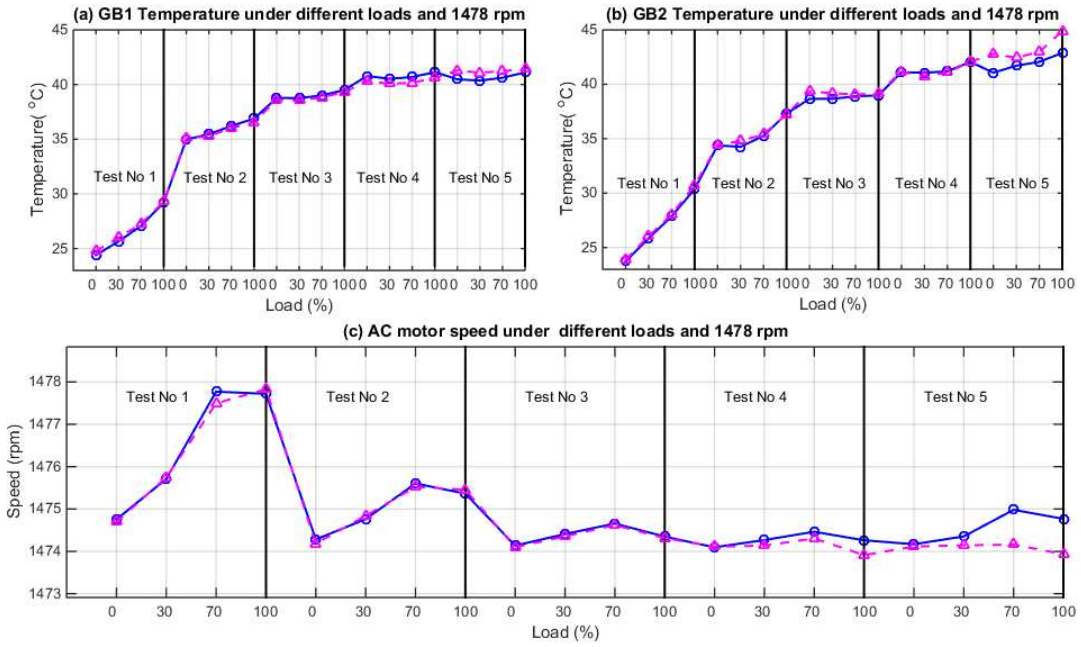

Figure 4.8 Temperature and speed under different load conditions for two sets of runs

The temperature stabilisation affects not only the oil inside the gearbox but also the circuitry performance of the electric and electronic components in the VSDs based system as well as the DC and AC motor windings. When it is under the lower temperature during the transient operation, the effect is stronger as the load and speed exhibit wider variation. That is, as shown in Figure 4.8 (c), during low temperature operation for the 1st and 2nd test runs the VSD has poorer performance in maintaining the speed of the system at the set-point, which leads to higher speed under high load. On the other hand, when the system reaches its stable conditions the VSD is then able to control the speed within the acceptable accuracy under different load settings. This can be clear for the speed results from testing runs 3rd to 5th. Therefore, in this study, particularly for oil tests, the analysis is performed by averaging and processing the results from the 3rd to 5th testing runs to obtain more reliable analysis. This can also be confirmed when checking the static data from the drive as in the following.

Figure 4.9 shows the comparison between signals from the 1st and 5th test cycles. Signals compared are motor current, torque and voltage as logged from the drive. The differences between the two cycles are clear which is consistent with the discussion

above. The motor draws more current for the first cycles than that of the 5th run and hence more torque. The oil in gearboxes is colder in the first runs than that in the last. Also resistances and inductances of both DC and AC motors are changed in value contributing to differences in the control and supply variables.

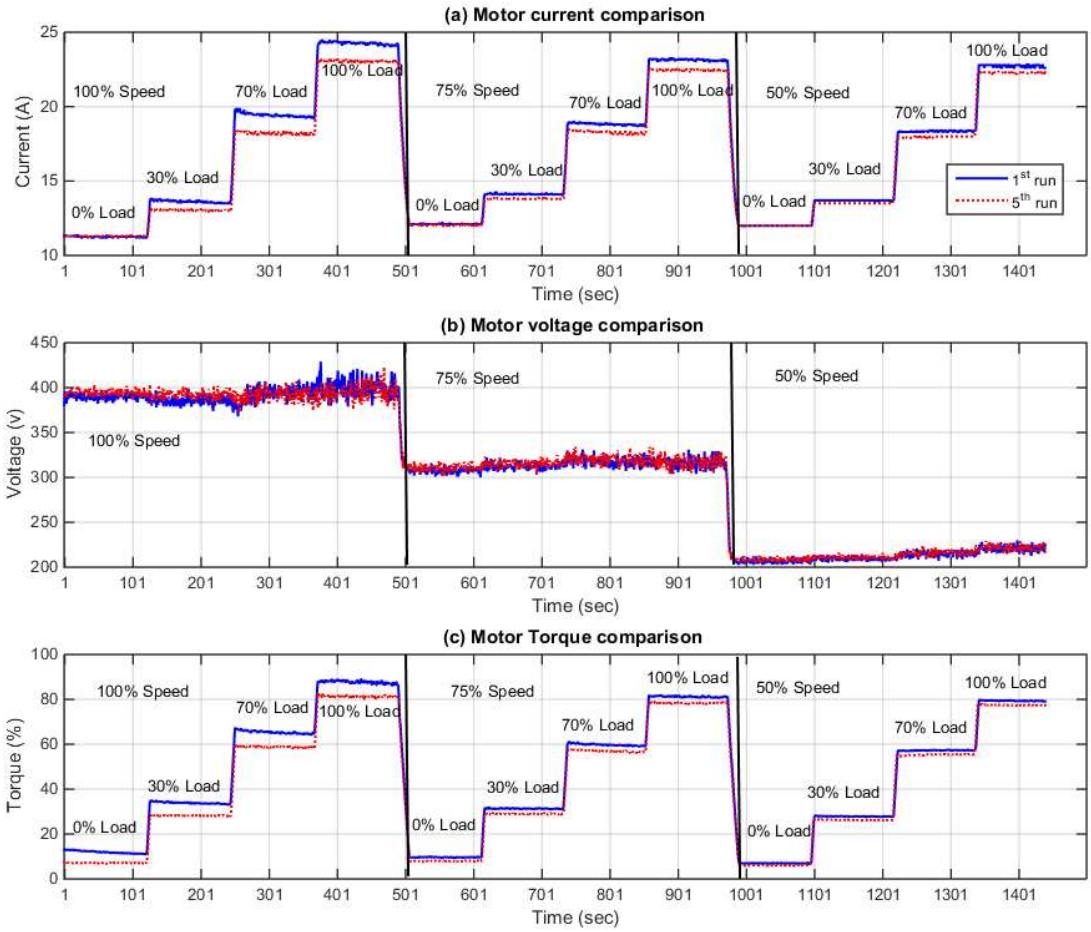

Figure 4.9 Current, voltage and torque static data under two different ambient conditions

Figure 4.10 shows the comparisons between power, I_q and I_d static data for the same test runs of the Figure 4.9. It shows clear differences between the two test runs for the three parameters. Figure 4.10 (c), describes the behaviour of I_d where it maintains constancy at speed under the rated speed value. While at 100% speed however, the amount of the I_d falls consistently with the load applied to allow for an additional voltage drop to recover any decrease in the motor speed due to load increase as well as

providing improved dynamic torque response. This is due to the field weakening strategy the drive applied.

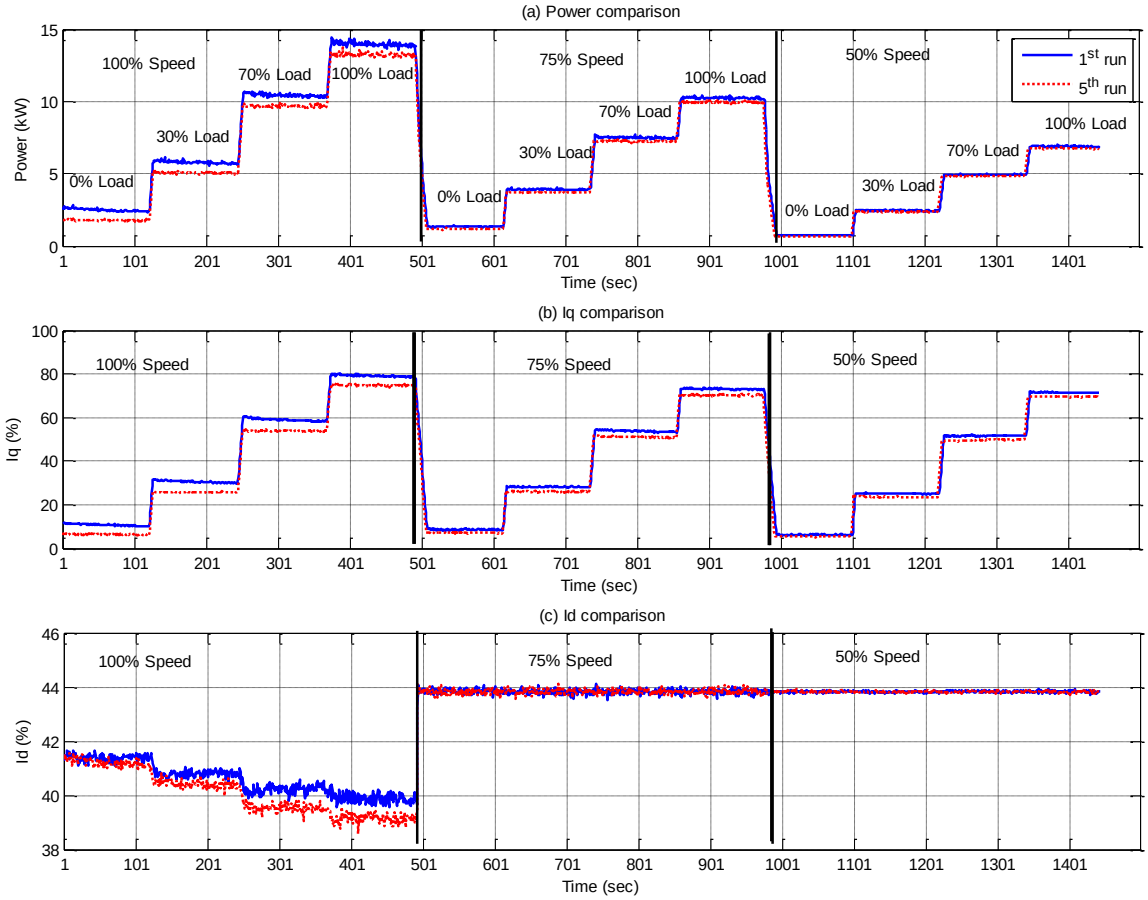

Figure 4.10 Power, I_q and I_d static data under two different ambient conditions

To conclude, data is collected after warming up the rig when most parameters are stabilised. Additionally, the signals from the last three testing runs can be averaged in order to obtain more reliable and representative results.

4.6.3 Repeatability Check

The static data from the drive has been investigated for the different test runs to ensure the repeatability of the rig. Different signals can be investigated for such a repeatability test. The current, voltage and torque static data from the 5th runs of the two tests are presented in Figure 4.11. It shows clear consistency between the different parameters where approximately the same test conditions are applied

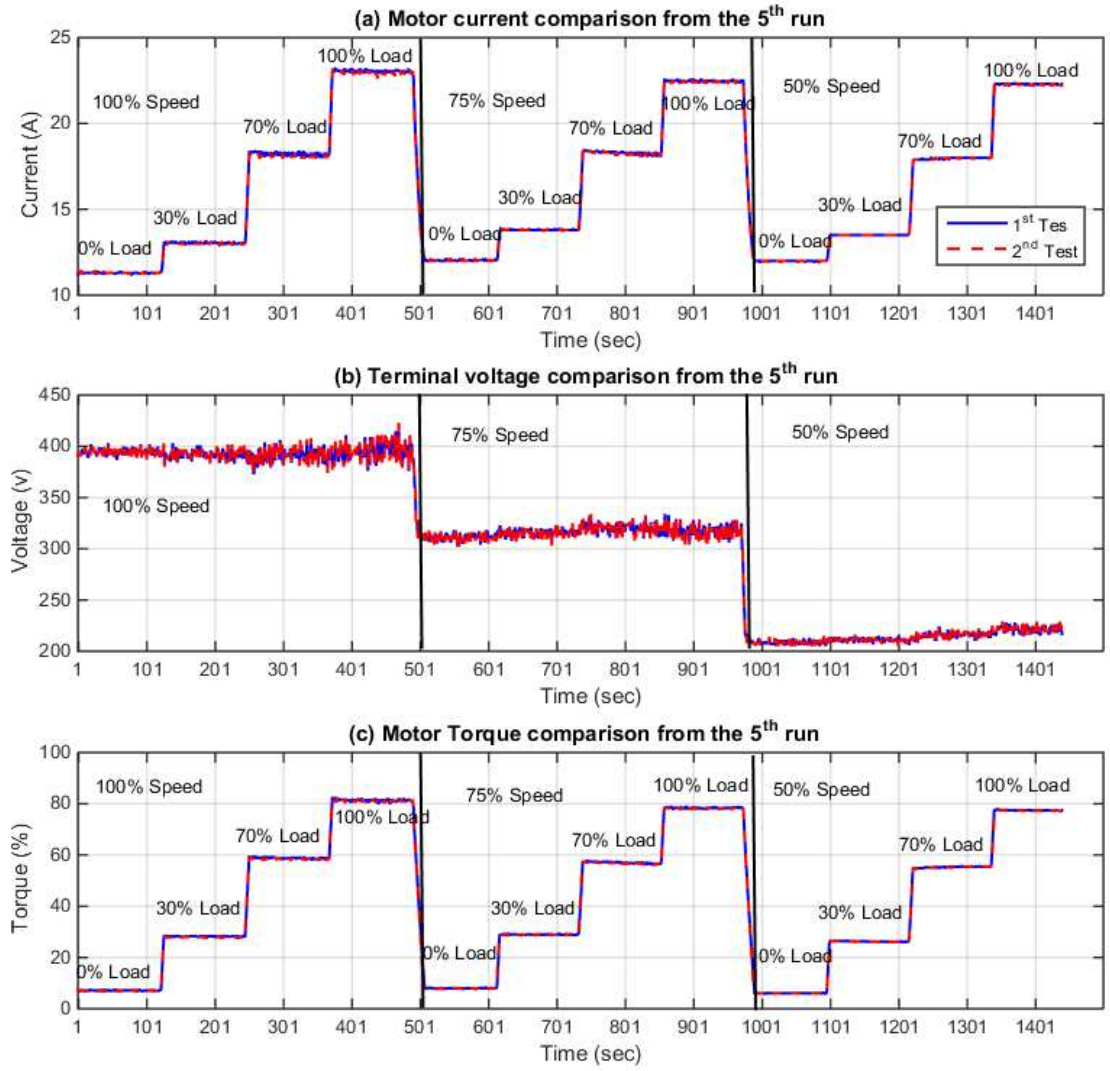

Figure 4.11 Current, voltage and torque static data repeatability check

Power, I_q and I_d static data have also been investigated for data repeatability and the results of the fifth test runs are shown in Figure 4.12. Results indicate that power, I_q and I_d static parameters showed repeatable behaviours when the test conditions are nearly the same.

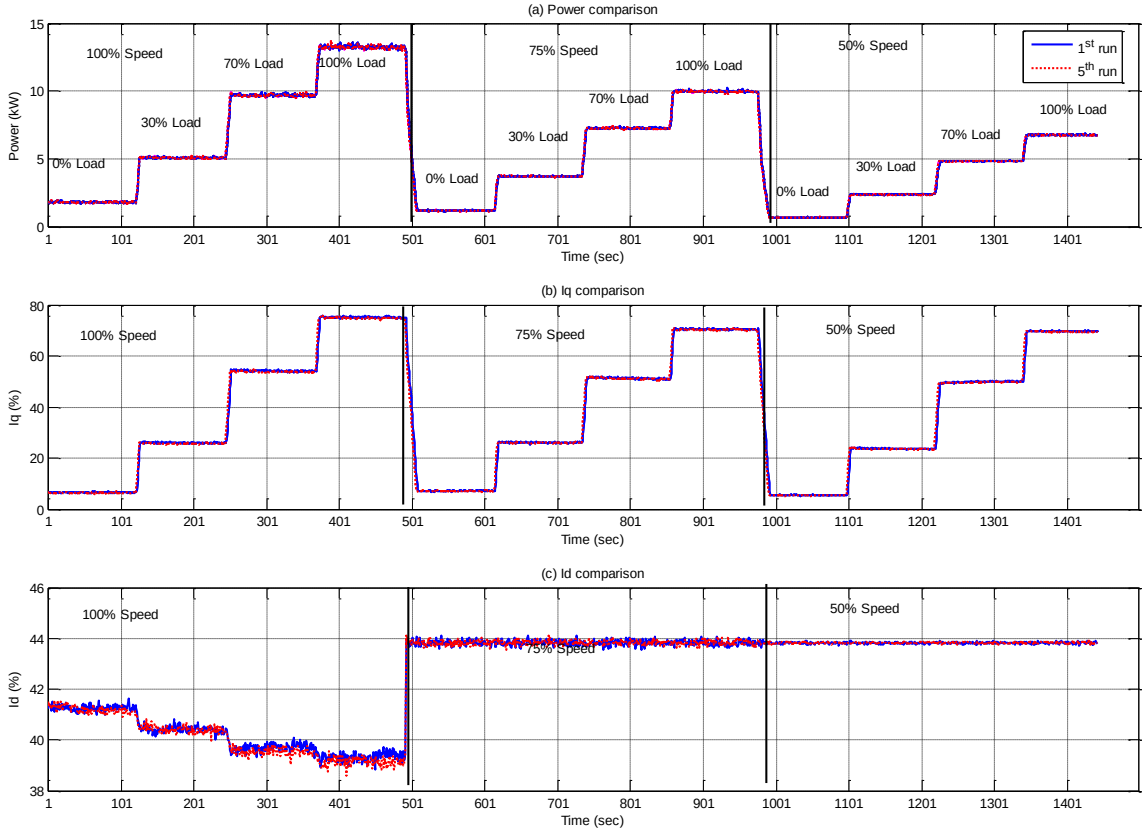

Figure 4.12 Power, I_q and I_d static data under two different ambient conditions

Figures 4.11 to 4.12 illustrate that under temperature and load test conditions the rig provides repeatable behaviours. This can also be confirmed by checking another test run where the rig is initialised at the room temperature, i.e. the first testing runs, as shown in Figure 4.13. It shows the behaviours of current, voltage and torque static data from the first testing runs. These testing runs represent the cold state for the two repeatability check tests. Figure 4.13 indicates that almost all control parameters behave in the same manner.

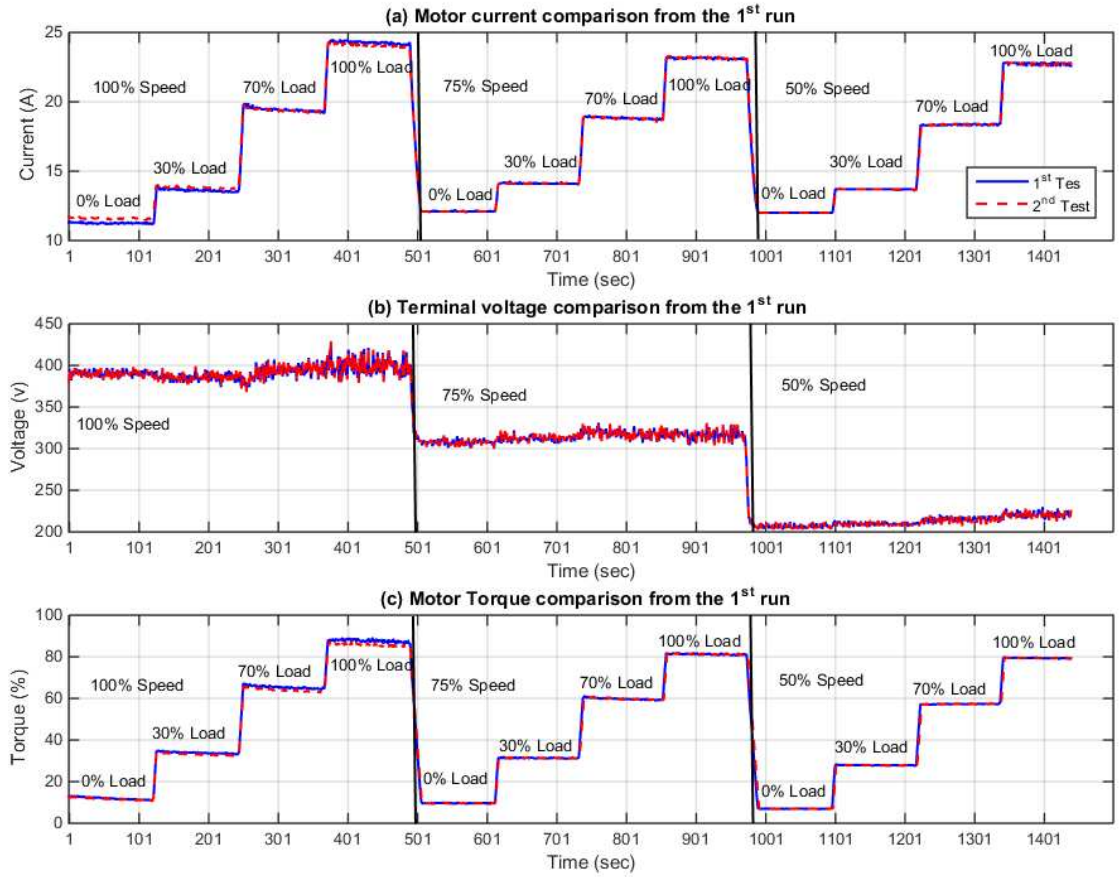

Figure 4.13 The first test runs from the two repeatability check tests

4.6.4 Dynamic Data Characteristics

The measured data from sensors are referred to as dynamic data, and it is possible to present it in the frequency domain. The frequency domain is obtained by processing the data with the fast Fourier transformation to investigate the spectra of data recorded. Many features can be then obtained from the signal spectrum depending on the type of signal. Chapter 7 provides details on the dynamic data characteristics in the frequency domain. In this chapter electrical data characteristics are briefly introduced in the time domain, while the characteristics of the rig vibration signals are discussed in more detail.

4.6.4.1 Electrical Parameters Signals

The three phase line currents were measured as explained earlier. Figure 4.14 (a) shows the line current signals as logged from the three phase measurement unit at the full speed under different loads. However, due to the fact the induction motor in the rig is delta connected, the phase currents are instead utilised. The line currents i_1 are therefore transferred into phase currents as represented in Figure 4.14 (b), with the following formula used for i_a:

$$i_1 = \sqrt{3} i_a \angle -30^o \tag{4.13}$$

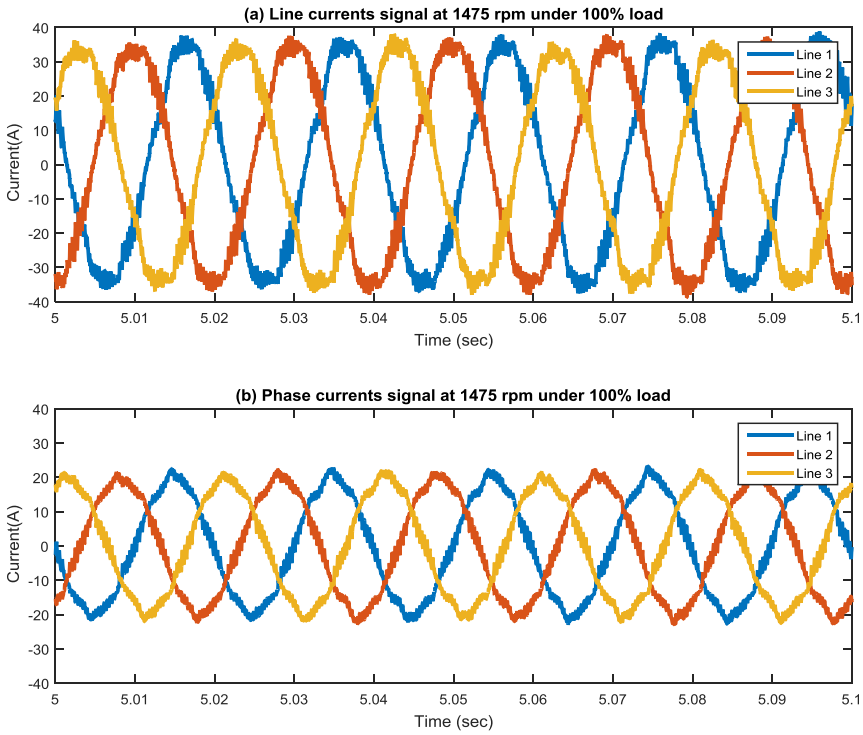

Figure 4.14 Line and phase currents at 100% speed under 100% load

The different shaft frequencies and the supply frequency are mostly in the lower frequency ranges. Therefore, current signals are low pass filtered to remove the noise associated with the measuring device, drive switching, and electrical mains. Figure 4.15, shows the filtered three phase currents at 100% speed under 100% load.

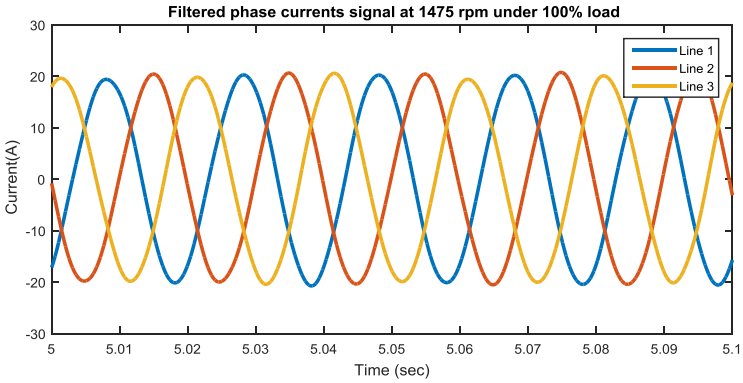

Figure 4.15 Filtered phase currents at 100% speed under 100% load

The three phase voltage signals from the VSD are different to that of current signals in that they are not purely sinusoidal as clear in Figure 4.16 (a) Therefore, voltage signals are also low pass filtered to remove the switching frequency and other associated noise. Figure 4.16 (b) depicts the filtered voltage signals:

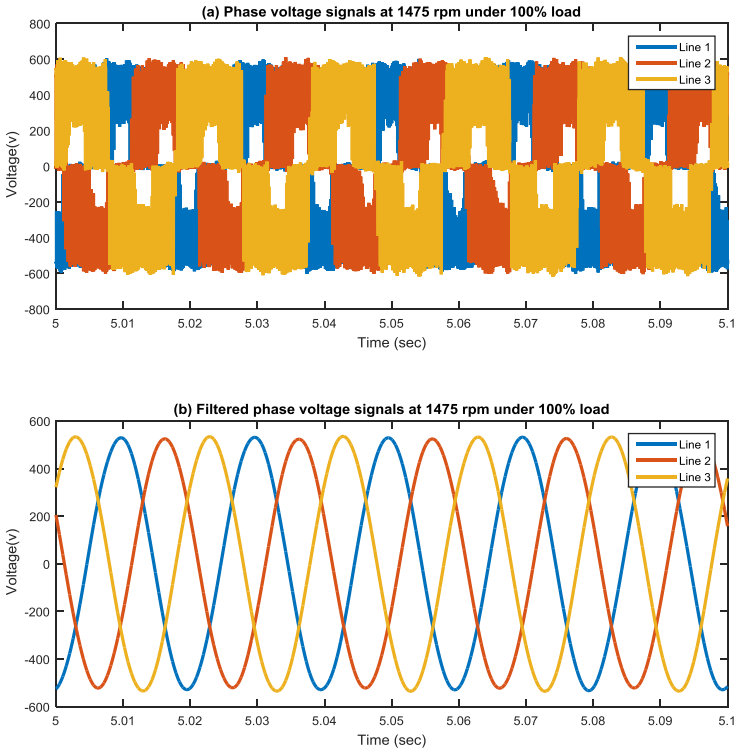

Figure 4.16 Phase voltage signals before and after filtering

The instantaneous power supply is calculated from the sum of the power at each phase. Both voltage and current signals are first filtered, the resulting power is then processed

for analysis. Figure 4.17 shows the instantaneous power signal at full speed under 100% load:

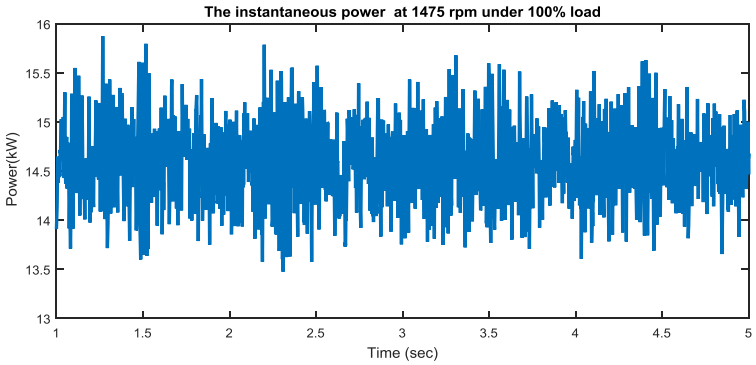

Figure 4.17 The instantaneous power at 100% speed under 100% load

The rig characteristic frequencies are calculated from different dynamic signals. Changes in the amplitudes at these frequencies may indicate for a certain fault. Therefore, amplitudes at these frequencies for different fault cases are compared with the corresponding of the baseline. Any consistent changes due to the abnormality seeded will indicate for the fault.

4.6.4.2 Vibration Signals

As indicated in section 4.6.1, two frequency ranges can be explored when dealing with vibration signals, i.e., low frequency range that relates to stage frequencies and a high frequency range related to the meshing frequencies. The vibration analysis may be carried out principally by investigating the root mean square (rms) of the time domain (raw) data. This can point to whether there is any change in the entire system vibration when compared with the previous time domain data. However, this cannot give detailed information on the system, and spectrum analysis is required.

Figure 4.18 shows the vibration signals of the 5th testing run as received from the accelerometer on the GB1 under different operational conditions. It shows that vibration increases as the load and speed increase. Analysis of the raw signals from accelerometers however is limited in informative content [136].

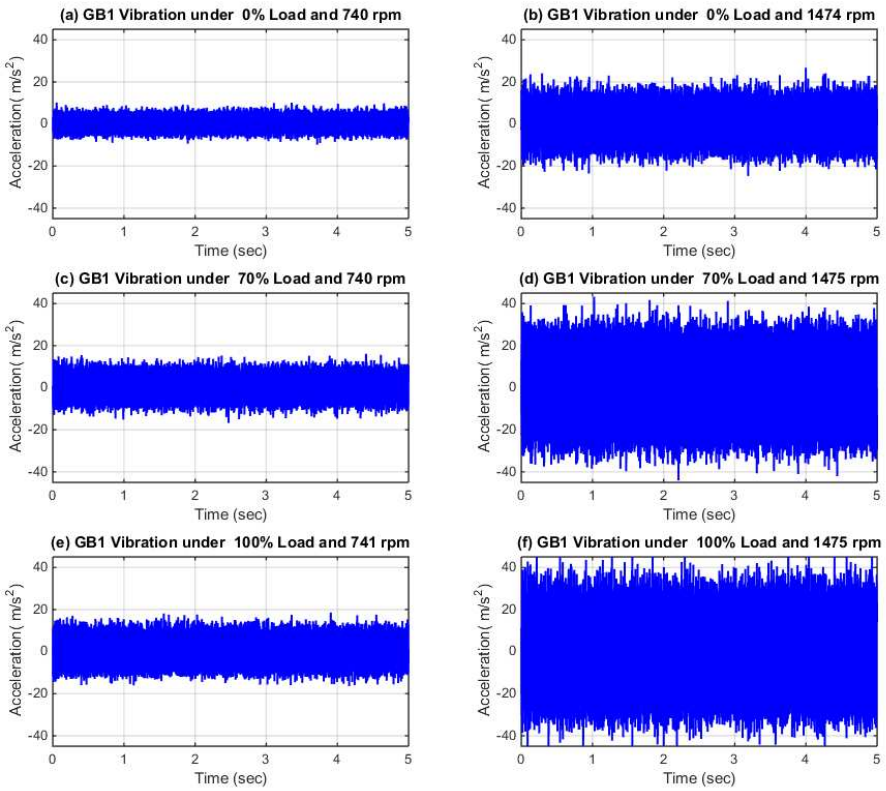

Figure 4.18 GB1 vibration (in time domain)

As shown in Figure 4.19, the vibration spectra (frequency domain) of the signals in Figure 4.18 at 100% speed possess more detailed information than that in the time domain. The main gear frequency components can be clearly identified. Some of the important frequencies are shown in the figure. Figure 4.20 shows the vibration spectra for the same raw vibration data shown in Figure 4.18 at the 50% speed. The same frequency components are shown clearly in the figure, indicating the distinct influences of both speed and load on the vibration. The increase in speed increases the vibration at different frequency components. The load also has the same effect.

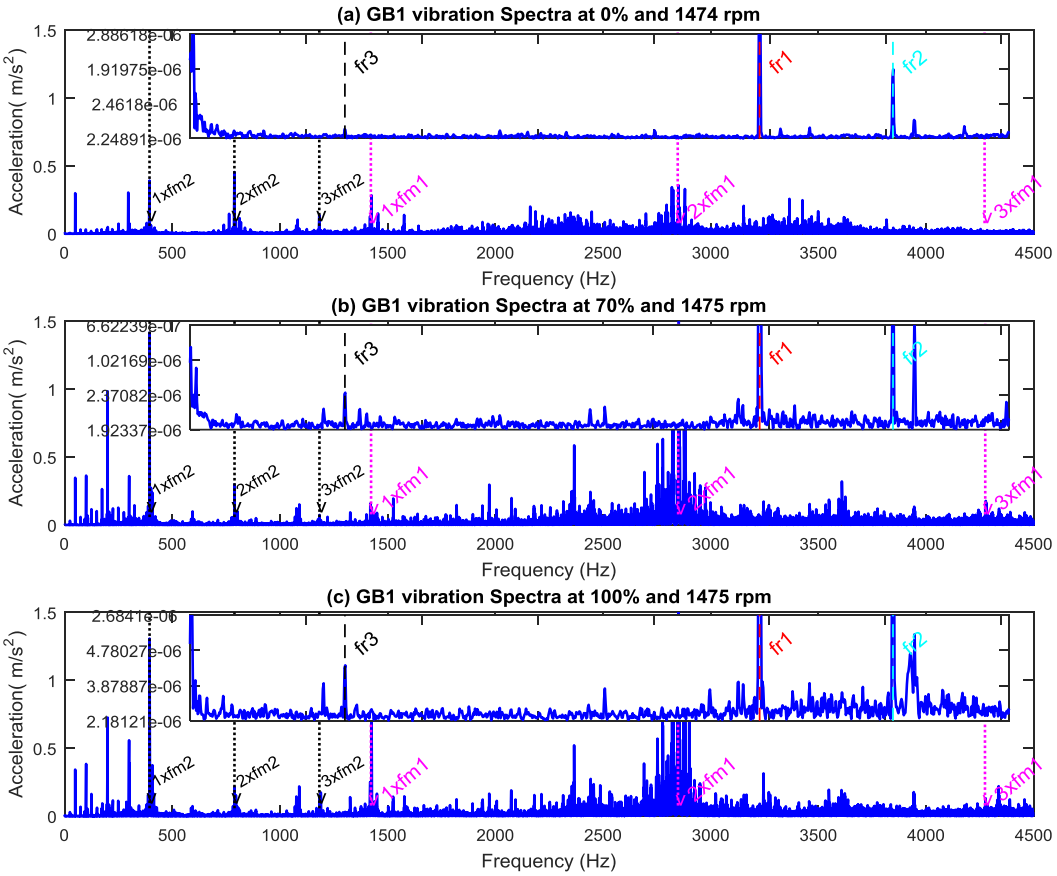

Figure 4.19 Vibration spectra under different loads at 100% speed

As mentioned earlier, any changes in each frequency component would indicate an abnormality in the system. Features are investigated and compared with that of the baseline to detect any changes. In this study, the vibration signals are used for benchmarking and comparison reasons.

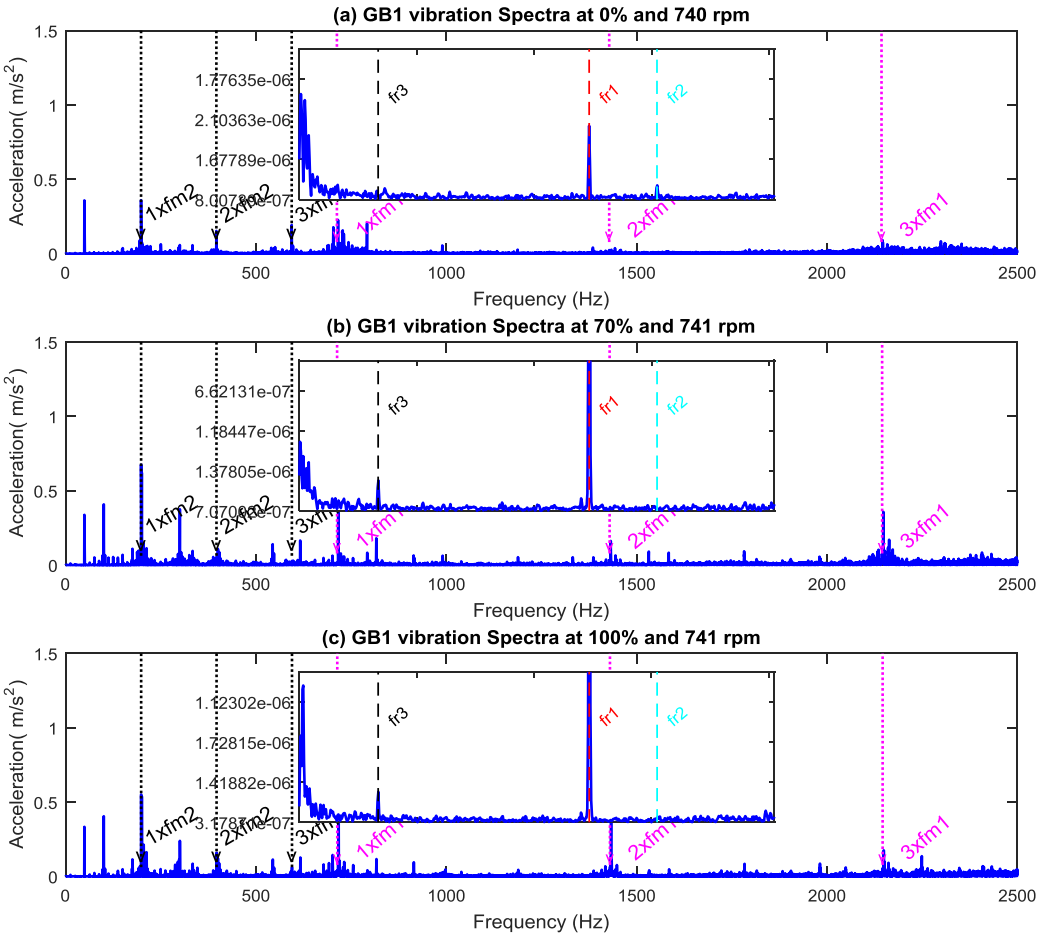

Figure 4.20 Vibration spectra under different loads at 50% speed

4.6.4.3 Time Synchronising Averaging Resampling of Vibration Signals

Time synchronised averaging (TSA) is based on dividing the vibration signal into adjacent segments that are equal in lengths. The length is normally the same as the shaft rotating period. Segments are then averaged to enhance the periodic signals and improve the signal/noise ratio, producing an average signal for one shaft revolution. Next the signal is resampled based on shaft revolutions rather than time, meaning that the corresponding frequency components are associated with shaft orders rather than frequency. Details on the TSA and order resampling analysis are in Appendix I.

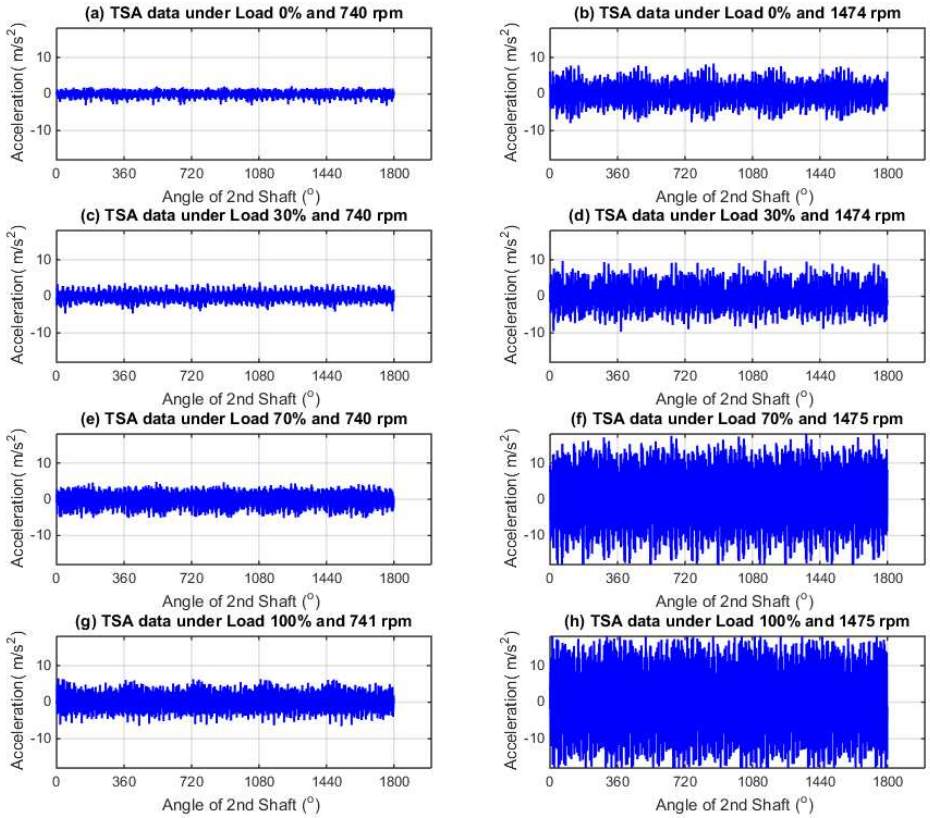

Figure 4.21 Time synchronous averaged (TSA) signals

Figure 4.21 shows the averaged vibration signals from the fifth runs under different operational conditions. Comparing the results in Figure 4.21 with that in Figure 4.18 would indicate the level of noise removed by the averaging process. Figures 4.22 and 4.23 show the order resampled spectra based on the second shaft of the GB1 at 100% speed and 50% speed respectively. The two figures show that features are no longer related to the frequency but rather the shaft order.

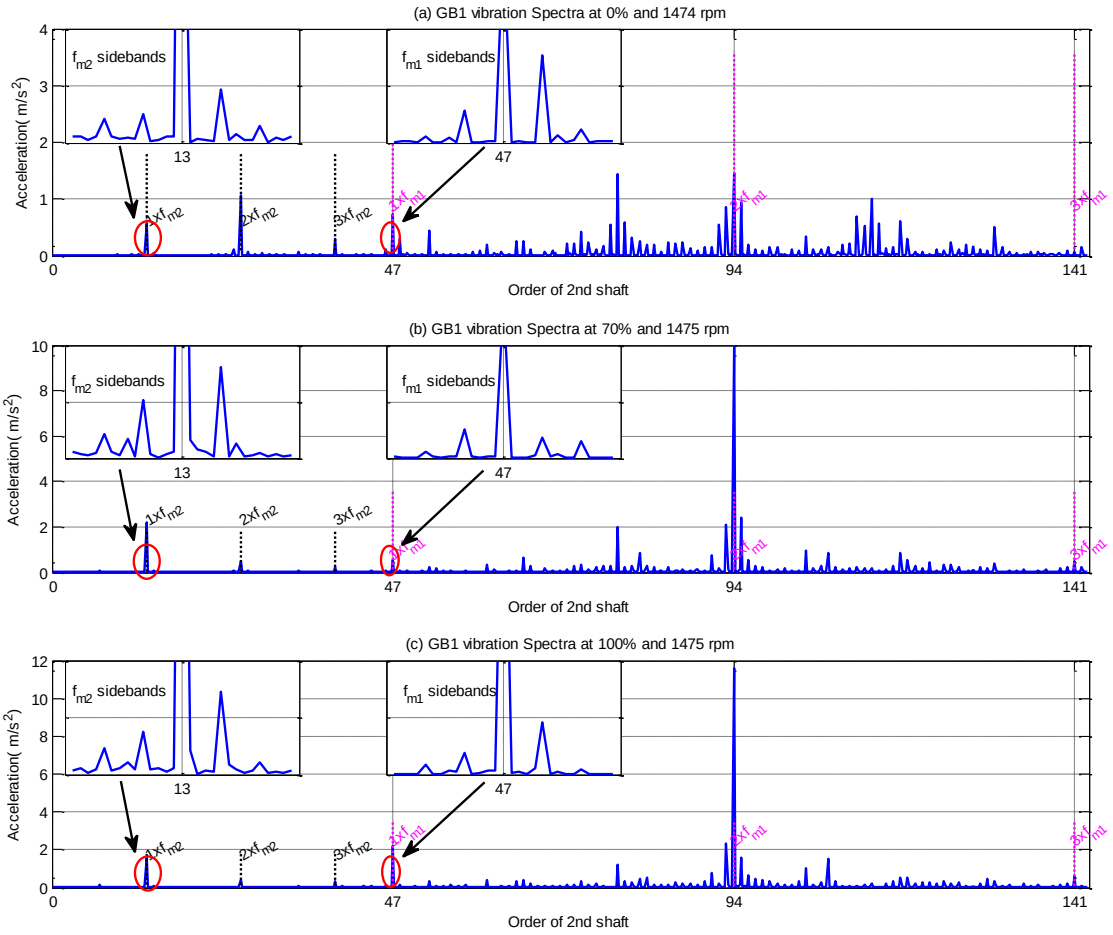

Figure 4.22 Order spectrum based on the 2nd shaft of the GB1 at 100% speed

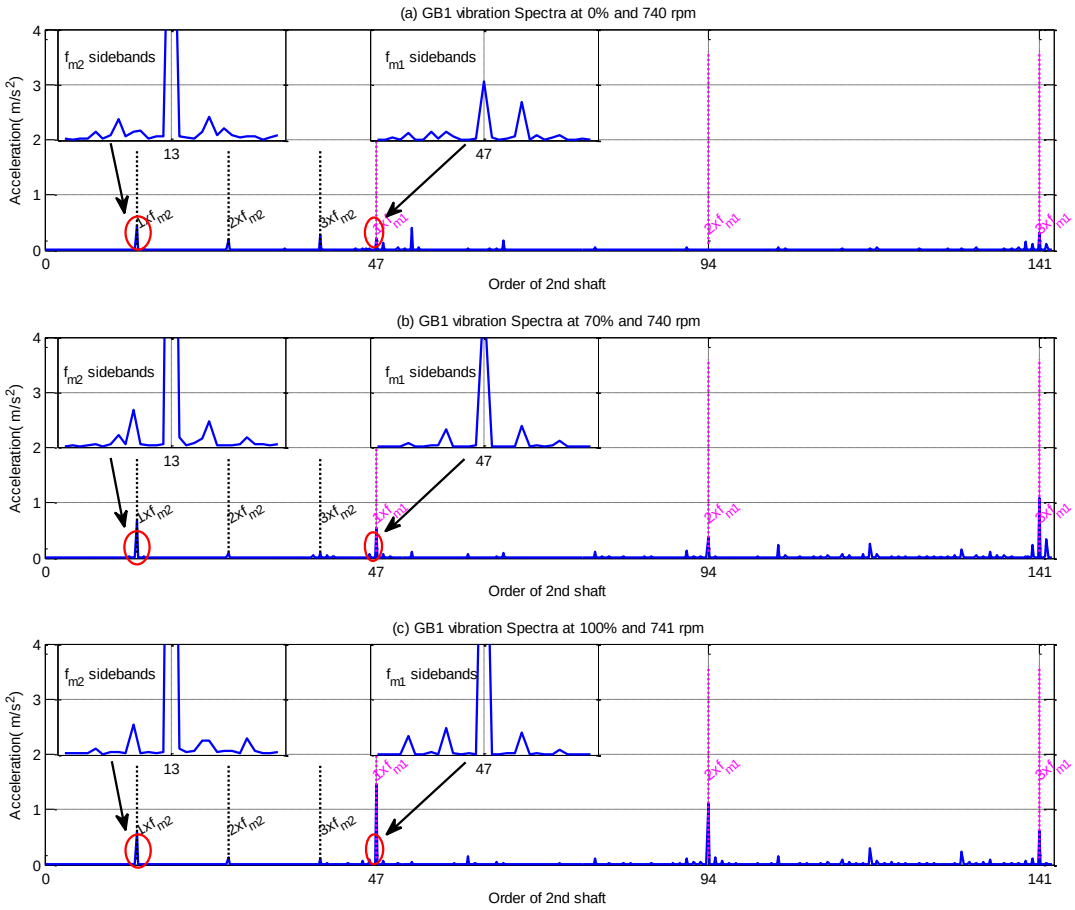

Figure 4.23 Order spectrum based on the 2nd shaft of the GB1at 50% speed

Chapter 5
The Mathematical Model of the IM with Sensorless VSDs and MRAS Observers

This chapter describes the implementation of a field oriented variable speed drive utilising the Simulink/MATlab environment. The applied model is selected from the ready to use modules presented in the Simulink library and modified to suit the test rig induction motor. Firstly the induction motor mathematical model is explained followed by a mathematical description of the principles of the field oriented control. Next the model reference adaptive speed observer is explained. Finally the results obtained from the model are verified with those from the rig and discussed. This study provides an in-depth understanding of the effects of load oscillations on the response of the sensorless VSDs.

5.1 Introduction

Mathematical modelling together with computer simulation can be used to effectively examine, obtain greater insight and enhance understanding of sensorless variable speed drive behaviour. This includes investigation of the system response within different load and speed conditions. The dynamic state of the motor combined with the drive is mathematically represented and implemented using the MATLAB/Simulink environment.

The choice of the Matlab/Simulink environment is based on its ease of use and inclusion of ready to use sets of embedded components that are appropriate for different applications. Moreover a wide range of built-in modules are suitable for the simulation of power and electrical systems such as power electronics converters and machines. Modules are for general use and in many cases can be modified to suit any particular application [7, 47].

In conclusion this chapter aims at describing the mathematical models of the induction motor with the field oriented control (FOC) drive and performing a computer

simulation. The model is used for studying the effects of load oscillations as a result of mechanical faults on the system response, i.e. torque and electrical supply parameters. Results clearly show, in a simple form, the behaviour of the control system in the presence of mechanical faults. This can then be used as a basis for diagnosis and fault detection. The motor parameters used in the test rig are applied for the model hence the model indicates similar features to those of the test rig.

5.2 Mathematical Model of the AC IM and FOC Drive

5.2.1 AC Induction Motor Mathematical Model

Many different models in literature simulate AC three phase induction motors [59]. However, the model implemented in this study is based on the following assumptions [93, 137]: the three stator windings are identical and symmetrically aligned alongside the stator axis; the three rotor windings are symmetrically distributed around the rotor axis; there is a smooth air gap; the different stator and rotor windings generate sinusoidal magneto-motive forces along the air gap; there is infinite iron permeability and constant temperature operation. Figure 5.1 illustrates rotor ($\vec{O}_{ra}$, $\vec{O}_{rb}$, $\vec{O}_{rc}$) and stator ($\vec{O}_{sa}$, $\vec{O}_{sb}$, $\vec{O}_{sc}$) phases distribution and their axis position in the electrical space. The electrical angle (θ) is calculated by multiplying the number of pole pairs by the mechanical speed [93].

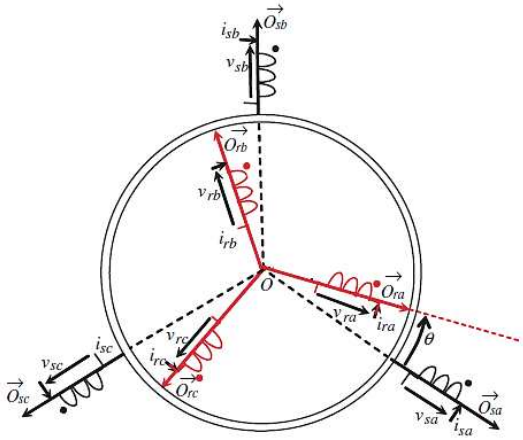

Figure 5.1 Rotor and stator windings in the electrical space [93]

Generally, the mathematical model of the induction motor is derived through the assistance of the electrical equivalent circuit. Figure 5.2 represents the per phase squirrel cage induction motor equivalent circuit [13, 138].

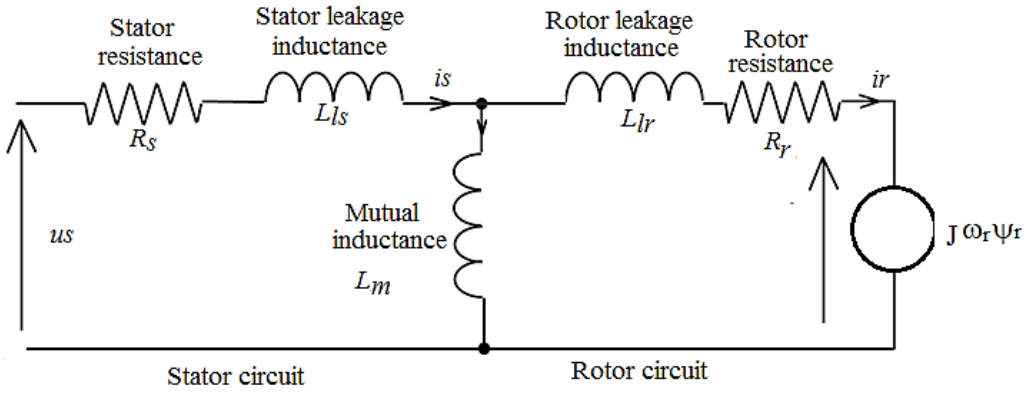

Figure 5.2 The per phase induction motor equivalent circuit

The squirrel cage IM model is obtained by describing the stator and rotor electrical circuits' equations based on stator voltage vectors and stator and rotor current vectors, as follows [137-139]:

$$\frac{d\psi_s}{dt} = u_s - R_s i_s \tag{5.1}$$

$$\frac{d\psi_r}{dt} = -R_r i_r \tag{5.2}$$

$$\psi_s = L_s i_s + L_m i_r = \frac{L_m}{L_r}\psi_r + \sigma L_s i_s \tag{5.3}$$

$$\psi_r = L_r i_r + L_m i_s \tag{5.4}$$

$$L_s = L_{ls} + L_m \tag{5.5}$$

$$L_r = L_{lr} + L_m \tag{5.6}$$

while an equation describing the motor electromagnetic torque (T_e) represents the mechanical model of the IM [139]:

$$T_e = J\frac{d\omega_r}{dt} + B_m\omega_r + T_l \tag{5.7}$$

The model above is complex and challenging to employ for applications such as FOC drives, where each electrical variable, i.e. current, voltage and flux, is in a vector form and represents the three phase values (matrix) [78].

The IM model can be simplified by performing the Clark and Park vector transforms. The sinusoidal three phase system is firstly transferred into an equivalent two orthogonal stationary reference frame using the Clark transform as follows [59, 94]:

$$\begin{bmatrix} X_\alpha \\ X_\beta \\ X_0 \end{bmatrix} = \begin{bmatrix} \frac{\sqrt{2}}{\sqrt{3}} & \frac{-1}{\sqrt{6}} & \frac{-1}{\sqrt{6}} \\ 0 & \frac{1}{\sqrt{2}} & \frac{-1}{\sqrt{2}} \\ \frac{1}{\sqrt{3}} & \frac{1}{\sqrt{3}} & \frac{1}{\sqrt{3}} \end{bmatrix} \begin{bmatrix} x_a \\ x_b \\ x_c \end{bmatrix} \tag{5.8}$$

The reverse Clark transformation is given by the following formula:

$$\begin{bmatrix} x_a \\ x_b \\ x_c \end{bmatrix} = \begin{bmatrix} 1 & 0 & \frac{1}{\sqrt{2}} \\ \frac{-1}{2} & \frac{\sqrt{3}}{2} & \frac{1}{\sqrt{2}} \\ \frac{-1}{2} & \frac{-\sqrt{3}}{2} & \frac{1}{\sqrt{2}} \end{bmatrix} \begin{bmatrix} X_\alpha \\ X_\beta \\ X_0 \end{bmatrix} \tag{5.9}$$

Note that the variable $X_0 = \frac{1}{\sqrt{3}}(x_a + x_b + x_c) = 0$, for the balanced sinusoidal systems.

Next, the stationary reference frame is converted into a rotating reference frame that rotates through a certain angle using the Park transform (d-q) [140] as shown in the following expression [93]:

$$\begin{bmatrix} x_d \\ x_q \end{bmatrix} = \begin{bmatrix} \cos(\theta) & sin(\theta) \\ -sin(\theta) & \cos(\theta) \end{bmatrix} \begin{bmatrix} x_\alpha \\ x_\beta \end{bmatrix} \tag{5.10}$$

The system is returned back into the two phase stationary system using the inverse Park transformation as follows:

$$\begin{bmatrix} x_\alpha \\ x_\beta \end{bmatrix} = \begin{bmatrix} \cos(\theta) & -sin(\theta) \\ sin(\theta) & \cos(\theta) \end{bmatrix} \begin{bmatrix} x_d \\ x_q \end{bmatrix} \tag{5.11}$$

The three reference frames are shown in Figure 5.3 [93].

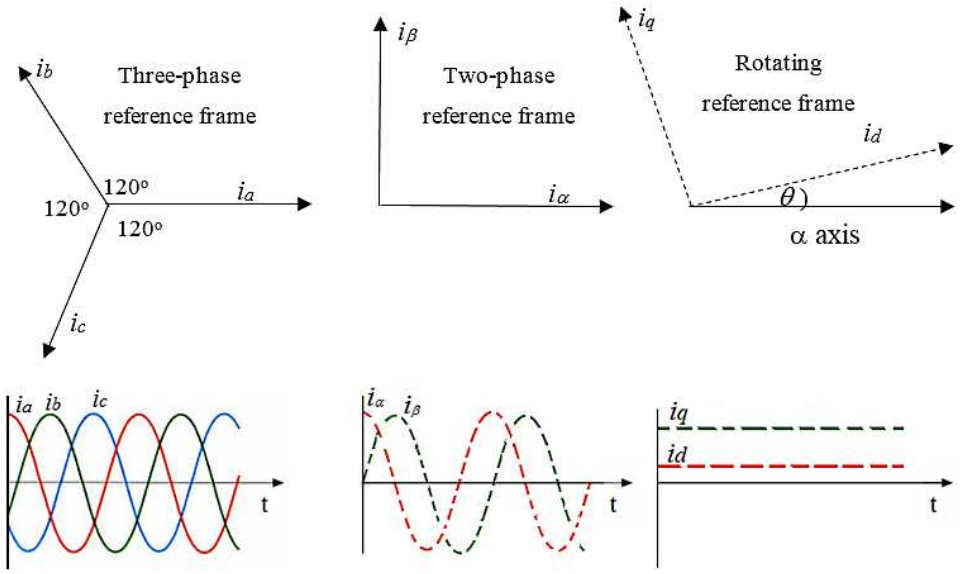

Figure 5.3 The three reference frames

Hence the stationary reference frame components are projected to a frame of reference that rotates within a certain rotating angle (θ). The selection of the frame of reference will define the angle (θ). For instance, in the synchronised reference frame the $\theta = \theta_s$, where θ_s is the electrical angle of the stator flux; while the rotor reference frame implies that $\theta = \theta_r$, where θ_r is the electrical angle of the rotor flux; and the stationary reference frame is obtained by making $\theta = 0$ [94].

The squirrel cage IM model can be then derived from the d-q motor equivalent circuit shown in Figure 5.4, by stating the voltage equations of both stator and rotor [7, 141-143]:

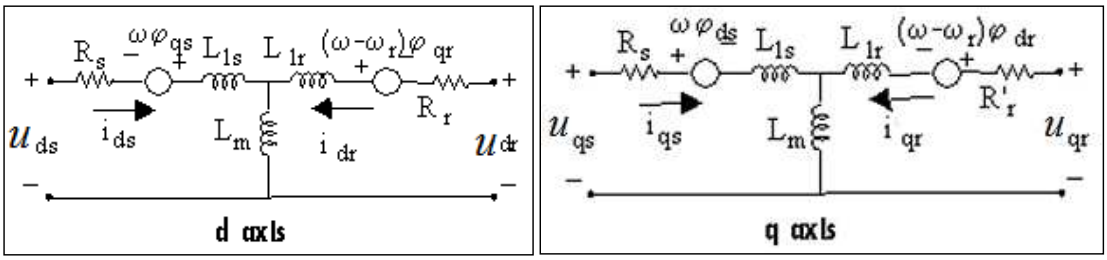

Figure 5.4 The d-q IM equivalent circuit [143]

$$u_{qs} = R_s i_{qs} + \frac{d\psi_{qs}}{dt} + \omega\psi_{ds} \tag{5.12}$$

$$u_{ds} = R_s i_{ds} + \frac{d\psi_{ds}}{dt} - \omega\psi_{qs} \tag{5.13}$$

$$0 = R_r i_{qr} + \frac{d\psi_{qr}}{dt} + (\omega - \omega_r)\psi_{dr} \tag{5.14}$$

$$0 = R_r i_{dr} + \frac{d\psi_{dr}}{dt} - (\omega - \omega_r)\psi_{qr} \tag{5.15}$$

where stator and rotor fluxes are obtained from:

$$\psi_{qs} = L_{ls} i_{qs} + L_m i_{qr} \tag{5.16}$$

$$\psi_{ds} = L_{ls} i_{ds} + L_m i_{dr} \tag{5.17}$$

$$\psi_{qr} = L_{lr} i_{qr} + L_m i_{qs} \tag{5.18}$$

$$\psi_{dr} = L_{lr} i_{dr} + L_m i_{ds} \tag{5.19}$$

Stator and rotor currents are derived from:

$$i_{qs} = \frac{1}{x_{ls}}(\psi_{qs} - \psi_{qm}) \tag{5.20}$$

$$i_{ds} = \frac{1}{x_{ls}}(\psi_{ds} - \psi_{dm}) \tag{5.21}$$

$$i_{qr} = \frac{1}{x_{lr}}(\psi_{qr} - \psi_{qm}) \tag{5.22}$$

$$i_{dr} = \frac{1}{x_{lr}}(\psi_{dr} - \psi_{dm}) \tag{5.23}$$

while rotor and stator inductances are calculated from:

$$L_s = L_{ls} + L_m \tag{5.24}$$

$$L_r = L_{lr} + L_m \tag{5.25}$$

The state space equations of the IM are then written as:

$$U = Ri + \frac{d\psi}{dt} + W\psi \tag{5.26}$$

$$\psi = Li \tag{5.27}$$

where:

$$U = \begin{bmatrix} u_{qs} \\ u_{ds} \\ u_{qr} \\ u_{dr} \end{bmatrix}, i = \begin{bmatrix} i_{qs} \\ i_{ds} \\ i_{qr} \\ i_{dr} \end{bmatrix}, \psi = \begin{bmatrix} \psi_{\mathrm{qs}} \\ \psi_{\mathrm{ds}} \\ \psi_{\mathrm{qr}} \\ \psi_{\mathrm{dr}} \end{bmatrix}, L = \begin{bmatrix} L_{ls} & 0 & L_m & 0 \\ 0 & L_{ls} & 0 & L_m \\ L_m & 0 & L_{lr} & 0 \\ 0 & L_m & 0 & L_{lr} \end{bmatrix},$$

$$R = \begin{bmatrix} R_s & 0 & 0 & 0 \\ 0 & R_s & 0 & 0 \\ 0 & 0 & R_r & 0 \\ 0 & 0 & 0 & R_r \end{bmatrix}$$

$X_{lm} = 1/\frac{1}{x_{ls}} + \frac{1}{x_{lr}} + \frac{1}{x_m}$, $x_{ls} = 2\pi * f * L_{ls}$; $x_{lr} = 2\pi * f * L_{lr}$; $x_m = 2\pi * f * L_m$ and

$$W = \begin{bmatrix} 0 & \omega & 0 & 0 \\ -\omega & 0 & 0 & 0 \\ 0 & 0 & 0 & \omega - \omega_r \\ 0 & 0 & -(\omega - \omega_r) & 0 \end{bmatrix}$$

The mechanical model is given as follows [7, 141, 142]:

$$T_e = \frac{3}{2} N_p \left(\psi_{ds} i_{qs} - \psi_{qs} i_{ds}\right) \tag{5.28}$$

while the motor speed is determined from the machine torque, load torque, and moment of inertia as follows [7, 141, 142]:

$$\frac{d\omega_{\mathrm{m}}}{dt} = \frac{1}{J}(T_e - B_m \omega_{\mathrm{m}} - T_l) \tag{5.29}$$

Where: $\psi' =$ d ψ /dt

5.2.2 Field Oriented Control Drive

To apply the FOC scheme the field current component i_{ds} is aligned with the rotor field, and the torque current component i_{qs} is perpendicular to the i_{ds}. To achieve this the reference frame is aligned to the rotor flux vector. This is performed by choosing w_e equal to the speed of the rotor flux, and hence information about the position of the rotor flux space vector is required as shown in Figure 5.5 [141].

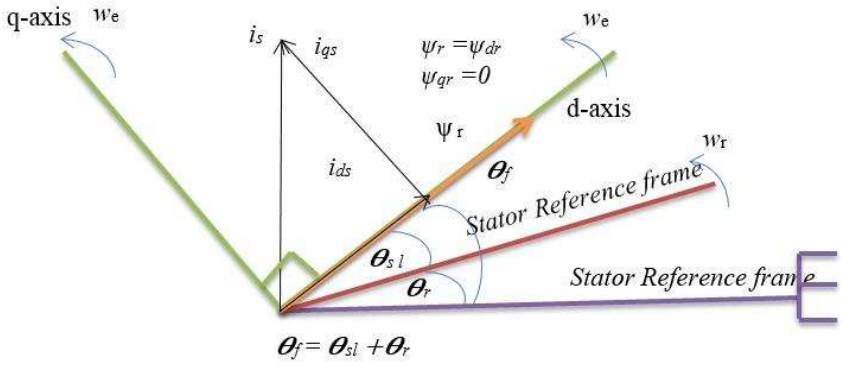

Figure 5.5 Principles of a field oriented control scheme [92].

As discussed earlier in chapter 3, the field oriented control sets the slip value to ensure the rotor flux vector is aligned with the synchronised reference coordinator. The simplified scheme of a field oriented control is shown in Figure 5.6 [102].

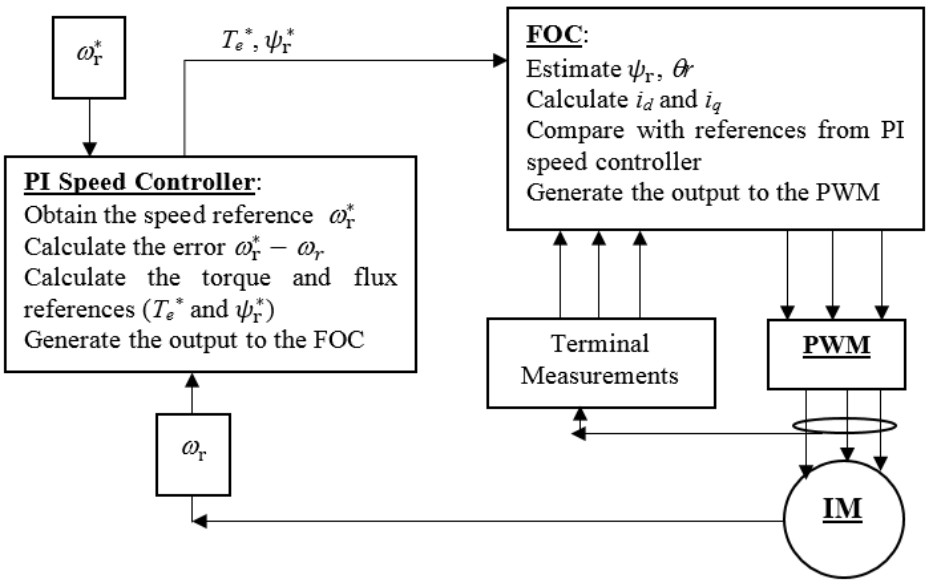

Figure 5.6 The simplified scheme of a field oriented control

Therefore, the rotor flux is aligned with the d axis, as shown in Figure 5.6, so that $\psi_r = \psi_{rd}$ and $\psi_{rq} = 0$; and hence from Equations 5.14-5.15 and Equations 5.18- 5.19 the rotor flux is estimated using the following equation [101, 102]:

$$\psi_r = \frac{L_m}{1+T_r s}(i_{ds}) \tag{5.30}$$

The i_{ds}^* is determined from the reference rotor flux as follows [101, 102]:

$$i_{ds}^{*} = \frac{\psi_r^{*}}{L_m} \tag{5.31}$$

while the slip frequency is determined using the i_{qs}^{*} as follows [101, 102]:

$$\omega_{sl} = \frac{L_m}{T_r \psi_r} i_{qs}^{*} \tag{5.32}$$

Next the electrical flux angle is determined in the following way [101, 102]:

$$\theta = \int (\omega_{sl} + \omega_m)\, dt \tag{5.33}$$

The i_{qs}^{*} is derived based on the torque reference as indicated [101, 102]:

$$i_{qs}^{*} = \frac{2}{3}\,\frac{1}{p}\,\frac{L_r}{L_m}\frac{T_e^{*}}{\psi_r} \tag{5.34}$$

The current reference values of the stator current components are then converted into three phase current references, i_a^{*}, i_b^{*}, i_c^{*}, in order to compare them with the measured values in the current regulators. The current regulators then produce the reference voltage for the inverter gating signals [102].

Equations 5.30-5.34 show that the electromagnetic torque can be separately adjusted while maintaining the flux constant. Also, the electromagnetic torque is proportional to the i_{qs}, and the flux is correlated to the field current component i_{ds} by a linear first order function with the rotor time constant T_r.

5.2.3 MRAS Speed Estimation

The FOC needs two important pieces of data from the machine. The first is the terminal currents which are measured by the drive using in-built sensors. The second is the mechanical speed which may be measured using a speed encoder or estimated using the induction motor equations. The VSD used in the rig is based on an MRAS scheme to estimate the motor mechanical speed.

MRAS is generally implemented by representing one variable in two different sets of equations. The first is independent of the estimated variable and used as a reference. While the other uses the estimated variable as an adjusting parameter. An adaptation mechanism is used to adjust the estimated variable based on the the difference between the two models. The estimated variable is continually adjusted to ensure the difference

between the two models goes to zero. The general structure of MRAS is represented in Figure 5.7 [97].

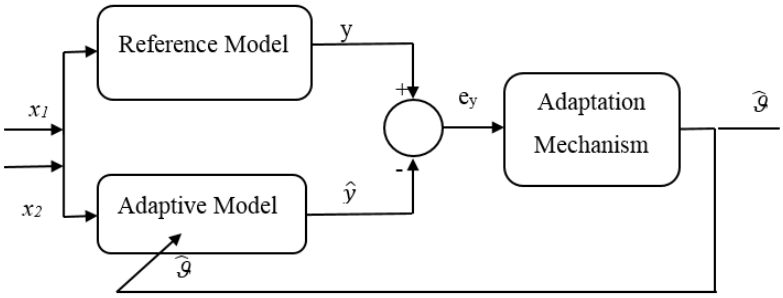

Figure 5.7 The general structure of MRAS

For induction motor speed estimation, different schemes have been suggested based on the MRAS estimator [97, 144-146]. In this case the rotor flux is described by the IM voltage and current equations to build the reference and the adjustable models respectively, in the stationary reference frame. This scheme was selected as it is the scheme used by the rig drive. The voltage and current measurements are firstly converted into the stationary reference frames as follows:

$$i_\alpha^s = i_a \tag{5.35 }$$

$$i_\beta^s = \left(1/\sqrt{3}\right)(i_a + 2\, i_b) \tag{5.36}$$

$$u_\alpha^s = \left(1/3\right)(u_a + u_c) \tag{5.35}$$

$$u_\beta^s = \left(1/\sqrt{3}\right) u_b \tag{5.36}$$

The reference model is represented in Figure 5.8 , given as follows [97, 98]:

$$\frac{d\psi_{\alpha r}^u}{dt} = \frac{L_\mathrm{r}}{L_\mathrm{m}}\left(u_{\alpha s} - R_s i_{\alpha s} - \sigma L_s \frac{di_{\alpha s}}{dt}\right) \tag{5.37}$$

$$\frac{d\psi_{\beta r}^u}{dt} = \frac{L_\mathrm{r}}{L_m}\left(u_{\beta s} - R_s i_{\beta s} - \sigma L_s \frac{di_{\beta s}}{dt}\right) \tag{5.38}$$

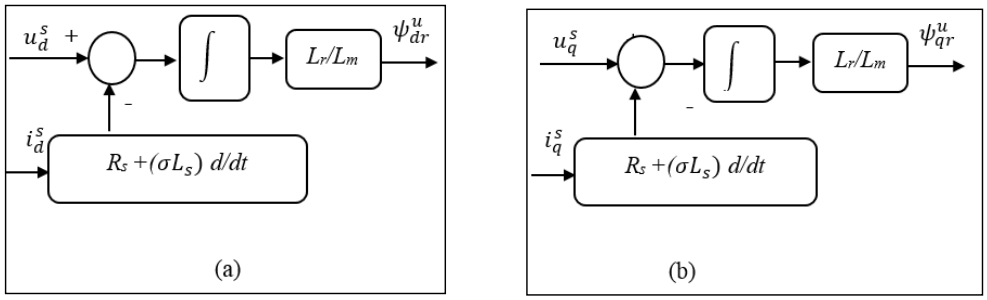

Figure 5.8 Reference Models, (a) d flux component, (b) q flux component

while the adjustable (adaptive) model is represented as shown in Figure 5.9 [97, 98]:

$$\frac{d\psi_{\alpha r}^i}{dt} = \frac{1}{T_r}\left(L_m i_{\alpha s} - \psi_{\alpha r}^i - \hat{\omega}_r \psi_{\beta r}^i\right) \tag{5.39}$$

$$\frac{d\psi_{\beta r}^i}{dt} = \frac{1}{T_r}\left(L_m i_{\beta s} - \psi_{\beta r}^i + T_r \hat{\omega}_r \psi_{\alpha r}^i\right) \tag{5.40}$$

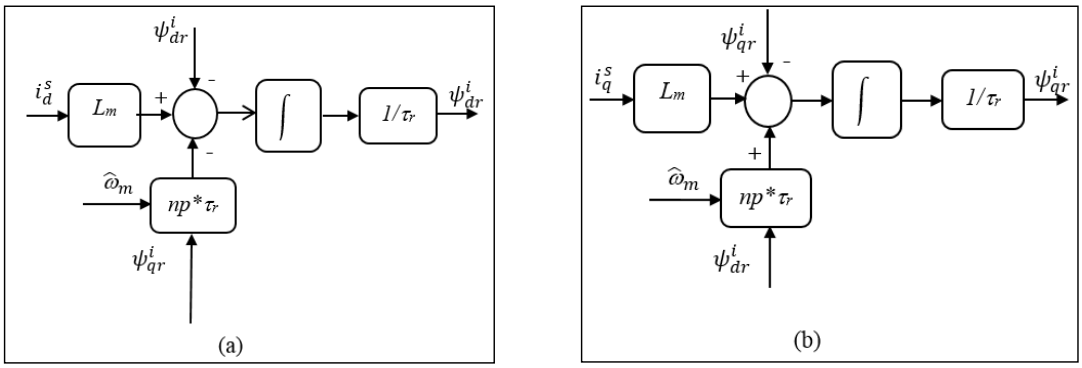

Figure 5.9 Adaptive Models, (a) d flux component, (b) q flux component

Many adaptation mechanisms have been developed in the literature [97, 98, 145, 147], however they are generally based on the PI controller which is depicted in Figure 5.10 and described as follows [97]:

$$\hat{\omega}_r = K_p\left(\psi_{\beta r}^u \psi_{\alpha r}^i - \psi_{\alpha r}^u \psi_{\beta r}^i\right) + K_i \int \left(\psi_{\beta r}^u \psi_{\alpha r}^i - \psi_{\alpha r}^u \psi_{\beta r}^i\right) dt \tag{5.41}$$

where the superscripts i, u refer to current and voltage models respectively, the superscript ^ refers to the estimated value

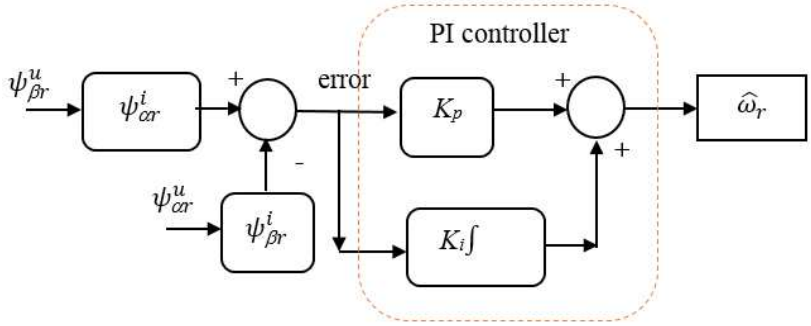

Figure 5.10 The MRAS adaptation scheme.

The stability of MRAS models has been widely examined and discussed. One of the most important issues with MRAS is the PI controller gains. The PI controller gains must be prudently chosen to ensure the system remains stable for a wider speed range. This is normally performed by PI tuning. Different schemes have been examined and suggested for the tuning process, including Nicolas-Ziegler and auto tune variation methods. K_p, K_i coefficients can also be tuned using trial and error methods, where values are chosen based on the response of the system. The values are adjusted and the response is observed continually until a satisfactory response is obtained [97, 98, 145, 147].

5.2.4 The PI Speed Controller

The speed controller compares the reference and the feedback speeds and generates the error signal. The error signal is then processed by a PI controller so that the output sets the torque reference value to the field oriented control. There is also another part of the speed controller that sets the reference value for the flux. The flux reference is defined based on the reference speed and the rated motor speed. If the reference is less than the rated speed, the reference flux is set to the rated value while in other cases the reference flux is reduced by the inverse of the rotor speed ($1/\omega_r$) [148].

5.2.5 The Three Phase PWM

The inverter selected is the universal bridge block that implements a three-phase power converter based on six power switches connected in a bridge configuration. The power electronic devices selected are the IGBT/Diode which are utilised by the rig VSD.

5.3 Simulation Results and Validation

The parameters of the induction motor used for the rig have been taken from the variable speed drive. Certain parameters were derived from the motor's nameplate while others were estimated during the auto-tune process performed by the drive. The induction motor specifications listed in Table 1 are used. The motor nominal inertia together with total load inertia (obtained from equipment datasheets) is 0.36kg.m^2. The model commenced with 0% load at 100% speed for 0.5 seconds, line currents are represented in Figure 5.11.

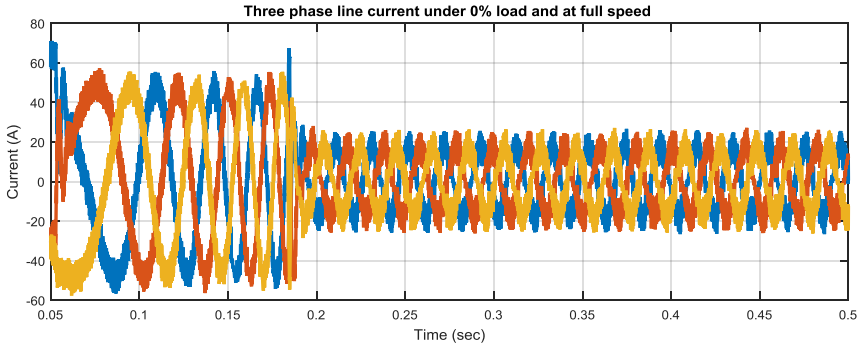

Figure 5.11 Three phase currents from the model

The response of the system to the speed reference change is examined by varying the speed reference and observing the response of speed feedback. Figure 5.12 depicts the response of the model to speed reference changes. The speed reference is set to 25, 50, 75 and 100% of rated speed under 0% and 100% loads.

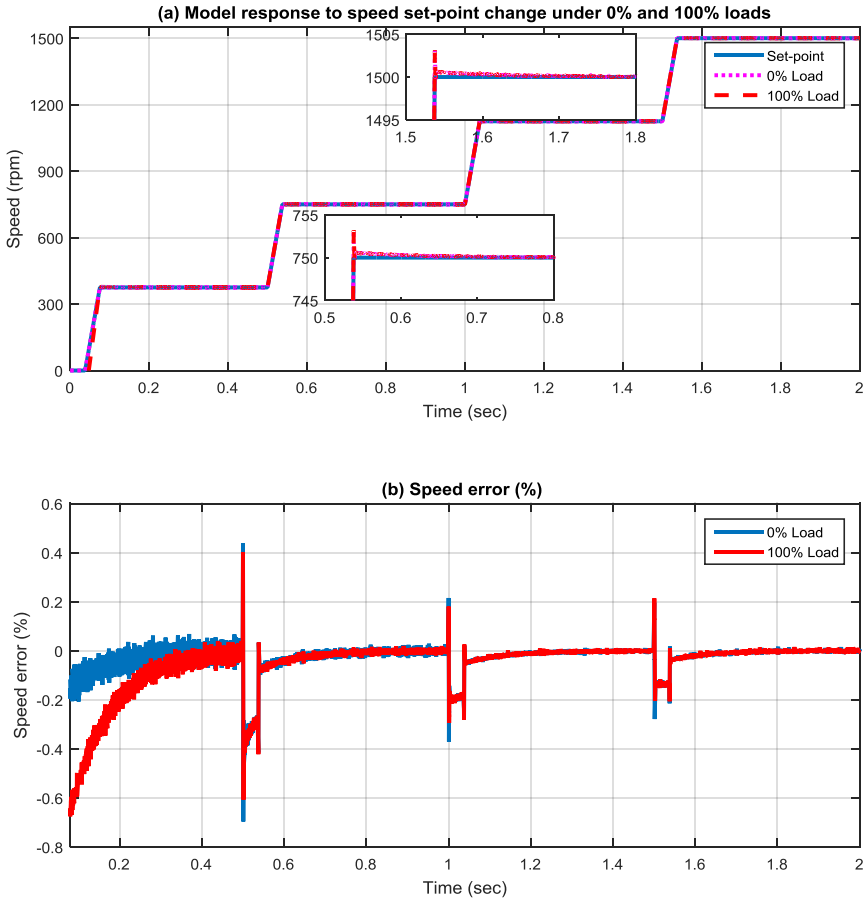

Figure 5.12 Model response to speed set-point change under 0% load

Figure 5.12 (a) shows that the drive has maintained the motor speed around the reference within an acceptable error. Additionally the transient response, describing the transition between speed set into another, shows acceptable behaviours. The error in percentage to the reference point is kept minimal at less than ±0.6% even at transient response as shown in Figure 5.12 (b). Further this figure shows that the speed response improves as speed increases. This is due to the integration involved in the estimation processes and control scheme. The integration gain increases as the frequency decreases which results in drifts in the estimated variables at low speed. Additionally, the PI controllers bandwidth limits contribute to the drifts. The PI controller's parameters are fixed and hence the bandwidth of each control loop is limited to these parameters. Speed control performance degrades when working around the PI loops bandwidth limits.

The response of the model to variable load has also been investigated. The speed reference is set at the full speed. While the load reference is varied taking the values of 0, 26.85, 46.85 and 70 N.m, for 0.5 seconds per load set. As shown in Figure 5.13 (a), the drive has successfully maintained the motor speed at the reference within an acceptable error. The behaviours at the transitions also show good response, i.e. the overshoot is less than 0.1% of the full speed under the highest load case.

Additionally, as indicated in Figure 5.13 (b) the electromagnetic torque shows a good level of response to load changes. The reference torque changes as the load alters. Further the motor electromagnetic torque follows the reference torque set by the FOC.

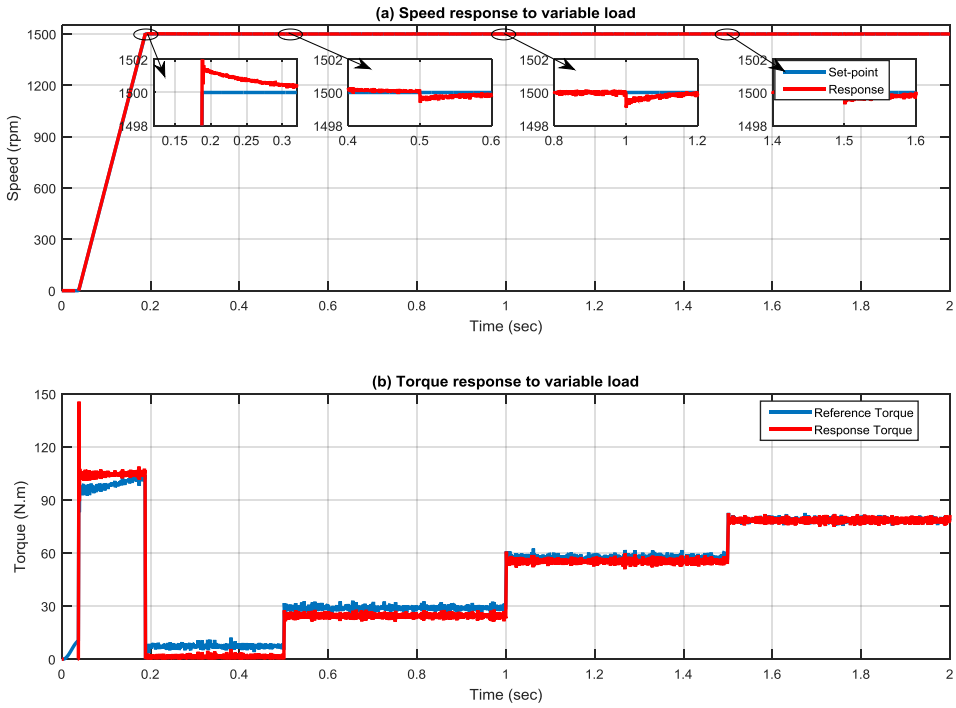

Figure 5.13 Speed response under variable load conditions

Figures 5.12 and 5.13 show that the model reveals effective responses to both speed and load changes. Motor speed and the electromagnetic torque exhibited acceptable responses to changes in load demands and with satisfactory transient and steady state behaviours.

The reference and measured speeds from both the model and rig have been investigated to verify how far the results from the model correspond with the results from the rig's

VSD and motor. Figure 5.14(a) shows the speed reference and speed response from the rig's drive under variable load conditions, i.e. 0%, 30%, 70% and 100% of the rig full load, while Figure 5.14(b) presents the reference and feedback electromagnetic torque signals.

Both speed and electromagnetic responses show effective regulation from the drive's control system. Figure 5.14(a) indicates that speed was maintained at the required reference even when different loads were applied. The electromagnetic torque shown in Figure 5.14(b) was also maintained appropriately within the reference. However, in contrast to the model responses, transitions from one load to another are not clearly indicated in the rig's responses which can be due to the signals filtering scheme in the drive.

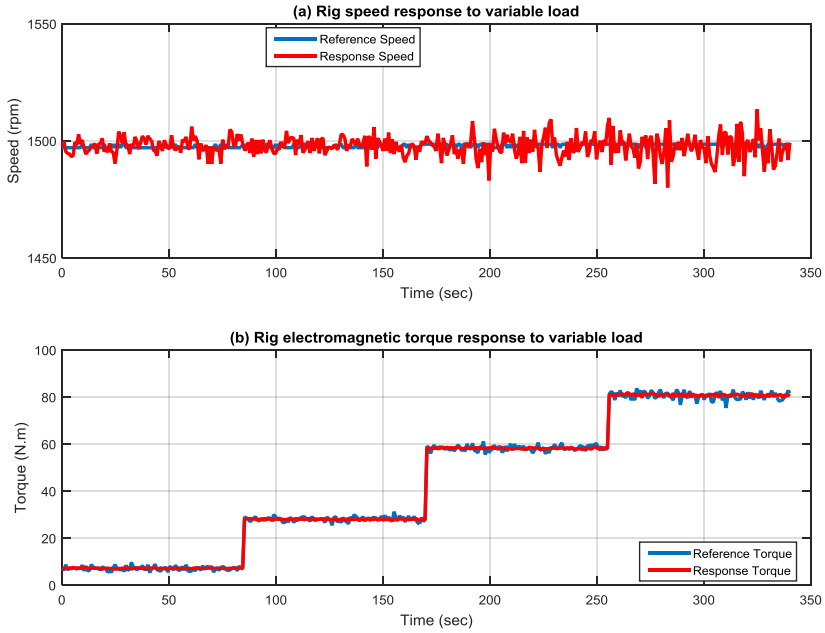

Figure 5.14 Rig speed and electromagnetic torque responses to variable loads

Line current and voltage signals from both model and rig were also compared as shown in Figure 5.15. The comparison has been made at the steady state conditions and full speed under 0% load. Figure 5.15 (a and b) describe the current and voltage signals in the time domain, while Figure 5.15 (c and d) represent them in the frequency domain. Current and voltage signals from the model showed similar changes to those from the rig in both the time domain and frequency domain under 0% load condition. This is

further observable when the load is increased to the full load. Both time domain and frequency domain current and voltage signals are compared as shown in Figure 5.16.

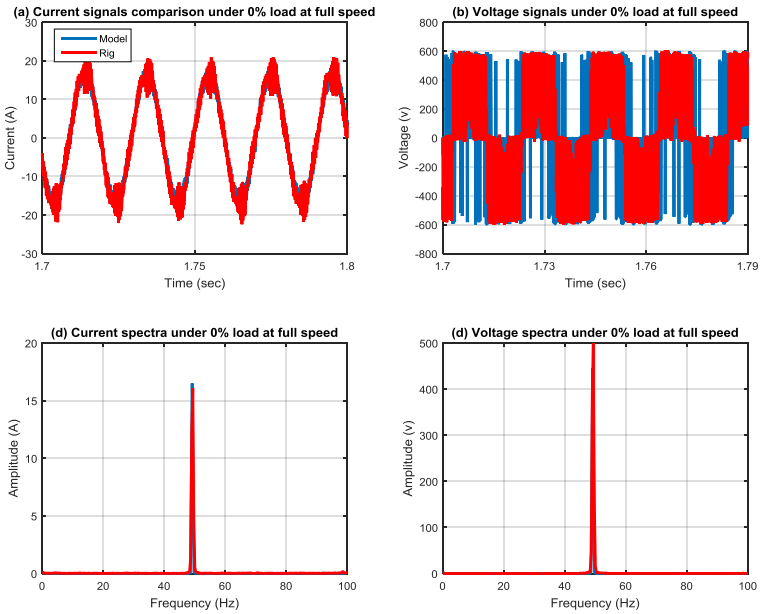

Figure 5.15 Current and voltage signals comparison at full speed under 0% load

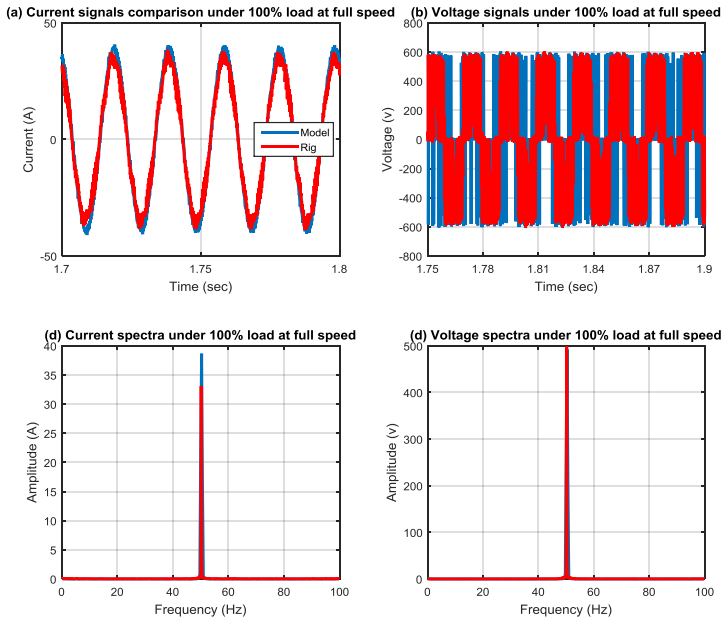

Figure 5.16 Current signals comparison at full speed under 100% load

The electrical power has also been compared. Figure 5.17 represents the comparison between power signals under different load conditions.

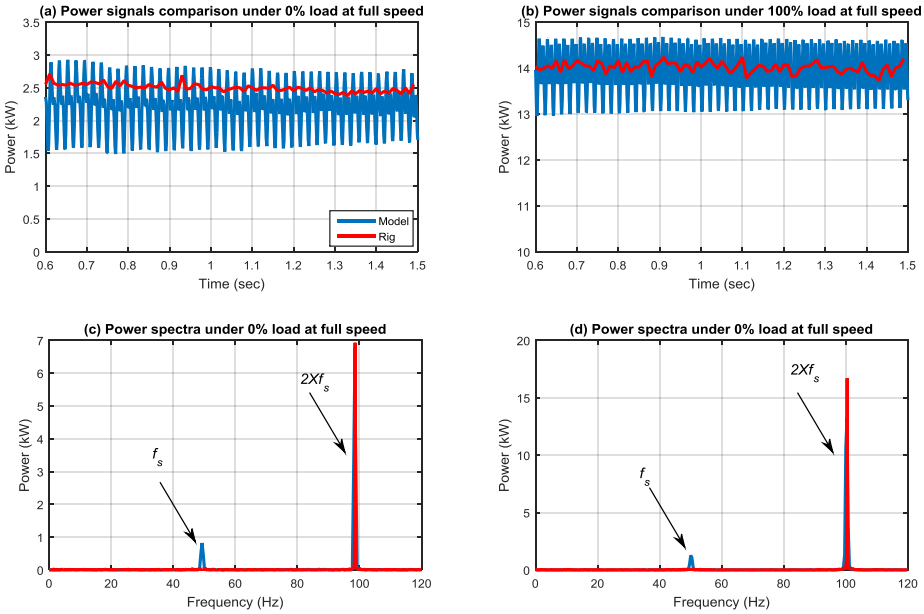

Figure 5.17 Power signals comparison at full speed under 100% load

The motor line current rms and electromagnetic torque values were further evaluated and summarised in Table 13. Results from the simulation show similarity to that from the rig indicating that the model, to some extent, represents the real application and can be used for further analysis in relation to the influence of load and speed oscillations, and ensuing faults, on the system as well as the response of the drive in cases of abnormalities.

Table 13. Rig and model torque and current rms values

	Current (A)		Torque (N.m)	
	0% load	100% load	0% load	100% load
Model	11.7022	26.0428	7.6631	81.4304
Rig	12.2244	24.8712	7.0464	80.7609

To examine the response of the system under load oscillation conditions, oscillatory signals around the system angular speed were added to the load reference. The system angular speed is integrated and passed through a cosine function and multiplied by a gain and then added to the load reference. Hence, the oscillation with an amplitude of ΔT will be modulated by the system speed, while ΔT sets the size of oscillations

representing the fault severity. The oscilation is added to the load torque reference value as follows:

$$T_{osc} = \Delta T cos(\theta) \tag{5.42}$$

$$\theta = \int \omega_r \, dt \tag{5.43}$$

Three different ΔT values have been used aimed at representing three different degrees of severities: 0 denoting baseline (BL), and 0.1 and 0.2 referred to as (0.1 Osc) and (0.2 Osc) respectively.

The model was run at the full speed under 2N.m load representing the minimum load and 70N.m for 4 seconds. Following this the spectra of the current, voltage and power signals were calculated and compared with that of the oscillation-free signals (BL). Further a direct comparison between the averaged torque signals, representing static components, was made to observe the influence on the torque response.

Figure 5.18 depicts the torque demand and torque response signals under the two tested loads. The electromagnetic torque oscillates sinusoidal indicating that the noise has been successfully induced to the model. The torque demand from the drive, presented in Figure 5.18 (a-b), shows that the drive sets the torque to a nearly constant value; however the response oscillates with the load. This is attributable to the fact that the drive is a speed controller where increased emphasis is placed on controlling speed rather than torque.

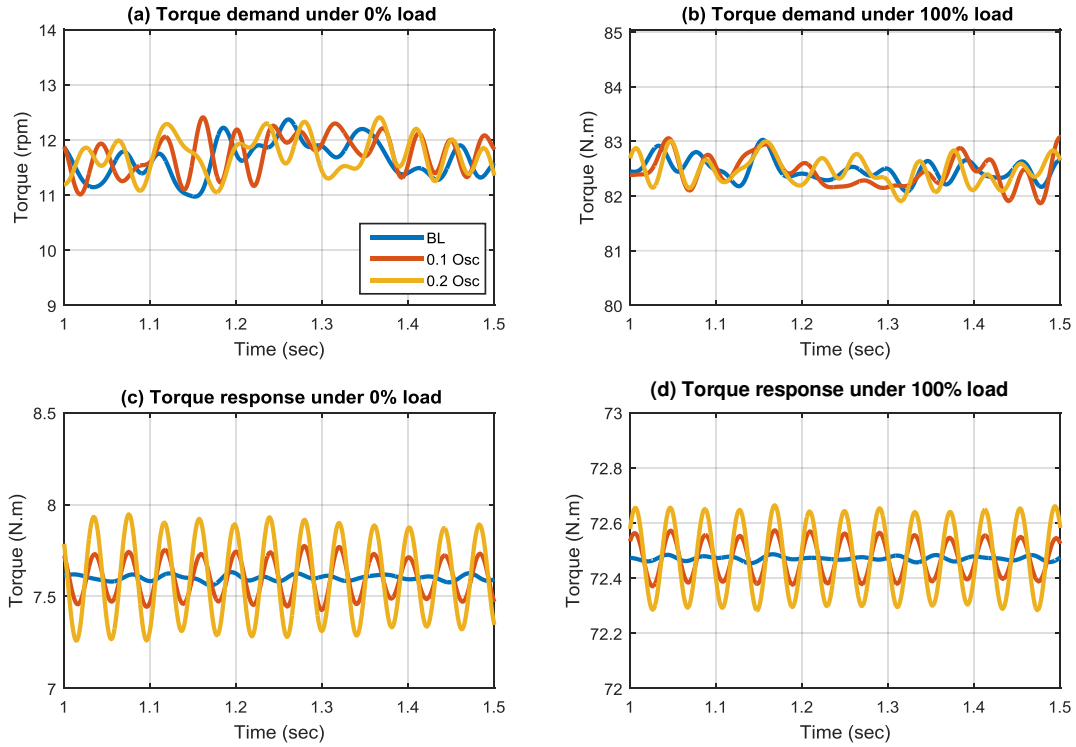

Figure 5.18 Electromagnetic torque demand and response signals under 0% and 100% loads

To observe the influence of the induced load oscillations on the speed response of the model, both speed demand and speed response signals were collected and are represented in Figure 5.19. The drive compensates for the oscillations induced by reflecting the oscillations onto the speed demand signals as can be seen in Figure 5.19(a-b). This is aimed at preventing the load oscillations from affecting the motor speed. The drive has therefore maintained the speed at the reference and minimised the fluctuations in the speed response as shown in Figure 5.19(c-d). That is the motor speed indicates highly similar responses under different oscillatory conditions. The strategy of field oriented control therefore is to maintain motor speed and in the meantime provide sufficient torque signal to the system. Any changes in the mechanical load are compensated by the drive to prevent it from changing the speed.

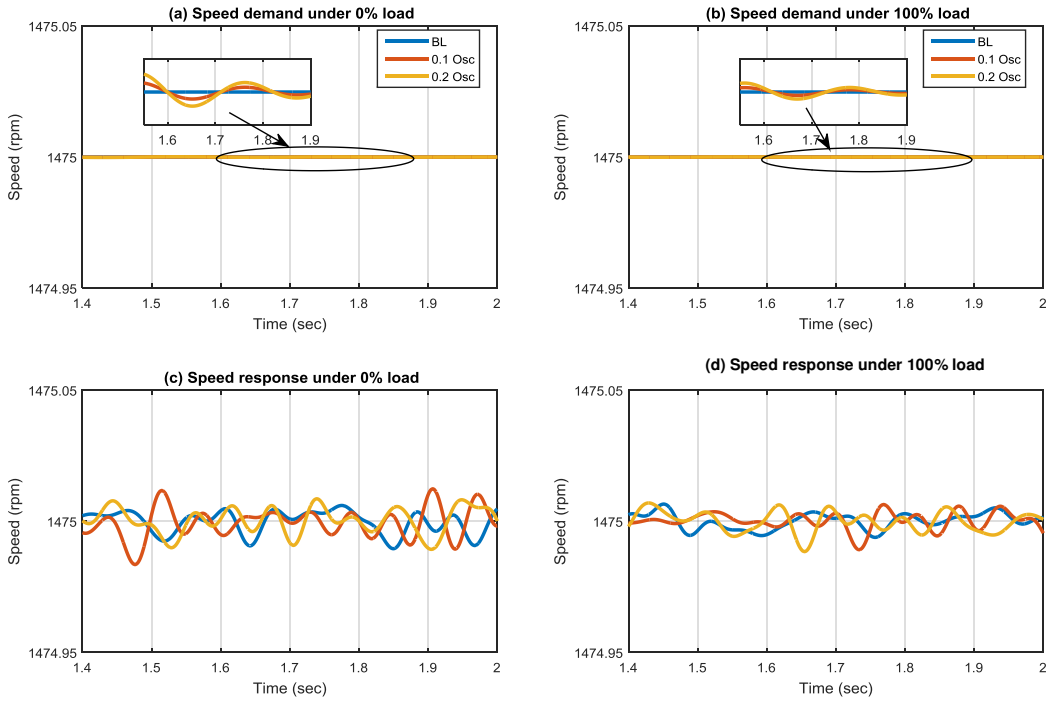

Figure 5.19 Electromagnetic torque demand and response signals under 0% and 100% loads

Figure 5.20 illustrates the current spectra comparison for the three load oscillation cases. It is clear that load oscillations have created frequency components, sidebands, across the fundamental supply frequency. Amplitudes at these sidebands increase as the level of oscillation increases. Further Figure 5.20 shows that the supply frequency has increased with the load. The drive increases the supply frequency to compensate for the load maintaining the speed closer to the reference speed.

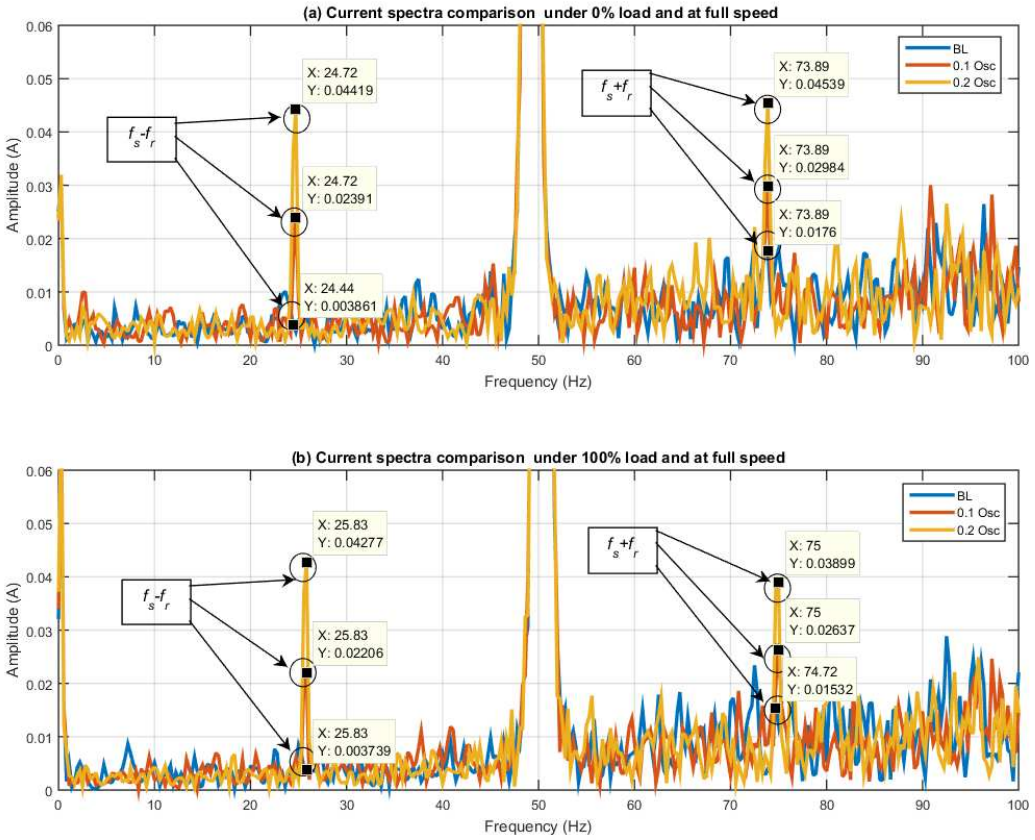

Figure 5.20 Current spectra comparison under different load oscillation levels

A similar observation can be made for the voltage signals where the oscillations have also modulated the voltage signals and created sidebands across the supply frequency as shown in Figure 5.21. Further amplitudes at these sidebands increased with oscillations.

The spectra of electrical power additionally show similar behaviours. Figure 5.22 represents a comparison of the electrical power spectra from the tree different cases.

This confirms the theory discussed earlier proposing that in the event of a mechanical fault such as shaft misalignment or a gearbox lubricating fault, load oscillations will modulate the electrical supply parameters. The drive reacts against such oscillations in order to maintain a smooth system speed response. Analysing the power supply parameters can therefore lead to the detection of faults occurring in downstream mechanical systems.

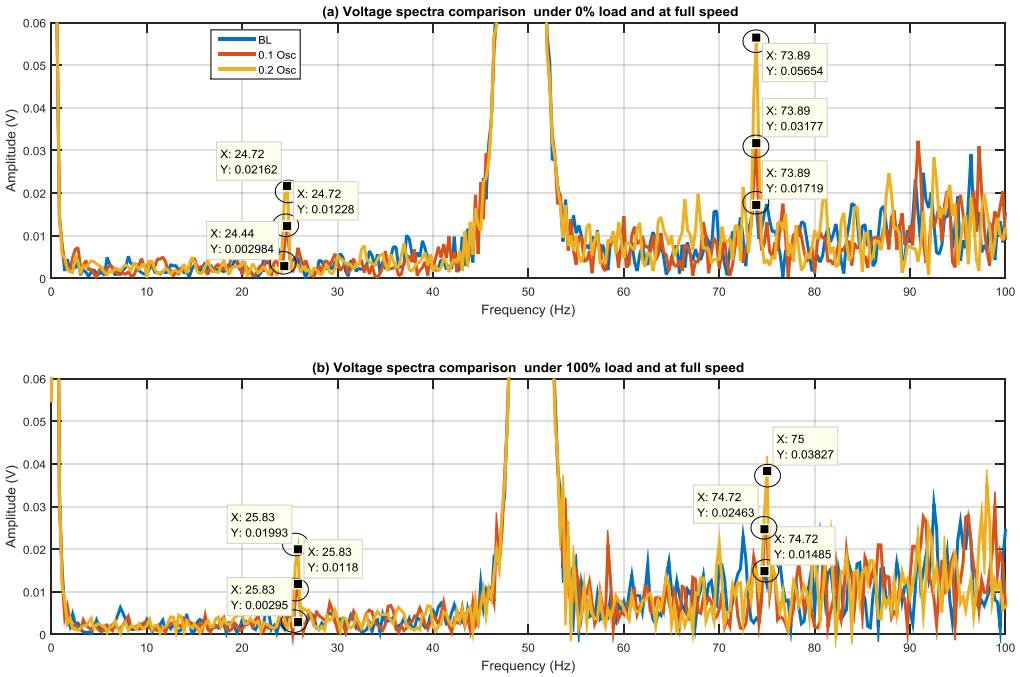

Figure 5.21 Voltage spectra comparison under different load oscillations

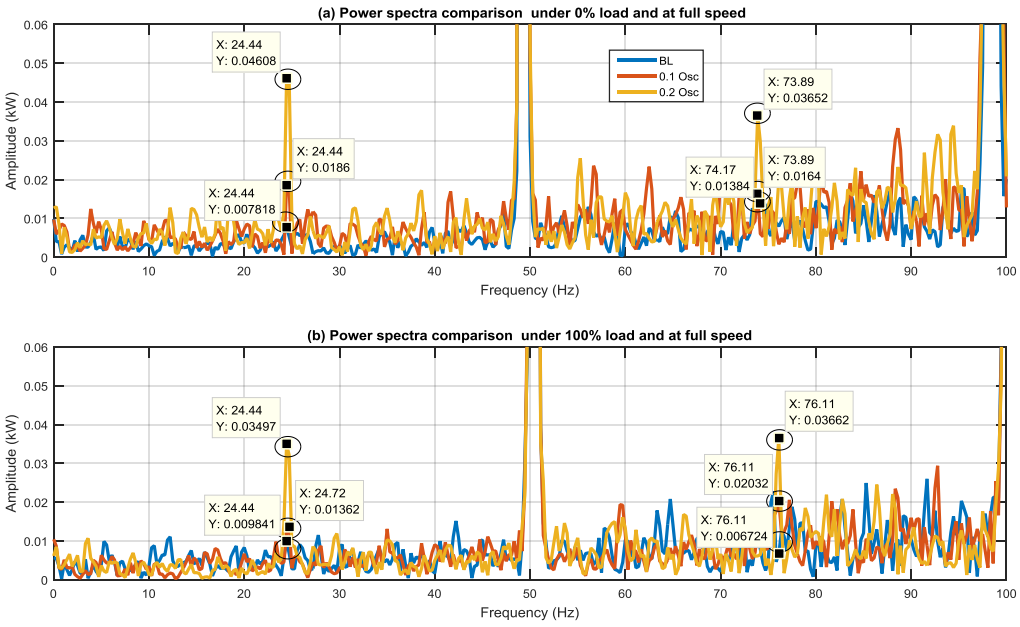

Figure 5.22 Power spectra comparison under different load oscillations

To evaluate the performance of each signal, amplitudes at left, right sidebands and their average have been calculated in percentage to the rated values, as listed in Table 14:

Table 14. Current, voltage and power at sideband amplitudes in percentage							
		Current %		**Voltage %**		**Power %**	
		0% load	**100% load**	**0% load**	**100% load**	**0% load**	**100% load**
Left	BL	0.0142	0.0138	0.0007	0.0007	0.0521	0.0656
	0.1Osc	0.0881	0.0813	0.0030	0.0028	0.1240	0.0908
	0.2Osc	0.1629	0.1576	0.0052	0.0048	0.3072	0.2331
Right	BL	0.0649	0.0565	0.0041	0.0036	0.0923	0.0448
	0.1Osc	0.1100	0.0972	0.0077	0.0059	0.1093	0.1355
	0.2Osc	0.1673	0.1437	0.0136	0.0092	0.2435	0.2441
Average	BL	0.1651	0.0351	0.0024	0.0021	0.0722	0.0552
	0.1Osc	0.0396	0.0893	0.0053	0.0044	0.1167	0.1131
	0.2Osc	0.0991	0.1507	0.0094	0.0070	0.2753	0.2386

The table indicates that electrical supply parameters show consistent changes with load oscillations at the examined sidebands, indicating their utility for fault detection and diagnosis. It can be seen that the left and the right sidebands have been averaged to obtain more accurate and reliable results. Power amplitudes at the investigated sidebands exhibit the highest changes with load oscillations, while contrastingly the voltage signals provided the poorest diagnostic performance. This agrees with the experimental results in that power signals showed superior diagnostic performances than that of current and voltage as discussed later in Chapters 7 and 8.

The mean values from the electromagnetic torque signals are also compared as depicted in Figure 5.23. The effect of the load oscillations is clear in that the average value of the electromagnetic torque increases as the oscillation increases. The drive increases the electromagnetic torque to overcome the effect of the oscillations and prevent them from appearing in the speed signal. The static electromagnetic torque is changed based on the rate of oscillations.

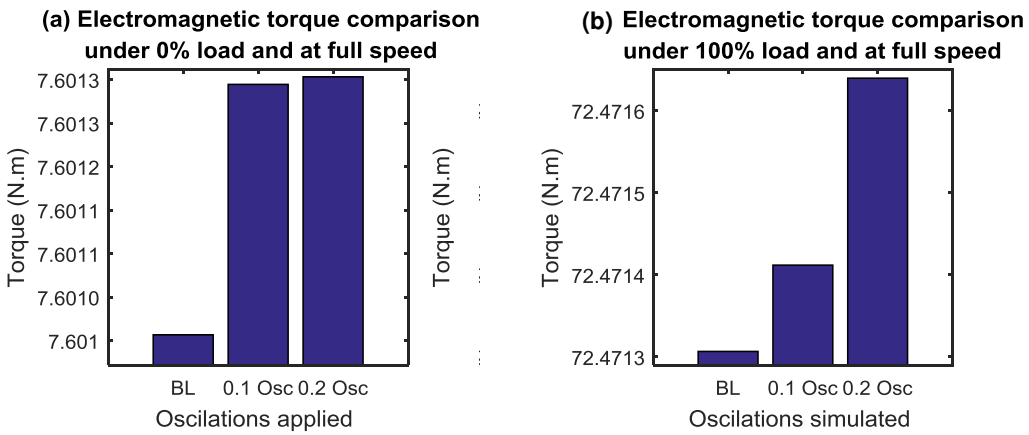

Figure 5.23 Electromagnetic comparison

To conclude, results show that load oscillations generally generated by mechanical faults can be detected when the AC motor is driven with a VSD. The oscillations modulate current, voltage and power signals at a frequency components related to the oscillation frequency. The speed and electromagnetic torque demands are adjusted by the drive to compensate for the load changes and to maintain the system speed stable at the reference. Therefore mechanical faults, which in most cases cause additional oscillations that modulate at the fault frequency, can be monitored and detected in electrical power signals as well as the static components of electromagnetic torque.

This agrees with the experimental results in that shafts, which are rotating in different frequencies, can be found in current, voltage and power spectra. For instance f_{r1}, f_{r2} and f_{r3} of the GB1 can be observed clearly in the current, voltage and power spectra as depicted in Figures 7.9, 7.10 and 7.11. Additionally, when a fault, such as shaft misalignment, occurs amplitude at these frequency components change consistently with the fault, as described in Figure 7.16. Also Figures 7.24 and 7.25 represents the static data changes due to the faults applied. A consistent change with fault severity is remarkable and can be taken as a measure of fault severities. The results from the model, therefore, constitute the diagnostic strategy in this research in that both dynamic and static data can be combined to indicate and locate faults.

Chapter 6
Observer Based Fault Detection

This chapter details the theoretical background underpinning the observer based fault detection method. It further describes the residuals generation process and their use for condition monitoring and fault detection applications. Details of the scheme the observers developed for speed and flux estimation which are used for fault detection are described. Additionally this chapter explains the residuals generation method used based on the measured and estimated powers and finally illustrates the residual evaluation schemes developed for fault detection.

6.1 Introduction

6.1.1 Overview

Model based techniques are widely used for fault detection and diagnosis in automated systems [15]. The monitored process is mathematically modelled to produce quantifiable analytical information that can be used for health measures and the severity of the abnormality detected. Generally, process mathematical models together with parameter observers, state estimation and analytical processing methods are utilised for analysis and diagnosis. Special features, for example physical defined process coefficients or special filtered or transformed residuals, are then isolated as indications for system health. Based on the features extracted, a comparison between the current and healthy cases is conducted for fault detection and severity estimation [149, 150].

A comparison between the estimated variables with the measured signals is continually performed to ensure system health and to diagnose for any developing faults. The mathematical model of the monitored process is utilised for parameter estimation and/or state estimation. Residuals are then generated by computing the differences between the measured quantities and the corresponding values generated by the model [151].

As explained in the previous chapter, sensorless variable speed drives require accurate flux information for speed and torque regulation. Hence, the drive needs to estimate

both flux and speed without any additional sensors. To do so, elements such as resistances, inductances and name plate parameters are incorporated together with the motor model. Therefore the utilised motor model together with speed and flux estimators and observers can also be incorporated in the fault diagnosis and isolation process.

6.1.2 Theoretical Background

In model based fault detection approaches, when a fault occurs particular process parameters will be physically influenced and their signals will be changed accordingly. Such changes can lead to alterations in some parameters that can be calculated by the process mathematical model. Hence, monitoring parameters or states which are calculated mathematically would indicate for the fault and may locate it. However, in many circumstances the relevant processes include complex relations and equations and deriving its mathematical models is challenging. Additionally, mathematical models can be time consuming to develop and not always be accurate enough to represent the process [20]. Moreover, signals from the model can be corrupted with model uncertainties and unknown disturbances. Therefore further analysis processes may be required on the generated residuals to differentiate between different faults and distinguish the effects of faults and noise [152] This suggests that when a model-based fault diagnosis technique is applied following modelling of the process the main issues which need to be addressed are the manner in which necessary information on the produced residuals is filtered and extracted [151, 152].

Model based fault detection is in essence implemented by developing the process model mathematically and representing it in a computer programme form. The model replicates the system hardware and operates in parallel to the system within the same system inputs [152]. When a fault occurs, it will cause differences between system model outputs and corresponding actual system measurements. These differences are called residual signals or fault symptoms [151]. Figure 6.1 illustrates the simplified construction of the model based fault detection and diagnosis [152].

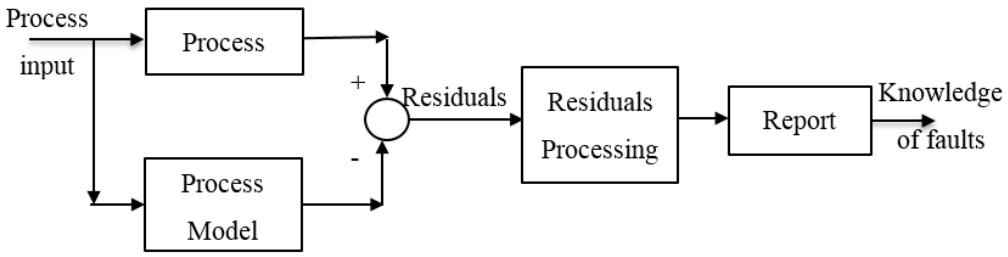

Figure 6.1 Simplified construction of the model based fault detection and diagnosis

It was earlier indicated that the most critical issues when implementing a model based fault detection are the existence of unknown disturbances, the model uncertainties and the signal processing required for fault identification and isolation [152]. To overcome these problems many methods have been suggested in the last few years [151], for instance observer based schemes, parameter identification based methods and parity space methods. Observer based and parity space based techniques show significant similarity and can be structurally the same. This is due to the fact that parity space methods generate particular types of observers and hence they can be included under the framework of the observer based fault detection schemes [152 361].

As stated by [152], utilising an observer instead of the process model is preferable so as to avoid model uncertainties and disturbances, increase the robustness of the fault detection process, and to obtain better process output estimation. Moreover, its flexibility [151] has meant that its usage is widespread.

Observers are used for state and parameters estimations when these parameters are not known and not easy to measure. However, certain measurements at the output and/or the input are needed for the observer. So if the process is described in a state-space form as follows [20]:

$$\dot{x} = Ax(t) + Bu(t) \tag{6.1}$$

$$y(t) = Cx(t) \tag{6.2}$$

Where $u(t)$ and $y(t)$ are process input and output measurements respectively, and A, B, C are the process parameters.

The state observer then can be used to describe the unknown process variable based on the measured inputs and outputs and assuming A,B,C are precise. The observer is expressed as follows [151]:

$$\hat{\dot{x}} = A\hat{x}(t) + Bu(t) + He(t) \tag{6.3}$$

$$e(t) = y(t) - \hat{y}(t) = y(t) - C\hat{x}(t) \tag{6.4}$$

Where H represents the observer gains, and $e(t)$ represents the output error. The state estimation error is defined as follows [20]:

$$\tilde{x}(t) = x(t) + \hat{x}(t) \tag{6.5}$$

$$\dot{\tilde{x}}(t) = [A - HC]\tilde{x}(t) \tag{6.6}$$

The state error goes to zero in the infinite time [20]:

$$\lim_{t\to\infty} \tilde{x}(t) = 0 \tag{6.7}$$

The stability of the observer is achieved by appropriately selecting the observer feedback gains H. Figure 6.2 represents the process with the observer.

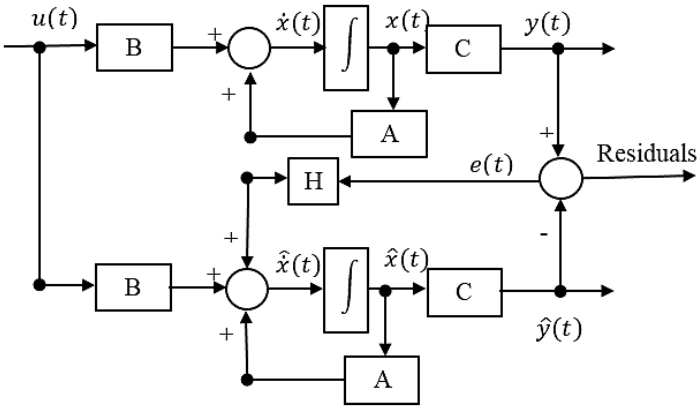

Figure 6.2 Process and observer structure, redrawn [152].

When the system is affected by disturbances and faults, such effects need to be added so they can be seen in both the input and output signals. Figure 6.3 shows the addition of disturbances and faults to the process shown in Figure 6.2.

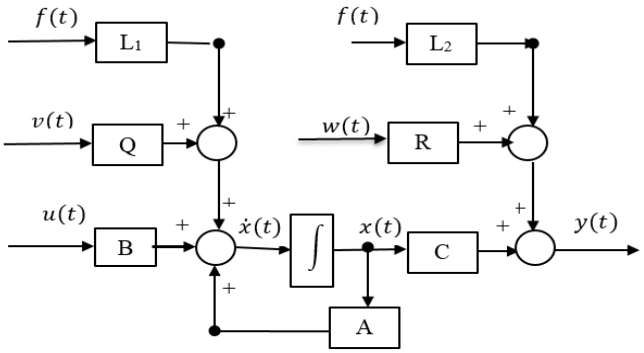

Figure 6.3 Process with faults and disturbances, redrawn from [151]

The system with faults and disturbances then can be formed as follows [151]:

$$\dot{x}(t) = Ax(t) + Bu(t) + L_1 f(t) + Qv(t) \tag{6.8}$$

$$y(t) = Cx(t) + Rw(t) + L_2 f(t) \tag{6.9}$$

Where $f(t)$ denotes the additive fault vector, $v(t)$ and $w(t)$ are the un-measurable disturbances at the input and output respectively. The state estimation error and the output error are then calculated from the following equations, respectively, assuming $v(t) = w(t) = 0$ [20]:

$$\dot{\tilde{x}}(t) = [A - HC]\tilde{x}(t) + L_1 f(t) - HL_2 f(t) \tag{6.10}$$

$$e(t) = C\tilde{x}(t) + L_2 f(t) \tag{6.11}$$

However, if the fault effects on the system parameters, changes in A, B and/or C will be represented as ΔA, ΔB and ΔC, and the process is represented then as:

$$\dot{x} = (A + \Delta\mathrm{A})x(t) + (B + \Delta\mathrm{B})u(t) \tag{6.12}$$

$$y(t) = (C + \Delta\mathrm{C})x(t) \tag{6.13}$$

And the state and output errors are represented as:

$$\dot{\tilde{x}}(t) = [A - HC]\tilde{x}(t) + \Delta\mathrm{Ax(t)} + \Delta\mathrm{Bu(t)} \tag{6.14}$$

$$e(t) = C\tilde{x}(t) + \Delta\mathrm{Cx(t)} \tag{6.15}$$

Equations 6.12 to 6.15 show the role that the system parameters play when building observers. Changes in system parameters will cause changes in the residuals due to the changes they make on the input and state variables [20].

To conclude, model based fault detection can be implemented by mathematically representing the process of interest. However, in many cases it is time consuming and not always easily possible to represent the process mathematically. Observer based fault detection then can be used to effectively monitor the process variables and generate the residuals to indicate the existence of a fault. Though, generated residuals are mostly influenced by changes in process parameter and un-measurable disturbances. Residuals are therefore carefully examined and processed to extract accurate results.

6.2 Residuals and Symptoms

The core tool for observer based fault detection is the generation of a fault-indicating signal or residual. The information available from input and output signals is utilised to generate the residuals that indicate for a set of faults [153]. Residuals, sometimes called "symptoms", need to be clearly defined for the system monitored so they are independent of the system states and depend on the faults of interest. In many cases they are generated by simple comparison between the actual system measurements and the corresponding system model outputs [151]. To have better understanding of the residual generation process, Figure 6.4 illustrates the redundant signal structure used for residual generation processing. The observer $W_1(u, y)$ outputs the signal z(t) which then together with the process output are processed by $W_2(z, y)$ to compute the residuals [153]:

$$z(t) = W_1(u, y) \tag{6.16}$$

$$r(t) = W_2(z, y) \tag{6.17}$$

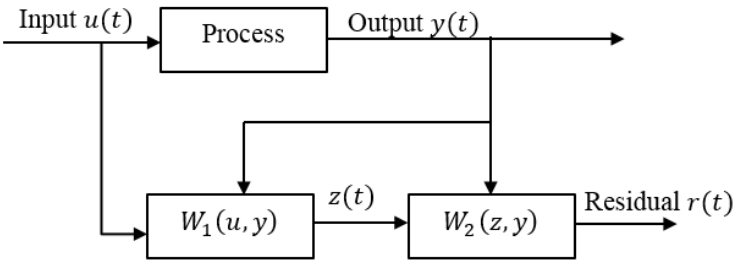

Figure 6.4 The redundant signal structure in residual generation, redrawn from [153]

The observer therefore uses the process input and output to generate the estimation of the process output. Therefore, the estimated parameters are influenced by process input and output signals, while the estimation is based on a linear function of the output ($My(t)$), i.e.[151]:

$$W_1(u,y) = My(t) \tag{6.18}$$

$$W_2(z,y) = W(z(t) - My(t) \tag{6.19}$$

Where W is a weighting matrix.

Therefore, the symptoms are generated by processing the system inputs and/or outputs based on linear processing functions. Figure 6.5 shows a generalised structure of the residual generation process in the time domain based on the system inputs [151].

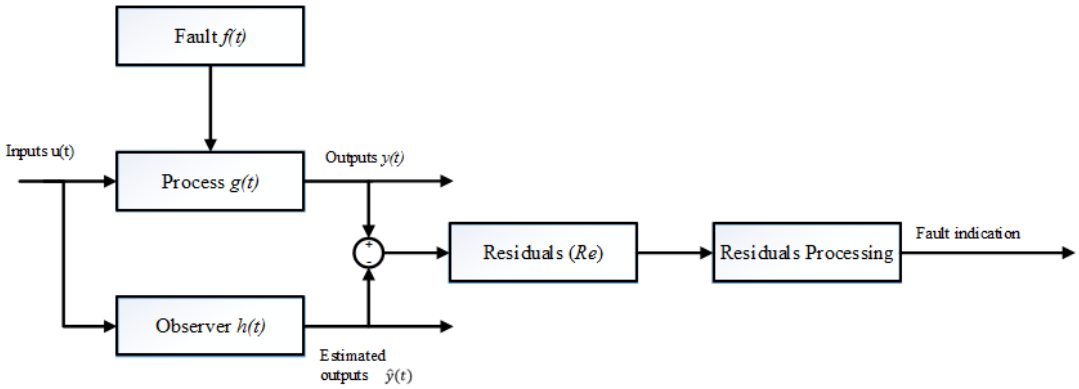

Figure 6.5 Observer and residual generator general structure, redrawn from [15]

The mathematical expression of the observer shown in Figure 6.5 is as follows [153]:

$$r(t) = h_u(t)(u(t) + f(t)) - y(t) \tag{6.20}$$

The strategy described in Figure 6.5 therefore uses the input variables to estimate the output variable. This different to that depicted in Figure 6.4 where both input and output variables are included for observation. The advantage of using the scheme explained in Figure 6.5 is that no need for measuring the output variables.

Generated residuals are then processed and analysed to extract the fault of interest. Residuals processing, as indicated earlier, should eliminate the effects of random and immeasurable disturbances, meanwhile considers parameters changes during the operation.

6.3 Monitoring and Diagnosis

Predominantly then the observer based fault detection is based on the mathematical equations of the process. The residuals generator should be able to indicate for the fault and false alarms, mainly occurring due to random noise and un-measurable disturbances, need to be avoided.

As shown in Equation 6.20, the performance of the residual generator is highly dependent on the transfer matrices $h_u(t)$ and $h_y(t)$ which must be appropriately selected to ensure the stability of the observer on the one hand and to provide valuable information about system health on the other. It should provide zero index for the fault free case, i.e. r(t) = 0 if f(t)= 0 and:

$$u(t)g(t) - u(t)h(t) = 0 \tag{6.21}$$

From Equations 6.20 and 6.21 different residual generators can be developed using different forms of $h(t)$ [153]. The generated residuals are then used for fault detection by investigating whether a certain threshold (T(t)) is exceeded. An evaluation function based residual (J(r(t))) is compared to the threshold function to generate the fault alarm [153]. An alarm signal ($f_a(t)$) is turned off if the comparison result is 0, see Equation 6.22, or turned on if the comparison result is 1, as shown in Equation 6.23 [20].

$$\text{If} \quad J(r(t)) \leq T(t) \; then \; f_a(t) = 0 \tag{6.22}$$

$$\text{If} \quad J(r(t)) > \; T(t) \; then \; f_a(t) = 1 \tag{6.23}$$

Different schemes [151, 152] can be used to separate noise and unknown disturbances in the process from the faults as well as evaluating the performance of residuals generated. Techniques may include fuzzy likelihood-ratio-test, space victor and neural networks [150]. However, such techniques may need additional resources in the drive and additionally they are mathematically complicated. In the following section, a new scheme is developed when applying observer based fault detection using observers designed for control purposes.

6.4 Applying the Observer Based Condition Monitoring Scheme

6.4.1 MRAS Speed Observer

Observer based approaches are commonly embedded in sensorless variable speed drives. The observer estimates state variables to produce errors or residual signals in conjunction with corresponding measurements. Observers used in Sensorless VSDs for speed estimation and control purposes can be simultaneously used for fault detection. Yet, in this case observers should be designed so that they robust against random noise and to prevent the control system from following the fault conditions. A compromise is required when developing observers for state estimation and simultaneously for fault detection.

To develop the observer based scheme, the observer is firstly implemented as it can produce the required state variables for the control scheme and generate the desired residuals for the fault detection process. The MRAS observer is built based on a MATLab code as detailed in chapter 5.

The PI controller parameters are empirically defined for each operating point. The output from PI controller replaces the estimated speed value and forces the difference between reference and adjustable flux models to zero. The outputs from this MRAS speed estimator are the estimated speed and estimated rotor flux components ψ_{dr} and ψ_{qr} where $\psi_r = \sqrt{\psi_{dr}^2 + \psi_{qr}^2}$ and the phase angle (position of the flux victor) is calculated form $\theta = tan^{-1}(\frac{\psi_{dr}}{\psi_{qr}})$.

For stability and robustness the estimated speed can be filtered before sending it to the speed control system. However, the speed signal used for fault detection and diagnosis is not filtered in order to keep faults features. The unfiltered speed signal is used for flux and load torque observers. Figures 5.7 to 5.10 in Chapter 5 illustrate the structure of this estimator.

To verify the accuracy of this estimator data sets from the test rig used for model verifications in Chapter 5 previously are also used here for observers' verifications. The current and voltage measured signals have been used as inputs to the speed estimator. The output speed is compared with corresponding real speed measurements from the encoder. Figure 6.6 shows comparison between the estimated and measured speeds when the rig is run under different operating conditions. Results show acceptable agreement between the estimated and the measured values at different speed and load conditions.

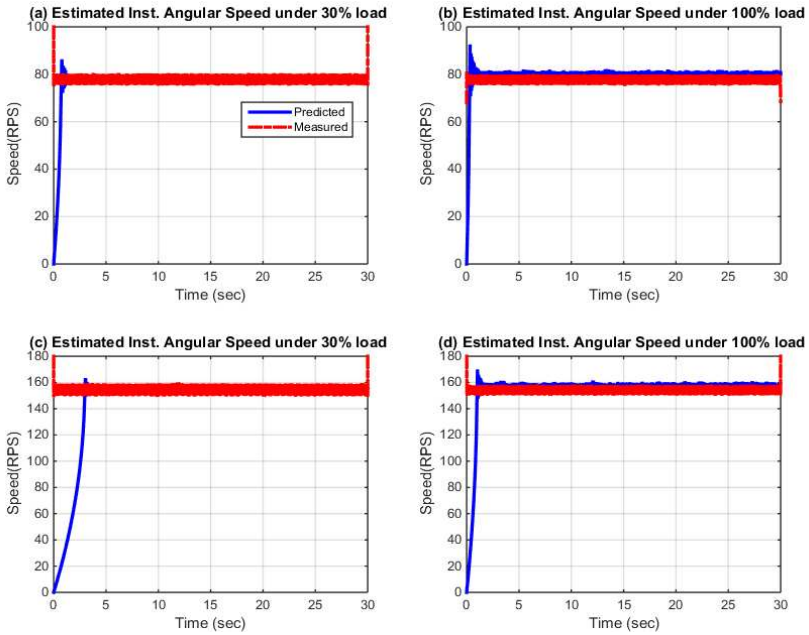

Figure 6.6 Estimated and measured speed comparison under different operating conditions.

6.4.2 MRAS Rotor Flux Observer

Due to the fact that the drive used by the rig is a commercial industrial drive, it restricts information about the detailed structure of the drive as well as details in relation to

dynamic measurements and estimation techniques. Therefore, another rotor flux observer is needed to confirm the flux estimated by the speed observer. This will help in obtaining more accurate rotor flux, position and torque values. Different schemes have been suggested for rotor flux observation [145]. Here, the MRAS flux observer detailed in [65] will be used with some amendments. The relationship between rotor and stator fluxes is represented as follows [154]:

$$\frac{\mathrm{d}\psi_{dr}}{dt} = \frac{L_r}{L_m}(\psi_{ds} - \sigma L_s i_{ds}) \tag{6.24}$$

$$\frac{\mathrm{d}\psi_{qr}}{dt} = \frac{L_r}{L_m}\left(\psi_{qs} - \sigma L_s i_{qs}\right) \tag{6.25}$$

From equations 4.12 and 4.13 the stator flux in the stationery reference frame is represented as:

$$\frac{\mathrm{d}\psi_{\mathrm{qs}}}{\mathrm{dt}} = \mathrm{u_{qs}} - \mathrm{R_s} i_{qs} \tag{6.26}$$

$$\frac{\mathrm{d}\psi_{\mathrm{ds}}}{\mathrm{dt}} = \mathrm{u_{ds}} - \mathrm{R_s} i_{ds} \tag{6.27}$$

By using Equations 6.26 and 6.27 in 6.24 and 6.25 respectively:

$$\frac{\mathrm{d}\psi_{dr}}{dt} = \frac{L_r}{L_m}(\int(\mathrm{u_{ds}} - \mathrm{R_s} i_{ds})dt - \sigma L_s i_{ds}) \tag{6.28}$$

$$\frac{\mathrm{d}\psi_{qr}}{dt} = \frac{L_r}{L_m}\left(\int(\mathrm{u_{qs}} - \mathrm{R_s} i_{qs})dt - \sigma L_s i_{qs}\right) \tag{6.29}$$

The rotor flux is also represented by the current equations and speed as previously described when the current model was developed for the speed estimator, i.e. Equations 5.39 and 5.40 which are rewritten as follows:

$$\frac{d\psi_{dr}}{dt} = \frac{1}{T_r}\left(L_m i_{\mathrm{ds}} - \psi_{dr} - \widehat{\omega}_r \psi_{qr}\right) \tag{6.30}$$

$$\frac{d\psi_{qr}}{dt} = \frac{1}{T_r}\left(L_m i_{qs} - \psi_{qr} + T_r \widehat{\omega}_r \psi_{dr}\right) \tag{6.31}$$

Equations 6.30 and 6.31 can be used as the reference model where the speed is obtained from the MRAS speed estimator and the current signal is measured at the motor terminals. Equations 6.28 and 6.29 are utilised for the adjustable model. A PI controller is used for the adaptation mechanism and adjusting the adaptive model based on the

difference between both fluxes. The output of the PI controller is fed back to the adaptive model where it is subtracted from the output of the integrator (stator flux). The structure of this model is shown in Figure 6.7.

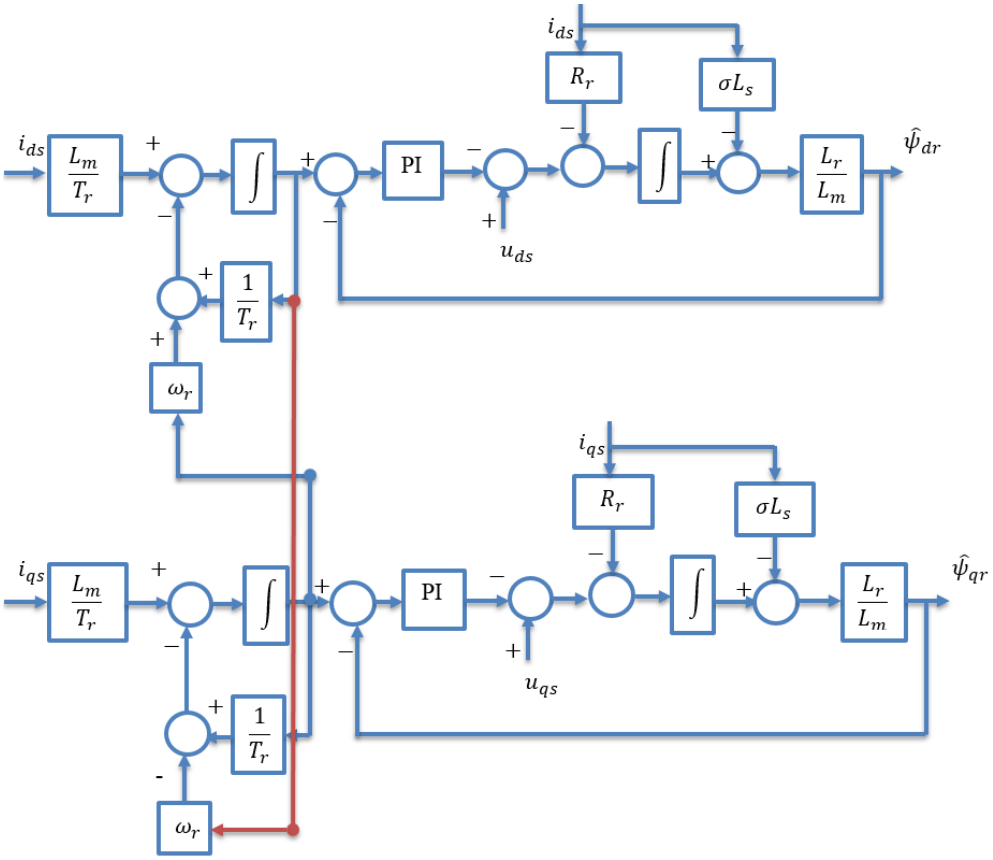

Figure 6.7 Rotor flux observer

The amendment made here is that in [65] the output of the PI controller is used as voltage signal to adjust the stator voltage. Additionally in [65]a positive feedback signal is used to adjust the adjustable model. Contrastingly in this study the feedback signal is flux type and is negatively fed back to the adjustable model. The idea is to ensure that the noise in the error signal is not added to estimated fluxes. Additionally, this would prevent the error signal from being treated by the integrator in the adjustable model and ensures that the fault features are not affected by the integrator.

Similarly, for verification purposes, data sets utilised in Chapter 4 have been used for flux observer verification. Voltage and current together with the estimated speed are inputs to the flux observer, while the estimated flux component signals are the outputs.

The estimated flux components from the speed estimator and flux observer are compared, and certain results are represented in Figures 6.8 and 6.9. Results indicate a high level of agreement between the estimated signals from both observers.

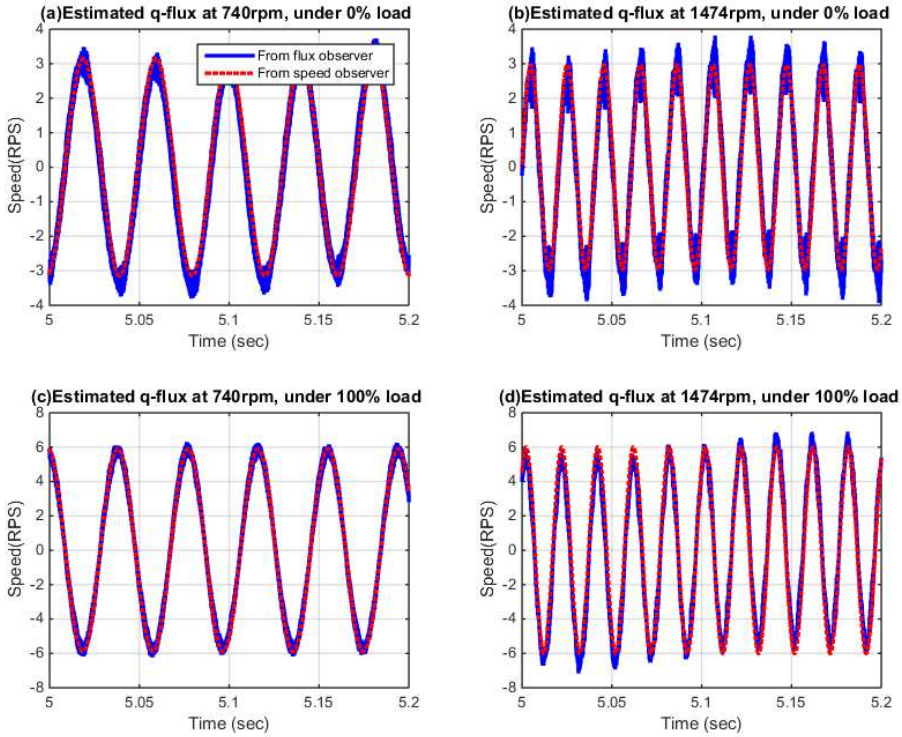

Figure 6.8 q-flux component from speed and flux observers' comparison

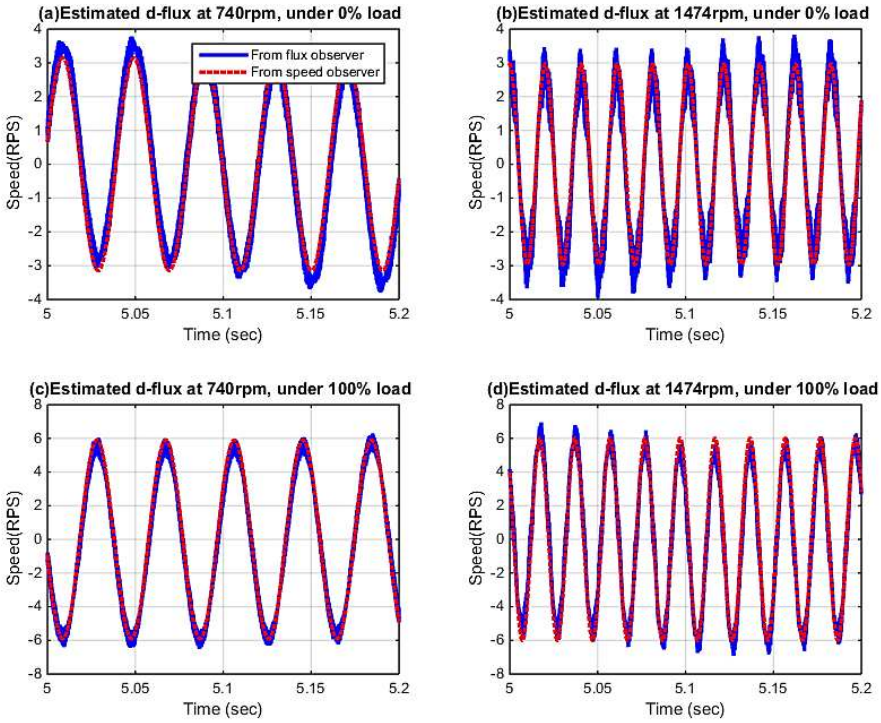

Figure 6.9 d-flux component from speed and flux observers' comparison

6.4.3 Electromagnetic Torque and Load Torque Oscillation Estimation

The electromagnetic torque of an induction is calculated based on measurement of the three phase supply signals from one of the following formulas [155]:

$$Te = \frac{3}{2} N_p \left(i_{qs} \psi_{ds} - i_{ds} \psi_{qs} \right) \tag{6.32}$$

$$Te = \frac{3}{2} N_p \frac{L_m}{L_r} \left(i_{qr} \psi_{dr} - i_{dr} \psi_{qr} \right) \tag{6.33}$$

$$Te = \frac{3}{2} N_p \frac{L_m}{\sigma L_s L_r} \left(\psi_{qs} \psi_{dr} - \psi_{ds} \psi_{qr} \right) \tag{6.34}$$

When equation 6.32 is applied to estimate the electromagnetic torque of the motor, stator flux is calculated from the voltage model expressed by Equations 6.26 and 6.27.

A low-pass filter is used to eliminate the influence of ripples due to the integration required for stator flux components calculations and to enhance the stability of the observer. However the instantaneous torque signal is used for estimating the load torque oscillations while the filtered electromagnetic signal can be used for the control system.

Data sets utilised in Chapter 5 have also been used here for torque estimation verification. Voltage and current signals are fed into the torque estimator to produce the estimated torque signals. Figure 6.10 shows comparison between the measured electromagnetic torque from the drive with the corresponding estimated electromagnetic torque under different load and speed conditions. The figure shows that the estimated torque signals are nearly identical with the corresponding measured signals from the drive.

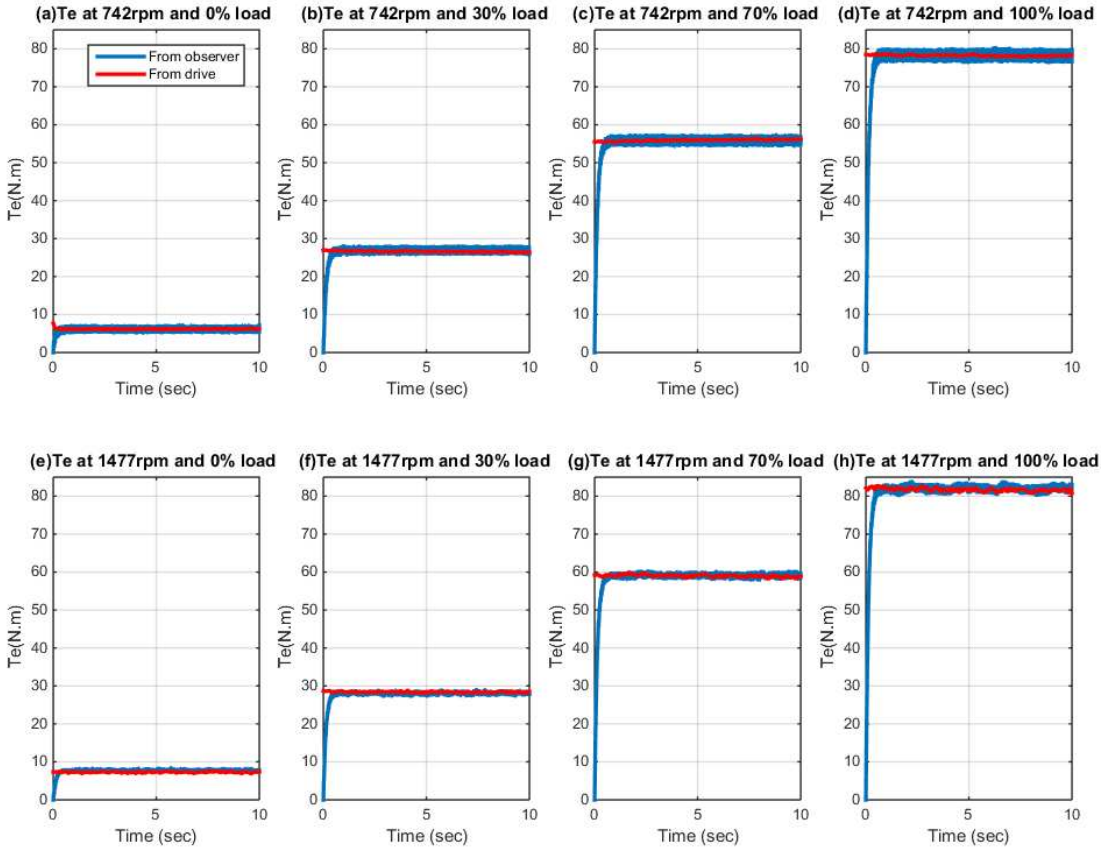

Figure 6.10 Measured and predicted electromagnetic torque comparison

The load torque oscillation or torsional load torque vibration is estimated using the most popular mechanical equation of the induction motor, without considering the viscous friction coefficient, as follows [94]:

$$T_{load} = \frac{1}{J}(T_e - \frac{d\omega_r}{dt}) \tag{6.35}$$

6.4.4 Residual Generation

When a fault occurs it will affect the process parameters and changes the system variables including the system speed, terminal voltages and stator currents. The drive will manipulate the motor supply to compensate for the changes generated by the fault. However, the complex structure and the noise level from the drive make it difficult to detect small changes in the supply signals directly. Nevertheless the drive actions will change the input power to the motor; meanwhile the fault will affect the output power of the system by oscillating the load torque and the speed, as described in Section 3.7.2 Chapter 3.

The suggested scheme therefore employs both measured inputs together with the calculated (estimated) outputs to generate residuals R_e. Specifically, by developing a relationship between: the calculated mechanical power $\hat{P}_{mec}$, which is calculated using the estimated torque and speed quantities; and the measured power P_{elec}, which is the product of the measured supply currents and voltages:

$$\hat{Y} = \hat{P}_{est} = f(P_{elec}, \hat{P}_{mec}) \tag{6.36}$$

The measured instantaneous power P_{elec} is obtained from the three phase current and voltage measurements at the drive terminals as follows [101]:

$$P_{elec} = i_a * u_a + i_b * u_b + i_c * u_c \tag{6.37}$$

where $i_a, i_b,$ and $i_c$represent the phase quantities of the induction motor stator current and u_a, u_b, u_c are the phase quantities of the stator voltage. The induction motor utilised in the test rig is delta connected. Hence the phase voltage is equal to the line voltage, while the phase current $i_a$and the line current i_l are related as[156]:

$$i_a = {}^{1}/_{\sqrt{3}}\ i_l \angle -30^o \tag{6.38}$$

The mechanical power $\hat{P}_{mec}$ is calculated from the estimated values of motor torque $\hat{T}_e$(N.m) and motor speed $\hat{\omega}_m$ (revolution per second) as follows [141]:

$$\hat{P}_{mec} = \hat{\omega}_r \hat{T}_e \tag{6.39}$$

As indicated in [152], the residual vector r can be expressed based on the disturbances and parameter deviation contents $H_d(P)d$ and the fault function $H_f(P)f$ which are related as follows [152]:

$$Re = \mathrm{H}_d(P)d + H_f(P)f \tag{6.40}$$

where P refers to the design parameters of the observer, i.e. induction motor parameters. Based on Equation (6.40), the disturbance content d needs to have least influence, while on the contrary the operator f is required to be at maximum. In other words, residuals should show greater sensitivity to faults.

A decoupling scheme needs to be developed to make the residual r independent of disturbances $\mathrm{H}_d(P)d$. Studies indicate significant work towards developing decoupling schemes that perform improved disturbances. More details of these methods can be found in [152] [10, 15, 68]. Nevertheless these techniques are mostly dedicated to observers designed for condition monitoring purposes. When an observer is designed for control purposes, the generated residuals will also be influenced by induction motor parameters and load disturbances as illustrated in Figure 6.11. In such surrounding changeable conditions if not considered appropriately this can lead to false fault indication.

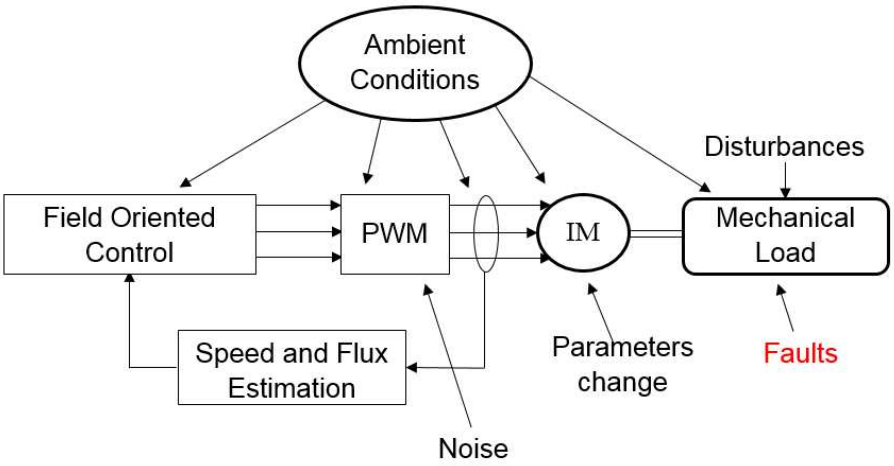

Figure 6.11 Conditions influencing sensorless VSD driven mechanical load

In industrial process control systems [157, 158] a curve fitting scheme is used to detect actuator faults in the control loop. Controller outputs and process variables are fitted piece wise to a certain waveform based on the diagnosed actuator. Any deviations from the fitted curves will indicate a fault in the monitored actuator. The curve fitting scheme,

also referred to as local regression [159, 160], is widely used to formulate a relationship that attempts to describe important patterns in the data, while removing noise.

To show how the output power changes with the input power, Figure 6.12(a) describes this relationship under different operating conditions from the baseline data.

The main concern of the fitting process is to make the residuals robust against motor parameter inaccuracy and any disturbances from load variation. Hence, both estimated and measured signals are normalised to the reference setting values by fitting the output across different loads. Figure 6.12(b) shows the fitting process performed at 100% speed across different loads, where the fitting is performed by the MATLAB fitting tool to find the best fitting. As shown in the figure, the base setting values fit the quadratic curve of the following form:

$$\hat{y}(t) = \mathrm{a}_1 x(t)^2 + \mathrm{a}_2 x(t) + a_3 \tag{6.41}$$

where, coefficients a_1, a_2 and a_3 are -0.083019, 3.4656 and -20.29 respectively.

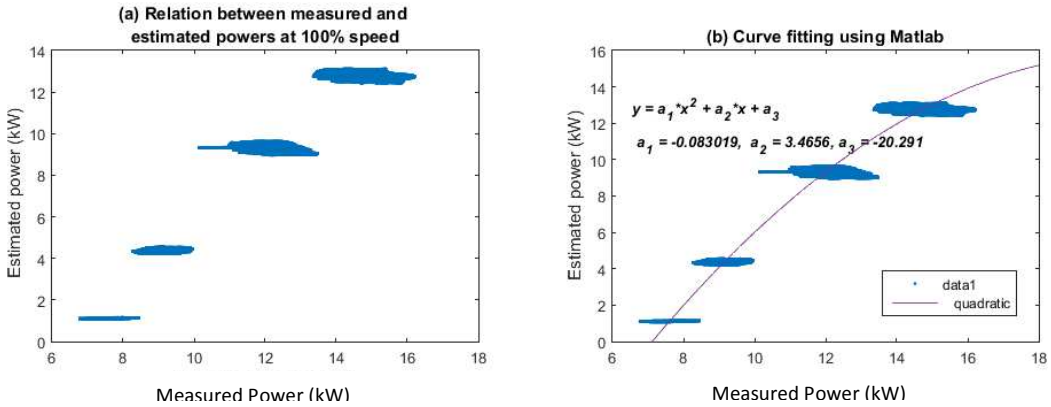

Figure 6.12 The fitting process

When the relationship is developed from the baseline data, a polynomial model is defined to describe this relationship as outlined in Equation 6.41. Residuals are then calculated from the difference between the model output (estimated power) and the mechanical power as follows:

$$R_e(t) = \left|P_{mes}(t) - \hat{P}_{est}(t)\right| = \left|\hat{P}_{mec}(t) - \hat{y}(t)\right| \tag{6.42}$$

Additionally, a first order digital low pass filter with time constant τ is suggested to remove high frequency noise. The transfer function of the digital low pass filter in terms of Laplace transform is:

$$G_f(s) = \frac{1}{1+\tau s} \tag{6.43}$$

Finally the residuals generated are quantified, represented in percentage to the motor base power. The developed scheme is represented in Figure 6.13.

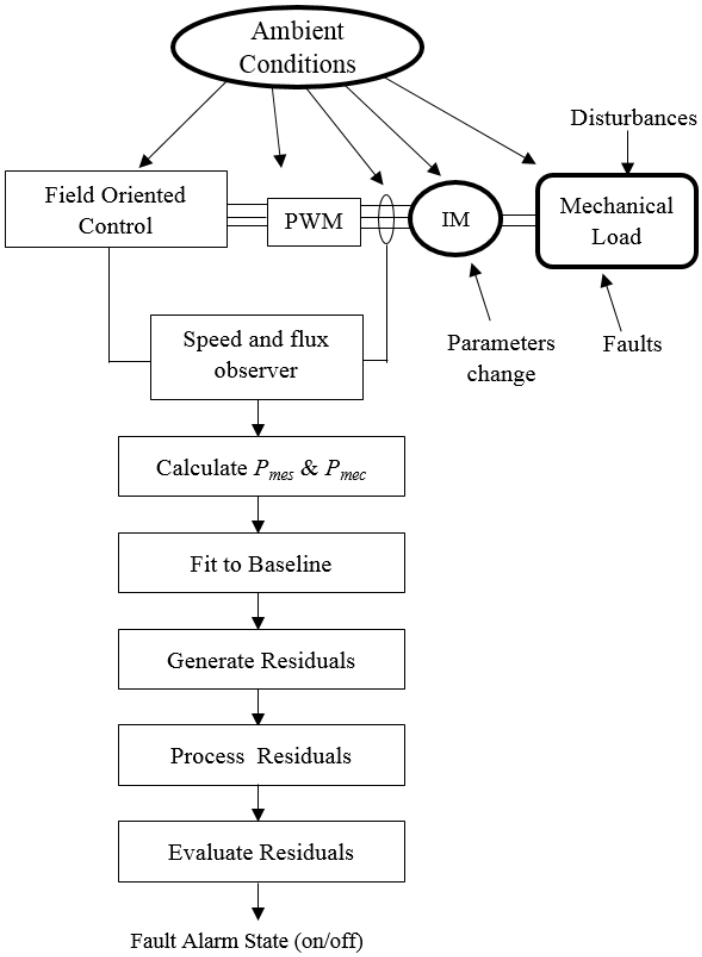

Figure 6.13 The schematic of the suggested scheme

6.4.5 Residuals Evaluation

To complete the fault detection task, residuals need to be evaluated based on a certain threshold. A threshold value I_{th} is required as residuals cannot be zero even in the case of fault absence due to measurement noise and model uncertainty [159]. There are

different schemes used to set up a predetermined threshold for fault detection and residual evaluation purposes. However, as indicated in [159, 160] each identification method as well as each process will has its own residual evaluation strategy hence developing a specific threshold setting mechanism.

As the aim at this point is to detect small changes in the signals, the threshold is set based on running the system under normal operating conditions several times and visualising the highest residuals values [161]. Figure 6.14 represents residuals resulting from two different baseline runs. As is clear from the figure, the normalised residuals are not zero even for healthy operations. Further residuals are changed with speed values therefore each speed operating point will have its particular threshold value. The worst case is when the residuals reach the maximum values under the normal baseline conditions. The maximum operating point has been calculated from the baseline and then a gain margin of 30% is chosen to which the threshold is set. The resulting thresholds of the three tested speeds are: 0.0290, 0.0481, and 0.1157 for 50%, 75% and 100% speed respectively.

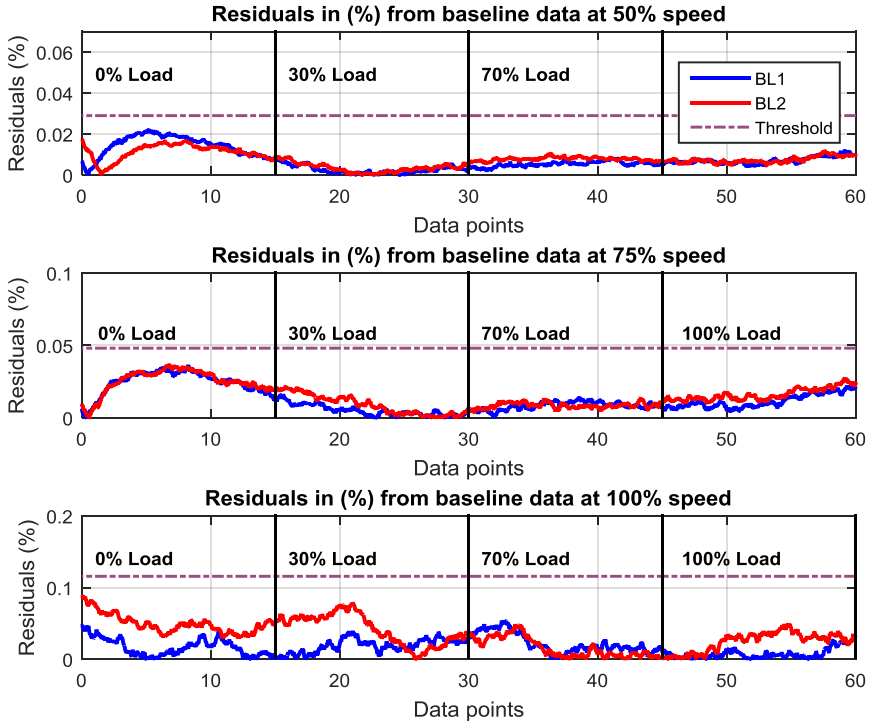

Figure 6.14 Two baseline tests for threshold identification

To conclude, in this chapter the theoretical background of observer based fault detection and the residual generating scheme has been briefly provided. Following that, speed and flux observers for sensorless VSDs are implemented and results are verified based on the real rig measurements. This is followed by the development of a new residual based generating method. The method uses both measured power and estimated mechanical power to develop polynomial models that describe the relationship between both powers. The models are then trained to the baseline data and used to generate the power residuals. This scheme is proposed to make residuals robust to load changes and motor parameter inaccuracy. Residuals are then low-pass filtered and represented as a percentage to the base motor power. The thresholds are experimentally defined by taking a worst baseline result and developing a 30% gain margin. When residuals reach this value a fault alarm is triggered. An off line diagnosis process is then required to identify and locate the fault.

Chapter 7
Diagnosis of Mechanical Shaft Misalignments

Mechanical shaft misalignments with four degrees of severities are tested to examine the residuals and the sensorless VSD responses to mechanical fluctuations caused by faults. Firstly, an introduction is provided followed by brief details on the effect of the shaft misalignment on the mechanical and electrical system. The characteristics of the rig baseline in open loop and sensorless operating modes are then explained. The chapter continues with an analysis and discussion of the vibration response to different faults applied followed by details and discussion of the results from tests performed under an open loop operating response. Finally, the response of the system under the sensorless operating mode is provided and analysed.

7.1 Introduction

In the following, results obtained from tests explained in Chapter 4 are discussed. The analysis is made based on a systemic comparison of different control parameters between two common control operation modes: open loop and sensorless control modes. This can lead to definition of the role of the sensorless VSD in case of mechanical fault occurrence and differentiate it with that of the open loop actions.

7.2 Base Line Characteristics

7.2.1 Open Loop Operating Mode

Under the open loop operating mode the drive provides current signal with constant frequency. The drive maintains fixed V/Hz ratio during the operation based on the speed setting. For this particular set of tests, misalignment tests, data is collected only when temperature is stabilised. Figure 7.2 (a,b) represents GB1 and GB2 temperature values respectively. It is clear that both GB1 and GB2 have the same temperature behaviours and temperature changes with nearly the same trend exhibited in both.

The system speed under open loop operating mode is shown in Figure 7.2 (c). When the drive is in open loop control mode, there is no speed feedback to the drive regulators. The drive provides supply with fixed frequency based on the reference speed. The consequence of load increase is reduction in the speed due to the load torque. However, the drive does not compensate for this increase in the load and preserves constant electromagnetic torque by maintaining the V/Hz ratio constant.

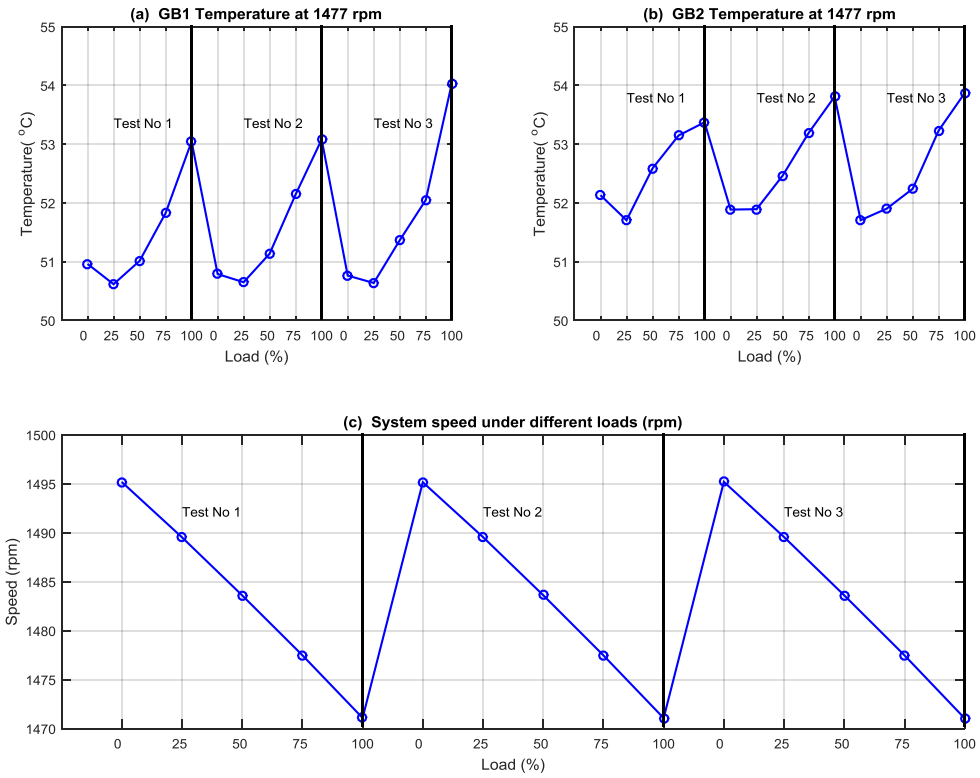

Figure 7.1 Temperature and speed response under different load conditions

To further understand the behaviours of the system under the open loop control drive, the current spectra of the baseline is calculated and presented in Figure 7.3. The present current spectra are shown for the system under 0%, 50% and 100% load settings. As clear from the figure, the fundamental frequency component of the current f_s is kept fixed at about 49.9Hz for the different load settings. Additionally, feature frequency components related to the gearbox shaft frequencies are increased in amplitudes with load. As the load increases the oscillations of these shafts will also increase and hence

there are more excitations across the fundamental frequency components of the current signal.

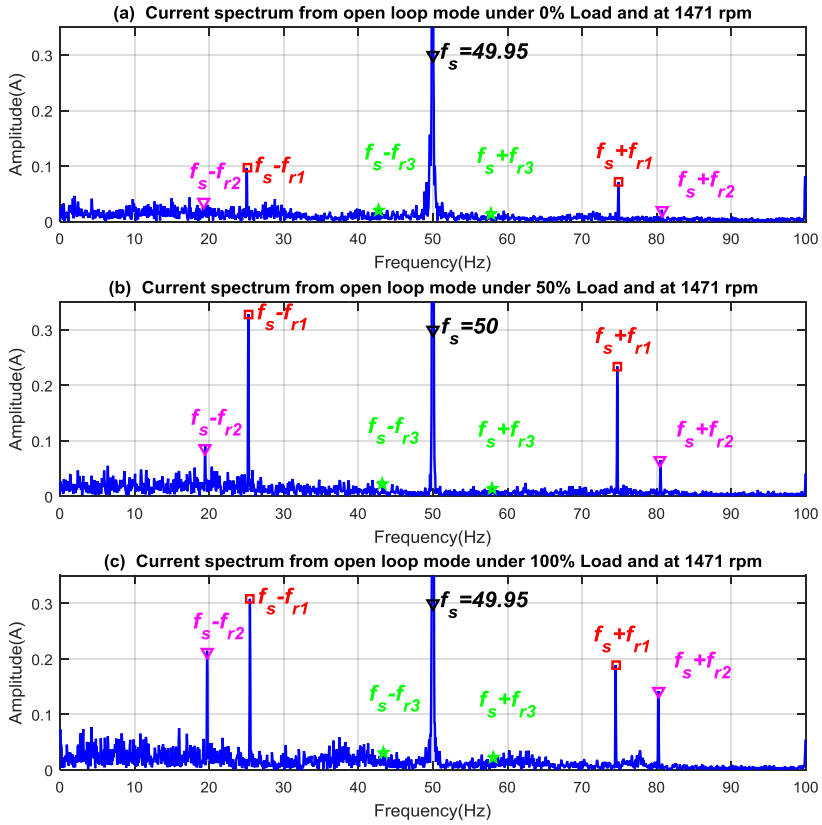

Figure 7.2 Current spectrum under open loop operating mode

Voltage spectrum has also been calculated when the system is under open loop operating mode. Figure 7.4 depicts the voltage spectra of the baseline under 0%, 50% and 100% load. The voltage spectra shows the same fundamental frequency component under different load conditions, i.e. fs= 59.95Hz. Additionally, sidebands of the shaft frequencies can also be found in the voltage spectra although the left sidebands show different behaviours to that of the current spectra as they do not show clear changes with load. This is due to the fact that drive maintains the voltage signal constant in all circumstances and prevents it from changing in order to keep a constant V/Hz ratio fixed for every speed reference value.

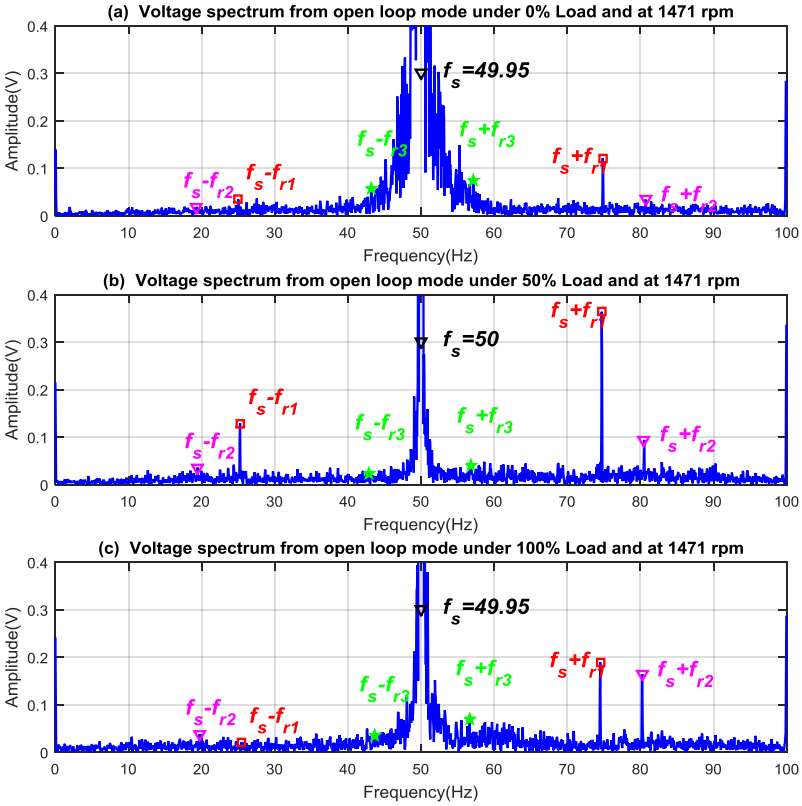

Figure 7.3 Voltage spectra from open loop mode under different load conditions

Similarly, the spectra of the electrical power are calculated. Figure 7.5 represents the electrical power spectra under different load conditions. The main sidebands of the shaft frequencies can be found across the supply frequency. Additionally, these sidebands show the same behaviours to that of the current spectrum in that they increase as the load increases.

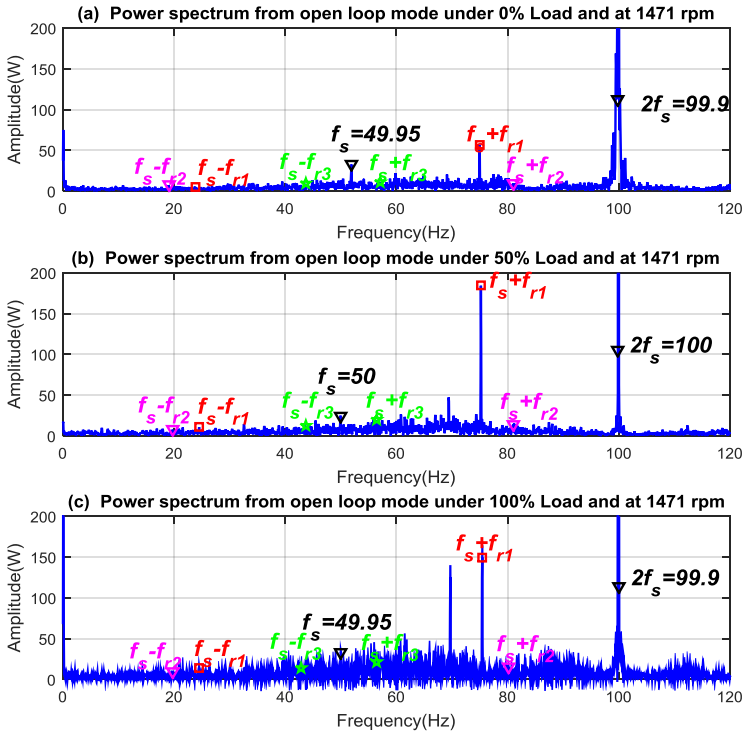

Figure 7.4 Power spectra from open loop mode under different load conditions

Static data from the drive has additionally been logged for analysis. Figure 7.6 illustrates the main electrical parameters that the drive uses for control purposes. Despite the fact that when the drive is in the open loop control mode the regulators do not affect all of these signals, the drive continues to calculate all such parameters. As shown in Figure 7.6 (a,b,c, and d), current, torque, power and torque current component systematically increase with the load. On the other hand voltage signal and supply frequency, as shown in Figure 7.6 (e and f), are kept nearly constant.

For diagnosis purposes, in any test case, the average of each signal at each particular load is calculated and then compared with the corresponding baseline values. Figure 7.7 presents the averaged signals against load values.

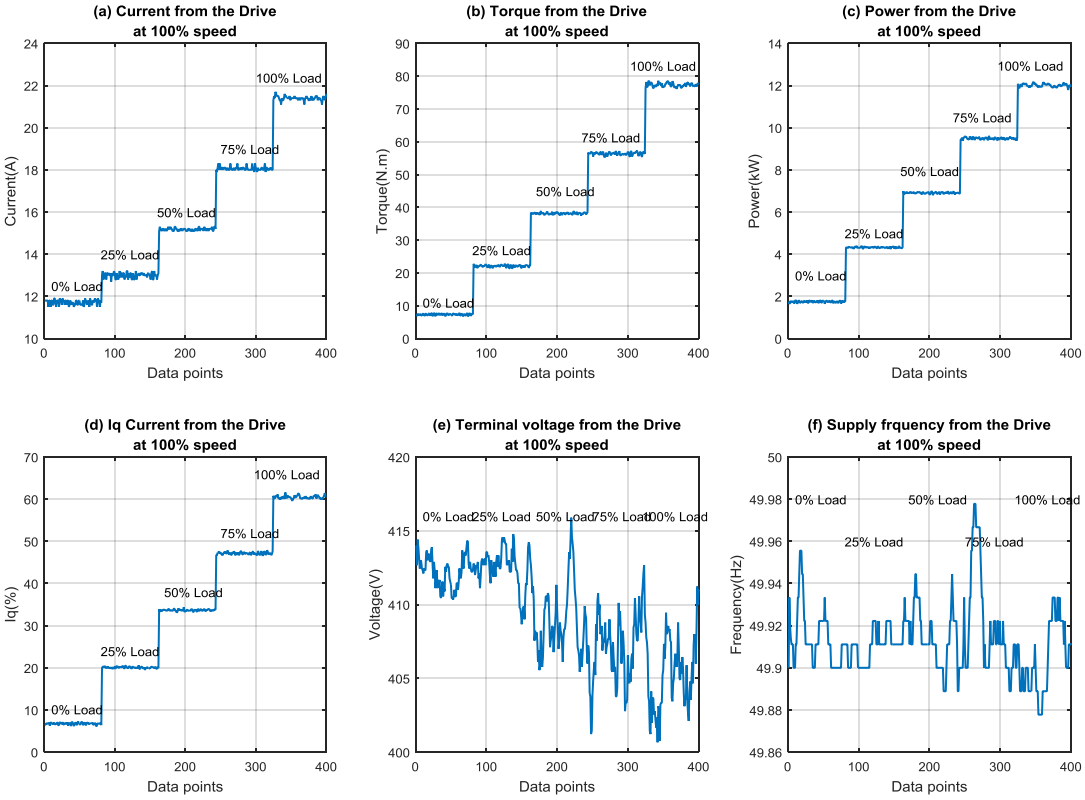

Figure 7.5 Static data from the drive under different load conditions

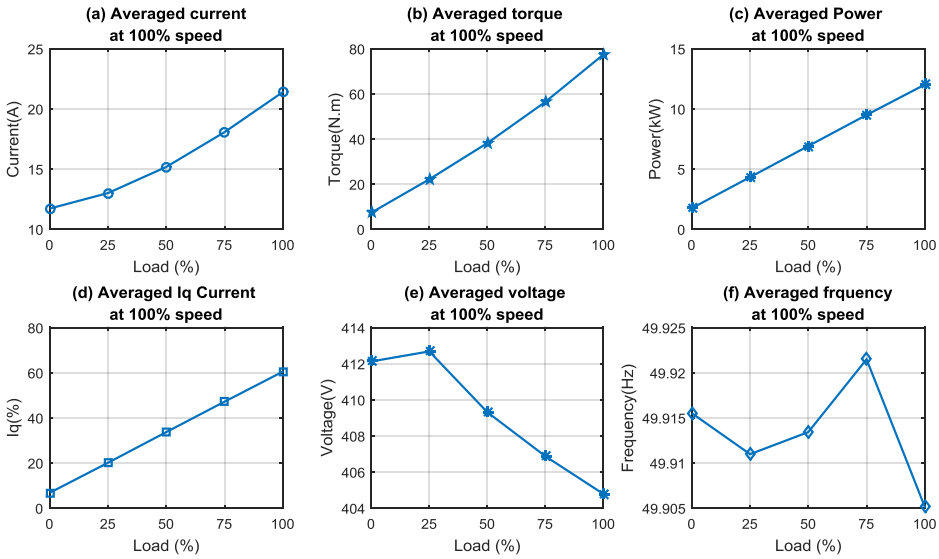

Figure 7.6 Averaged static data from the drive under different load conditions

7.2.2 Sensorless Operating Mode

To evaluate the operating conditions of the system under the sensorless control mode, GB1 and GB2 temperature values are recorded and averaged as shown in Figure 7.8 (a and b), in addition to the system speed during the three testing runs as in Figure 7.8 (c). Both gears have approximately the same temperature trend and close values. Additionally, compared to the speed of that from the open loop control mode, there is limited variation in the speed even under different load settings. The drive maintains constant and stable speed and prevents load oscillations and demand from changing the stability condition of the system.

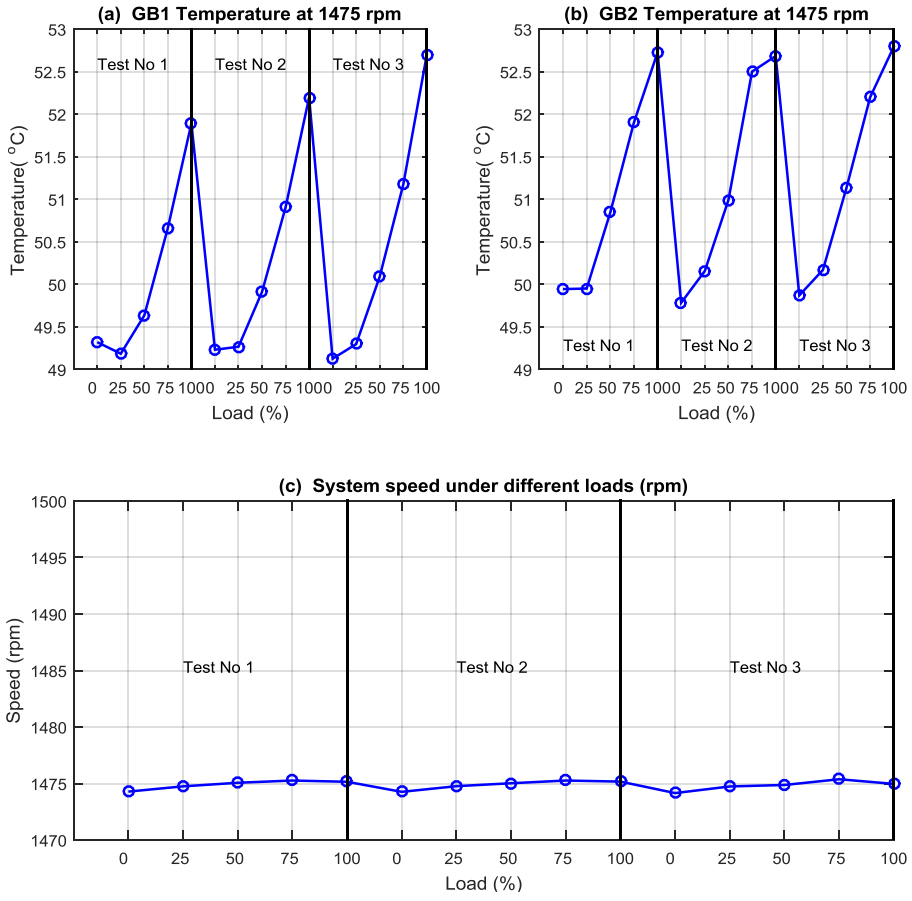

Figure 7.7 Test rig operational conditions under sensorless control mode

The current spectra has also been calculated when the system is under sensorless control mode to investigate the different frequency component under this particular operating mode. Figure 7.9 shows the current spectrum characteristics when the system is under

sensorless control mode. As shown in Figure 7.9, the main feature frequency components can be found. However, they are associated with lower amplitudes compared with those from the open loop test runs. Additionally as the load increases amplitude at this frequency components also increase. Remarkably, the fundamental supply frequency has increased with load. The VSD changes the supply frequency to compensate for the speed drop caused by the load that occurred in the open loop mode.

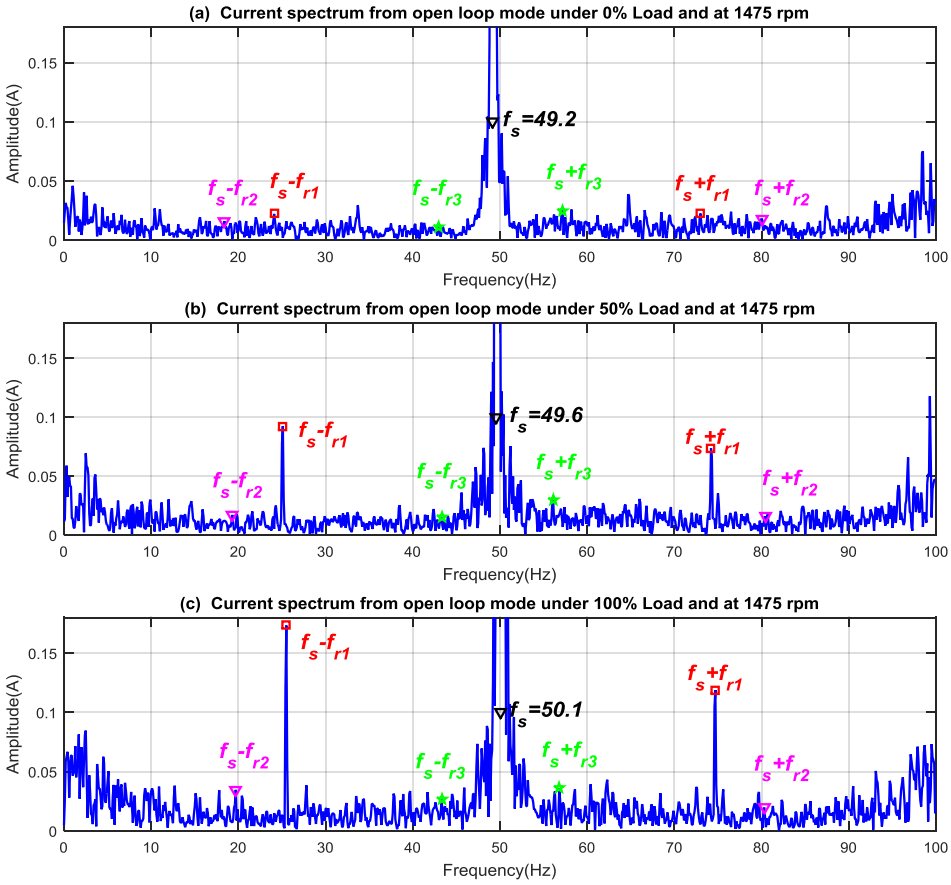

Figure 7.8 Current spectra under sensorless control mode

Similarly, the voltage spectra from the sensorless operating mode have been calculated as presented in Figure 7.10. The voltage spectra from the sensorless control mode are richer in information than that from the open loop control mode. Accordingly other sidebands can be obtained, particularly $f_s \pm f_{r3}$. Additionally, unlike the open loop mode, the amplitudes at feature frequency components are increasing with load. This is due to the fact that the drive is responding to any changes in demand or disturbances by

altering the voltage supply to the motor. This is also clear from the discernible effort exhibited by the drive in relation to the supply frequency. Change in the fundamental frequency with the load is also clear from the voltage spectra.

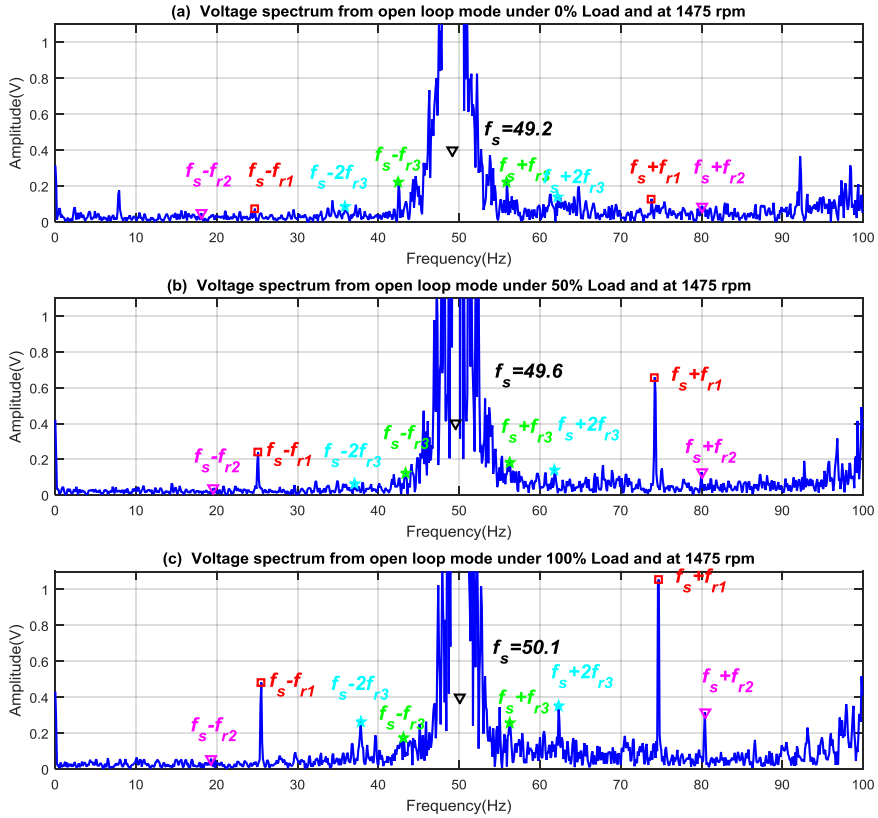

Figure 7.9 Voltage under sensorless control mode

The spectra of the electrical power supply signals under sensorless control mode have further been calculated. Figure 7.11 shows the power supply spectra under different load conditions and at 100% speed. Power under this control mode showed the same behaviours to that of voltage and current. The main feature frequency components can be found with these features showing higher amplitudes as the load increases. Finally the supply frequency changes as the load alters due to the regulation effect of the drive.

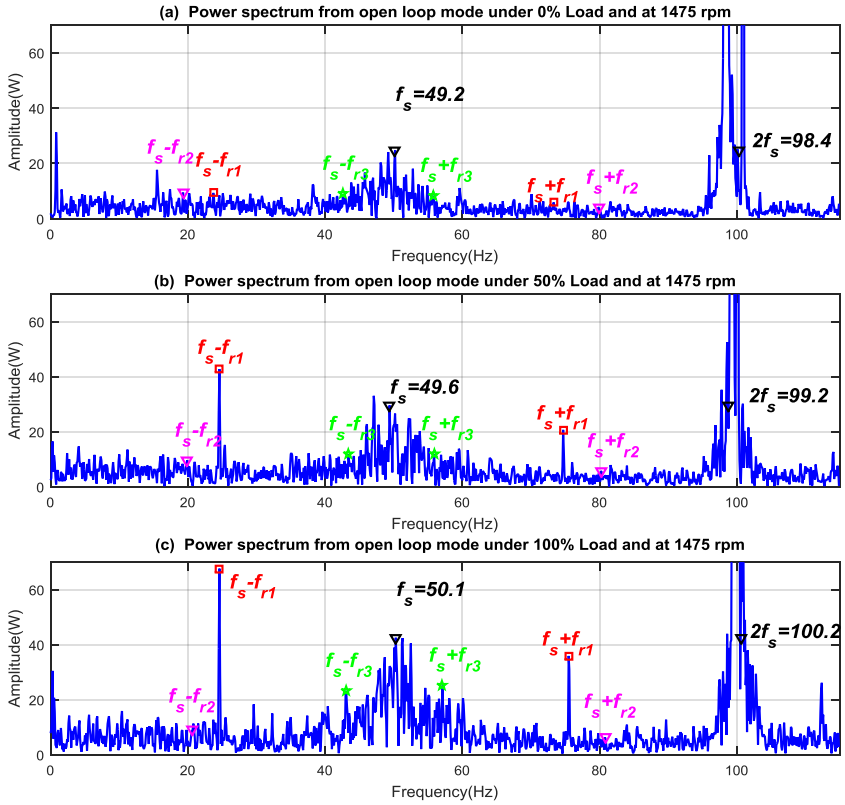

Figure 7.10 Electrical power spectra under sensorless control mode

The static control data has been logged from the drive during the operation. Figure 7.12 depicts the main control data from the drive under the sensorless control mode. The torque related variables, i.e. current, torque and power, reveal a similar trend as that indicated in the open loop control mode, as shown in Figure 7.12 (a, b and c). However, the torque current component in Figure 7.12 (d) has slightly increased as the control system changes it when in the sensorless control mode. This is to provide better torque response and prevent speed drop due to the load increase. Additionally, the voltage signal shown in Figure 7.12 (c) is further regulated by lower values compared to that of the open loop mode. Finally, a systematic increase in the supply frequency is noticeable as represented in Figure 7.12 (f). The drive changes the frequency of the electrical supply to the motor to compensate for the increase in load.

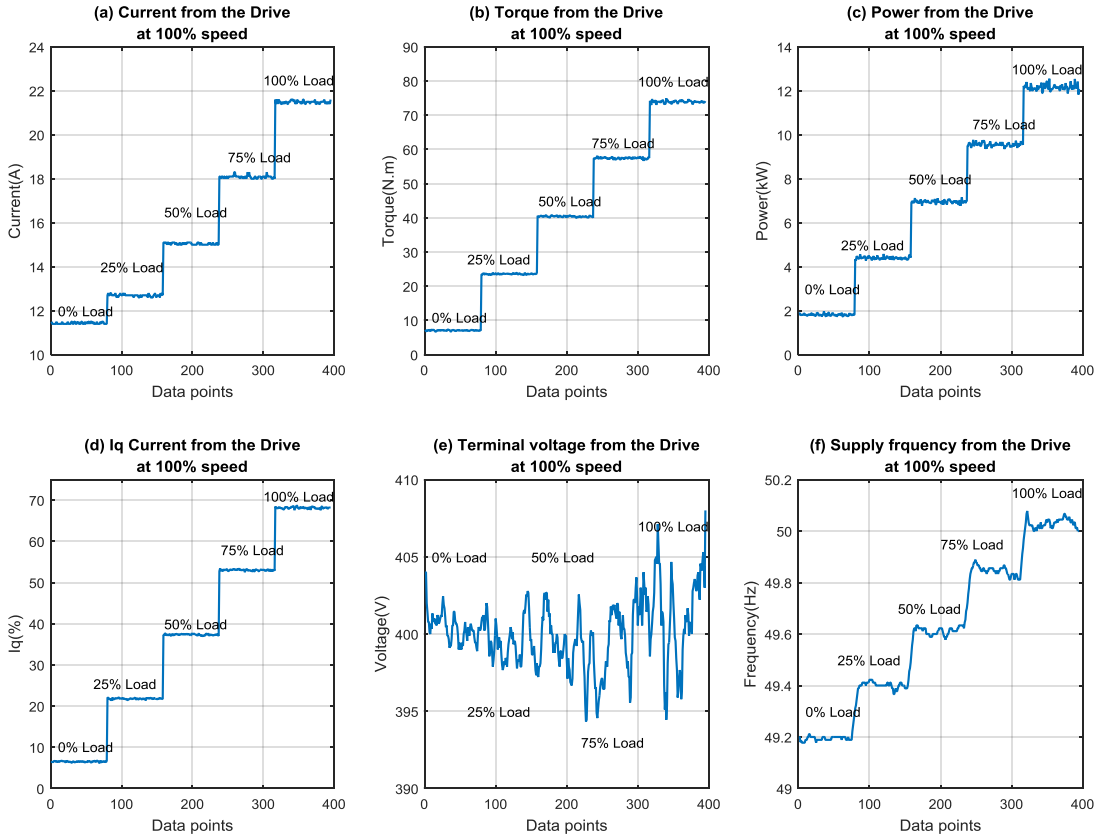

Figure 7.11 Control parameters under sensorless control mode

7.3 Fault Detection Based on Power Residuals

To investigate the performance of the scheme developed in Chapter 6, changes of residuals are examined under different load and fault conditions. Figure 7.13 shows the residuals under different misalignment severities and operating conditions. Residuals show good performance in that the faulty conditions show higher residual values corresponding to fault severity and values higher than the pre-set threshold. It is also clear that the load changes do not significantly affect the residual amplitudes. Therefore, the residual indicators provide reliable detection results of the presence and the severity of the tested faults.

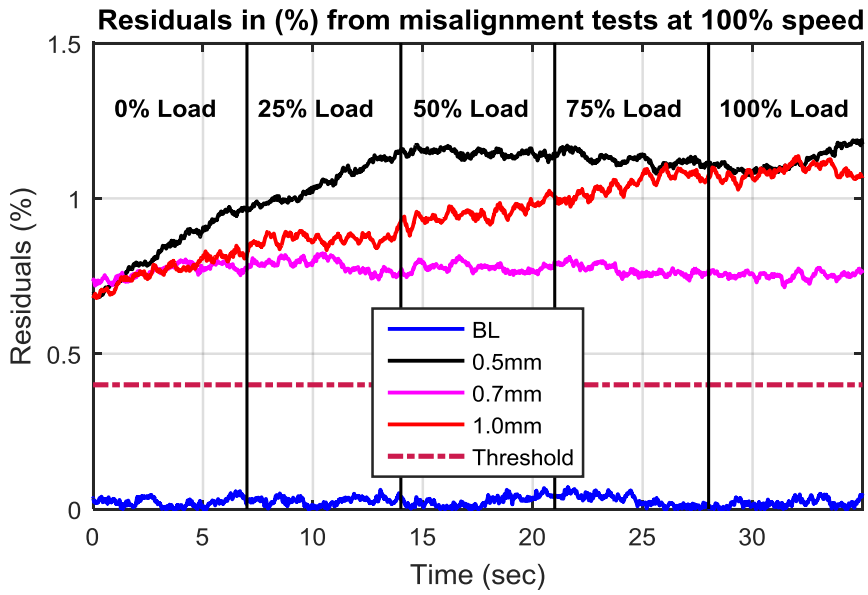

Figure 7.12 Residuals from misalignment tests under different operating conditions

7.4 Response under Different Fault Conditions

7.4.1 Vibration Responses

Different degrees of misalignment have been applied, as explained in chapter 4, on the GB1 by placing different standard pre-cut shims under the gearbox. The vibration signals from GB1 and GB2 have been measured and processed to obtain the vibration spectrum for analysis. Figure 7.14 shows the vibration signals from GB1 and GB2 under different misalignment degrees of severities and loads. It can be seen that the vibration signals have been increasing consistently with the degrees of the misalignment, as in Figure 7.14 (a). Noticeably, the 0.3mm case indicates very small changes compared to the other two fault cases. The misalignment tolerance of the rig couplings is 0.4mm and hence it was able to absorb some vibration resulting from the misalignment. Additionally, no significant changes in the vibration signals can be seen in the GB2, as shown in Figure 7.14 (b), despite the minimal increase in the vibration signals for the 0.5mm and 0.7mm fault cases indicating that vibration signals have been transferred to the GB2. However, the 1.0mm misalignment case exhibits rms vibration drop, which can be explained as a result of the nonlinear behaviour of the coupling. The

nonlinear characteristic of the rubber spider has influenced the response of the vibration signal. Rubber spider couplings can have high torsional compliance for fractional loading. As a result of this property, the coupling appears to be compensating for the misalignment, particularly as the misalignment increases frictional forces and hence increases the nonlinearity of the couplings.

Also as clear from Figure 7.14, the results from the three tests showed the same trend and similar values confirming the repeatability of the test rig. However for more reliable analysis, the results from the three testing runs are averaged for further analysis and discussion.

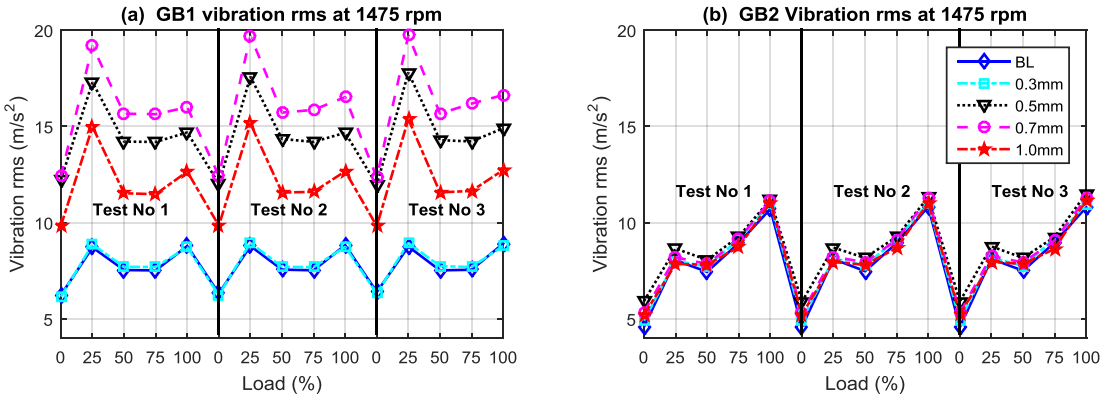

Figure 7.13 GB1 and GB2 vibration rms signals comparison

As indicated in [122], the type of couplings used is an important factor in specifying the feature frequency component. In this test rig the couplings are three jaw. Hence it is worth examining the third harmonics of the shaft frequencies, f_{r1}, f_{r2} and f_{r3}. Figure 7.15 shows the vibration signals from GB1 under different misalignment severities and loads. It can be seen that the vibration amplitudes at 3X of f_{r1} and of f_{r3} increase consistently with the degree of misalignment. Particularly, the 0.5mm, 0.7mm and 0.1mm fault cases show higher amplitudes than that of the baseline. However, due to the fact that the 0.3mm fault case is lower than the maximum permissible misalignment of the coupling, it shows amplitudes close to those of the baseline. Therefore, these results can operate as a benchmark for the electrical power signals analysis and diagnosis.

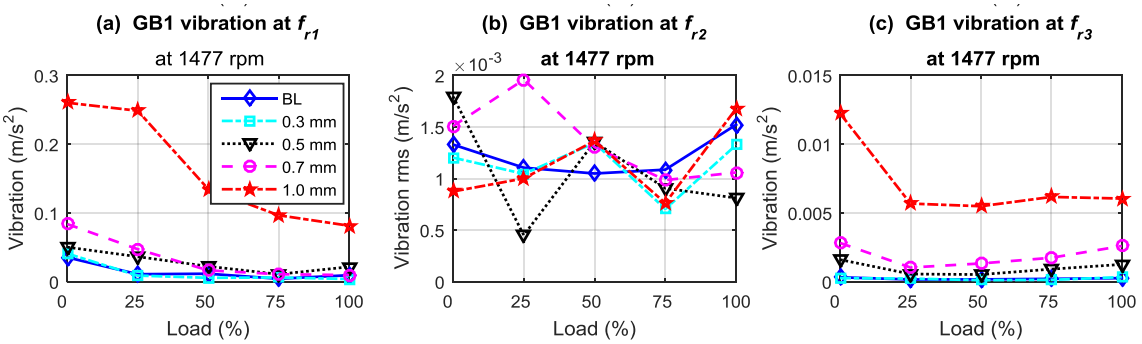

Figure 7.14 Vibration signals comparison at 3X of f_{r1}, f_{r2} and f_{r3} under different severities

7.4.2 Response under Open Loop Mode

To understand the general characteristics of the current signal response under a fault case, Figure 7.16 shows a comparison between current spectrum of 1.0 mm misalignment and the baseline under 50% and 100% load. It can be seen that the components at f_{r3} are distinctive and the 3X components are higher than the first and the second, showing the basic feature of the three jaw coupling. Moreover, amplitude at f_{r3} sidebands increases with the degree of misalignment, which is consistent with fault severities. However, the amplitude decreases with load due to the effect of the nonlinear behaviour of the coupling.

Components at 3X f_{r1} indicate changes with the misalignment but the amplitudes are not clearly identifiable due to high background noise from the VSD. The component at 1x of f_{r2} shows slight change with fault severity as this is the internal shaft in the gearbox.

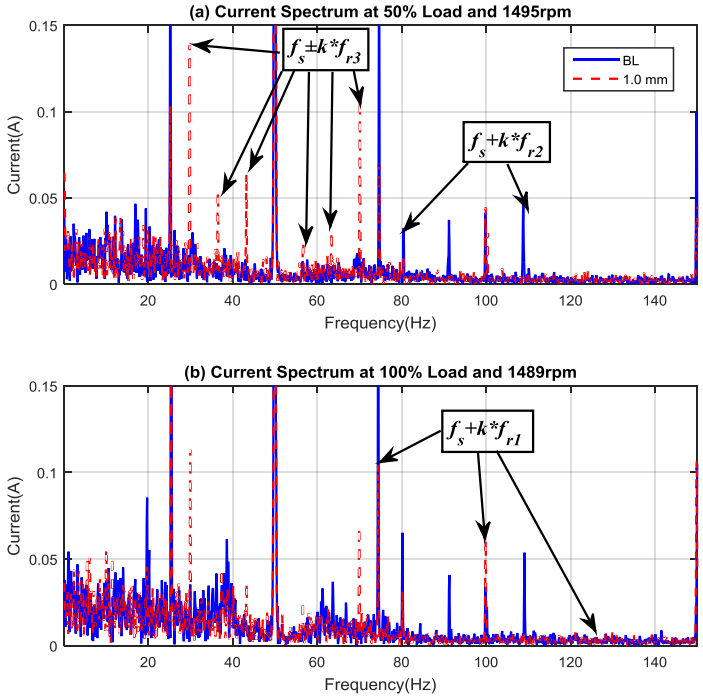

Figure 7.15 Current spectra of 1.00mm and baseline comparison under different loads

To diagnose the fault severity, sideband components at the 3X f_{r1} and 3X f_{r3} are extracted and presented against loads in Figure 7.17. Figure 7.17 (a) shows the misalignment on the first shaft is just detectable by the current spectrum at the high severity of 1.00mm. On the other hand, the misalignment on the third shaft can be detected and quantified starting from 0.7mm, as shown in Figure 7.17 (b). The reason for higher sensitivity to the third shaft is that it undertakes a torsional load 3.6 times of the first shaft.

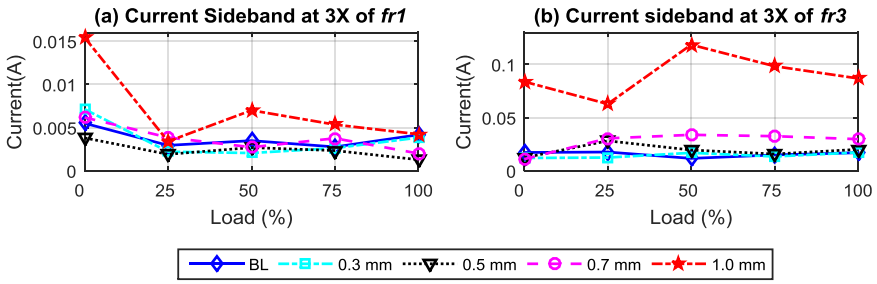

Figure 7.16 Current at 3X of $f_{r1}$and f_{r3} comparison under different fault and load conditions

To study the response of the voltage signal under different misalignment severities, the sideband components of the voltage at the 3X f_{r1} and 3X f_{r3} are calculated and presented

with loads in Figure 8.18. Figure 7.18 (a) shows that the first shaft is changing but not consistent with the misalignment. The third shaft shows the same behaviours as that of the current signal, as shown in Figure 7.18 (b).

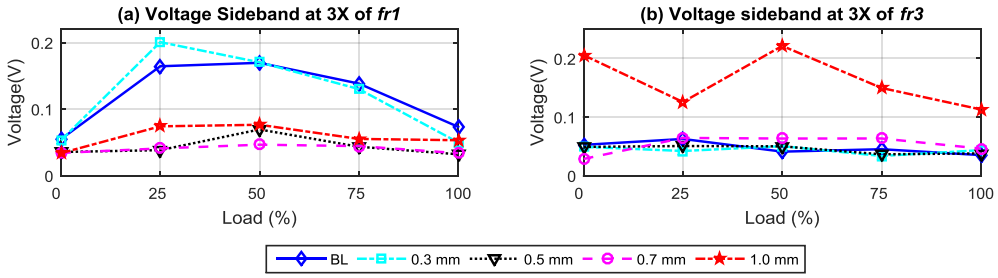

Figure 7.17 Voltage at 3X of $f_{r1}$and f_{r3} comparison under different fault and load conditions

Indicated earlier in Chapter 3 the spectrum of the power contains additional components contrary to that of current and voltage spectra. These are sidebands across the double supply frequency $2f_s \pm kf_r$ in addition to the shaft frequencies kf_r and their sidebands across the supply frequency components $f_s \pm kf_r$. In this case as the above analysis showed that f_{r3} is more sensitive to the shaft misalignment, its frequency component and sidebands are extracted from the spectra of the power, i.e. $3f_{r3}$, $f_s \pm 3f_{r3}$ and $2f_s \pm 3f_{r3}$, as represented in Figure 7.19.

Figure 7.19 (a) shows the misalignment is detected by the $3f_{r3}$ starting from the 0.5mm cases. However it fails to detect the 0.5mm and 0.7mm fault cases when the system is unloaded. Meanwhile, poorer power performance is noticeable at $f_s \pm 3f_{r3}$ where indistinguishable amplitudes are exhibited as shown in Figure 7.19 (b). Nonetheless, the $2f_s \pm 3f_{r3}$ exhibits performance similar to that of the current signals at 3X of f_{r3}.

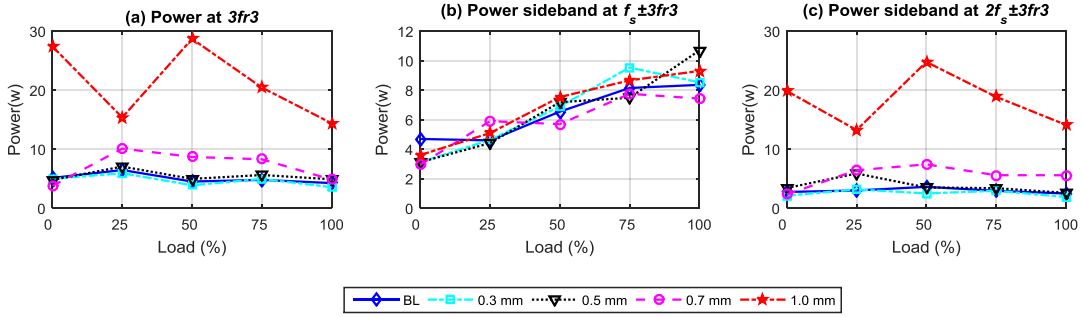

Figure 7.18 Power at $3f_{r3}$, $f_s \pm f_{r3}$ and $2f_s \pm 3f_{r3}$ comparison under different load conditions

To investigate the response of the open loop control mode to the different misalignment severities, the static data from the drive has been extracted and averaged. The main considered signals are motor current, torque current component Iq, field current component I_d and torque signals as shown in Figure 7.20. It shows that both the torque and torque current component I_q describes a gradual increase with misalignment degree of severity. As such they can be used for fault classification. Nevertheless, the field current component I_d has no clear change related to the fault severity. Noticeably even when the misalignment is as small as 0.3mm it can be clearly detected from both torque and I_q signals. This shows that the static data has better sensitivity than that of the dynamic data under the open loop operation.

In fact under open-loop mode, there is no speed feedback to the drive rather the drive provides a constant V/Hz ratio. In the case of the misalignment an additional frictional torque is induced. This friction causes additional static load onto the motor which in turn causes an increase in electromagnetic torque and more current in the motor. Consequently, static torque and current signals are most likely to be affected by such faults.

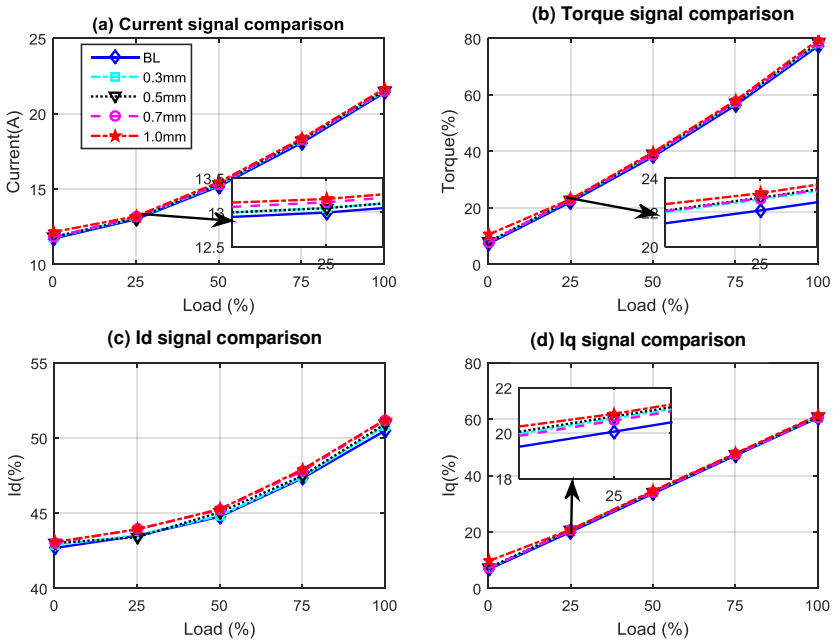

Figure 7.19 Static data comparison under different load conditions

7.4.3 Response under Sensorless Mode

In the sensorless control mode, the drive adjusts the motor supply parameters based on the motor speed estimation. When a fault occurs the motor electrical and mechanical parameters will also change. The drive will consequently alter the supply fed to the motor to maintain the speed stable at the reference. However, this control process generates more noise from the IGBs on the PWM, meaning that sideband frequency components of electrical power signals are not easily observed. As depicted in Figure 7.21 (a), the current amplitudes at rotor frequency f_{r1} sidebands do not show any clear changes correlated with the fault severities. On the other hand, the components at 3X of f_{r3} show identifiable changes at 1.0 mm, as detailed in Figure 7.21 (b). However, severities at and below the 0.7 mm are difficult to discriminate. Voltage amplitudes at these two particular frequency components have also showed similar changes to that of the current as depicted in Figure 7.21 (c and d).

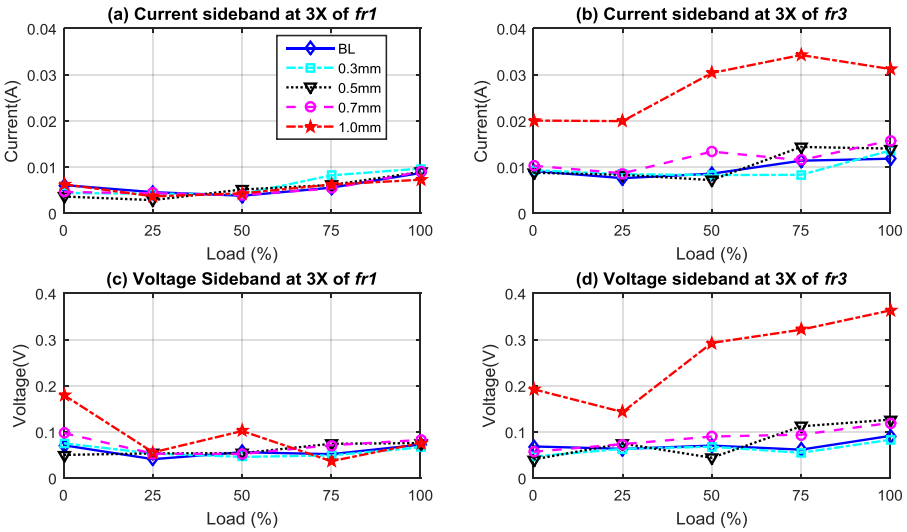

Figure 7.20 Current and voltage at $3Xf_{r1}$, and $3X\ f_{r3}$ under different operating conditions

The power at the characteristic frequencies related to the f_{r3} has also been extracted as illustrated in Figure 7.22. It shows that rotor frequency f_{r3} of the power spectrum and its sidebands show changes with the fault severities similar to that of the current and voltage signals. This shows that it is less possible to detect and diagnose the small

misalignment faults under the sensorless mode compared with that of the open loop mode.

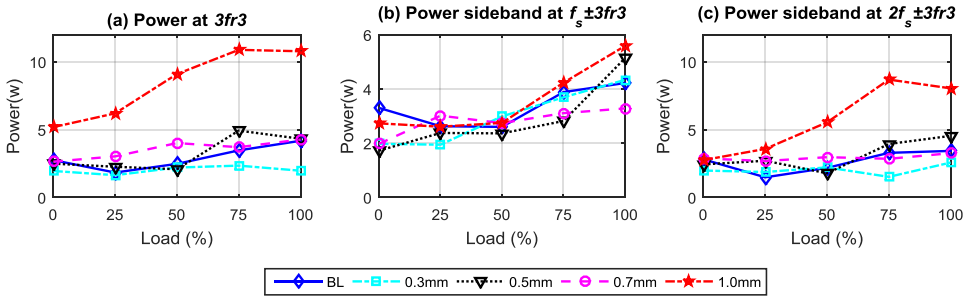

Figure 7.21 Power at f_{r3}, and corresponding sidebands under different operating conditions

To investigate the performance of the static data under the sensorless control mode, data from the drive was acquired at the same time as the dynamic data was collected under the sensorless operation. Figure 7.23 shows the system variables under different degrees of severity and loads. It shows that current, Iq components and torque signals vary with the fault severity. This is due to the fact that the motor requires more torque to recover from the disturbances ensuing from the misalignment. However, the 0.3 is not detectable as it is within the permissible misalignment limits of couplings. This shows that misalignment has induced a static load in addition to the dynamic oscillations. Conversely, I_d is changing, but not however in correlation with the fault severity. In order to maintain the speed at the desired value the drive feeds more current compensating for any disturbances due to misalignment. Therefore most torque related signals are changing with the fault severity. In the early stages of this research a new cost effective technique utilising data from sensorless VSDs for mechanical misalignment detection has been developed. Polynomial models have been developed and trained for baseline conditions. In cases of abnormalities these generate residuals related to the fault severities, more details of which can be found in [121].

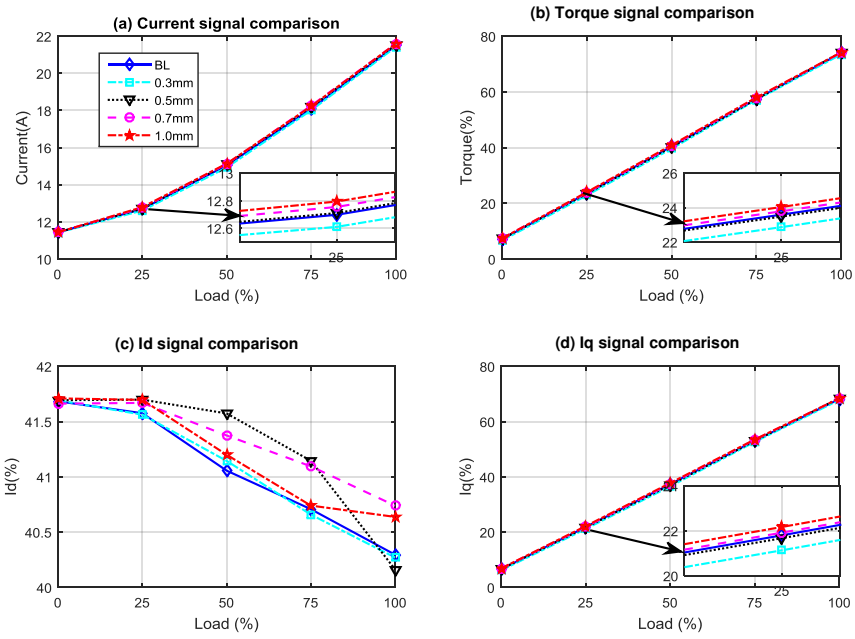

Figure 7.22 Static data response comparison under different operating conditions

To evaluate the performance of the static data components, the differences between different fault cases to the corresponding baseline data is calculated in percentage to the base values of each parameter. Figure 7.24 presents comparison results for the considered static components. As can be seen from the graphs, apart from the 0.3mm fault case, the differences between baseline and faulty signals are clear. These show that either of the variables can be used for both misalignment detection and diagnosis. Furthermore, the feedback torque signal produces the highest detection capability particularly when the fault severity is 0.7mm or higher. However, when the misalignment is as small as 0.5 mm the current signal gives better detection. Meanwhile I_q has obtained good detection capability for 0.7mm and 1.0 mm. Notably, I_d has shown the poorest detection ability over the different test situations. This is understandable as under the normal operation conditions I_d is independent of load variation and is rather a speed independent variable. Thus it is not highly influenced by load disturbances due to misalignments.

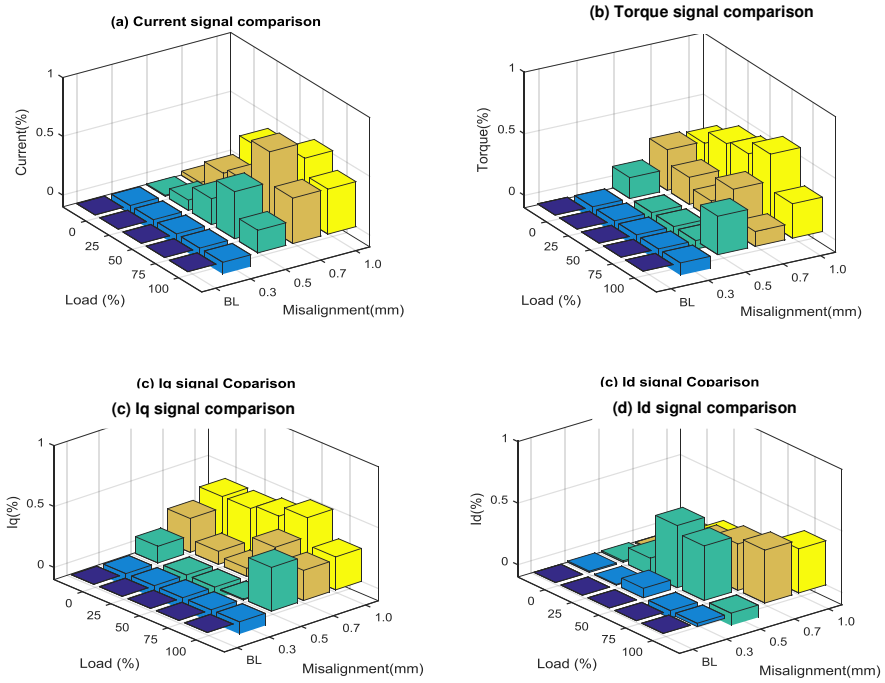

Figure 7.23 Static data performance comparison under different operating conditions

7.5 Conclusions from Misalignment Tests

Static data from sensorless VSDs can be used effectively in detection of shaft misalignment. The strategy developed in this research is novel. That is static data from the drive under both the open and sensorless operations is effectively used to detect and diagnose different levels of misalignments. Moreover comparison between open loop and sensorless control modes shows that features normally used for misalignment fault detection can still be used for systems under the sensorless control mode. Additional conclusions from the misalignment test results can been drawn as follows:

- ✓ Shaft misalignment creates additional frictions and hence static loads to the systems which need more electrical power to overcome it.
- ✓ Particularly the torque related variables such as i_q current and torque signals show consistent changes correlated with the degree of severities.
- ✓ Static data based misalignment detection outperforms that of the dynamic data and indicates performances close to that of conventional vibration analysis.

Chapter 8
Diagnosis of Lubrication Problems

In this chapter, the results from three common oil problems in industrial gear transmission systems are presented. Namely, water contaminated oil, oil with different viscosities and oil leakage represented by different oil levels. In each case, the vibration signals are firstly analysed in preparation for comparison and benchmarking, followed by an investigation of the static data from the drive to detect any changes consistent with the faults applied. Finally, the dynamic signals of current, voltage and power are investigated based on the feature frequencies found in their spectra.

8.1 Introduction

In the following sections results are obtained from tests performed to investigate the potential of detecting gearbox oil degradation, namely water in oil contamination, oil with different viscosities and different oil levels, in transmission systems driven with sensorless variable speed.

8.2 The Response under Different Fault Conditions

8.2.1 Water in Oil Contamination

8.2.1.1 Fault Detection Based on Residuals

To examine the performance of the power residual and their responses to water contaminated oil, signals are treated as explained in Chapter 6 and presented in Figure 8.1 which shows the results from water in oil tests under different operating conditions. Residuals show good performance at 50% speed as shown in Figure 8.1 (a). That is the faulty conditions show higher residual values corresponding to fault severity which are also higher than the pre-set threshold under all tested loads. Residuals at 75% speed also indicate high performance as shown in Figure 8.1 (b) apart from the 0% load where some cases revealed values lower than the threshold. However these values increased over time and achieved above the threshold value. For the 100% speed residuals exhibit

better performance in that they separate the fault cases from the threshold. However, the 4kppm case has lower values than that of the threshold and at this particular speed a fault alarm may not raise. This particular case however is under the 1% of water content allowed. Therefore, the residual indicators give reliable detection results of the presence and the severity of the water contaminated oils.

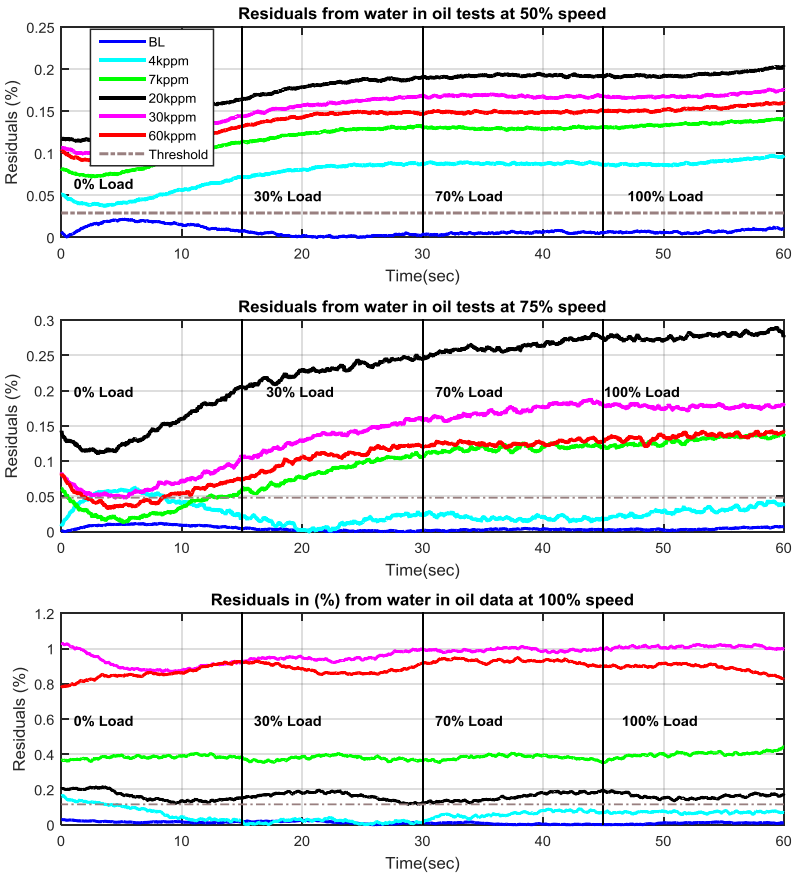

Figure 8.1 Power residuals values under different operating conditions

8.2.1.2 Effect of Water on Lube Viscosity

The oil viscosity was measured after each water content test and taken as a reference for lubrication deterioration. As shown in Figure 8.2, the viscosity values are presented at 30°C, 35°C, 40°C, 45°C, 50°C and 55°C. This is close to the operating temperature range measured during tests. Viscosity shows a slight increase from that of base oil then a monotonic decrease with water. However, when water content is 20kppm, the viscosity systematically increases with water content, which is slightly different to the

result published in [129] and [128]. The effect of a very small amount of water is to decrease the viscosity, up to a certain level i.e. at around 20kppm where it starts to increase due to the interaction of the water droplets. Viscosity increases to be higher than the base oil when water content is about 30kppm. It should be noted that this confirms that the water content was added effectively according to the test design. Figure 8.2 also shows that temperature has a considerable influence on the viscosity in which the higher the temperature the lower the viscosity.

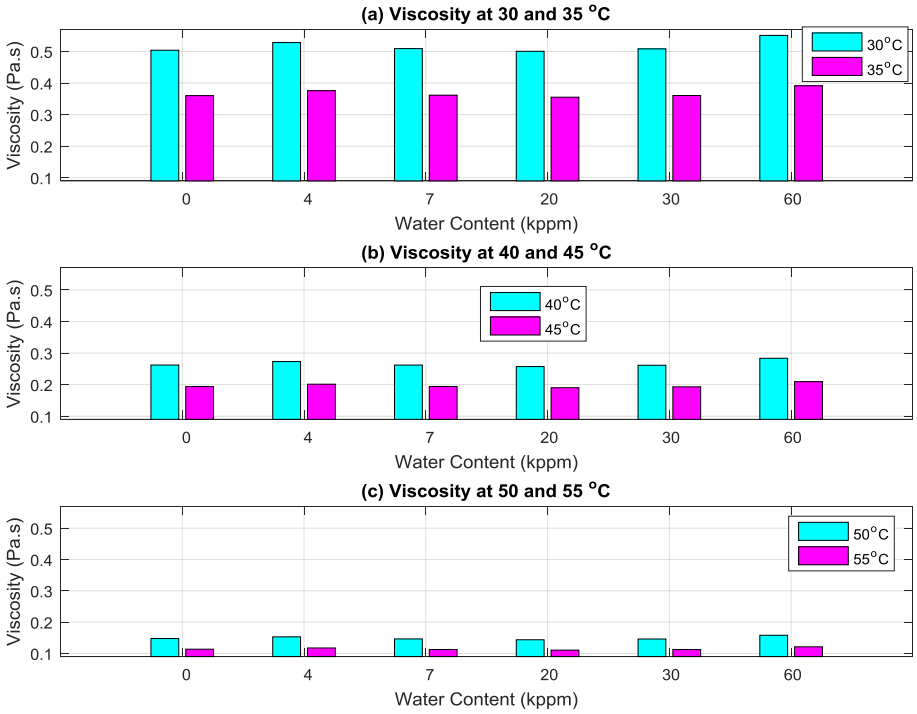

Figure 8.2 Viscosity with different water contents at different temperature values

8.2.1.3 Temperature Change during Tests

Figure 8.3 represents the average of the temperature during tests. It shows that oil temperature is slightly different from one case to another due to the fact that the operating temperature is partially dependent on a variety of other factors beyond control, e.g. ambient temperature. From the figure it can be seen that temperatures start increasing up to around 50-55ºC where they stabilise while all cases follow the same trend for the different cases and operating conditions. This will affect the system speed as shown in Figure 8.4, where the system speed stabilises in the third testing run.

Therefore, for reliability and accuracy only data from the last three tests will be considered. Data is averaged based on the signals from the last three tests and represented for investigation and analysis.

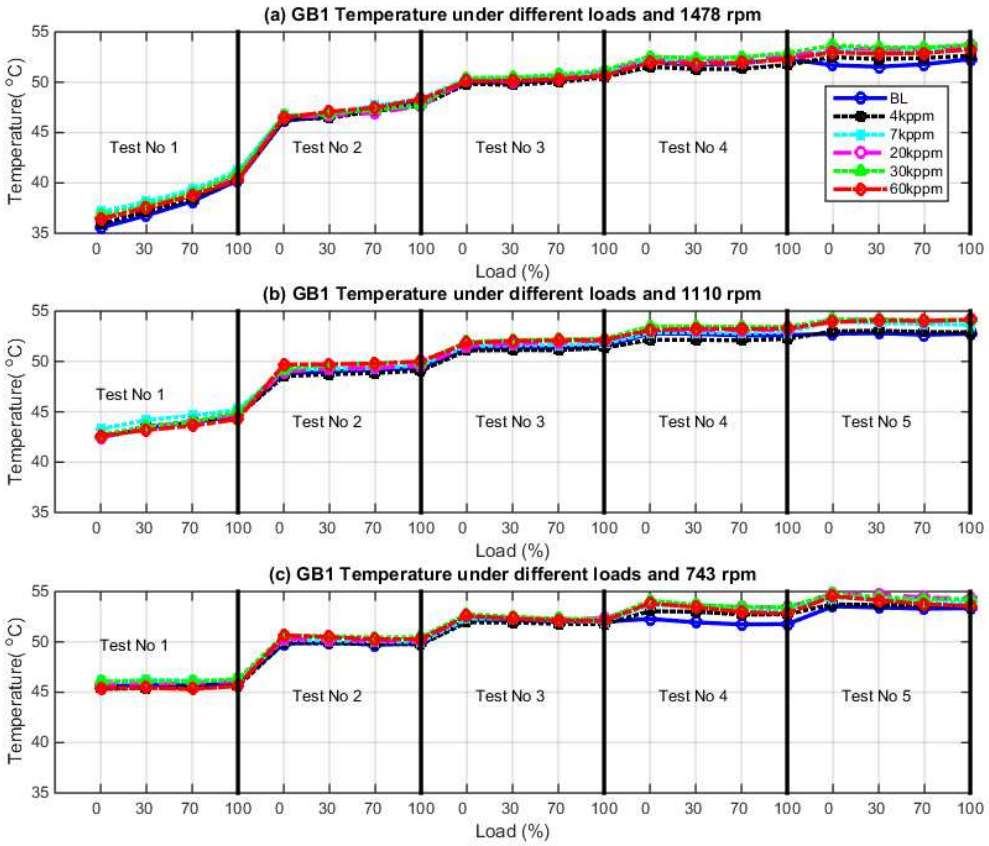

Figure 8.3 Temperature comparison during tests

Kept

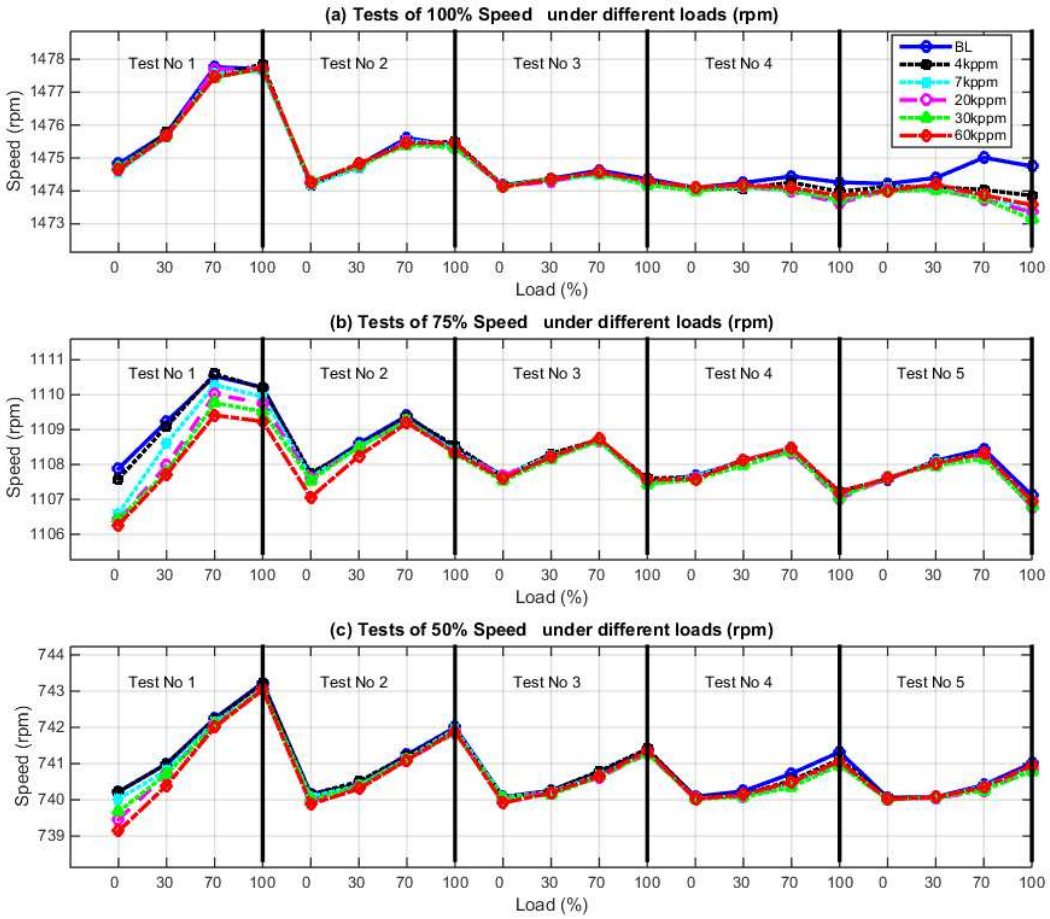

Figure 8.4 Speed behaviour under different operating conditions

8.2.1.4 Diagnosis using Vibration

The vibration signals are processed by time synchronised averaging (TSA) to suppress noise influences, and then the rms values of the resulting signals are calculated to show the dynamic effect of the water content. Figure 8.5 shows the averaged results of the last three test runs. It can be seen that the vibration levels for different water content are higher than that of the base line, as the water degrades the lubrication performances and causes more friction between the surfaces of meshing teeth. The vibration changes of GB1 are clearly significant and can be used to indicate the water contamination. However when the load and speed are at the maximum values as indicated in Figure 8.5(l), the 7, 20, 30 and 60kppm show lower vibration levels due to the fact that under this condition different forces are acting on each other, particularly churning and

splashing forces in addition to frictional forces and oil squeezing which are speed, load and temperature dependent forces.

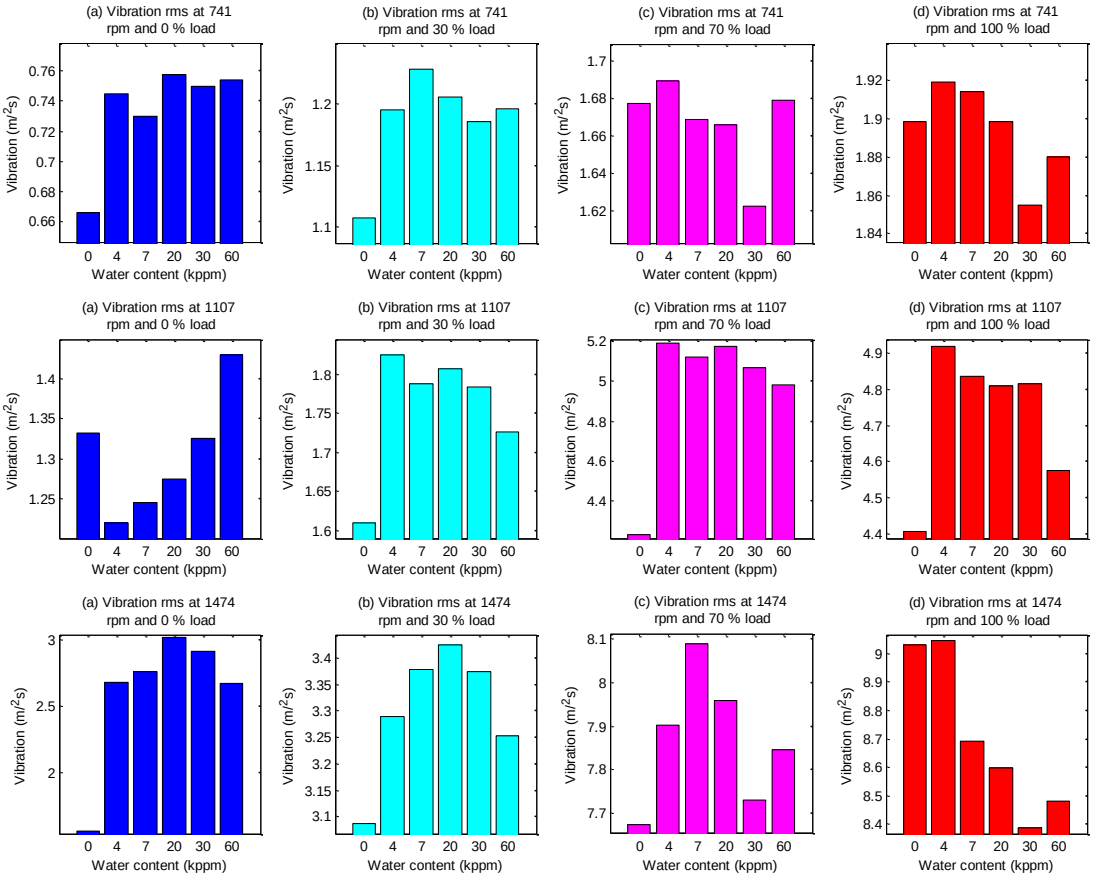

Figure 8.5 GB1 vibration (rms) under different operating conditions

To further understand the effect of water on the vibration, the subsequent order spectrum resulting from the TSA procedure have been analysed based on the second shaft frequency (f_{r2}). Figure 8.6 (a) presents amplitudes of vibration signal at the f_{m1} mesh frequencies of the GB1, which is more associated with gear dynamics. Amplitudes of vibration at f_{m1} at the high speed stage with low load indicate higher amplitudes compared with the baseline when the system is under the full load, see Figure 8.6 (d, h and l). Particularly under high loads the load dependent forces are the most dominant and the performance of the oil is important to separate surfaces. The water damages the oil structure and causes poorer lubrication causing additional vibration at this frequency component. Therefore, this frequency component shows

good performance with water contents at the full load, in that cases of water show higher peaks than that of the baseline test case.

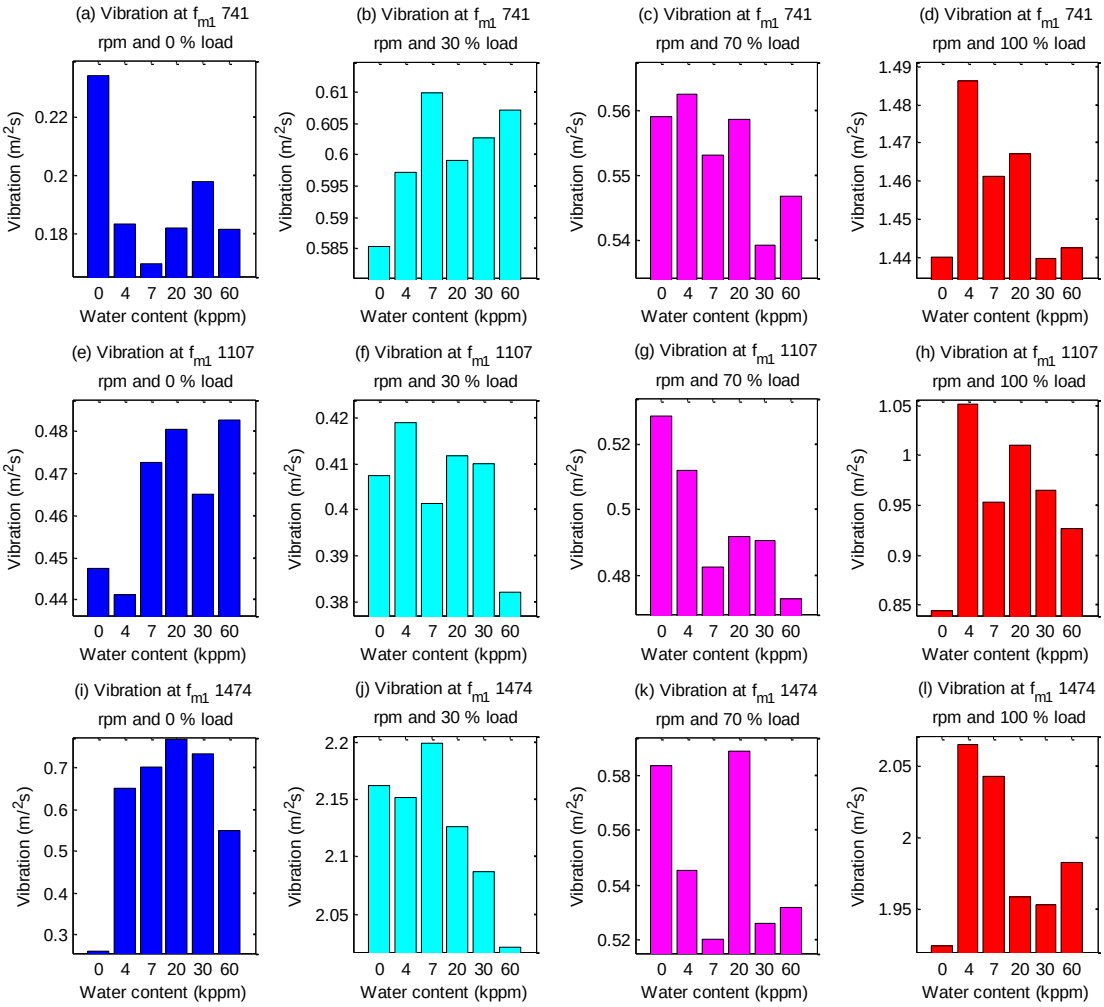

Figure 8.6 GB1 vibration at f_{m1} under different operating conditions

The vibration at the second mesh frequency which is the low speed stage with high load also shows higher amplitudes compared with the baseline and that of the higher speed stage and exhibits more beneficial behaviour than that of $f_{m1,}$ as shown in Figure 8.7. This indicates that the high load stage is significantly influenced by the change in lubrication. This is consistent with the theory that the support a hydrodynamic oil film receives is lessened due to the relative velocity between meshing tooth surfaces changes its direction at the pitch line. In addition, these vibration changes are consistent with

that in [15]. This shows that the second f_{m2} meshing frequency has superior performance than that of the first mesh frequency f_{m1} in detecting water content faults.

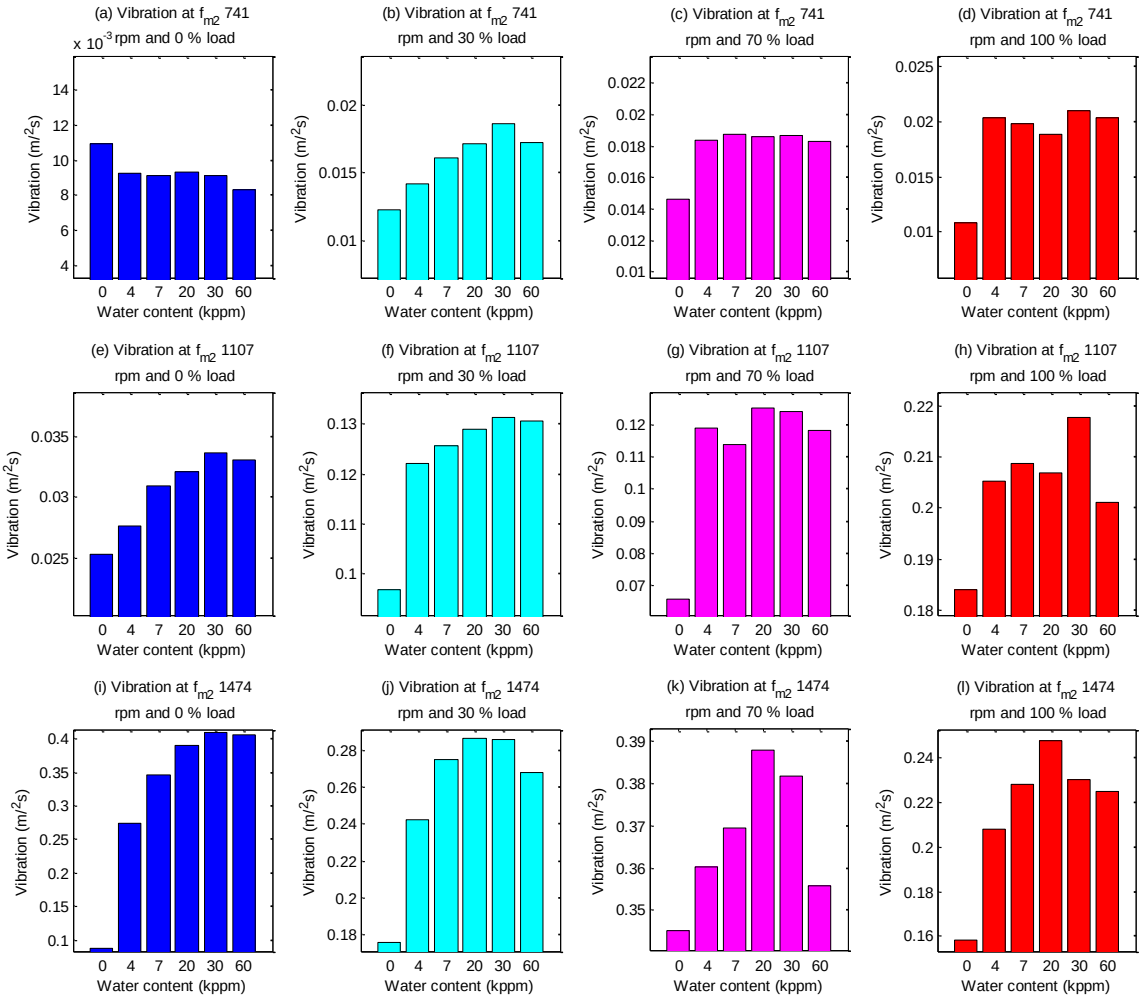

Figure 8.7 GB1 vibration at f_{m2} under different operating conditions

8.2.1.5 Diagnosis using Static Control Data

The sensorless VSD adjusts the motor supply parameters in order to maintain the system speed at the required value. Any changes in the demand or supply are recovered in stable conditions without a feedback encoder. When a problem in the gearbox lubrication occurs the stability conditions are changed. The drive's regulators will adjust the machine's supply to compensate for the effects of such oil degradation on system speed. Actions of the control system in the drive are further analysed in order to investigate the potential of detecting water in oil faults.

Figure 8.8 shows the average of the current signals between the lubricants with different water contents under different operating conditions. These results were obtained by averaging the results from the 3rd, 4th and 5th testing runs in (A). Notably current signals visibly change but are not consistent with water contents, instead appearing to change with the oil viscosity particularly under low load conditions, i.e. 0% load and at different applied speeds as shown in figure 8.8 (a and e). Meanwhile when the system is loaded current signals decrease with rising water contents. This behaviour indicates that the current rms signal may not be suitable for detecting water contamination.

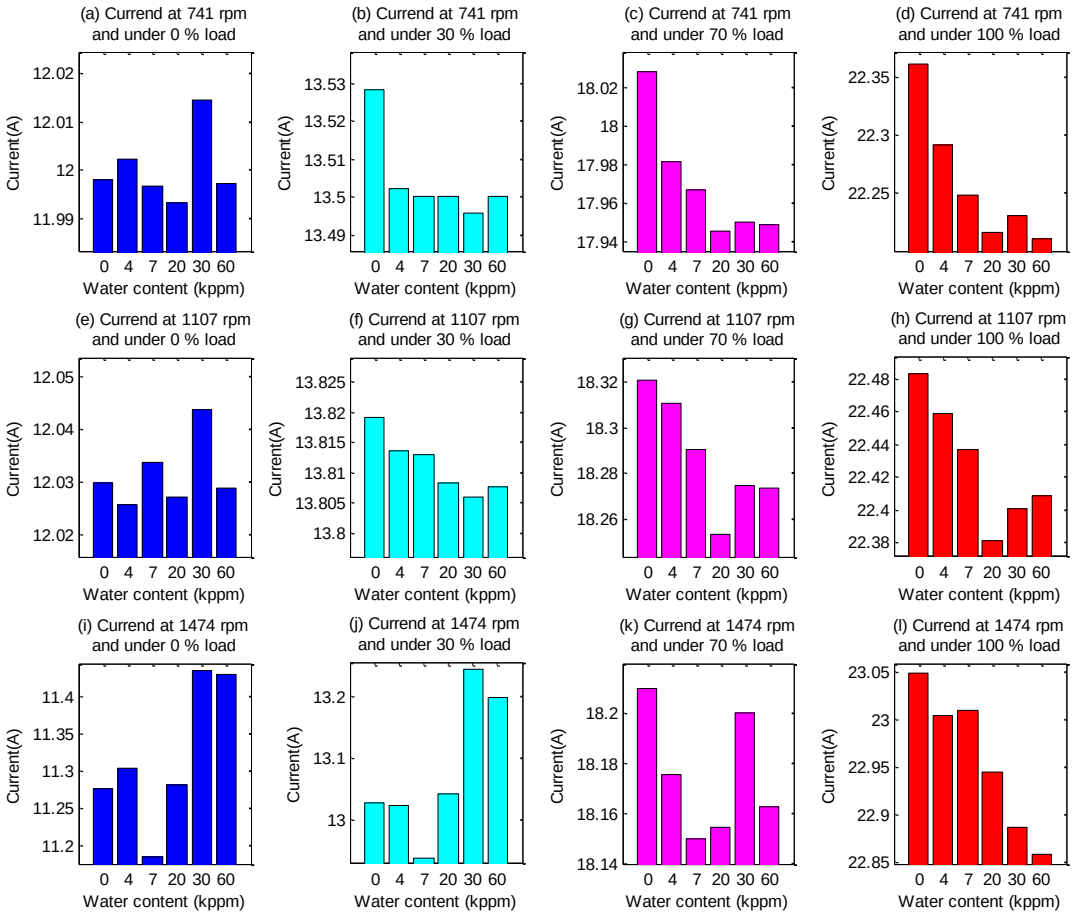

Figure 8.8 Current static data comparison

The terminal voltage, indicated in Figure 8.9, shows higher values in most fault circumstances compared with the baseline and exhibits superior behaviour than that of the current signal, reflecting the good performance of the base oil in reducing friction. When water was added to the oil at the levels of 4kppm and 7kppm the viscosity values

increased and lead to more churning losses, particularly at low and moderate loads. This means that more power is required to overcome these losses and maintain constant speed operation. Therefore the voltage shows higher values for these cases. The viscosity of the 20kppm test case has closer value to that of the base oil, and hence in most test conditions required similar voltage values. However, the 30kppm case shows the highest voltage values in most cases due to other effects such as increased oil squeezing and churning losses in addition to poorer lubrication and hence higher frictional forces. For the 60kppm case, the viscosity is much higher than the base oil and the effect of viscosity appears to be above that of oil squeezing, leading to lower voltage values than that of the 30kppm case.

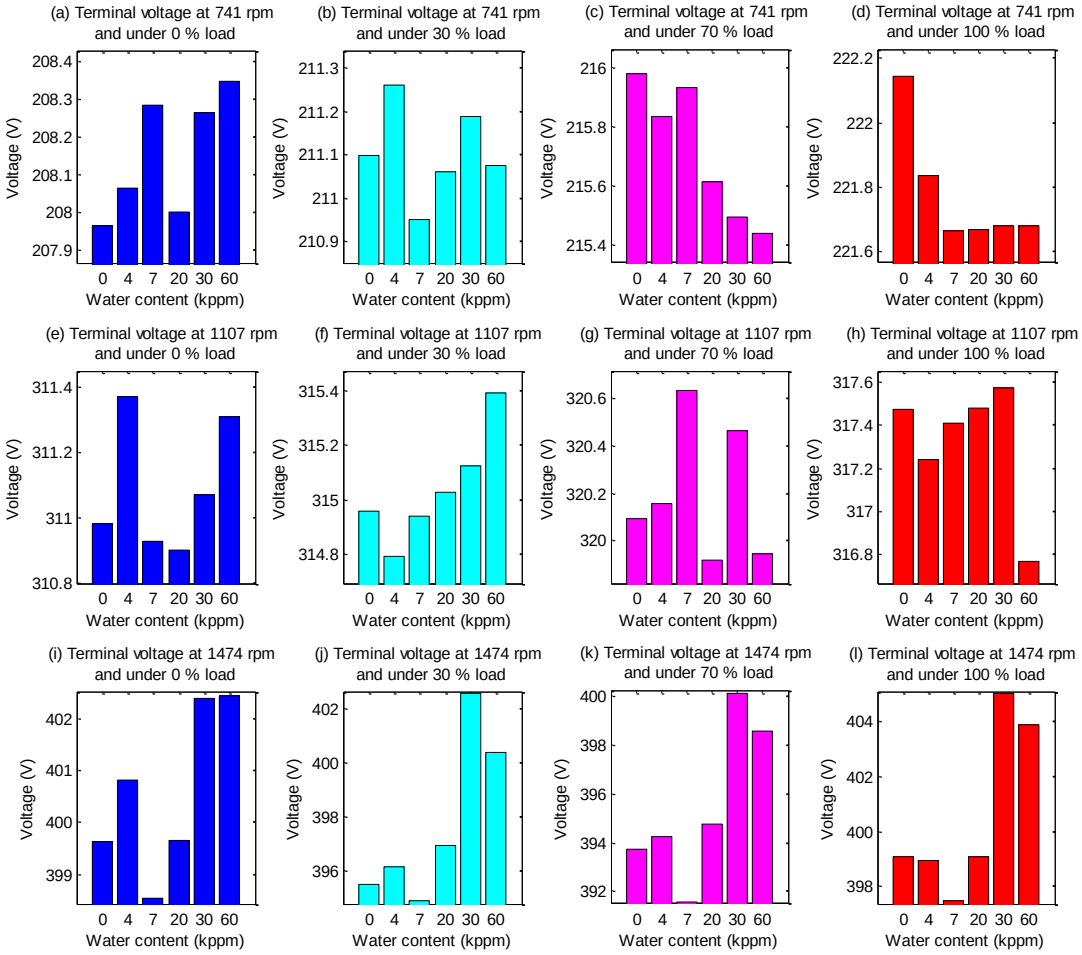

Figure 8.9 Terminal voltage static data comparison

The corresponding power consumption characteristics are greatly reflected by the voltage behaviours as indicated in Figure 8.10. In essence the power consumption shows better consistency with changes of the oil viscosity at 0% load, as depicted in Figure 8.10 (a, e, i), where the load dependent power losses in the gearbox are minimal, i.e. frictional losses, and the load independent power losses are maximal, i.e. churning and splashing losses. However for moderated speeds and loads, i.e. 50 and 75% speed and under 30 and 70% load the power consumption does not show consistent changes with viscosity. This can be explained due to the interference of both independent and dependent power losses under these particular operating conditions. Nonetheless, under moderate loads and speeds it seems that the load independent power losses are more dominant than load dependent losses.

While under full load operating conditions, as shown in Figure 8.10 (d, h and l), the power feature components show poor performance in detecting water contents, more greatly reflecting current behaviours than voltage. When the motor is at the rated speed and under the full load conditions, the maximum torque is provided. The VSD regulators adjust both voltage and current to keep providing sufficient electromagnetic torque to the system. This may include lowering the field current component to meet the additional power from frictional forces resulting from the fault. Therefore power consumption characteristics are reflected by the current signals under these conditions.

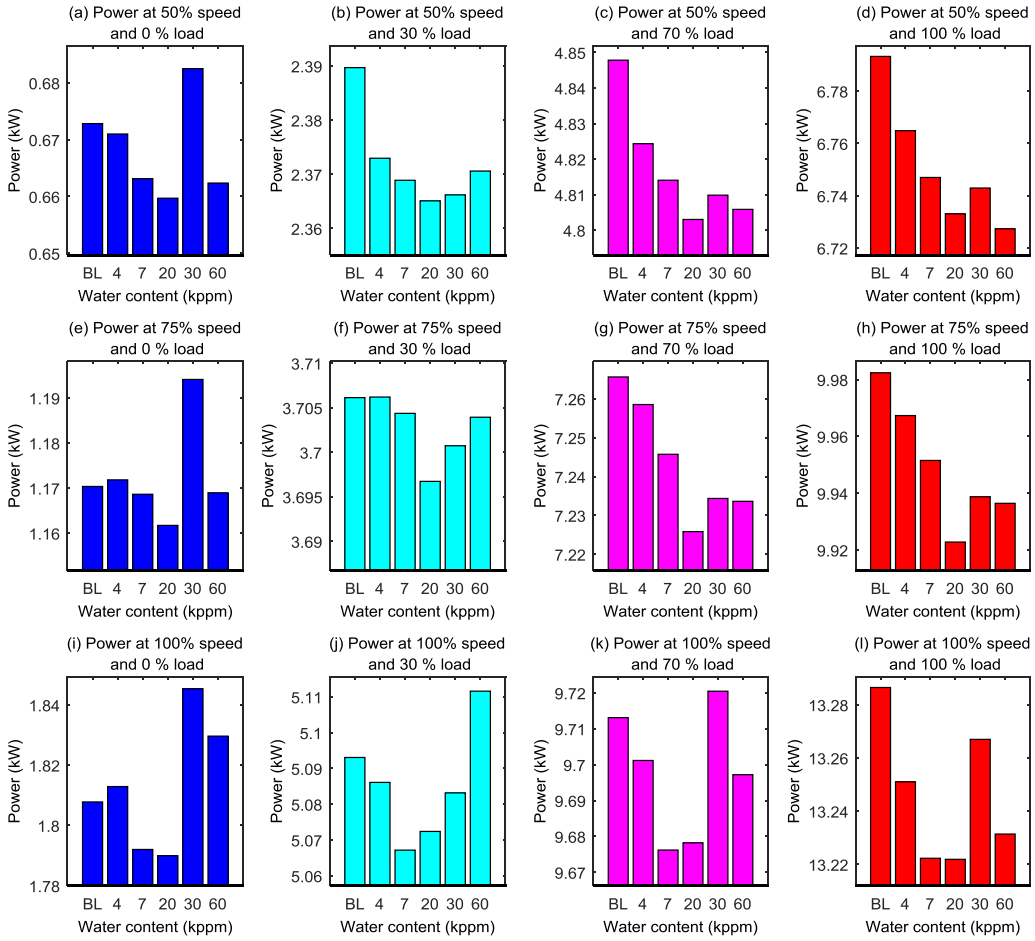

Figure 8.10 Power static data comparison

8.2.1.6 Diagnosis using Dynamic Data of Electrical Power

The dynamic data has been also investigated to analyse the influence of the oil contamination with water on the dynamic behaviour of the electrical power supply under the sensorless SD. The spectra of current, voltage and corresponding power signals are calculated and the amplitudes at frequency components related to the GB1, i.e. f_{r1}, f_{r2}, f_{r3} and corresponding harmonics and sidebands are examined. However, here only the electrical power components are presents. Other power supply parameters are presented in the Appendix III.

It is worth mentioning that both f_{r1} and f_{r3} are connected with couplings and they are influenced by them. However tests were performed without affecting the misalignment conditions, as explained earlier in chapter 4, and both f_{r1} and f_{r3} may indicate for the

health of the oil inside the gearbox as they are connected to the gears. In the presented results both amplitudes at the left and right sidebands are obtained and averaged for more reliable analysis and greater accuracy.

The dynamic components of power signals have also been investigated. Figure 8.11 represents the power at (f_s- f_{r1}). It exhibits good performance in detecting water contents. The power at this frequency component shows more visible changes with water contents than those from the current and voltage signals, Appendix III, indicating the potential of using it for diagnosis. It also indicates that at the lower speed as disclosed in Figure 8.11 (a), the separation between the different cases is clear, except for the 7 ppm and 30kppm cases. The 7kppm has the lowest viscosity and hence higher frictional forces and greater oscillations which increase more as a result of the presence of water. On the other hand the 30kppm has the highest viscosity and hence a thicker oil film meaning less frictional forces is generated. However the result remains over the base line as the performance of the 30kppm is much less than that of the base oil due to water.

Moreover the detection performance decreases as the system speed increases, although results show that the base oil has the lowest oscillations. This can be explained due to the fact that the higher the speed the more mass circulates with gears resulting in a greater level of oscillation and also more noise from oil churning and splashing.

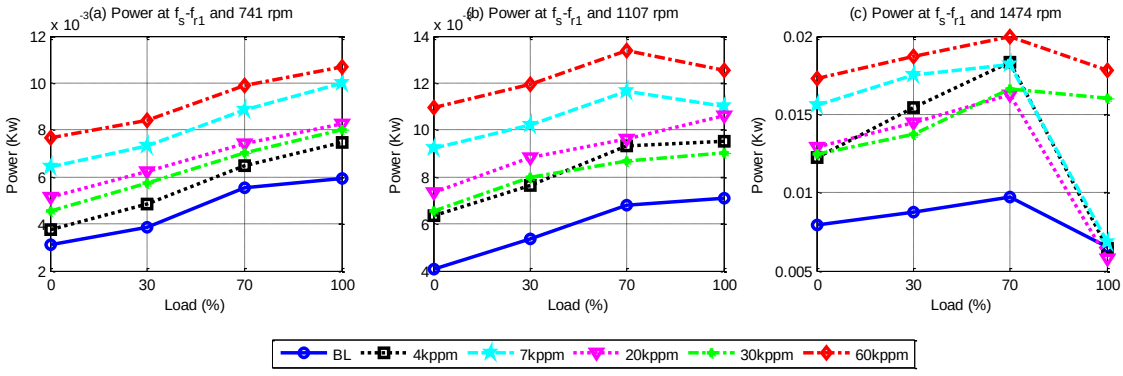

Figure 8.11 Power at (f_s- f_{r1}) frequency component comparison

8.2.2 Different Oil Viscosities

8.2.2.1 Viscosity Measurement Results

The viscosity of each type of oil was measured before tests. The measurement was conducted based on a rotary viscometer test method. Further details on the method used can be found in Appendix II. The results are given as an absolute dynamic viscosity in centipoise (cP). As represented in Figure 8.12, differences in viscosity values are clear between tested oils and become smaller as temperature increases.

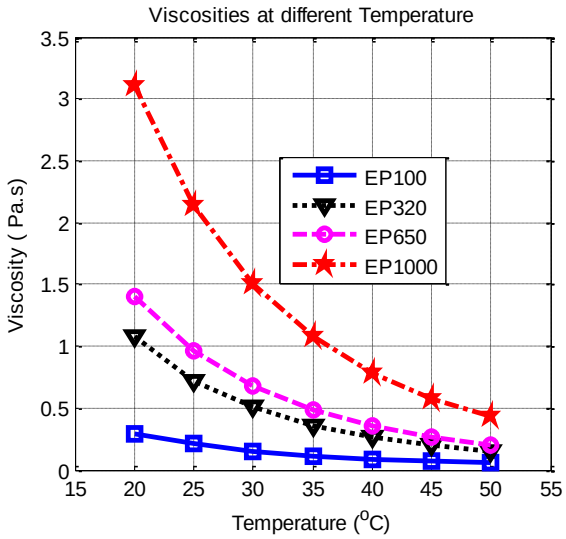

Figure 8.12 Viscosity values of tested oils at different temperatures

8.2.2.2 Influence of Temperature

To examine the influence of temperature when different oil viscosities are used, signals from the lubricant temperature sensors in GB1 and GB2 are processed to obtain their static feature values. Figure 8.13 shows temperature measurements against testing run numbers under different operating conditions. It can be seen that temperature in GB1 and GB2 increases gradually and reaches a stable state by the 3rd test when the system stabilised. This is consistent with results from the previous section, and also with tests performed in chapter 4.

Notably differences in temperature values between different lubricants in GB1 represented the viscosity values. This result agrees with theory in that higher viscosity

is held to increase the internal oil friction and hence increase the temperature. In addition, the similarity of temperature trends in GB2 shows that tests were conducted with good consistency between different tests, critically indicating that the churning loss is much more significant than the frictional loss. However, test number 5 shows a clear temperature drop for the EP 1000 oil test case when the speed is full, as clear in Figure 8.13 (a), indicating instability due either to lubricant inside the gear or ambient temperature effects.

Based on these observations, it can be concluded that measurements from the 3rd and 4th test runs have less transient effects and are more stable for examining the effect of lube viscosity accurately; hence for this test the results from the 3rd and 4th testing runs have been averaged and presented for analysis and discussion in this section.

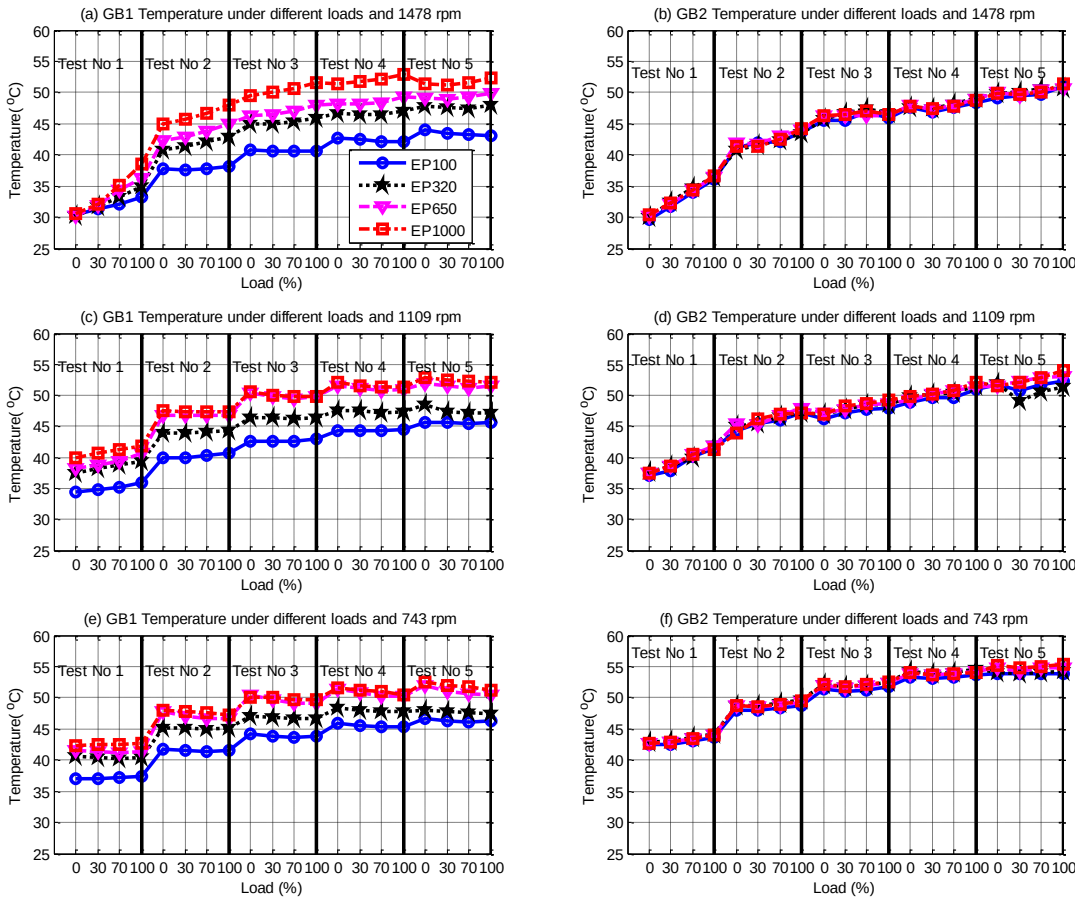

Figure 8.13 Temperature values under different operating conditions during tests

Speed values during tests have also been recorded and averaged as shown in Figure 8.14. It shows the same behaviours explained in chapter 4, as well as that of the water in oil tests, in that the system is stabilised from the 3rd testing runs. The figure also shows that there was no considerable effect made on the system speed by changing the viscosity. The drive forces the induction motor supply parameters to maintain speed stability at the reference.

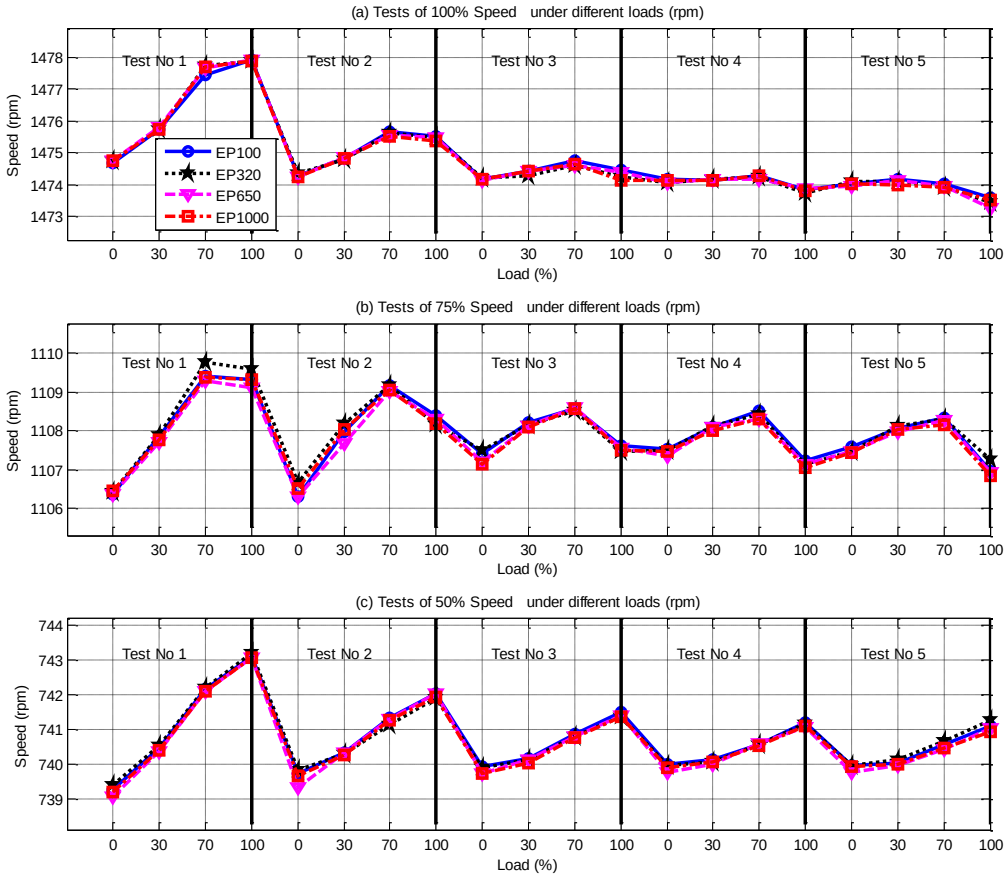

Figure 8.14 Speed comparison under different operating conditions

8.2.2.3 Fault Detection Based on Residuals

Power residuals have been examined for detecting oil with different viscosities. Figure 8.15 shows these residuals under different operating conditions. The residuals indicated superior performance to that of the water content cases. All different cases were detected and showed values higher than the threshold. Therefore an alarm signal would

be raised whenever the residual value exceeds the threshold and further analysis would be needed for diagnosing the fault.

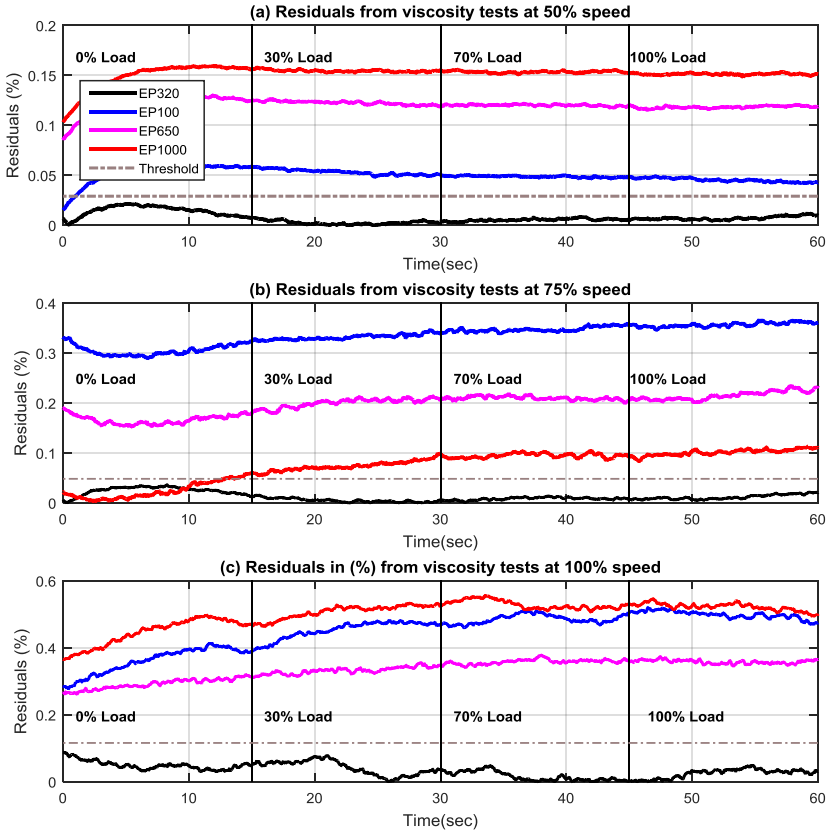

Figure 8.15 Power residuals values under different operating conditions

8.2.2.4 Diagnosis using Vibration

To study the effect of oil viscosity on the gearbox vibration, the rms values of the vibration signals from GB1 TSA are presented in Figure 8.16. As clear from Figure 8.20 vibration levels in GB1 are varied according to the viscosity tested. The lowest vibration is from the EP320, describing the performance of the design criteria used when selecting the viscosity. The EP100 which is the lowest oil viscosity shows the highest vibration levels under different speed and load conditions. This is due to the fact that lower oil viscosity leads to thinner film thickness and greater friction which causes higher vibration levels. However, detailed analysis of the vibration signals is needed to understand the oil viscosity change effects on the vibration signals for fault

detection and diagnosis. Therefore in the following the meshing frequency related features are extracted for more detailed analysis.

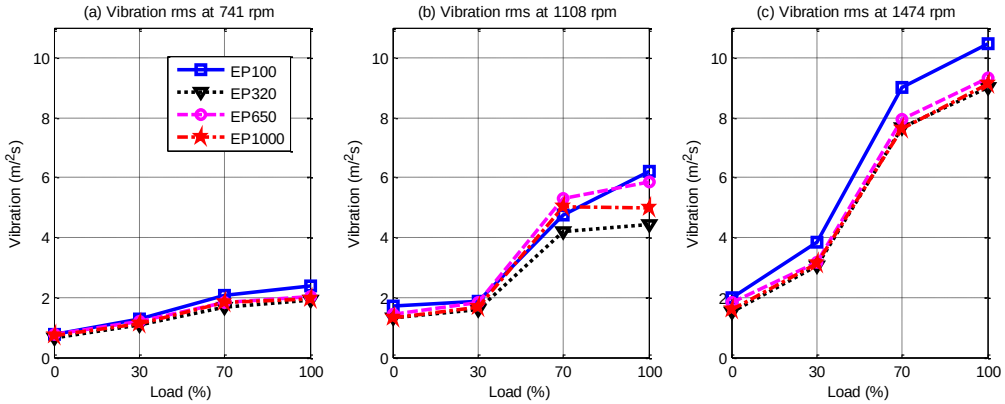

Figure 8.16 Vibration comparison under different operating conditions

The vibration at the f_{m1} is shown in Figure 8.17. Vibration at this frequency component changes with viscosity. Again, at this frequency component, EP320 has the lowest vibration in almost all cases showing better lubrication performance than other oils. Additionally, the EP 100 shows the highest vibration levels at most cases showing that the damping ratio has decreased with viscosity consistent with the findings in [126]. However, in general the trend of vibration change at this frequency cannot be easily correlated with viscosity, which agrees with the finding of [171]. The second meshing frequency component f_{m2} has also been also examined against different oil types. Figure 8.18 shows this frequency component.

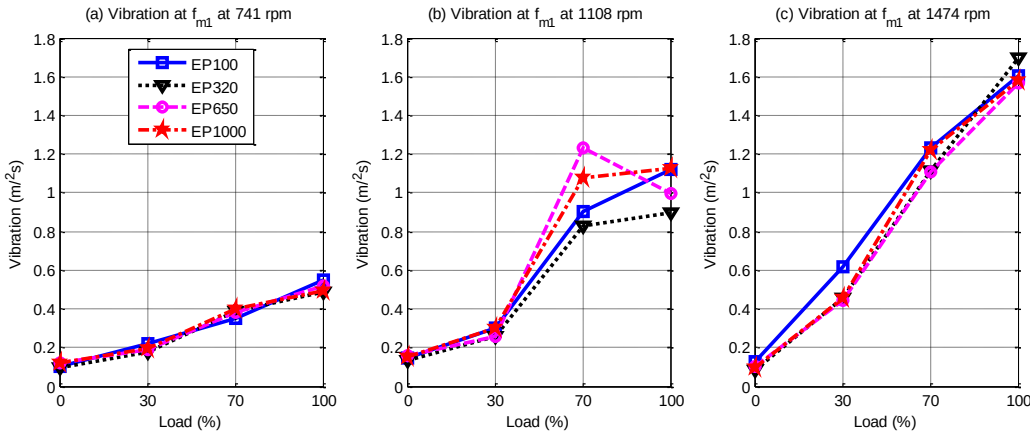

Figure 8.17 Vibration at f_{m1} comparison under different operating conditions

The f_{m2} frequency represents the lower frequency side and hence the higher load torque. Changes of vibration at this frequency cannot be correlated with the viscosity change. The EP320 shows lowest vibration at this frequency while the EP 100 indicates the highest. On the other hand the EP1000 directed the lowest vibration values in most cases indicating the damping effects of the viscosity.

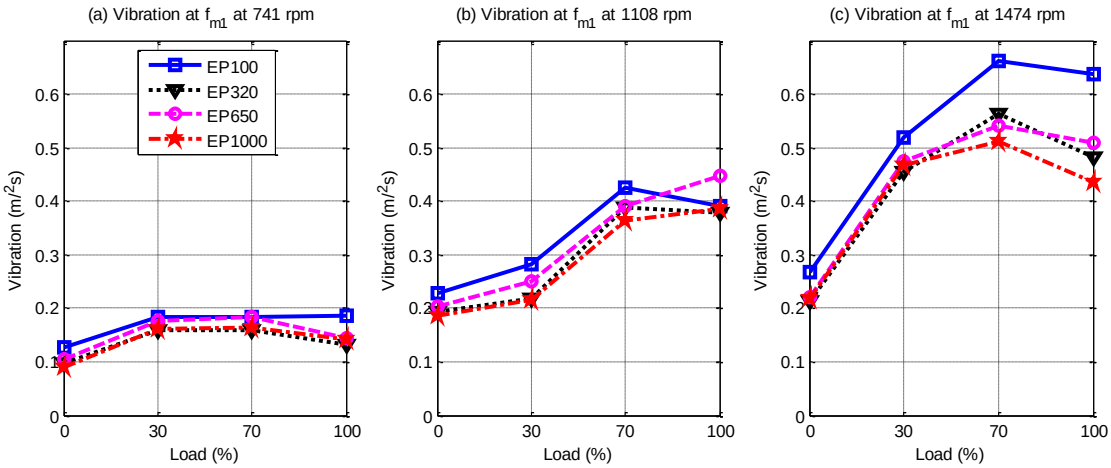

Figure 8.18 Vibration at f_{m2} comparison under different operating conditions

To conclude, the general vibration trend investigated using rms values comparison shows that the lower the viscosity the higher the vibration. However, the EP320 indicates the lowest vibration levels as it is the result of the design criteria. On balance however analysis of vibration signals shows that it is not simple to correlate vibration changes with viscosity changes.

8.2.2.5 Diagnosis using Static Control Data

To analyse the performance of the current signal based on the static data provided by the drive, the averaged results from the 3rd and 4th testing runs have been calculated. As depicted in Figure 8.19 (a-c), the current signal changes slightly due to the viscosity change. To obtain more detailed understanding, differences to the EP100 currents have been implemented and are illustrated in Figure 8.19 (d-f).

It shows that the lowest current is from the EP100 oil and the current values increase mostly with viscosity. This indicates that the churning losses are the dominant losses, in which an increase in oil viscosity leads the drive to provide more current to

compensate the losses from viscosity related power. Noticeably, under the full load and 100% full speed, the current signal from the EP650 oil falls. Despite the fact that changes in the current static data represent the differences in viscosity in some cases, particularly under low loads, it fails to indicate this relationship in most other cases, therefore it cannot be used for detecting and diagnosing oil viscosity changes.

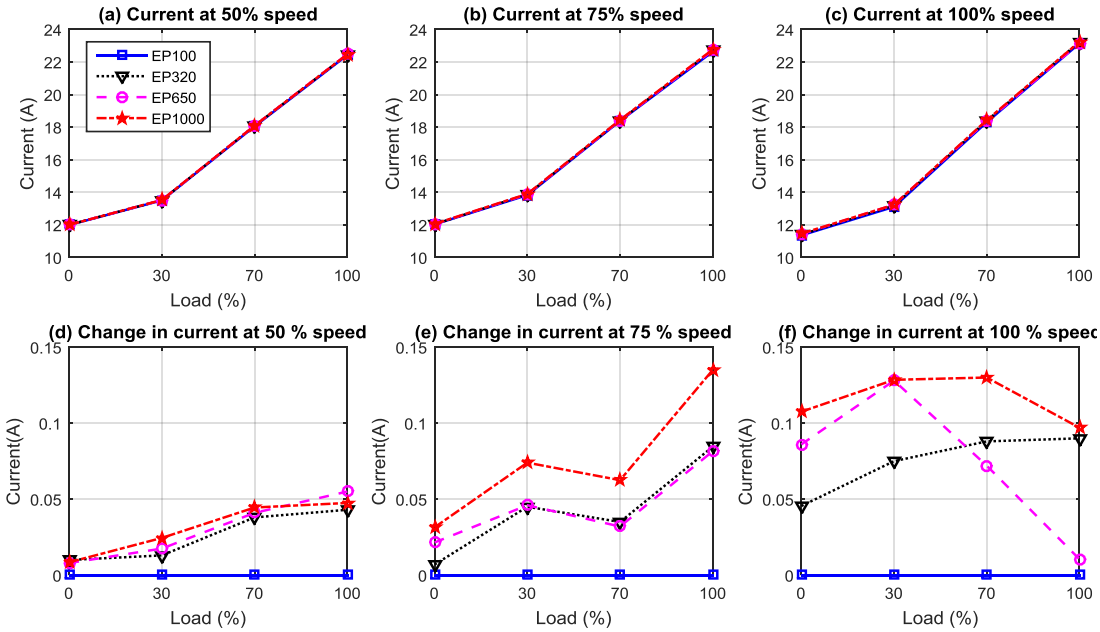

Figure 8.19 Current static data comparison

Figure 8.20 (a-c) shows the terminal voltage signals as obtained from the drive. The voltage signals show slight changes due to oil viscosity variation. Similar to the current signals, the variations between different oils tested have been made in relation to the EP100 oil as represented in Figure 8.20 (d-f).

This shows that terminal voltage static data exhibits superior performance to the current data, in that it reflects the power needs for maintaining the system speed. This is particularly clear when the system is at the 100% speed where the power losses due to churning are maximal. Additionally under the full load, where the frictional forces are at maximum the role of viscosity is important to form the oil film. However, voltage signals are influenced by the control system and failed to describe clearly the changes in the oil viscosity and hence cannot be used for viscosity change detection.

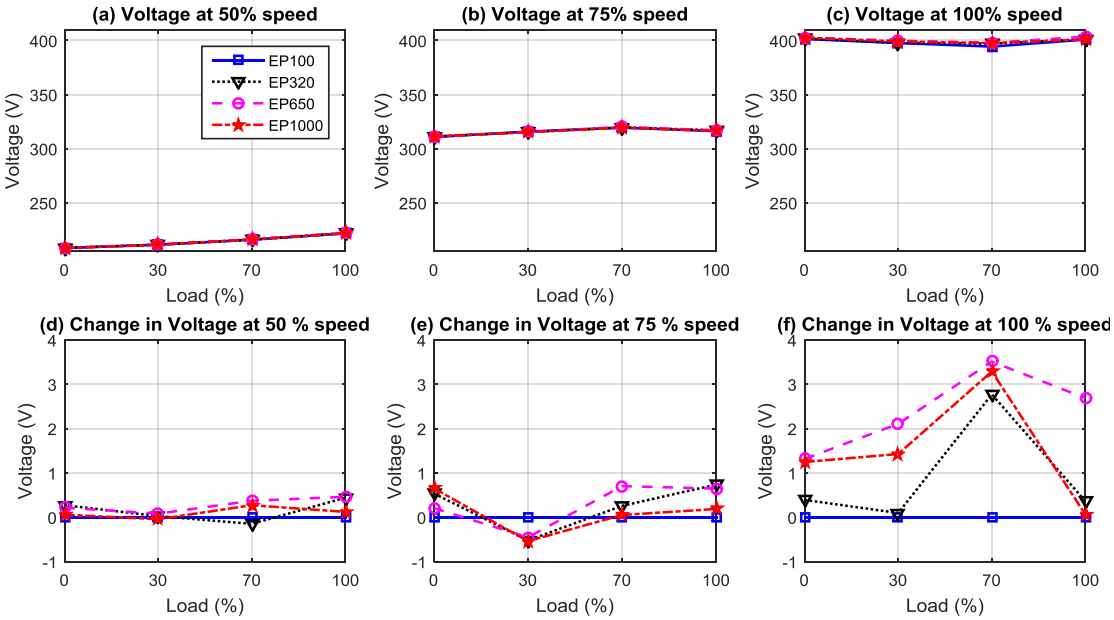

Figure 8.20 Terminal voltage static data comparison

The corresponding power consumption characteristics indicate improved performance in detecting viscosity changes, as shown in Figure 8.21. Figure 8.21 (a-c) represents the power static data from the drive while Figure 8.25 (d-f) presents the disparities between different cases to the EP100 oil.

Power consumption exhibits noticeable changes with viscosity indicating the potential of using this for diagnosis. As clear from Figure 8.21 (d-e), the motor speed has a significant effect, in which the higher the speed the more mass circulates with gears and hence more oscillations and increased power is required. The mass formed around rotating gears depends on the oil properties, particularly density and viscosity. The inertia of the rotating shaft also changes as the viscosity changes, resulting in changes in the power with viscosity.

Particularly under full speed operating conditions, as shown in Figure 8.21 (f), the static power feature showed good performance where the load related power losses are minimal and losses are mainly from viscosity related properties. The VSD regulators adjust both voltage and current to maintain provision of sufficient electromagnetic torque to the system compensating for these power losses. Therefore power

consumption characteristics are reflected by losses from oil viscosity under full speed conditions. On the other hand at lower speed the power signals are more influenced by the control actions and the load related power losses. Hence the power components showed poorer diagnosis performance than that when the system at the full speed.

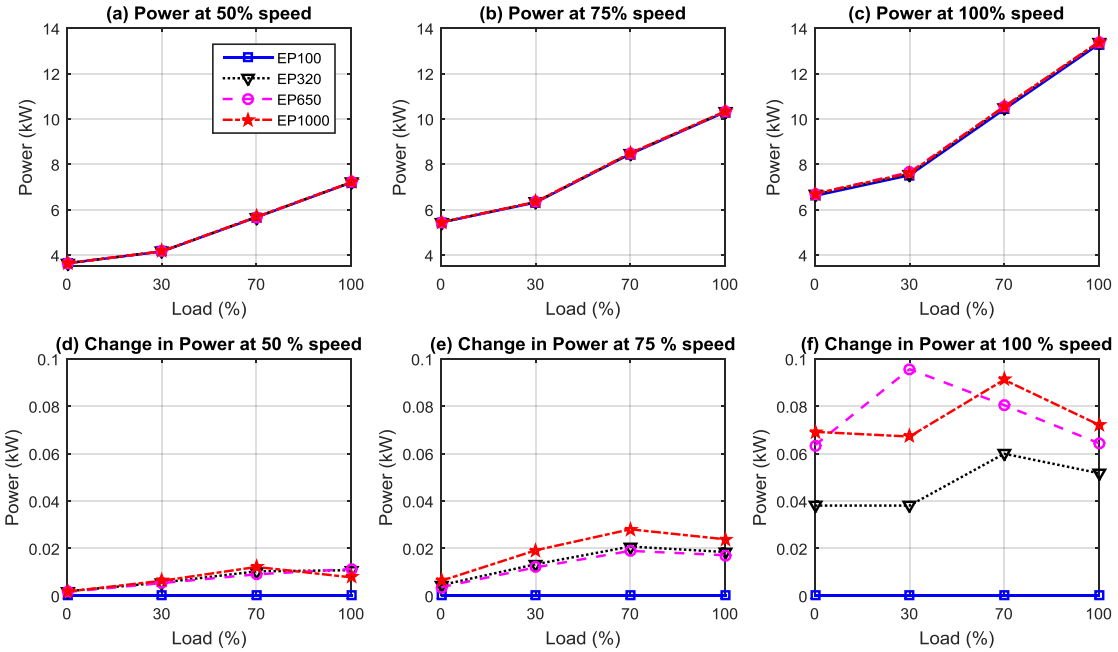

Figure 8.21 Power static data comparison

The static data of the electromagnetic torque has been also investigated. Figure 8.22 (a-c) shows the averaged electromagnetic torque as estimated from the drive under different operating conditions. Figure 8.22 (d-f) presents the differences in torque signals which is made to the torque from the EP100 oil testing runs.

The torque signals show superior performance to those of the static components of power signals. The torque signal changes with oil viscosity and represents the viscosity values, specifically at moderate speed, i.e. 75% speed. In fact at moderate speed the fluctuation is balanced between frictional forces and splashing disturbances. Also, when the speed is full the drive runs the motor in the field weakening mode where the torque is influenced by the lowering of the field current component and the behaviours of the voltage changes. On the other hand, at low speed the torque is more likely to oscillate depending on the speed estimation. It is well known that at low speeds most

speed estimators suffer from stability problems due to the change of motor parameters. The dynamic performance of the drive during a low speed range is most likely to deteriorate. Therefore, changes in the torque represent the differences in oil viscosities at 75% speed. This makes it more suitable to diagnose changes in oil viscosities.

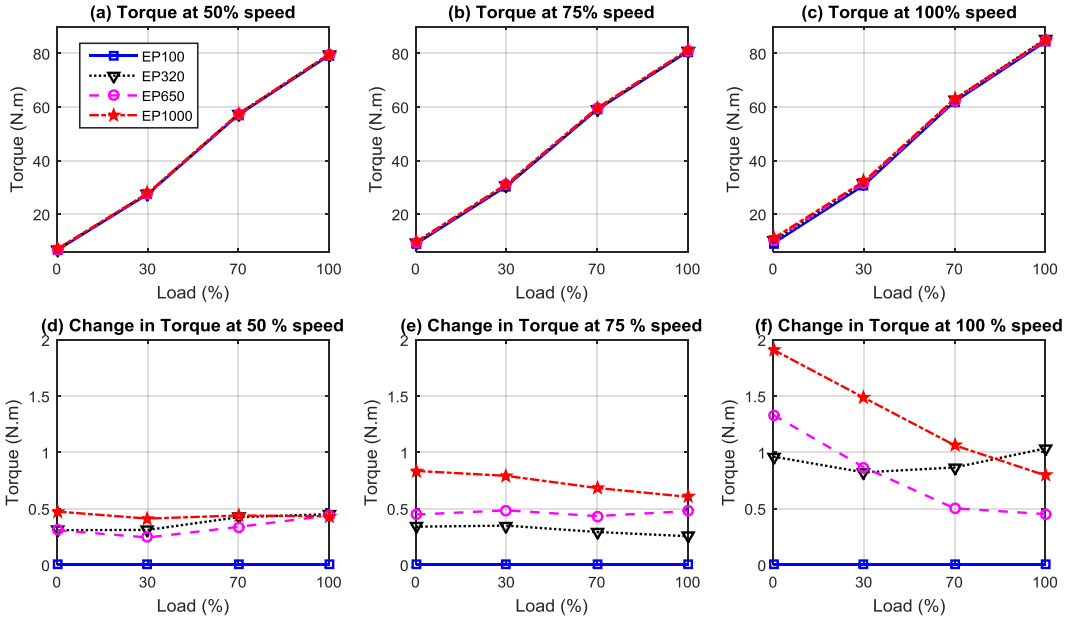

Figure 8.22 Torque static data comparison

8.2.2.6 Diagnosis using Dynamic Data of Electrical Power

The spectra of electrical power supply parameters, i.e. voltage, current and power have been calculated for investigating the potential of using them for oil viscosity changes. Amplitudes at both right and left sidebands of the f_{r1}, f_{r2} and f_{r3} have been averaged. The performance of both current and voltage signals showed poor performance in detecting oil viscosity changes and their results are represented in appendix IV.

On the other hand, Amplitudes at characteristic frequency components from the electrical power supply spectra have superior performance in diagnosing oil viscosity changes. Figure 8.23 displays the feature frequencies related to f_{r1}, particularly sidebands at the shaft frequency ($f_s \pm f_{r1}$). As clear from the figure, sidebands at this specific frequency component do not show clear changes in relation to viscosity.

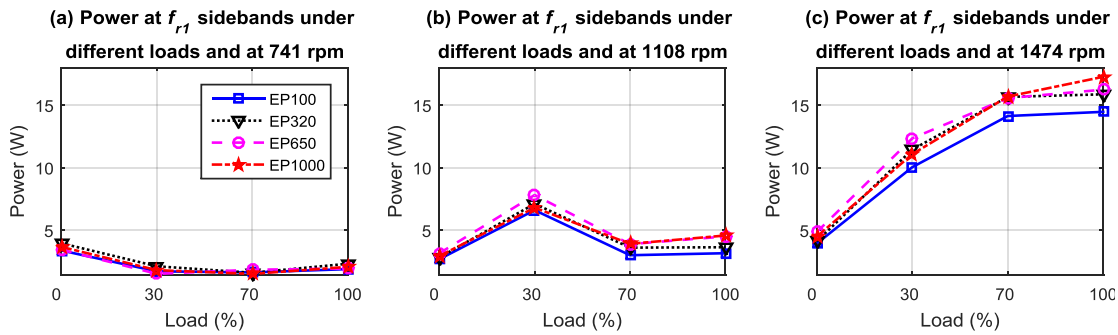

Figure 8.23 Amplitudes of power at f_{r1} sidebands

As shown in Figure 8.24, the power at $2f_{r1}$ exhibits visible changes with viscosity, indicating the potential of using them for diagnosis. It also shows that speed has a significant effect, where an increase in speed means that more mass circulates with gears leading to greater oscillations. When gear pairs rotate, a large quantity of oil circulates with the gear motion and amount of oil formed increases with the speed. This effect will decrease the oil level in the gearbox reservoir and consequently lowers the damping effect of the mass removed. Meanwhile, the mass formed is highly dependent on oil properties, particularly viscosity and density. The effective moment of inertia can also vary as the shape of the rotating oil is not perfectly uniform due to the inherent eccentricity and unbalanced mass. This generates more torsional oscillations at the shaft frequency which then modulate the supply component of the power system. However, the second and third shaft frequency components show indistinguishable changes with viscosity, as depicted in Appendix IV.

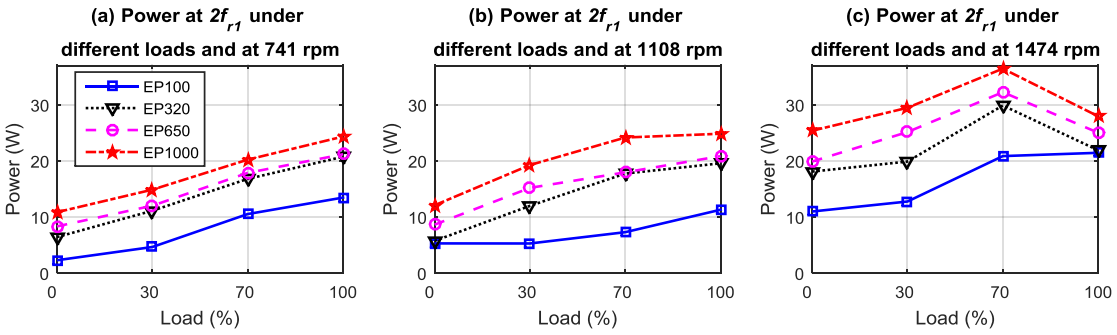

Figure 8.24 Amplitudes of power at $2f_{r1}$

The performance of the power at the $2f_{r1}$ frequency component is measured by calculating the differences between different cases and the EP100 oil test data. The

results are presented as a percentage to the rated motor power, i.e. 15kW. Figure 8.25 shows the results of this comparison. The performance of this frequency component shows good separation at 50% and 100% of the full speed. However, at the 100% speed it fails to separate the EP320 and the EP100 when the load is 100%. This can be explained due to the noise generated from the oil churning and the influence of temperature.

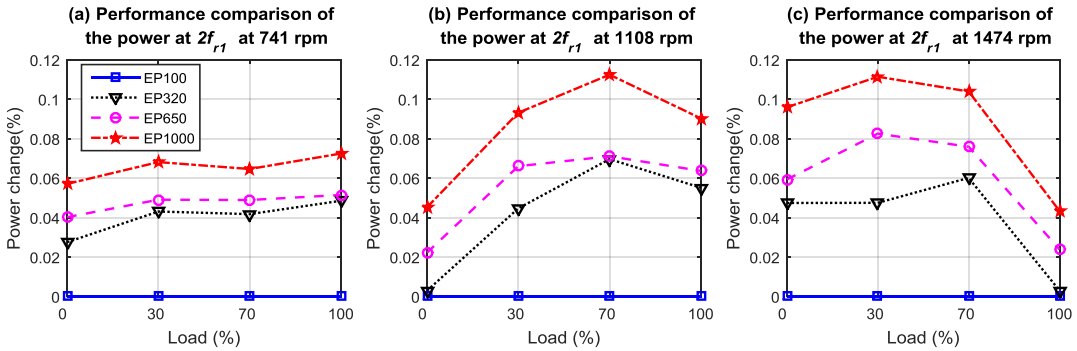

Figure 8.25 Amplitudes of power at $2f_{r1}$

8.2.3 Lube Oil Level Tests

Lubricants leakage in industrial gearboxes is a very common problem in industry. Leakage is normally visually investigated in periodical bases. This is time consuming and the efficiency of such investigation relies on time intervals between each investigation and another. There is therefore significant need for a reliable and cost effective lube leakage detection. Lube level tests have been performed as explained in Chapter 4. In the following, features from electrical and control parameters are studied to investigate the potential for detecting oil leakage problems in industrial gearbox transmission systems. The vibration signals are analysed firstly for the purpose of benchmarking and comparison.

8.2.3.1 Fault Detection Based on Residuals

The detection scheme based on the power residuals exhibits effective detection performance under different operating conditions as depicted in Figure 8.26. Particularly at the full speed residuals were able to separate fault cases as they all have

values greater than the threshold. Additionally they also indicate for the fault severity as they increase with fault. However, under 0% load at 50 and 75% speed they revealed a lower level of performance.

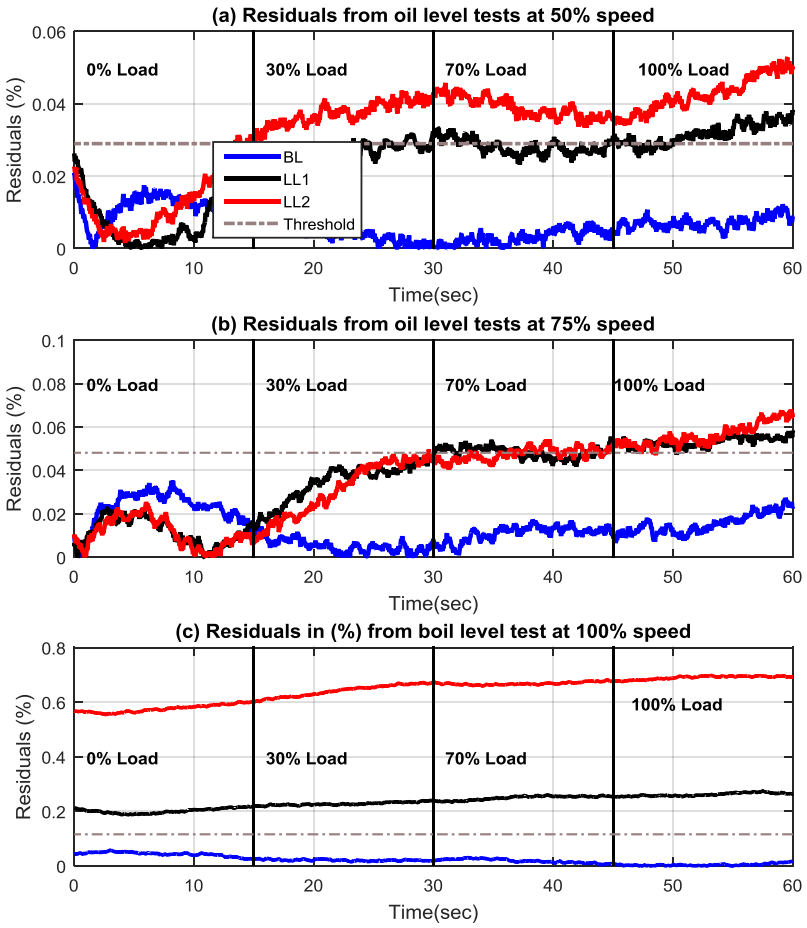

Figure 8.26 Power residuals values under different operating conditions

8.2.3.2 Change of Temperature with Different Oil Levels

The temperature of the oil inside the gearbox is captured during tests and averaged for each test cycle. Figure 8.27 represents the average temperature of the oil inside GB1 under different operating conditions. It shows that as the oil level decreased the temperature also reduced. This can be explained as a result of diminished internal friction in the oil which thus generates a lower temperature. System speed has been also investigated during tests as shown in Figure 8.28.

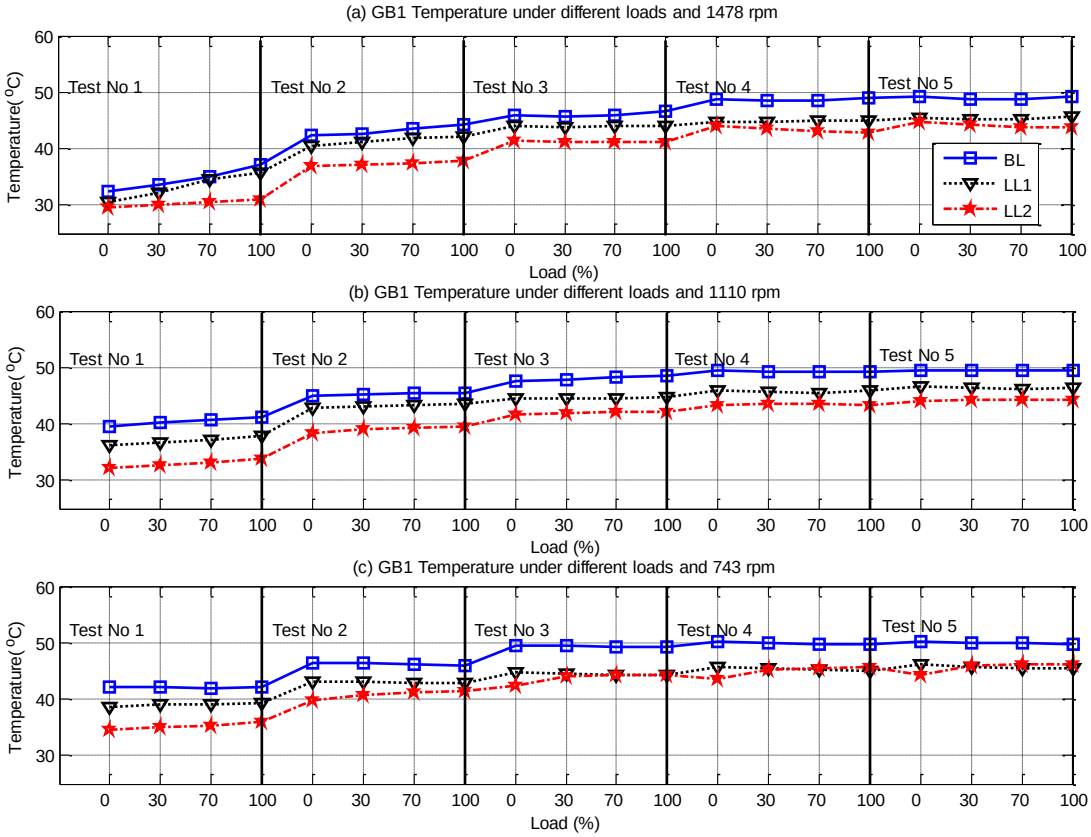

Figure 8.27 Temperature change under different oil level and operating conditions

The same speed behaviours explained in Chapter 4 are repeated here in Figure 8.28. The system speed is stabilised by the third test run where the temperature also begins to stabilise. Therefore, the results from the last three tests are considered in the following for analysis and investigation.

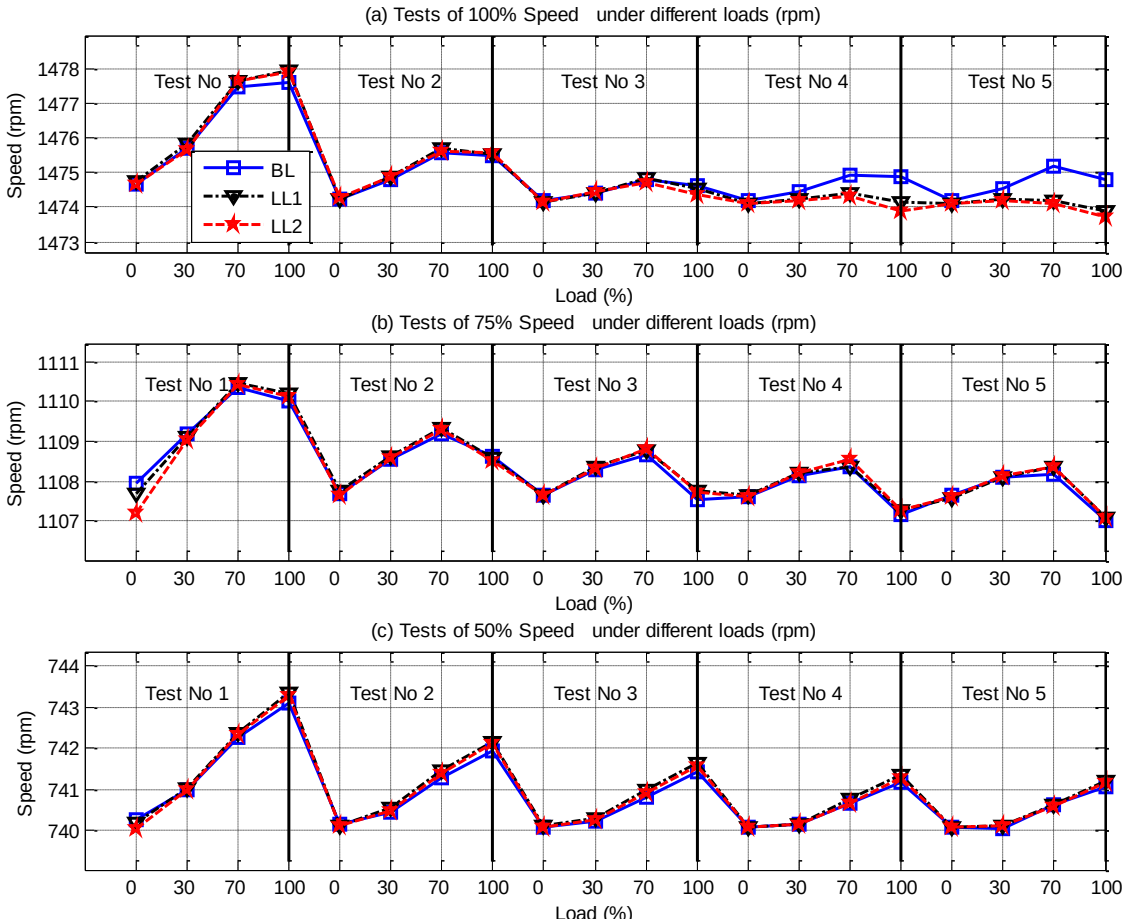

Figure 8.28 Temperature change under different oil level and operating conditions

8.2.3.3 Diagnosis using Vibration Analysis

The averaged GB1 rms vibration signal after being processed with the TSA scheme is presented in Figure 8.29. Except for the increase in the vibration levels under higher load conditions and at 100% speed, no significant changes can be seen in the vibration signals.

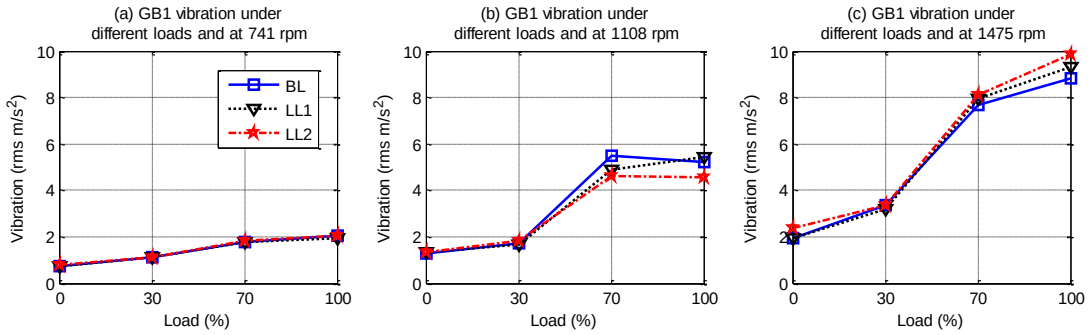

Figure 8.29 GB1 rms vibration signal under different operating conditions

To analyse the vibration signals further, the meshing frequencies have been calculated. Figure 8.30 illustrates the averaged first meshing frequency from the vibration signals after processing with the TSA scheme. The vibration at the f_{m1} frequency component shows changes similar to that of the rms vibration signals. Changes of the vibration signals at f_{m1} can be correlated with the oil level and hence cannot be used for level change detection.

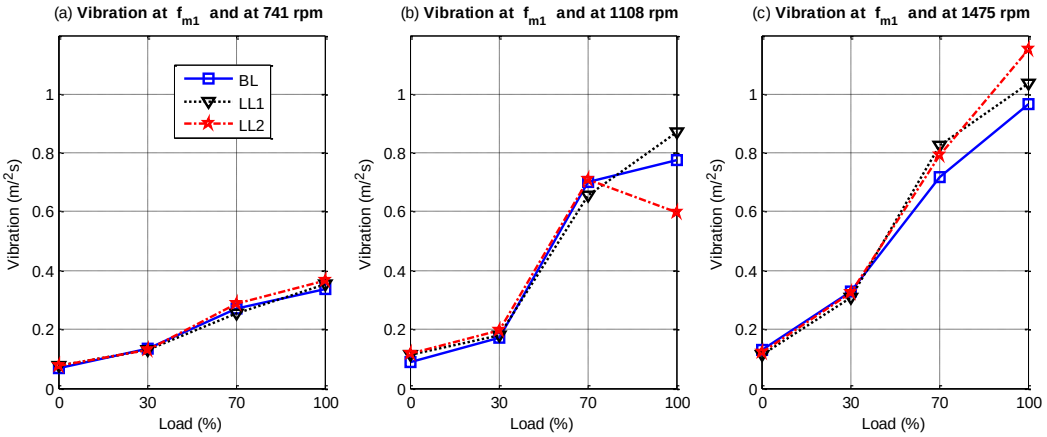

Figure 8.30 Vibration at f_{m1} frequency component

The second meshing frequency component was also investigated. Figure 8.31 represents the vibration signals comparison at this frequency component. Similarly, changes at fm1 cannot be correlated with the level changes and may not be used for oil level detection. This analysis shows that it may be difficult to detect small oil level changes using vibration signals due to leakage or evaporation in gearboxes.

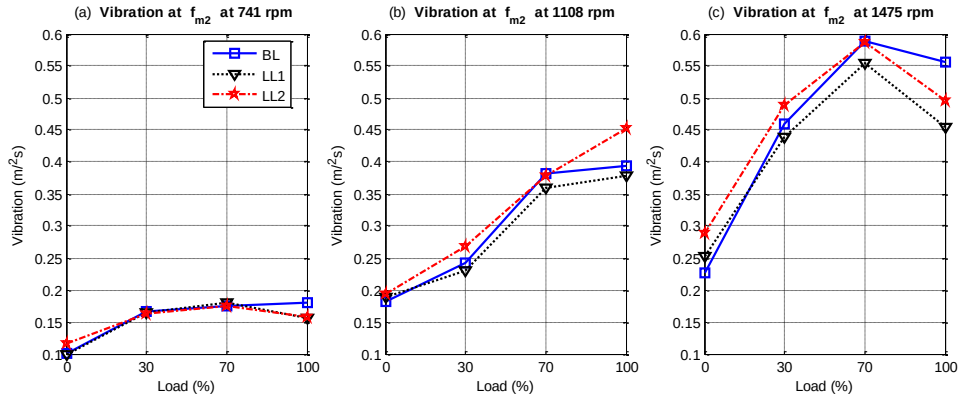

Figure 8.31 Vibration at f_{m1} frequency component

8.2.3.4 Diagnosis using Static Data

Static data of the current signals as obtained from the drive are represented in Figure 8.32. Figure 8.32 (a-c) indicates the averaged current under different operating conditions, and Figure 8.32 (d-f) shows the differences in current between different test cases and the corresponding baseline data. The static component of the static current drops as the oil level decreases. This can be explained due to the reduction in oil churning losses. However, when the load is high, the frictional forces are also high which requires more power if the oil film is not sufficient and hence requires more current to compensate for these forces.

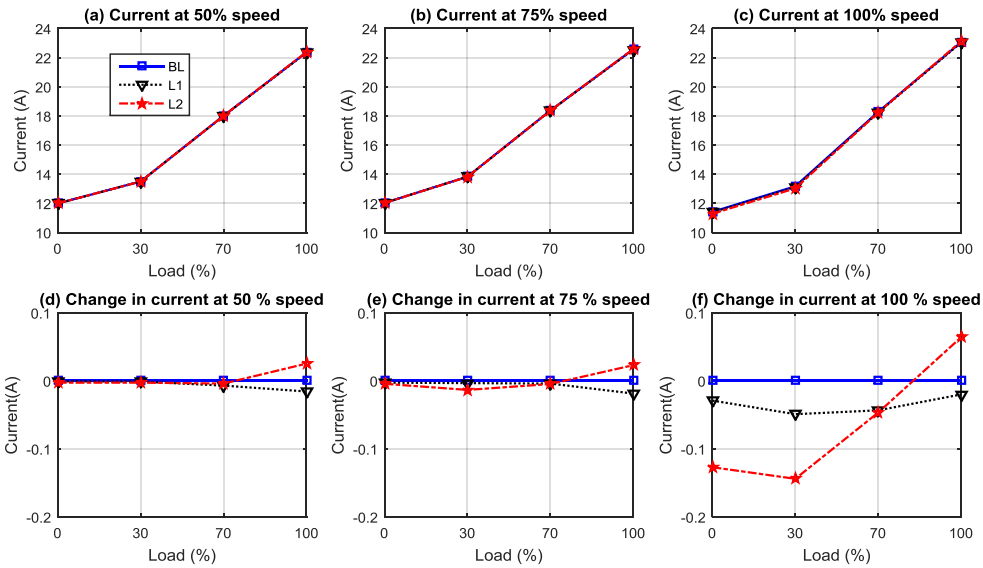

Figure 8.32 Current static data from the drive

The corresponding voltage static data have also been obtained and represented in Figure 8.33. The static component of the voltage data displays similar behaviours to that of current static data. However, as can be seen in Figure 8.33 (f) when the load is 100% the voltage signal of the LL-600 is higher than that of the baseline which may be explained due to the noise produced from oil splashing.

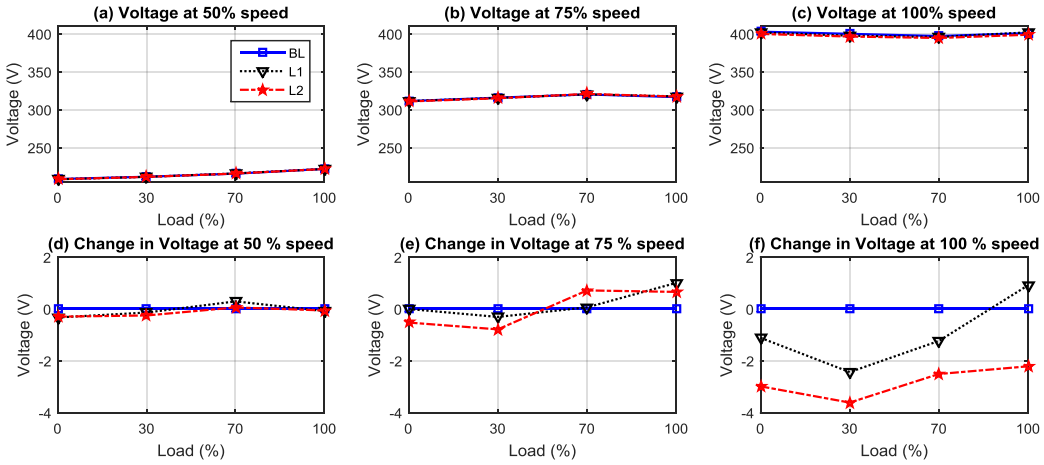

Figure 8.33 Voltage static data from the drive

The static data of the electrical power from the drive also shows changes that reflect the oil churning and splashing losses as presented in Figure 8.34. The power generally decreases with the oil level. The amount of the oil removed decreases the churning power losses; hence the static power reduces as the level of oil drops. However this shows that current, voltage and power static data may not be used for oil level change detection.

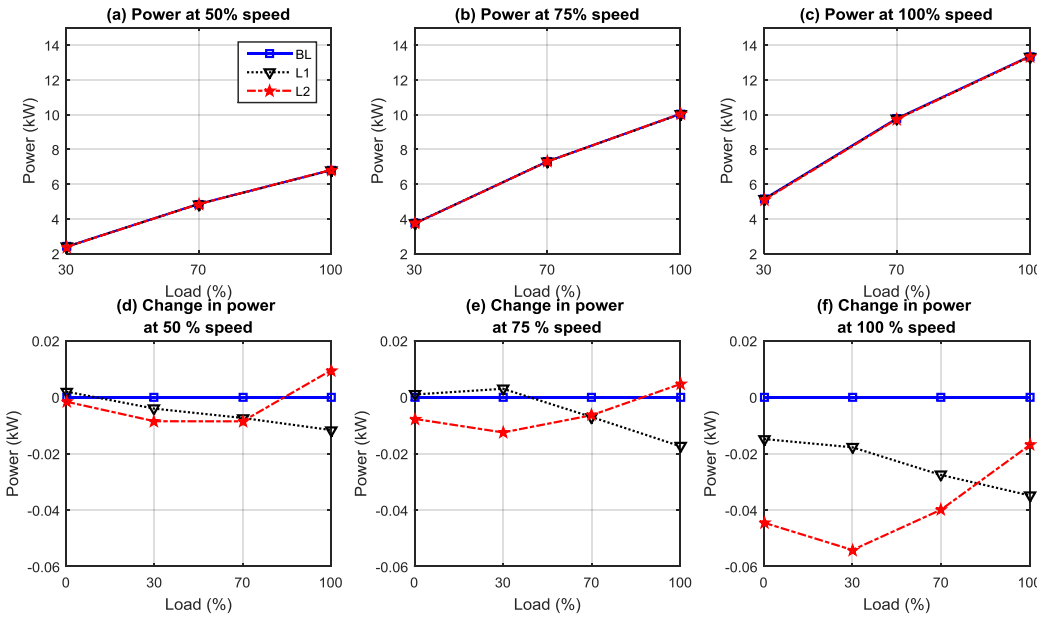

Figure 8.34 Power static data from the drive

Torque signals have also been acquired to investigate their potential for detecting changes in oil level. Figure 8.35 illustrates changes of the torque signal under different operating conditions. When the system speed is low, Figure 8.35 (a, b) shows that most oscillations result from oil churning and splashing and hence the power will decrease as the oil level lowers. However under full load the frictional forces are maximal which increases the fluctuations as a lower oil level causes a thinner oil film. On the other hand, at the full speed as shown in Figure 8.35(f), and particularly when the load is as high as 70% and 100%, frictional forces increase causing greater load torque fluctuations. This explains the need for the drive to generate more torque to compensate for such oscillations. However changes in the static component of the torque signal may not be useful for oil level change detection. The torque current component also shows changes similar to that of the torque signal, detailed in Appendix V.

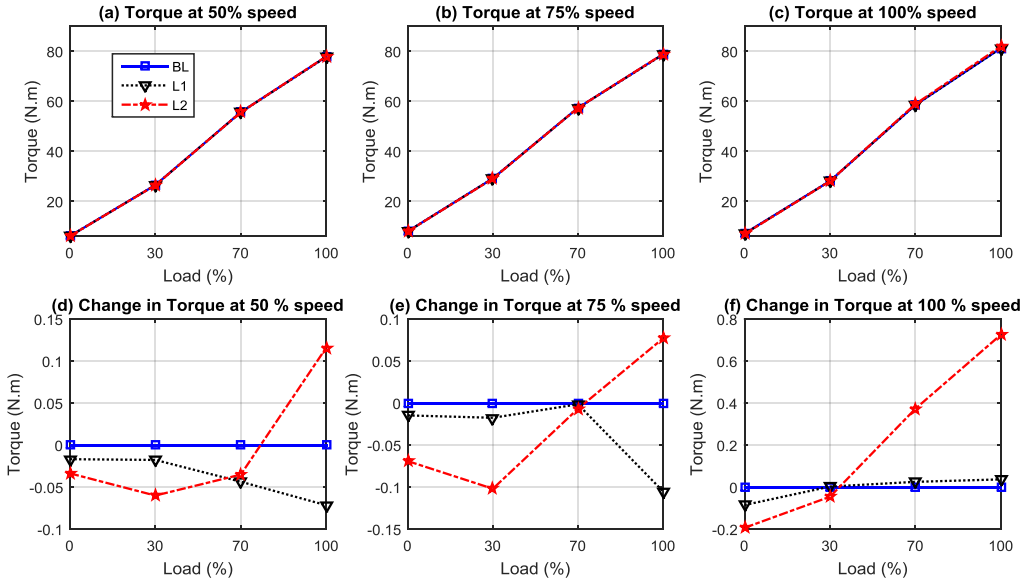

Figure 8.35 Torque static data from the drive

8.2.3.5 Detection using Dynamic Data

The features from the current, voltage and power spectra have been calculated to investigate if any changes consistent with oil level change can be detected. The left and right sidebands of each shaft frequency component have been calculated and averaged. Both current and voltage signals showed indistinguishable changes with oil levels. Only analysis of the electrical power spectra is represented here, while results from current and voltage analysis are represented in Appendix V.

The power amplitudes at the double shaft frequency component $2f_{r1}$ show notable changes with different oil levels as depicted in Figure 8.36. Changes of power at this particular frequency component therefore can be used for oil level change detection and diagnosis. The power results from both voltage and current, and hence it shows enhanced performance in comparison with either when a sensorless variable speed drive is in the control loop. The level of noise in current and voltage signals due to the drive prevents such changes from being visible in either. Contrastingly these changes can be clarified in the power spectra as it contains more frequencies resulting from the multiplication.

Despite the performance of this frequency component at full speed and under 100% load it is influenced by noise as shown in Figure 8.36 (c). However it exhibits effective performance at other speed and load ranges particularly at moderate speed, such as 75%, as shown in Figure 8.36 (b).

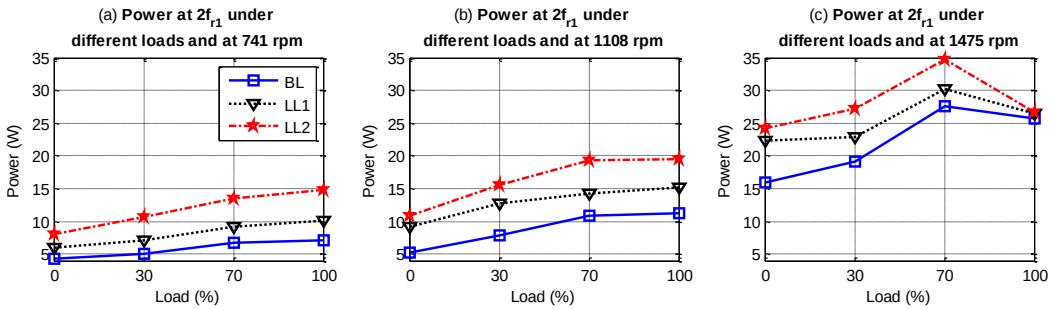

Figure 8.36 Power at 2 f_{r1} frequency component

In conclusion, oil level tests show that vibration as well as dynamic features of current and voltage signals have poor performance in detecting lubricating shortages in gearboxes. A similar assessment can be made for torque and related torque components, while the static features of voltage and the consequent power showed good performance at the full speed range. On the other hand the dynamic feature of the power signals at the $2f_{r1}$ frequency component showed consistent change with oil levels at different speed ranges and under different loads.

8.2.4 Conclusions from the Oil Degradation Tests

8.2.4.1 Conclusions from the water in oil test

Results from water contaminated oil test can be concluded as follows:

- ✓ The study showed promising results in detecting gearbox lubricant water contamination based on power supply parameters.
- ✓ Results show that viscosity decreases when a small portion of water (<20kppm) is added to the gear oil while a large portion of water increases the viscosity.
- ✓ Water contamination can be measurable using the static power supply parameters including the voltage and power.

- ✓ Results have been supported by vibration response analysis in that the vibration responses at the high load stage indicate significantly similar change due to water contents to that of the dynamic components of the power supply parameters.
- ✓ Power component at f_s-f_{r1} exhibits good response to different water contents and can be used for diagnosing this particular fault.
- ✓ The static components of torque related variables showed poor performance in diagnosing this particular fault.

8.2.4.2 Conclusions from different oil viscosity tests

Conclusions from oil viscosity tests can be outlined as follows:

- ✓ Change in oil viscosity due to oil degradation causes corresponding changes in both the static power consumption and the dynamic behaviour of a gearbox transmission system.
- ✓ The increase in oil viscosity leads to a measurable increase in the power consumptions due to the effect of viscous friction and oil churning.
- ✓ Simultaneously, the effect also changes the dynamics of the gear transmission system. That it leads to higher oscillations in the rotation system, which is eventually reflected by increasing sidebands around the supply frequency.
- ✓ The static power feature can show viscosity changes correctly at low and moderate speeds.
- ✓ The features of the torque component and the consequent torque current component show superior detection performance at moderate (75%) of the full speed under the entire tested loads.
- ✓ The dynamic feature of the power, i.e. amplitude at $2f_{r1}$, can distinguish viscosities at all tested speed and load ranges.
- ✓ Vibration signals, in comparison, show less effective performances than that of electrical and control parameters in detecting lube viscosity changes.

8.2.4.3 Conclusions from lubrication shortage tests

The conclusions from lubrication shortage tests can be summarized as follows:

- ✓ Vibration as well as dynamic features of current and voltage signals indicate low performance in diagnosing lubrication shortages in gearboxes.
- ✓ This can also be observed for torque and related torque components.
- ✓ Static features of the voltage showed high performance at the full speed range.
- ✓ The dynamic feature of the power signals at $2f_{r1}$ frequency component shows consistent change with oil levels at different speed ranges under different loads.
- ✓ The static components can be employed to differentiate between oil viscosity changes and less lubrication faults. That is the static torque component shows changes with the oil viscosity at the moderate speed while no changes can be seen when less lubrication problems occur. Also static voltage and power components increase with decreasing lube levels.

Chapter 9
Conclusions and Future Work

This chapter summarises and presents the key conclusions arising from this study. This commences with a summary of the objectives, an explanation of how objectives were achieved and the key conclusions arising from this research. This is followed by a summary *of the author's* key contributions to knowledge and the novel aspects of the research undertaken. Finally recommendations are made for future research avenues in remote condition monitoring of gear transmission systems and for further improvements of the schemes developed in this thesis.

9.1 Objectives and Achievements

The primary aim of this research was to: 'To discover the diagnostic information from data available at the sensorless AC induction motor VSDs. It further seeks to identify the potential of developing a new cost effective and reliable approach for condition monitoring of mechanical systems by using information and signals available in sensorless ACIM VSDs for fault detection and diagnosis. The work includes the development of a mechanical fault detection technique based on the control system incorporated by the sensorless VSD'.

This central aim was achieved through an experimental study based on an induction motor driven mechanical transmission system with a standard commercial sensorless variable speed drive. Four different common faults were applied with different degrees of severities. A new power residual based fault detection scheme was developed based on observers normally utilised by the drive for control purposes. Residual data was found to be effective in detecting faults under different speed and load conditions. Both dynamic and static data, used by the drive to control the induction motor, was utilised to perform diagnostic tests. A conventional fault detection method, i.e. vibration analysis has been used in parallel for comparison and benchmarking purposes.

In the following a summary of the objectives and the key achievements achieved by this research is clarified by following that setup in Chapter 1 respectively:

Objective 1. To develop an observer based fault detection scheme based on the available observers in sensorless VSDs.

Achievement 1. MRAS speed and flux observers, which are normally used for control purposes, have been implemented. The observers are used for control purposes and to generate power residuals simultaneously. The residual were generated so that they less influenced by parameters change and load effects while more sensitive to faults. Chapter 6 details the observers developed and the results obtained.

Objective 2. To investigate residuals generation scheme from the developed observers to detect common mechanical fault under different operation conditions.

Achievement 2. The performance of the developed residuals have been experimentally investigated. Sets of common faults in degrees typical of such faults in industrial situations have been experimentally simulated. The developed residuals showed superior performance in detecting the tested faults. Chapters 7 and 8 details on the experimental results obtained.

Objective 3. To investigate/evaluate the diagnostic capability of the available information in the sensorless VSDs. This includes an effective data analysis scheme to explore the potential for detecting the mechanical faults without the need for additional resources

Achievement 3. Spectrum analysis was conducted on the power supply signals (current, voltage and power) while a systematic comparison was made for static data analysis. Results enabled the comparison between the detection performances in both open loop and sensorless operating control modes. Additionally, static components from the drive were examined for potential to using them in fault detection and diagnosis. Chapter 7 and Chapter 8 discussed in detail the corresponding results from different tests applied.

Objective 4. To replicate common mechanical faults in gear transmission systems driven with industrial sensorless VSDs. Faults are in degrees typical of such faults in industrial situations.

Achievement 4. Four types of common mechanical faults in gear transmission systems were simulated. Namely shaft misalignment, water contaminated oil, oil viscosity

changes and lubrication shortages. All faults applied in degrees typical to such faults in industry. Almost all these faults have not been detected previously using the sensorless VSDs' control dynamic and static components. The results are discussed in details in Chapter 7 and Chapter 8.

Objective 5. To perform a literature review and establish the theory, evidence and knowledge gaps in relation to the application of control system for the detection of mechanical faults within driven mechanical systems.

Achievement 5. An extensive literature review of related studies was conducted to establish the theoretical developments and evidence in this field. Chapter 2 includes a critical discussion of key studies in this area. Additionally, the review extended to the common mechanical fault that typical in industry. Results from the review influenced the focus of this study to address issues and gap in the knowledge identified. A unique and significant theoretical contribution knowledge has been made.

Objective 6. To theoretically study the response of the IM VSD in the case of mechanical load oscillations using induction motor and VSD's models.

Achievement 6. The ready to use modules facilitated by the Simulink/MATLab programme were used to study the induction motor with the sensorless variable speed drive. The rig's motor and the drive data were loaded into the model and a series of runs were performed under different speed and load conditions. The model is used to examine the performance of the control system under different fault conditions. Oscillations are induced in the load torque and the response of the model were analysed. Both dynamic and static responses indicated changes compared to that of the normal operations. The model, its verifications and results are detailed in Chapter 5.

9.2 Conclusions

This research investigated the sensorless variable speed behaviour in the case of mechanical fault in the driven systems. The key conclusions from this study can be summarised as follows:

1. Sensorless variable speed drives are rich in information that can be utilised to indicate the health of the system.

2. A new online fault detection scheme has been developed based on sensorless speed control observers.
3. The developed scheme is a cost effective in that observers which are normally employed for control systems are utilized simultaneously to generate the residuals. Therefore no additional resources are required.
4. Robust power residuals have been generated from the developed scheme. The generated power residuals have succeeded to differentiate different mechanical faults and separate the fault cases from the healthy.
5. A set of static data in a sensorless VSD has been effectively utilised for fault diagnosis.
6. Shaft misalignment and gear oil degradation, i.e. water contaminated oil, lubrication shortage and lubrication viscosity changes, faults have been detected and diagnosed using power supply and control data.

9.3 Novelty and Contribution to the Knowledge

This research has led to a number of novel developments in the subject that have not considered by previous researchers. For clarification, key novel aspects are summarized as follows:

The development of power residuals utilising VSD speed and torque observers is entirely novel. The residuals are based on the differences between measured and estimated powers. No research found until the time of writing has developed such residuals based on observers utilised for speed control purposes. Additionally, the developed residuals are processed in that they are decoupled from the load disturbances and parameter accuracy. The curve fitting method used is not new in itself, however it is entirely novel to apply it for decoupling the power residuals from load disturbances and induction motor parameter changes.

Moreover, although the use of residuals in fault detection is not new, the use of power residuals for detecting mechanical faults in a driven mechanical transmission system is entirely novel. The developed power residuals are capable of detecting the mechanical faults tested under different operating conditions.

Other important novel aspects presented in this research is the detection and diagnosis of four different mechanical faults in mechanical transmission systems under sensorless VSDs. For instance, the mechanical shaft misalignments with different degrees of severities have been detected and diagnosed utilised pure static data from the drive. No work has been found describing in any detail the detection and diagnosing shaft misalignments utilising static control data under sensorless VSDs.

Moreover, incorporating static data with dynamic data available at sensorless VSDs is also entirely novel. No literature has been found which has used the developed scheme based on the combination of dynamic and static data to detect the mechanical faults.

The detection and diagnosis of three different types of oil degradation using power and control parameters is another important contribution and is entirely novel. Three different types of oil degradation were detected and diagnosed under sensorless control systems, i.e. water contaminated gear oil, lubrication oil viscosity changes and lubrication oil level changes have been successfully detected and fault cases separated from the healthy cases using the developed strategy. No work has been found describing, in any detail, the detection and diagnosing such oil faults using electrical power supply parameters and/or static control data under sensorless VSDs.

9.4 Recommendations for Future Work

- **Recommendation One:**

  To further examine the sensitivity and reliability of the developed power residuals, it is recommended to conduct additional experimental research. The experimental work should include other mechanical fault types with different degrees of severities.

- **Recommendation Two:**

  Investigate the possibility of developing adaptive dynamic thresholds that can help perform more effective fault identification processes and avoid false fault alarms. The investigated signals showed very small changes and hence more advanced and reliable schemes can provide a basis for improving the threshold setting method.

- **Recommendation Three:**

  Based on the results from this study demonstrated, the developed schemes can be enhanced by obtaining more detailed information about the drive used. This requires

communication with the drive manufacturers as they limit the knowledge provided on the drive design details due to commercial issues. This may help in improving the performance of static data in fault detection.

- **Recommendation Four:**

Results from this research showed significant potential for incorporating the detection of oil degradation problems online. It is recommended to develop an algorithm based oil degradation scheme that can be employed with the drive control system. Signals used for the developed schemes already exist at the drive and no need for additional resources in the drive. Again this requires communication with the manufacturer as access to the exceptionally low programming level of the drive is needed.

- **Recommendation Five:**

This study is performed based on conventional spectral analysis of dynamic data and systematic comparisons of the static data. It is believed that more valuable information can be extracted if other advanced signal processing schemes are used. This may include the use of modulation signal bispectrum (MSB), wavelet and time frequency analysis. Techniques such as neural networks, fuzzy logic and intelligent artificial systems can further be applied to analyse the static data response from sensorless VSDs.

- **Recommendation Six:**

Further experimental work is recommended to investigate the response of the sensorless VSD to combined mechanical faults. This will also form an important step for evaluating the performance of the developed power residuals in this circumstance. Combined faults such as gear tooth breakage together with misalignment or faulty couplings can be a challenging task as they both modulate the electrical power signals at the shaft frequency components, while their static features remain obscure.

- **Recommendation Seven:**

Observers developed showed poor performance in only very limited cases.

Therefore this should be a priority for further development.

- **Recommendation Eight:**

Observers have been designed to maintain features in the dynamic components of the flux and torque. It would therefore be worthwhile to examine the response of these two dynamic signals under different operating conditions.

References

[1] H. Su and K. T. Chong, "Induction machine condition monitoring using neural network modeling," Industrial Electronics, IEEE Transactions on, vol. 54, pp. 241-249, 2007.

[2] B. S. Payne, Condition monitoring of electric motors for improved asset management: University of Manchester, 2003.

[3] Z. Gao, L. Turner, R. S. Colby, and B. Leprettre, "A frequency demodulation approach to induction motor speed detection," Industry Applications, IEEE Transactions on, vol. 47, pp. 1632-1642, 2011.

[4] "Report of Large Motor Reliability Survey of Industrial and Commercial Installations, Part I," Industry Applications, IEEE Transactions on, vol. IA-21, pp. 853-864, 1985.

[5] P. Tavner, L. Ran, and J. Penman, Condition monitoring of rotating electrical machines vol. 56: IET, 2008.

[6] M. Zaggout, P. Tavner, C. Crabtree, and L. Ran, "Detection of rotor electrical asymmetry in wind turbine doubly-fed induction generators," Renewable Power Generation, IET, vol. 8, pp. 878-886, 2014.

[7] C.-M. Ong, Dynamic simulation of electric machinery: using MATLAB/SIMULINK vol. 5: Prentice Hall PTR Upper Saddle River, NJ, 1998.

[8] D. Polka, Motors and Drives: A Practical Technology Guide: ISA, 2003.

[9] S. Abusaad, A. Benghozzi, A. Smith, F. Gu, and A. Ball, "The Detection of Shaft Misalignments Using Motor Current Signals from a Sensorless Variable Speed Drive," in Vibration Engineering and Technology of Machinery, ed: Springer, 2015, pp. 173-182.

[10] G.-A. Capolino, J. Antonino-Daviu, and M. Riera-Guasp, "Modern Diagnostics Techniques for Electrical Machines, Power Electronics, and Drives," Industrial Electronics, IEEE Transactions on, vol. 62, pp. 1738-1745, 2015.

[11] Z. Gao, C. Cecati, and S. Ding, "A Survey of Fault Diagnosis and Fault-Tolerant Techniques Part II: Fault Diagnosis with Knowledge-Based and Hybrid/Active Approaches," 2015.

[12] V. Ghorbanian and J. Faiz, "A survey on time and frequency characteristics of induction motors with broken rotor bars in line-start and inverter-fed modes," Mechanical Systems and Signal Processing, vol. 54, pp. 427-456, 2015.

[13] A. Hughes and B. Drury, Electric motors and drives: fundamentals, types and applications: Newnes, 2013.

[14] Z. Hou, J. Huang, M. Cheng, H. Liu, and L. Zhao, "Rotor Faults Diagnosis in Rotor Field Oriented Controlled Induction Motors Based on Torque Current," in Electrical Machines and Systems (ICEMS), 2014 17th International Conference on, 2014, pp. 988-992.

[15] R. Patton and J. Chen, "Observer-based fault detection and isolation: robustness and applications," Control Engineering Practice, vol. 5, pp. 671-682, 1997.

[16] E. Fournier, A. Picot, J. Regnier, M. T. Yamdeu, J.-M. Andrejak, and P. Maussion, "Current-based detection of mechanical unbalance in an induction machine using spectral kurtosis with reference," Industrial Electronics, IEEE Transactions on, vol. 62, pp. 1879-1887, 2015.

[17] M. Seera, C. P. Lim, S. Nahavandi, and C. K. Loo, "Condition monitoring of induction motors: a review and an application of an ensemble of hybrid intelligent models," Expert Systems with Applications, vol. 41, pp. 4891-4903, 2014.

[18] S. Grubic, J. M. Aller, B. Lu, and T. G. Habetler, "A survey on testing and monitoring methods for stator insulation systems of low-voltage induction machines focusing on turn insulation problems," Industrial Electronics, IEEE Transactions on, vol. 55, pp. 4127-4136, 2008.

[19] P. Zhang, Y. Du, T. G. Habetler, and B. Lu, "A survey of condition monitoring and protection methods for medium-voltage induction motors," Industry Applications, IEEE Transactions on, vol. 47, pp. 34-46, 2011.

[20] R. J. Patton, P. M. Frank, and R. N. Clark, Issues of fault diagnosis for dynamic systems: Springer Science & Business Media, 2013.

[21] A. Davies, Handbook of condition monitoring: techniques and methodology: Springer Science & Business Media, 1997.

[22] R. S. Beebe, Predictive maintenance of pumps using condition monitoring: Elsevier, 2004.

[23] M. A. A. Elmaleeh, N. Saad, and M. Awan, "Condition monitoring of industrial process plant using acoustic emission techniques," in Intelligent and Advanced Systems (ICIAS), 2010 International Conference on, 2010, pp. 1-6.

[24] S. H. Kia, H. Henao, and G.-A. Capolino, "Gear tooth surface damage fault detection using induction machine stator current space vector analysis," Industrial Electronics, IEEE Transactions on, vol. 62, pp. 1866-1878, 2015.

[25] T. Loutas, D. Roulias, E. Pauly, and V. Kostopoulos, "The combined use of vibration, acoustic emission and oil debris on-line monitoring towards a more effective condition monitoring of rotating machinery," Mechanical Systems and Signal Processing, vol. 25, pp. 1339-1352, 2011.

[26] M. El Hachemi Benbouzid, "A review of induction motors signature analysis as a medium for faults detection," Industrial Electronics, IEEE Transactions on, vol. 47, pp. 984-993, 2000.

[27] W. T. Thomson and M. Fenger, "Current signature analysis to detect induction motor faults," Industry Applications Magazine, IEEE, vol. 7, pp. 26-34, 2001.

[28] F. Gu, Y. Shao, N. Hu, A. Naid, and A. Ball, "Electrical motor current signal analysis using a modified bispectrum for fault diagnosis of downstream mechanical equipment," Mechanical Systems and Signal Processing, vol. 25, pp. 360-372, 2011.

[29] O. V. Thorsen and M. Dalva, "A survey of faults on induction motors in offshore oil industry, petrochemical industry, gas terminals, and oil refineries," Industry Applications, IEEE Transactions on, vol. 31, pp. 1186-1196, 1995.

[30] A. Siddique, G. Yadava, and B. Singh, "A review of stator fault monitoring techniques of induction motors," Energy Conversion, IEEE Transactions on, vol. 20, pp. 106-114, 2005.

[31] A. Alwodai, T. Wang, Z. Chen, F. Gu, R. Cattley, and A. Ball, "A Study of Motor Bearing Fault Diagnosis using Modulation Signal Bispectrum Analysis of Motor Current Signals," Journal of Signal and Information Processing, vol. 4, p. 72, 2013.

[32] M. E. H. Benbouzid, M. Vieira, and C. Theys, "Induction motors' faults detection and localization using stator current advanced signal processing techniques," Power Electronics, IEEE Transactions on, vol. 14, pp. 14-22, 1999.

[33] Z. Chen, T. Wang, F. Gu, M. Haram, and A. Ball, "Gear transmission fault diagnosis based on the bispectrum analysis of induction motor current signatures," Journal of Mechanical Engineering, vol. 48, pp. 84-90, 2012.

[34] C. Kar and A. Mohanty, "Multistage gearbox condition monitoring using motor current signature analysis and Kolmogorov–Smirnov test," Journal of Sound and Vibration, vol. 290, pp. 337-368, 2006.

[35] J. Zhang, J. Dhupia, and C. Gajanayake, "Stator Current Analysis from Electrical Machines Using Resonance Residual Technique to Detect Faults in Planetary Gearboxes," 2015.

[36] I. M. Cecílio, S.-L. Chen, and N. F. Thornhill, "Importance of auxiliary systems for process fault detection and diagnosis," in Control & Automation (MED), 2011 19th Mediterranean Conference on, 2011, pp. 952-957.

[37] A. Kingsmill, S. Jones, and J. Zhu, "Application of new condition monitoring technologies in the electricity transmission industry," in Electrical Machines and Systems, 2003. ICEMS 2003. Sixth International Conference on, 2003, pp. 852-855 vol.2.

[38] D. Dasgupta, K. Krishnakumar, D. Wong, and M. Berry, "Immunity-based aircraft fault detection system," in Proceedings of the 1st Intelligent System Technology Conference, Chicago, Illinois, 2004, pp. 20-22.

[39] Z. Ma and S. Wang, "Online fault detection and robust control of condenser cooling water systems in building central chiller plants," Energy and Buildings, vol. 43, pp. 153-165, 2011.

[40] M. Schlechtingen and I. F. Santos, "Wind turbine condition monitoring based on SCADA data using normal behavior models. Part 2: Application examples," Applied Soft Computing, vol. 14, Part C, pp. 447-460, 2014.

[41] K. Kim, G. Parthasarathy, O. Uluyol, W. Foslien, S. Sheng, and P. Fleming, "Use of SCADA data for failure detection in wind turbines," in ASME 2011 5th International Conference on Energy Sustainability, 2011, pp. 2071-2079.

[42] I. Al-Tubi, H. Long, P. Tavner, B. Shaw, and J. Zhang, "Probabilistic analysis of gear flank micro-pitting risk in wind turbine gearbox using supervisory control and data acquisition data," IET Renewable Power Generation, 2015.

[43] R.-E. Precup, P. Angelov, B. S. J. Costa, and M. Sayed-Mouchaweh, "An overview on fault diagnosis and nature-inspired optimal control of industrial process applications," Computers in Industry, 2015.

[44] N. Erez and A. Wool, "Control variable classification, modeling and anomaly detection in Modbus/TCP SCADA systems," International Journal of Critical Infrastructure Protection, 2015.

[45] K. Patan and T. Parisini, "Identification of neural dynamic models for fault detection and isolation: the case of a real sugar evaporation process," Journal of Process Control, vol. 15, pp. 67-79, 2005.

[46] A. Bellini, F. Filippetti, G. Franceschini, and C. Tassoni, "Closed-loop control impact on the diagnosis of induction motors faults," Industry Applications, IEEE Transactions on, vol. 36, pp. 1318-1329, 2000.

[47] C. C. Cunha and R. Lyra, "Detection of rotor faults in torque controlled induction motor drives," in Power Electronics and Applications, 2007 European Conference on, 2007, pp. 1-10.

[48] C. Kral, R. S. Wieser, F. Pirker, and M. Schagginger, "Sequences of field-oriented control for the detection of faulty rotor bars in induction machines-the Vienna Monitoring Method," Industrial Electronics, IEEE Transactions on, vol. 47, pp. 1042-1050, 2000.

[49] C. Kral, F. Pirker, and G. Pascoli, "Model-based detection of rotor faults without rotor position sensor-the sensorless Vienna monitoring method," Industry Applications, IEEE Transactions on, vol. 41, pp. 784-789, 2005.

[50] F. Duan and R. Zivanovic, "Condition monitoring of an induction motor stator windings via global optimization based on the hyperbolic cross points," Industrial Electronics, IEEE Transactions on, vol. 62, pp. 1826-1834, 2015.

[51] R. M. Tallam, T. G. Habetler, and R. G. Harley, "Stator winding turn-fault detection for closed-loop induction motor drives," Industry Applications, IEEE Transactions on, vol. 39, pp. 720-724, 2003.

[52] A. Demenko, P. Kolodziejek, and E. Bogalecka, "Broken rotor bar impact on sensorless control of induction machine," COMPEL-The international journal for computation and mathematics in electrical and electronic engineering, vol. 28, pp. 540-555, 2009.

[53] S. Cruz and A. Cardoso, "Diagnosis of rotor faults in closed-loop induction motor drives," in Industry Applications Conference, 2006. 41st IAS Annual Meeting. Conference Record of the 2006 IEEE, 2006, pp. 2346-2353.

[54] A. Masmoudi, P. Kolodziejek, and E. Bogalecka, "Broken rotor symptoms in the sensorless control of induction machine," COMPEL-The international journal for computation and mathematics in electrical and electronic engineering, vol. 31, pp. 237-247, 2011.

[55] D. Ashari, M. Lane, F. Gu, and A. Ball, "Detection and Diagnosis of Broken Rotor Bar Based on the Analysis of Signals from a Variable Speed Drive," 2014.

[56] B. Trajin, J. Regnier, and J. Faucher, "Comparison between stator current and estimated mechanical speed for the detection of bearing wear in asynchronous drives," Industrial Electronics, IEEE Transactions on, vol. 56, pp. 4700-4709, 2009.

[57] M. Akar, "Detection of a static eccentricity fault in a closed loop driven induction motor by using the angular domain order tracking analysis method," Mechanical Systems and Signal Processing, vol. 34, pp. 173-182, 2013.

[58] A. Paladugu and B. H. Chowdhury, "Sensorless control of inverter-fed induction motor drives," Electric Power Systems Research, vol. 77, pp. 619-629, 2007.

[59] P. Vas, Vector control of AC machines vol. 22: Oxford University Press, USA, 1990.

[60] C. H. De Angelo, G. R. Bossio, S. J. Giaccone, M. I. Valla, J. Solsona, and G. O. García, "Online model-based stator-fault detection and identification in induction motors," Industrial Electronics, IEEE Transactions on, vol. 56, pp. 4671-4680, 2009.

[61] C. S. Kallesøe, "Model-based stator fault detection in induction motors," in Industry Applications Society Annual Meeting, 2008. IAS'08. IEEE, 2008, pp. 1-8.

[62] S. Bachir, S. Tnani, J.-C. Trigeassou, and G. Champenois, "Diagnosis by parameter estimation of stator and rotor faults occurring in induction machines," Industrial Electronics, IEEE Transactions on, vol. 53, pp. 963-973, 2006.

[63] C. Chakraborty and V. Verma, "Speed and current sensor fault detection and isolation technique for induction motor drive using axes transformation," Industrial Electronics, IEEE Transactions on, vol. 62, pp. 1943-1954, 2015.

[64] S. K. Kommuri, J. J. Rath, K. C. Veluvolu, and M. Defoort, "An induction motor sensor fault detection and isolation based on higher order sliding mode decoupled current controller," in Control Conference (ECC), 2014 European, 2014, pp. 2945-2950.

[65] S. Golabi, E. Babaei, M. B. B. Sharifian, and Z. Golabi, "Application of Speed, Rotor Flux, Electromagnetic, Load Torque Observers and Diagnostic System in a Vector-Controlled High-Power Traction Motor Drive," Arabian Journal for Science and Engineering, vol. 39, pp. 2979-2996, 2014.

[66] S. H. Kia, H. Henao, and G.-A. Capolino, "Torsional vibration effects on induction machine current and torque signatures in gearbox-based electromechanical system," Industrial Electronics, IEEE Transactions on, vol. 56, pp. 4689-4699, 2009.

[67] J. Guzinski, H. Abu-Rub, A. Iqbal, and S. Ahmed, "Shaft misalignment detection using ANFIS for speed sensorless AC drive with inverter output

filter," in Industrial Electronics (ISIE), 2011 IEEE International Symposium on, 2011, pp. 2138-2143.

[68] R. Isermann, "Model-based fault-detection and diagnosis–status and applications," Annual Reviews in control, vol. 29, pp. 71-85, 2005.

[69] J. Guzinski, M. Diguet, Z. Krzeminski, A. Lewicki, and H. Abu-Rub, "Application of speed and load torque observers in high-speed train drive for diagnostic purposes," Industrial Electronics, IEEE Transactions on, vol. 56, pp. 248-256, 2009.

[70] M. Lane, "Using AC Motor as a Transducer for Detecting Electrical and Electromechanical Faults," MRes Thesis, University of Huddersfield, 2011.

[71] D. R. Patrick and S. W. Fardo, Industrial Process Control Systems: Fairmont Press, Incorporated, 2009.

[72] J. O'Brien, Frequency-Domain Control Design for High-Performance Systems: Institution of Engineering and Technology, 2012.

[73] S. C. G. U. A. Bakshi, Control Systems Engineering: Technical Publications, 2007.

[74] H. A. Toliyat and G. B. Kliman, Handbook of electric motors vol. 120: CRC press, 2004.

[75] A. H. Bonnett and T. Albers, "Squirrel cage rotor options for AC induction motors," in Pulp and Paper Industry Technical Conference, 2000. Conference Record of 2000 Annual, 2000, pp. 54-67.

[76] R. Rajput, Alternating Current Machines: Firewall Media, 2002.

[77] A. M. Trzynadlowski, Control of induction motors: Academic press, 2000.

[78] F. Giri, AC electric motors control: Advanced design techniques and applications: John Wiley & Sons, 2013.

[79] R. Parekh, "AC Induction Motor Fundamentals," Microchip Technology Inc, 2003.

[80] J. Bird, Electrical and electronic principles and technology: Routledge, 2013.

[81] Z. Yu and D. Figoli, "AC Induction Motor control using constant V/Hz principle and Space Vector PWM technique with TMS320C240," Texas Instruments: Houston, TX, 1998.

[82] X. Xu and D. W. Novotny, "Selection of the flux reference for induction machine drives in the field weakening region," Industry Applications, IEEE Transactions on, vol. 28, pp. 1353-1358, 1992.

[83] R. Crowder, Electric Drives and Electromechanical Systems: Applications and Control: Newnes, 2006.

[84] M. H. Rashid, Power electronics handbook: devices, circuits and applications: Academic press, 2010.

[85] B. K. Bose, "Power electronics and variable frequency drives," ed: IEEE press Piscataway, New Jersey, 1997.

[86] B. Drury, Control techniques drives and controls handbook: IET, 2001.

[87] Eutrotherm, "The Theory of Vector Control," Eutrotherm Drives Training, issue K, 2011.

[88] B. Wu, High-power converters and AC drives: John Wiley & Sons, 2006.

[89] P. I.-H. Lin. Electrical Machines and Controls, Three-Phase Induction Motors [Online]. Available: http://www.etcs.ipfw.edu/~lin/ECET211/spring2014/1-Lectures/ECET211_Lect_3pIM.htm

[90] M. Pacas, "Sensorless drives in industrial applications," Industrial Electronics Magazine, IEEE, vol. 5, pp. 16-23, 2011.

[91] L. Harnefors and M. Hinkkanen, "Stabilization methods for sensorless induction motor drives—A survey," Emerging and Selected Topics in Power Electronics, IEEE Journal of, vol. 2, pp. 132-142, 2014.

[92] N. P. Quang and J.-A. Dittrich, Vector control of three-phase AC machines: system development in the practice: Springer Science & Business Media, 2008.

[93] B. Francois, P. Degobert, and J. P. Hautier, Vector Control of Induction Machines: Desensitisation and Optimisation Through Fuzzy Logic: Springer Science & Business Media, 2012.

[94] H. Abu-Rub, A. Iqbal, and J. Guzinski, High Performance Control of AC Drives with Matlab -Simulink Models: John Wiley & Sons Ltd, 2012.

[95] X. Zhang, "Sensorless Induction Motor Drive Using Indirect Vector Controller and Sliding-Mode Observer for Electric Vehicles," Vehicular Technology, IEEE Transactions on, vol. 62, pp. 3010-3018, 2013.

[96] A. H. O. Ahmed, "Speed Sensorless Vector Control of Induction Motors Using Rotor Flux based Model Reference Adaptive System," SUST Journal of Engineering and Computer Science (JECS), vol. 16, 2015.

[97] E. Zerdali and M. Barut, "MRAS based real-time speed-sensorless control of induction motor with optimized fuzzy-PI controller," in Sensorless Control for Electrical Drives and Predictive Control of Electrical Drives and Power Electronics (SLED/PRECEDE), 2013 IEEE International Symposium on, 2013, pp. 1-5.

[98] A. R. Haron and N. R. N. Idris, "Simulation of MRAS-based speed sensorless estimation of induction motor drives using MATLAB/SIMULINK," in Power and Energy Conference, 2006. PECon'06. IEEE International, 2006, pp. 411-415.

[99] I.-W. Jeong, W.-S. Choi, and K.-H. Park, "Sensorless Vector Control of Induction Motors for Wind Energy Applications Using MRAS and ASO," Journal of Electrical Engineering & Technology, vol. 9, pp. 873-881, 2014.

[100] ABB, "Technical Guide No. 100, High Performance Drives-speed and torque regulation," in High Performance Drives-speed and torque regulation

I. ABB Industrial Systems, Ed., ed: ABB Industrial Systems, Inc., 1996.

[101] P. C. Krause, O. Wasynczuk, S. D. Sudhoff, and S. Pekarek, Analysis of electric machinery and drive systems vol. 75: John Wiley & Sons, 2013.

[102] H. Le-Huy, "Comparison of field-oriented control and direct torque control for induction motor drives," in Industry Applications Conference, 1999. Thirty-Fourth IAS Annual Meeting. Conference Record of the 1999 IEEE, 1999, pp. 1245-1252.

[103] F. Gu, Y. Shao, N. Hu, B. Fazenda, and A. Ball, "Motor current signal analysis using a modified bispectrum for machine fault diagnosis," in ICCAS-SICE, 2009, 2009, pp. 4890-4895.

[104] S. F. Legowski, A. Sadrul Ula, and A. M. Trzynadlowski, "Instantaneous power as a medium for the signature analysis of induction motors," Industry Applications, IEEE Transactions on, vol. 32, pp. 904-909, 1996.

[105] R. R. Obaid, T. G. Habetler, and D. J. Gritter, "A simplified technique for detecting mechanical faults using stator current in small induction motors," in Industry Applications Conference, 2000. Conference Record of the 2000 IEEE, 2000, pp. 479-483.

[106] R. R. Schoen and T. G. Habetler, "Effects of time-varying loads on rotor fault detection in induction machines," Industry Applications, IEEE Transactions on, vol. 31, pp. 900-906, 1995.

[107] M. Blodt, P. Granjon, B. Raison, and G. Rostaing, "Models for bearing damage detection in induction motors using stator current monitoring," Industrial Electronics, IEEE Transactions on, vol. 55, pp. 1813-1822, 2008.

[108] L. Arebi, F. Gu, N. Hu, and A. Ball, "Misalignment detection using a wireless sensor mounted on a rotating shaft," 2011.

[109] S. Ganeriwala, S. Patel, and H. Hartung, "The truth behind misalignment vibration spectra of rotating machinery," in Proceedings of International Modal Analysis Conference, 1999, pp. 2078-205.

[110] I. Ahmed, M. Ahmed, K. Imran, M. S. Khan, and S. J. Akhtar, "Detection of eccentricity faults in machine using frequency spectrum technique," International Journal of computer and electrical engineering, vol. 3, pp. 111-118, 2011.

[111] R. Stanley and P. Sognate, "Alignment of critical and noncritical machines," orbit, 1995.

[112] H. A. Gaberson and R. Cappillino, "Energy losses caused by machinery misalignment and unbalance," in Proceedings of the In-ternational Modal Analysis Conference-IMAC, 1999, pp. 1322-1327.

[113] T. H. Patel and A. K. Darpe, "Experimental investigations on vibration response of misaligned rotors," Mechanical Systems and Signal Processing, vol. 23, pp. 2236-2252, 2009.

[114] S. Nagrani, S. Pathan, and I. Bhoraniya, "Misalignment fault diagnosis in rotating machinery through the signal processing technique-signature analysis," Int J Adv Eng Res Stud E-ISSN, pp. 2249-8974, 2012.

[115] L. Arebi, F. Gu, and A. Ball, "A comparative study of misalignment detection using a novel Wireless Sensor with conventional Wired Sensors," in Journal of Physics: Conference Series, 2012, p. 012049.

[116] A. K. Jalan and A. Mohanty, "Model based fault diagnosis of a rotor–bearing system for misalignment and unbalance under steady-state condition," Journal of Sound and Vibration, vol. 327, pp. 604-622, 2009.

[117] T. Wongsuwan, P. Tangamchit, C. Prapanavarat, and M. Pusayatanont, "Motor misalignment detection based on hidden markov model," in Communications and Information Technologies, 2006. ISCIT'06. International Symposium on, 2006, pp. 422-427.

[118] M. Blodt, M. Chabert, J. Regnier, J. Faucher, and B. Dagues, "Detection of mechanical load faults in induction motors at variable speed using stator current time-frequency analysis," in Diagnostics for Electric Machines, Power Electronics and Drives, 2005. SDEMPED 2005. 5th IEEE International Symposium on, 2005, pp. 1-6.

[119] R. R. Obaid, T. G. Habetler, and R. M. Tallam, "Detecting load unbalance and shaft misalignment using stator current in inverter-driven induction motors," in Electric Machines and Drives Conference, 2003. IEMDC'03. IEEE International, 2003, pp. 1454-1458.

[120] S. Prabhakar, A. Sekhar, and A. Mohanty, "Vibration analysis of a misaligned rotor—coupling—bearing system passing through the critical speed," Proceedings of the Institution of Mechanical Engineers, Part C: Journal of Mechanical Engineering Science, vol. 215, pp. 1417-1428, 2001.

[121] S. Abusaad, A. Benghozzi, Y. Shao, F. Gu, and A. D. Ball, "Utilizing Data from a Sensorless AC Variable Speed Drive for Detecting Mechanical Misalignments," Key Engineering Materials, vol. 569, pp. 465-472, 2013.

[122] M. Li and L. He, "The dynamics of a parallel-misaligned and unbalanced rotor system under the action of non-linear oil film forces," Proceedings of the Institution of Mechanical Engineers, Part C: Journal of Mechanical Engineering Science, vol. 224, pp. 1875-1889, 2010.

[123] M. Xu and R. Marangoni, "Vibration analysis of a motor-flexible coupling-rotor system subject to misalignment and unbalance, Part I: theoretical model and analysis," Journal of Sound and Vibration, vol. 176, pp. 663-679, 1994.

[124] A. Sekhar and B. Prabhu, "Effects of coupling misalignment on vibrations of rotating machinery," Journal of Sound and vibration, vol. 185, pp. 655-671, 1995.

[125] J. Zhu, "Online Industrial Lubrication Oil Health Condition Monitoring, Diagnosis and Prognostics," University of Illinois at Chicago, 2013.

[126] P. A. B. A. Perera, "Effect of lubricating oil characteristics on gear vibrations," 1986.

[127] S. Abusaad, A. Benghozzi, K. F. Brethee, F. Gu, and A. Ball, "Investigating the Effect of Water Contamination on Gearbox Lubrication based upon Motor Control Data from a Sensorless Drive," 2014.

[128] E. E. Johnsen and H. P. Rønningsen, "Viscosity of 'live'water-in-crude-oil emulsions: experimental work and validation of correlations," Journal of Petroleum Science and Engineering, vol. 38, pp. 23-36, 2003.

[129] B. Jakoby and M. J. Vellekoop, "Physical sensors for water-in-oil emulsions," Sensors and Actuators A: Physical, vol. 110, pp. 28-32, 2004.

[130] W. Musial, S. Butterfield, and B. McNiff, "Improving wind turbine gearbox reliability," in European Wind Energy Conference, Milan, Italy, 2007, pp. 7-10.

[131] J. Zhu, D. He, Y. Qu, and E. Bechhoefer, "Lubrication oil condition monitoring and remaining useful life prediction with particle filtering," in American Wind Energy Association (AWEA), WINDPOWER 2012 Conference Proceedings, 2012, pp. 2-6.

[132] M. S. Greenwood and J. A. Bamberger, "Measurement of viscosity and shear wave velocity of a liquid or slurry for on-line process control," Ultrasonics, vol. 39, pp. 623-630, 2002.

[133] A. Agoston, C. Ötsch, and B. Jakoby, "Viscosity sensors for engine oil condition monitoring—Application and interpretation of results," Sensors and Actuators A: Physical, vol. 121, pp. 327-332, 2005.

[134] M. D. Pall and M. Vesala. Setting Control Limits for Water Contamination in Hydraulic and Lube Systems [Online]. Available: http://ebookbrowsee.net/the-10th-scandinavian-international-conference-on-fluid-power-pdf-d55044223

[135] N. S. Mehta, N. J. Parekh, and R. K. Dayatar, "Improve the Thermal Efficiency of Gearbox Using Different Type of Gear Oils," International Journal of Engineering and Advanced Technology (IJEAT), vol. 2, pp. 120-123, 2013.

[136] J. Tuma, "Gearbox noise and vibration prediction and control," International Journal of Acoustics and Vibration, vol. 14, pp. 99-108, 2009.

[137] G. R. Slemon, "Modelling of induction machines for electric drives," Industry Applications, IEEE Transactions on, vol. 25, pp. 1126-1131, 1989.

[138] M. Wieczorek and E. Rosolowski, "Modelling of induction motor for simulation of internal faults," in Modern Electric Power Systems (MEPS), 2010 Proceedings of the International Symposium, 2010, pp. 1-6.

[139] J. S. Thomsen and C. Kallesoe, "Stator fault modeling in induction motors," in Power Electronics, Electrical Drives, Automation and Motion, 2006. SPEEDAM 2006. International Symposium on, 2006, pp. 1275-1280.

[140] H. Razik, Handbook of Asynchronous Machines with Variable Speed: John Wiley & Sons, 2013.

[141] P. C. Krause, Analysis of electric machinery: McGraw-Hill Book Company, 1986.

[142] B. Ozpineci and L. M. Tolbert, "Simulink implementation of induction machine model-a modular approach," in Electric Machines and Drives Conference, 2003. IEMDC'03. IEEE International, 2003, pp. 728-734.

[143] Matlab, "Simpower Systems User's guide," 2015a.

[144] H. Børsting, M. Knudsen, H. Rasmussen, and P. Vadstrup, "Estimation of physical parameters in induction motors," Estimation of physical parameters in induction motors, pp. 553-558, 1994.

[145] M. Comanescu, "Flux and speed estimation techniques for sensorless control of induction motors," The Ohio State University, 2005.

[146] S. Maiti, C. Chakraborty, Y. Hori, and M. C. Ta, "Model reference adaptive controller-based rotor resistance and speed estimation techniques for vector controlled induction motor drive utilizing reactive power," Industrial Electronics, IEEE Transactions on, vol. 55, pp. 594-601, 2008.

[147] G. Besançon and A. Ţiclea, "State observers for estimation problems in induction motors," AC Electric Motors Control: Advanced Design Techniques and Applications, pp. 57-77, 2013.

[148] S.-H. Kim and S.-K. Sul, "Maximum torque control of an induction machine in the field weakening region," Industry Applications, IEEE Transactions on, vol. 31, pp. 787-794, 1995.

[149] K. Emami, T. Fernando, B. Nener, H. Trinh, and Y. Zhang, "A functional observer based fault detection technique for dynamical systems," Journal of the Franklin Institute, vol. 352, pp. 2113-2128, 2015.

[150] J. Marzat, H. Piet-Lahanier, F. Damongeot, and E. Walter, "Model-based fault diagnosis for aerospace systems: a survey," Proceedings of the Institution of Mechanical Engineers, Part G: Journal of Aerospace Engineering, p. 0954410011421717, 2012.

[151] S. Simani, C. Fantuzzi, and R. J. Patton, Model-based fault diagnosis in dynamic systems using identification techniques: Springer Science & Business Media, 2013.

[152] S. X. Ding, Model-based fault diagnosis techniques: design schemes, algorithms, and tools: Springer Science & Business Media, 2008.

[153] J. Chen and R. J. Patton, Robust model-based fault diagnosis for dynamic systems vol. 3: Springer Science & Business Media, 2012.

[154] J. Zhang, H. Wen Xu, and Y. Hua, "Practical speed estimation method for induction motor vector control system using digital signal processor(DSP)," in Electrical Machines and Systems, 2008. ICEMS 2008. International Conference on, 2008, pp. 74-78.

[155] S. H. Kia, H. Henao, and G.-A. Capolino, "Torsional vibration monitoring using induction machine electromagnetic torque estimation," Industrial Electronics, IEEE Transactions on, pp. 3120-3125, Nov. 2008 2008.

[156] S. T. Karris, Circuit Analysis II: With MATLAB Computing and Simulink/SimPowerSystems Modeling: Orchard Publications, 2009.

[157] Q. P. He, J. Wang, M. Pottmann, and S. J. Qin, "A curve fitting method for detecting valve stiction in oscillating control loops," Industrial & engineering chemistry research, vol. 46, pp. 4549-4560, 2007.

[158] M. Jelali, "Control performance management in industrial automation," Advances in Industrial Control, DOI, vol. 10, pp. 978-1, 2013.

[159] G. Niu and B.-S. Yang, "Intelligent condition monitoring and prognostics system based on data-fusion strategy," Expert Systems with Applications, vol. 37, pp. 8831-8840, 2010.

[160] A. Ginart, I. Barlas, J. Goldin, and J. L. Dorrity, "Automated feature selection for embeddable prognostic and health monitoring (PHM) architectures," in Autotestcon, 2006 IEEE, 2006, pp. 195-201.

[161] M. Blödt, D. Bonacci, J. Regnier, M. Chabert, and J. Faucher, "On-line monitoring of mechanical faults in variable-speed induction motor drives using the Wigner distribution," Industrial Electronics, IEEE Transactions on, vol. 55, pp. 522-533, 2008.

[162] I. Redmond, "Study of a misaligned flexibly coupled shaft system having nonlinear bearings and cyclic coupling stiffness—Theoretical model and analysis," Journal of Sound and Vibration, vol. 329, pp. 700-720, 2010.

[163] K. Michaelis, B.-R. Höhn, and M. Hinterstoißer, "Influence factors on gearbox power loss," Industrial lubrication and tribology, vol. 63, pp. 46-55, 2011.

[164] K. Michaelis and H. Winter, "Influence of lubricants on power loss of cylindrical gears," 48th Annual Meeting, Calgary, Tribology Transactions, Alberta,, vol. 37, pp. 161-167, 1994.

[165] B. R. Höhn and K. Michaelis, "Influence of oil temperature on gear failures," Tribology International, vol. 37, pp. 103-109, 2004.

[166] H. Mizutani, Y. Isikawa, and D. P. Townsend, "Effects of lubrication on the performance of high speed spur gears," DTIC Document1989.

[167] J. Zhu, J. Yoon, D. He, B. Qiu, and E. Bechhoefer, "Online condition monitoring and remaining useful life prediction of particle contaminated lubrication oil," in Prognostics and Health Management (PHM), 2013 IEEE Conference on, 2013, pp. 1-14.

[168] J. Zhu, J. M. Yoon, D. He, and E. Bechhoefer, "Online particle-contaminated lubrication oil condition monitoring and remaining useful life prediction for wind turbines," Wind Energy, vol. 18, pp. 1131-1149, 2015.

[169] B. J.C. (2004, Predictive & Preventive Maintenance in Lubricating Systems. DES-CASE Europe sarl. Available: : http://www.descase-europe.com/uploads/1256143218_lubricated_systems.pdf

[170] A. I. Echin, G. T. Novosartov, and T. B. Kondrat'eva, "Effect of water on lubricating properties of synthetic oils," Chemistry and Technology of Fuels and Oils, vol. 19, pp. 80-83, 1983/02/01 1983.

[171] R. Almeida and L. R. Padovese, "Characterization of oil viscosity alterations in a gearbox through vibration signal analysis," Anais do COBEM, 2003.

[172] S. Rajagopalan, T. G. Habetler, R. G. Harley, T. Sebastian, and B. Lequesne, "Current/voltage-based detection of faults in gears coupled to electric motors," Industry Applications, IEEE Transactions on, vol. 42, pp. 1412-1420, 2006.

[173] C. Gorla, F. Concli, K. Stahl, B.-R. Höhn, M. Klaus, H. Schultheiß, et al., "CFD simulations of splash losses of a gearbox," Advances in Tribology, vol. 2012, 2012.

[174] N. E. Anderson and S. H. Loewenthal, Spur-gear-system efficiency at part and full load vol. 79: National Aeronautics and Space Administration, Scientific and technical Information Office, 1980.

[175] B.-R. Höhn, K. Michaelis, T. Vollmer, and A. G. M. Association, Thermal rating of gear drives: balance between power loss and heat dissipation: American Gear Manufacturers Association, 1996.

[176] L. Magalhães, R. Martins, C. Locateli, and J. Seabra, "Influence of tooth profile and oil formulation on gear power loss," Tribology International, vol. 43, pp. 1861-1871, 2010.

[177] A. Olver, "Gear lubrication—a review," Proceedings of the Institution of Mechanical Engineers, Part J: Journal of Engineering Tribology, vol. 216, pp. 255-267, 2002.

[178] R. Martins, J. Seabra, A. Brito, C. Seyfert, R. Luther, and A. Igartua, "Friction coefficient in FZG gears lubricated with industrial gear oils: Biodegradable ester vs. mineral oil," Tribology International, vol. 39, pp. 512-521, 2006.

[179] D. E. Gonçalves, C. M. Fernandes, R. C. Martins, and J. H. Seabra, "Torque loss in a gearbox lubricated with wind turbine gear oils," Lubrication Science, vol. 25, pp. 297-311, 2013.

[180] BS, "BS PD ISO/TR 18792:2008 Lubrication of industrial gear drives," vol. PD ISO/TR 18792:2008, ed. UK, 2008.

[181] B. I. 3448:1992, "Classification for Viscosity grades of industrial liquid lubricants," vol. UDC 665.765:532.133, ed. UK: BS, 1992.

[182] J. R. Davis, Gear materials, properties, and manufacture: ASM International, 2005.

[183] R. W. Bruce, CRC Handbook of Lubrication: Theory and Practice of Tribology, Volume II: Theory and Design vol. 2: CRC Press, 1988.

[184] R. Speyer, Thermal analysis of materials: CRC Press, 1993.

Appendix A

Time Synchronous Averaging (TSA)

The TSA reduces the random noise element and removes in-periodical vibration components. This improves the signal to noise ratio (SNR) of the collected signals for more accurate feature calculation. In addition, TSA aligns signals according to the angular position of a particular rotating shaft, which allows phase information to be taken into account and to eliminate the influences of random speed variations. TSA has been found to be very efficient in cleaning signals subject to time varying processes by suppressing random noise and noise from uncorrelated sources such as vibrations from nearby components.

There are many TSA methods. For computational efficiency and reliable implementation, a shaft encoder based method has been used. The shaft encoder, mounted on the input shaft, produces 100 pulses per turn as the angular position reference signal. The wireless vibration and reference signals were measured simultaneously and sampled at a rate of 96 kHz for 20 seconds at each of the operating settings.

The equation used to derive the synchronous average y(t) of time signal x(t) using trigger signal c(t) having a frequency f_t is equivalent to the convolution of x(t) and c(t) .

$$y(t) = c(t) * x(t) \quad \text{A.1}$$

Where c(t) is a train of N impulses of amplitude 1/N, spaced at intervals $T_t = 1/f_t$ given by;

$$c(t) = \frac{1}{N}\sum_{n=0}^{N-1} \delta(t + nT_t) \quad \text{A.2}$$

This equivalent to multiplication of Fourier transform X(f) of the signal by C(f) in the frequency domain and can be represented by;

$$Y(f) = C(f).X(f) \quad \text{A.3}$$

Where C(f) is a comb filter function of the form;

$$C(f) = \frac{1}{N}\,\frac{\sin(\pi N T_t f)}{\sin(\pi T_t f)} \quad \text{A.4}$$

Increasing the number of averages N narrows the peak of the comb and reduces the amplitude of the side lobes between the peaks. Thus, in the frequency domain, synchronous averaging for large values of N can be seen as the complete removal of all components except those that occur at integer multiples of frequency f_t.

Appendix B

Rotary Viscosity Measurements

The viscosity is measured by an instrument based on rotary viscometer test method, as shown in Figure B.1.

Figure B.1 the viscosity rotary meter

The tested oil is placed on a flat plate and covered by insulated block at varying controlled temperature. A metal spindle (with cone shape head) is placed in the oil leaving about 0.07 millimetre gap from the base metal and rotates at fixed rpm speed, i.e. at about 200rpm, see Figure 2.1. The instrument also regulates the temperature of the oil and measurements are taken at different temperature conditions. Thus, from knowing the rotational speed, torque, and the probe geometry both shear rate and shear stress can be determined. The oils absolute viscosity is then calculated based on the resistance to rotate that the oil made due to its shear stress. The absolute viscosity is given in centipoise (cP), equivalent to Pa·s in SI units[183, 184].

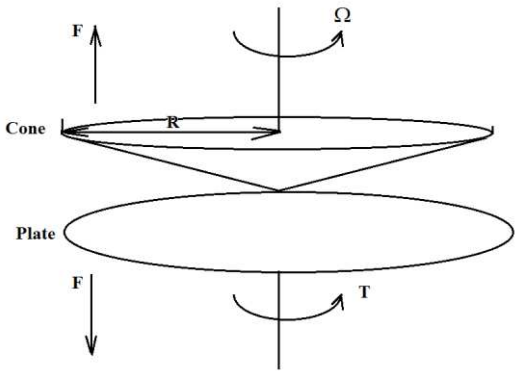

Figure B.2. Cone-Plate rotary viscometer

The viscosity is calculated from[183-185]:

$$\eta = \frac{\tau}{\dot{\gamma}} \tag{B-1}$$

Where: η the viscosity, τ shear stress, and $\dot{\gamma}$ the shear rate.

Both shear stress and shear rate can be determined from the torque, rotation speed and instrument geometry and therefor the viscosity can be calculated as follows[183-185]:

$$\eta = \frac{T}{\Omega} C \tag{B-2}$$

Additionally, using the same instrument the first normal stress (N1), which is resulted from the tension in the streamlines, is also measured. The idea is that the tension in the streamlines produces an axial violent lunge pushing the cone and plate separately with a force that can be measured. The first normal stress is calculated from [185, 186]:

$$N1 = \frac{2F}{\pi R^2} \tag{B-3}$$

Where: T measured torque, Ω rotation speed (rad/s), and C is a constant specific to the instrument, F resulted force, R cone radius.

Both normal stress difference and the shear viscosity are together called viscometric functions; and they are the material functions properties of the fluid in shear (viscometric) flow. When the cane rotates, the oil climbs around the centre; this called the "Weissenberg rod-climbing effect" or the viscoelasticity of the fluid. This is due to the fact that the fluid element being able to support a tension along a streamline (because of non-zero normal stress differences), which bulges the fluid up. The generated force works to separate the cone from the plate [185].

Therefore, results from oil analysis provided from the chemical laboratory include viscosity (Pa·s), torque (N.m), normal force (N), first normal stress difference (Pa) and shear stress (Pa). All parameters are measured at different temperature: 20, 25, 30, 35, 40, 45, 50 and 55 ^{o}c.

Appendix C

Additional Results from Water in Oil Contamination Tests

Current amplitudes at the f_{r1}, f_{r2} and f_{r3} sideband are not consistent with water contents.

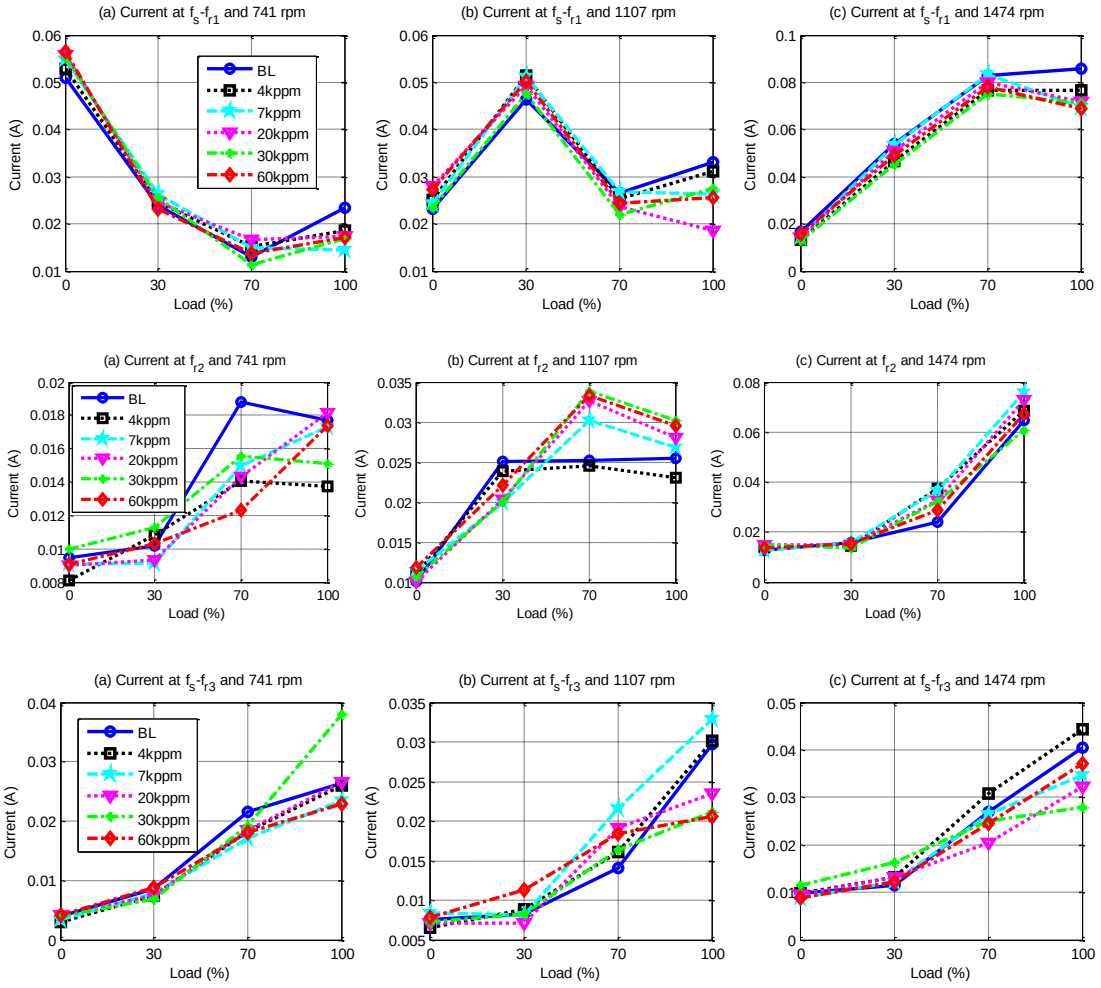

Similarly, voltage amplitudes at the f_{r1}, f_{r2} and f_{r3} sideband are not consistent with water contents.

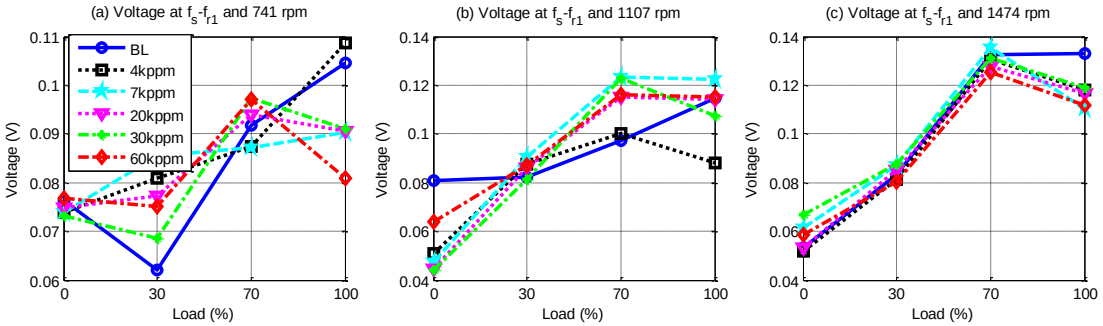

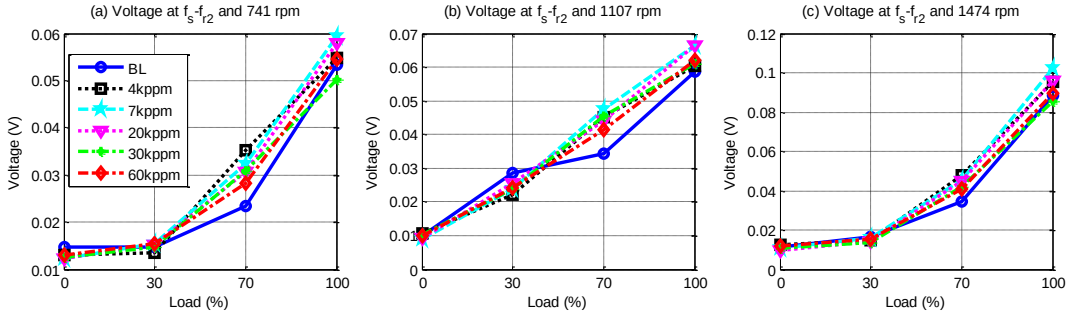

Motor torque has showed undistinguishable behaviours against water content levels.

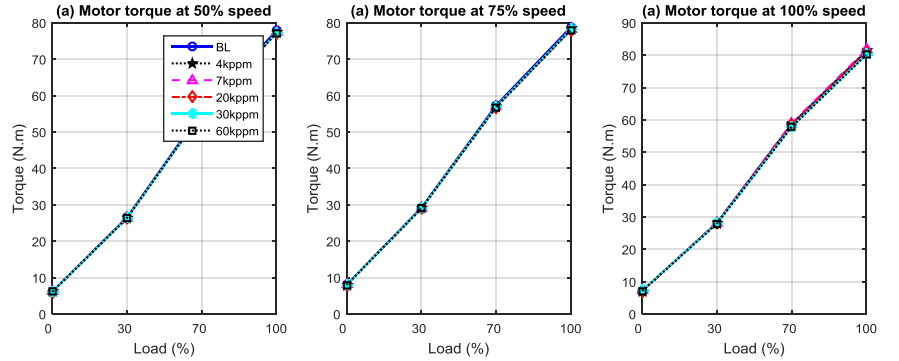

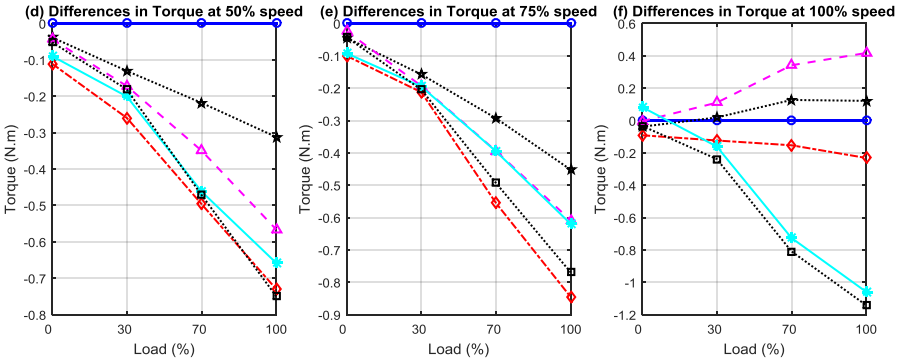

Appendix D

Additional Results from Viscosity Tests

Current amplitudes at the f_{r1}, f_{r2} and f_{r3} sidebands are not consistent with oil viscosity.

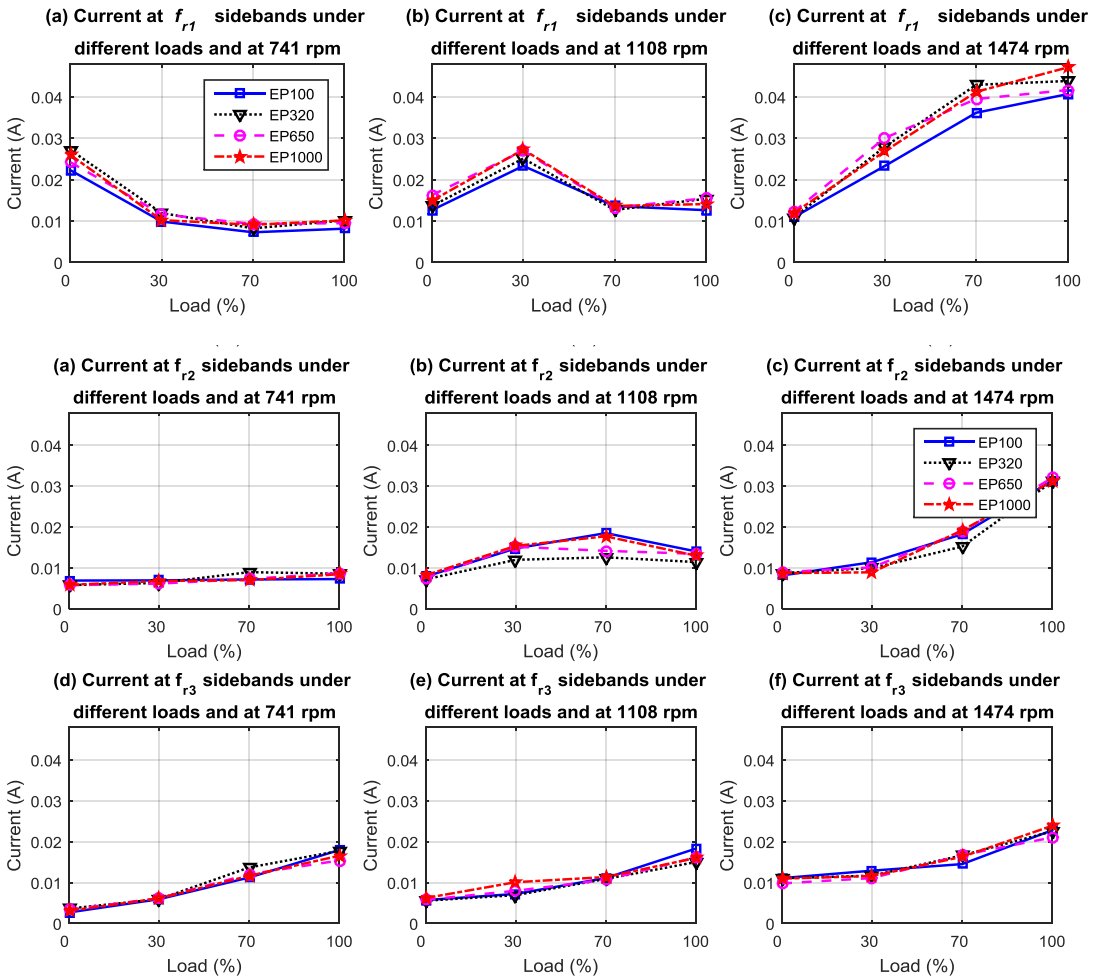

Voltage amplitudes at f_{r1}, f_{r2}, f_{r3} sidebands have changed inconsistently with viscosity.

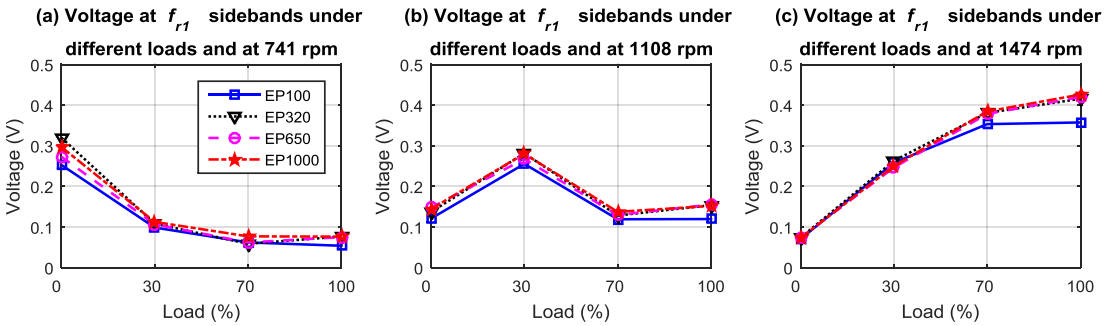

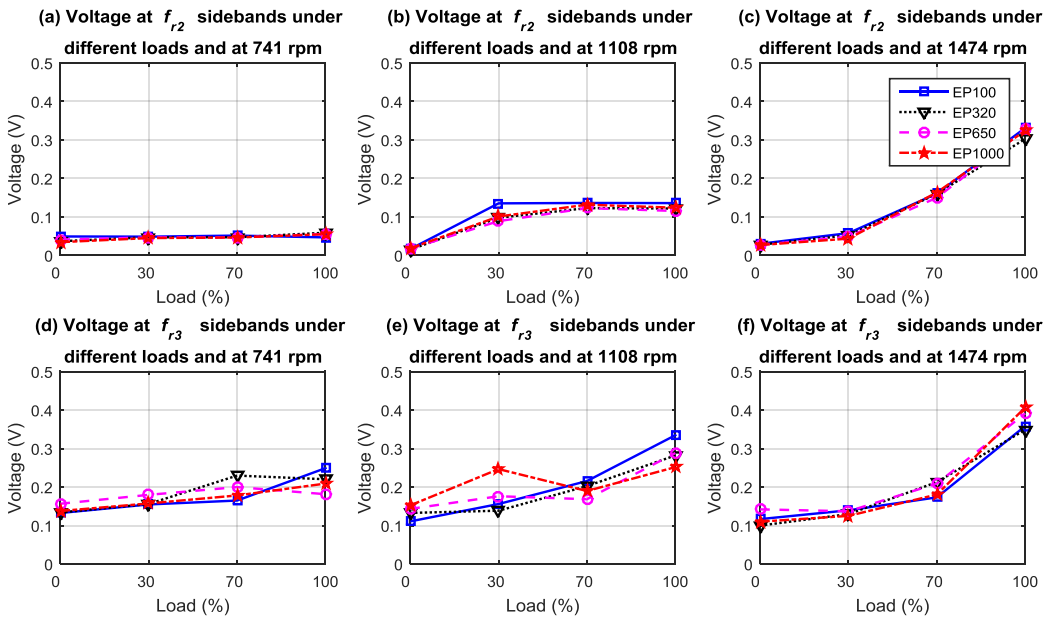

Power at f_{r2} and f_{r3} sidebands have also been changed inconsistently with viscosity

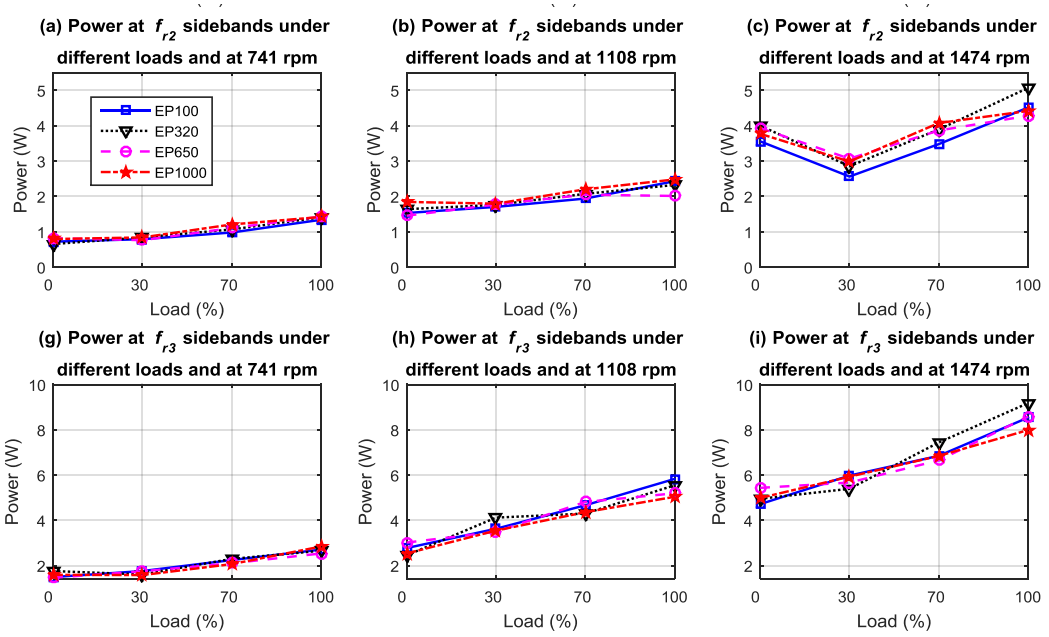

Appendix E

Additional Results from Oil Level Tests

Current amplitudes at the f_{r1}, f_{r2} and f_{r3} sidebands are not consistent with oil level.

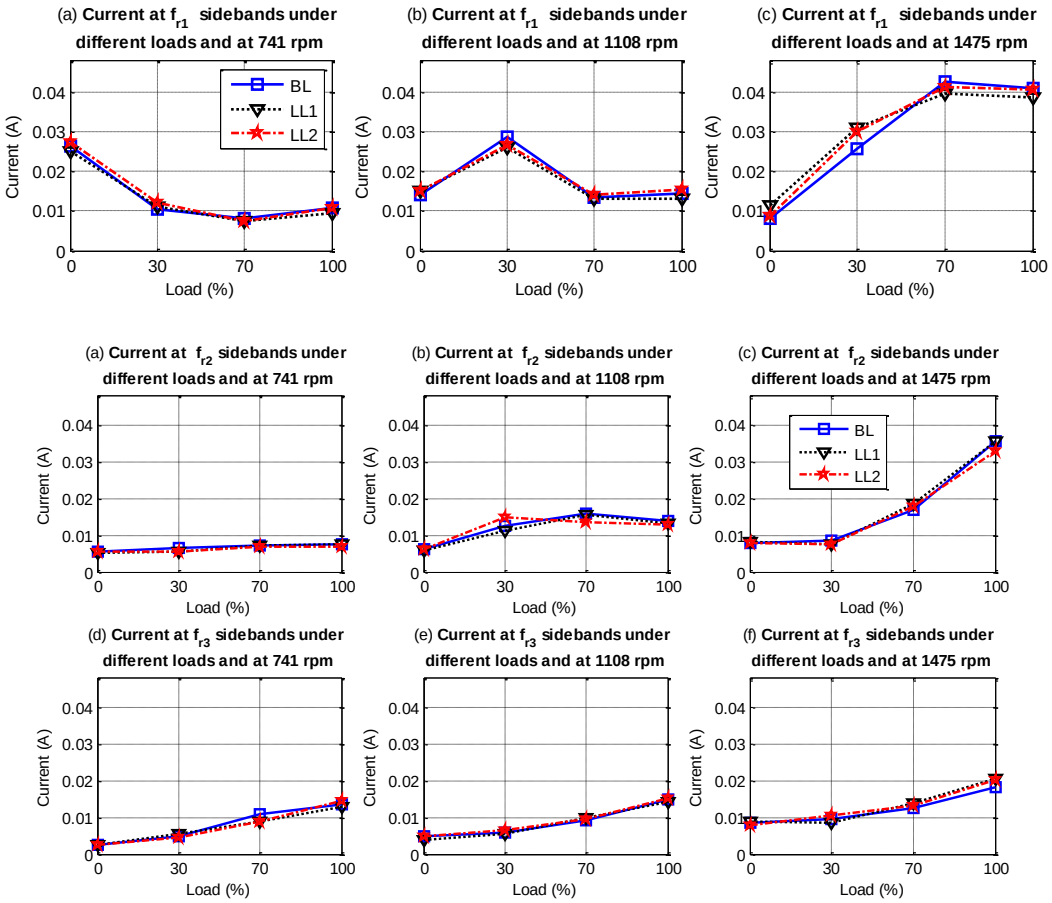

Voltage amplitudes at f_{r1}, f_{r2}, f_{r3} sidebands have changed inconsistently with viscosity.

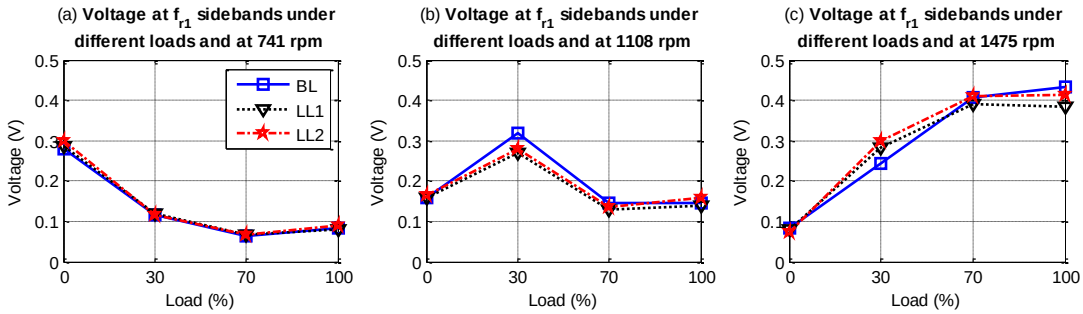

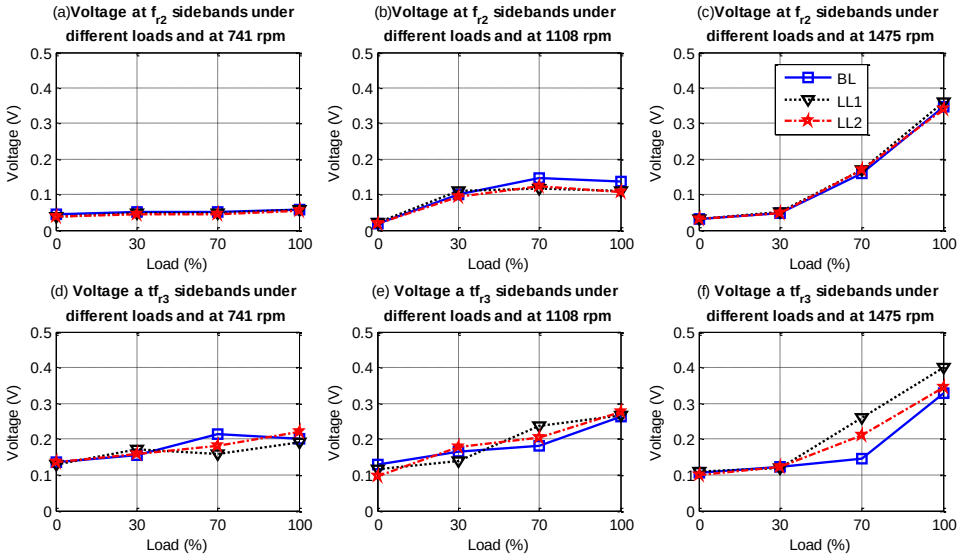

Power at $2f_{r2}$ and $2f_{r3}$